Understanding chemical, biogenic, and detrital magnetic signatures in sediments

Sophie C. Roud

München 2021

Understanding chemical, biogenic, and detrital magnetic signatures in sediments

Sophie C. Roud

Dissertation
zur Erlangung des Doktorgrades
an der Fakultät für Geowissenschaften
der Ludwig–Maximilians–Universität
München

vorgelegt von

Sophie C. Roud

München, den 9.9.2021

Erstgutachter: Prof. Dr. Stuart A. Gilder

Zweitgutachter: Prof. Dr. Ian Snowball

Tag der mündlichen Prüfung: 28.1.2022

Summary

Much of Earth's history is recorded by sediments and sedimentary rocks. Paleo- and environmental magnetism help to explore these geologic records by providing paleoenvironmental proxies, stratigraphic tie-points, information about continental plate motion and about geomagnetic field variations through time. A major challenge in paleo- and environmental magnetism is to distinguish depositional from post-depositional signatures. This thesis explores both types of magnetic signatures in natural sediment archives and provides fundamental research aiming to elicit bio- and geochemical processes that can modify the magnetic mineral inventory and overprint paleomagnetic records. A magnetostratigraphic study of fluvio-lacustrine sediments from Central Asia provides a chronology for the Mio-Pleistocene syn-tectonic deposits of the Issyk-Kul Basin. From these age constraints we determined the onset of mountain building and the timing of tectonic events, which transformed the area into a closed basin that now hosts one of the deepest mountain lakes on Earth. In a study of modern surface sediments, we investigated magnetotactic bacteria (MTB), which are ubiquitous in benthic environments worldwide and biosynthesize intracellular magnetic minerals. When preserved in the rock-record these magnetofossils represent ideal recorders of the Earth's magnetic field and their concentration has been linked to paleoclimatic variations. Understanding what controls MTB abundance remains, however, limited. By monitoring spatiotemporal changes in the population of MTB in a freshwater pond, we inferred coeval changes of the population size among nearby sites that were largely independent of season, temperature, and bottom water oxygen concentration. Variations of the magnetofossil concentration are treated in a separate study on marine sediments from the western Tropical Atlantic. Systematic glacial-interglacial variations were linked to changes in palaeoceanographic conditions at the site, which supports that magnetofossils represent sensitive paleoclimatic biomarkers. Finally, post-depositional chemical remagnetization is addressed through novel laboratory experiments that recreate this process under controlled conditions. Greigite (Fe_3S_4), a common authigenic magnetic mineral, was synthesized in artificial sediments under controlled magnetic field conditions. The formation pathway and magnetic properties of greigite are characterized, and the evolution of chemical remanent magnetization (CRM) monitored via real-time, in-situ magnetic measurements. Redeposition of the greigite-bearing sediments lead to depositional magnetizations that were 5-6 times weaker than the CRMs recorded by the same grains under the same magnetic field conditions. The results are consistent with theoretical models of the different magnetic recording mechanism and show for the first time how magnetic mineral growth in sediments can bias paleomagnetic reconstructions of Earth's magnetic field intensity.

Contents

On all these shores there are echoes of past and future: of the flow of time, obliterating yet containing all that has gone before; of the sea's eternal rhythms—the tides, the beat of surf, the pressing rivers of the currents—shaping, changing, dominating; of the stream of life, flowing as inexorably as any ocean current, from past to unknown future.

For as the shore configuration changes in the flow of time, the pattern of life changes, never static, never quite the same from year to year.

Rachel Carson, The Edge of the Sea, 1955

Preface

The vast majority of Earth's surface is covered by sediments—on land and on the ocean floor. Layer by layer, these sediments preserve Earth's history. By studying continuous sediment sequences, we can learn about the environmental conditions during the time the sediments were deposited and about organisms that inhabited these environments. Furthermore, we can explore the origin of the sediment's constituents, the dynamics of mountain building, erosion of the source areas, and sedimentary transport mechanisms. Diagenesis and tectonic deformation can erase this primary information but leave other traces that can themselves help understand the involved geological processes. The magnetism of sediments has contributed significantly to our current understanding of these processes and the geologic history of our planet.

Each chapter of this thesis explores a different aspect of sediment magnetism, and all are based on published articles or manuscripts in preparation for peer reviewed, scientific journals. My contributions to these articles are stated in the following *List of Publications* and described in more detail at the beginning of each chapter. In the introduction I briefly describe the fundamentals of what makes sediments magnetic and the significance of rock and paleomagnetism for understanding Earth's history. The introduction also serves as an outline for this thesis and points out how this work contributes to advancing some of the frontiers of the discipline.

Acknowledgments

Foremost I would like to express my gratitude to my advisor Prof. Stuart Gilder for facilitating science with an open mind, giving me the opportunity to work on diverse research projects, believing in my abilities, and for his persistence to gain funding for my work. Stu, thank you for your awesome support over the years, and patience to letting me science the things my way. I always appreciate you inspiring the impossible: brain chopping, rock drilling, bacteria tracking, figuring out the impossible greigite—hunting scientific elephants has been a winding road and tremendous fun.

I am grateful for financial support of the Deutsche Forschunggemeinschaft who supported three years of my research. I also like to thank the staff of the Department of Earth and Environmental Sciences at Ludwig-Maximilians University for providing the necessary infrastructure. This work would not have been possible, without the amazing LMU rock-mag lab. Thus, I would like to thank Prof. Dr. Stuart Gilder, Dr. Michael Wack, Dr. habil. Florian Lhuillier and all current and previous group members who helped creating and maintaining an excellent research facility. Also, the workshop teams around Markus Sieber and Günter Hesberg have been of great help, building new equipment that was instrumental for this work. Thanks to Rainer, Stefan and Max for your ideas and help constructing my odd greigite ovens. Moreover, I wish to thank Prof. Dr. Sohyun Park and Dr. Erika Griesshaber for their advice and help with X-ray diffraction and scanning electron microscopy analysis.

Thanks also go to all LMU colleagues, research guests and my collaborators particularly from Potsdam and Sao Paulo, for fruitful discussions, insightful comments, and suggestions. Shout-outs to the guys and gals, with whom I shared the office over the last years and special cheers to my loyal lunch people of the pre-pandemic times, in particularly to Prof. Nikolai Petersen for his encouragement and friendly council since many years.

Jan, thank you for being there, lighting up the cloudy and the sunny days, always.

List of Publications

Publication I

He, K., **Roud, S. C.**, Gilder, S. A., Egli, R., Mayr, C., & Petersen, N. (2018). **Seasonal variability of magnetotactic bacteria in a freshwater pond**. *Geophysical Research Letters*, *45*(5), 2294-2302. https://doi.org/10.1002/2018GL077213.

Roud S. C. contributions*: Investigation, Formal analysis, Writing – review & editing, Methodology.

Publication II

Mathias, G. L., **Roud, S. C.**, Chiessi, C. M., Campos, M. C., Dias, B. B., Santos, T. P., ... & Maher, B. A. (2021). **A Multi-Proxy Approach to Unravel Late Pleistocene Sediment Flux and Bottom Water Conditions in the Western South Atlantic Ocean**. *Paleoceanography and Paleoclimatology*, *36*(4), e2020PA004058. https://doi.org/10.1029/2020PA004058

Roud S. C. contributions*: Formal analysis, Investigation, Conceptualization, Writing - review & editing, Visualization.

Publication III

Roud, S. C., Wack, M. R., Gilder, S. A., Kudriavtseva, A., & Sobel, E. R. (2021). **Miocene to Early Pleistocene Depositional History and Tectonic Evolution of the Issyk-Kul Basin, Central Tian Shan.** *Geochemistry*, *Geophysics*, *Geosystems*, *22*(4), e2020GC009556. https://doi.org/10.1029/2020PA004058

Roud S. C. contributions*: Conceptualization, Writing - Original Draft, Formal analysis, Investigation, Visualization.

Manuscript IV

Roud, S.C., Gilder, S. A. and Park S. (2022). (in press) **Greigite (Fe_3S_4) formation in artificial sediments via solid-state transformation of lepidocrocite.** *Geochemistry*, *Geophysics*, *Geosystems.* https://doi.org/10.1029/2022GC010376

Roud S. C. contributions*: Conceptualization, Writing - Original Draft, Investigation, Formal analysis, Methodology, Visualization.

Manuscript V

Roud, S.C. and Gilder, S. A. (2022). **Chemical and Depositional Magnetic Recording in Greigite-bearing Sediments** [In preparation for *Journal of Geophysical Research: Solid Earth*]

Roud S. C. contributions*: Conceptualization, Writing - Original Draft, Investigation, Formal analysis, Methodology, Visualization.

*Author contribution statement following CRediT (Contributor Roles Taxonomy) https://credit.niso.org/

Introduction

1. Principles of rock and environmental magnetism of sediments

Rock- and environmental magnetism explores sedimentologic processes preserved in the rock-record by analyzing ferromagnetic constituents, usually iron oxides, or sulfides. These magnetic minerals are ubiquitous on Earth and generally occur in all rock types. Iron (Fe) is among the most common elements in the Earth's crust but not all Fe-compounds are magnetic (meaning ferromagnetic, ferrimagnetic, or antiferromagnetic). Although, magnetic particles often constitute less than 1% of the bulk sediment volume and are extremely small (nano to micron sized) they can easily be detected and analyzed in a non-destructive way in the bulk sediment *(Evans and Heller, 2003)*.

Common magnetic minerals are the iron oxides magnetite (Fe_4O_3), hematite (Fe_3O_2) and the oxyhydroxide goethite (αFeOOH), which can be distinguished by their unique magnetic properties. Magnetite can occur in various oxidation states and all Fe-oxides can contain metal substitutions such as titanium or aluminum that alter their magnetic signatures. The only known magnetic Fe-sulfides are greigite (Fe_3S_4) and pyrrhotite (Fe_7S_8), which commonly occur in reducing environments. Because the sulfides are oxygen-sensitive and rare in comparison to the oxides, their magnetic properties are less well studied and less well understood.

Magnetic properties depend strongly on grain size, which determines if a particle retains a magnetization in the absence of a magnetic field (magnetic remanence). Particles that can hold a remanent magnetization are classified into three categories, determined by the number of magnetic domains (regions of uniform magnetic direction) that they host - again a function of their grain size. From small to large size these are: single domain, SD, pseudo single domain, PSD, and multi domain, MD. As magnetic domains tend to cancel each other out, larger grains have a smaller magnetic remanence compared to their saturation magnetization in a strong magnetic field. Grains of a magnetic mineral that are too small to hold remanent magnetizations are referred to as super-paramagnetic, SP. The grain size threshold above which a particle becomes a permanent magnet then is referred to as the SP/SD threshold. In magnetite the SP/SD threshold lies commonly between 10-50 nm, but it is different for different types of minerals and furthermore depends on particle shape, magnetic interactions with nearby grains and temperature (Dunlop and Özdemir, 1997).

Rock magnetic techniques are fast, non-destructive, and sensitive to identify minute changes in the composition or grain size of the magnetic mineral fraction that can relate to the history of a sediment. Usually, sediments contain a mixed magnetic mineral assemblage. Magnetic proxy parameters then become non-unique, meaning they can be explained by different combinations of magnetic mineral types and grain ensembles. Thus, particularly when combined with geochemical and sedimentological investigations, rock magnetism is a powerful tool to decipher the history of sedimentary archives (e.g. Maher and Thompson, 1999).

2. Post-depositional changes in the rock magnetic record

Apart from primary (detrital) magnetic grains, sediments can contain secondary magnetic minerals that were produced in-situ through biotic or abiotic processes. One ubiquitous source of biogenic particles is magnetotactic bacteria (MTB), which are microbes that live along redox gradients in aquatic environments, usually close to the water-sediment interface. These organisms synthesize single domain nanoparticles inside their cells – so called magnetosomes – which are often arranged in chains. Their size and arrangement appear to be optimized to maximize the remanent magnetization of the organism for a passive alignment in the Earth's magnetic field. Possibly this creates an advantage for these specialized microbes to find and remain in their optimal microhabitats (Lefèvre and Bazylinski, 2013).

When preserved in the sediments, magnetosomes become magnetofossils that represent ideal SD magnetic carriers that, due to their unique magnetic signature, can be identified by rock-magnetic methods in the sedimentary "haystack", even when they represent only a minor fraction of the magnetic grain ensemble (Roberts et al., 2012). Some studies have suggested that the abundance and type of magnetofossils is related to environmental conditions when the microbes lived (Hesse, 1994; e.g. Kopp et al., 2007; Roberts et al., 2011b). Many aspects of MTB distributions in natural sediments, however, remain poorly understood, particularly aspects concerning their metabolism and living conditions.

Chapter I of this thesis aims to contribute to a better understanding of what governs the natural distribution of MTB and how well their population in one sampling site can reflect the conditions of an ecosystem. We investigated the living MTB population in a natural freshwater environment by analyzing the temporal and spatial variability in the abundances of three magnetotactic phenotypes over the course of two years. The study showed that,

while fluctuations in the number of one phenotype were mostly consistent in space and time, the growth rates of different MTB groups were generally unrelated, e.g. while rod shaped bacteria nearly died out at one point, other types were unaffected. The results suggested that in the investigated, shallow water environment, which was strongly affected by short term, seasonal variations, the total number of MTB was not a representative parameter, as the abundance of different MTB types was unrelated (**Publication I** titled "Seasonal variability of magnetotactic bacteria in a freshwater pond" by He, K., Roud, S. C., Gilder, S. A., Egli, R., Mayr, C., & Petersen, N. in the Journal Geophysical Research Letters, 2018).

This observation is however not directly transferable to other environments. For instance, in deep sea environments, where conditions are more stable for longer times, it appears reasonable that the microbial population is in better equilibrium with its environment and, thus, may reflect long term changes in the availability of basic nutrients.

Chapter II explores the rock magnetism of a marine environment. A sediment core from the continental slope off SE Brazil is investigated with a multiproxy approach, combining magnetic, sedimentologic and geochemical methods. From magnetic mineral concentration, elemental composition, and grain size of the bulk sediment, we reconstructed variations in the sediment transport by ocean currents. More detailed rock magnetic analyses showed that a "pool" of SD magnetite grains with typical characteristics of magnetosomes, was present throughout the core. The concentration of these presumed magnetofossils was unrelated to the concentration of terrigenous sediments but correlated with the organic matter concentration as well as with proxies for bottom water conditions. Assuming that the magnetofossil concentration was unaffected by post-depositional processes, the results indicate that the MTB population (as a whole) may have responded to environmental changes on glacial-interglacial timescales. (**Publication II** titled "A Multi-Proxy Approach to Unravel Late Pleistocene Sediment Flux and Bottom Water Conditions in the Western South Atlantic Ocean" by Mathias, G. L., Roud, S. C., Chiessi, C. M., Campos, M. C., Dias, B. B., Santos, T. P., ... & Maher, B. A. in the journal Paleoceanography and Paleoclimatology, 2021).

3. Paleomagnetism of sediments

Over 70 years ago, Johnson et al. (1948) first suggested that the remanent magnetization in sediments is controlled by the strength of the Earth magnetic field, which they demonstrated by re-depositing natural sediments in the laboratory under variable magnetic field conditions. The magnetic recording process during sedimentation is governed by a balance between the

aligning energy of magnetic torque that acts on a ferromagnetic grain and randomization by thermal energy (Brownian motion). The resulting natural remanent magnetization (NRM) is referred to as depositional (or detrital) remanent magnetization (DRM) (Nagata, 1961; Stacey and Banerjee, 1974).

Since then, countless studies on magnetism of natural sediments and the fundamental properties of DRM have shown that sedimentary sequences around the world collectively contain a nearly continuous record of the Earth's magnetic field. These paleomagnetic records have become a vital part for the general understanding of Earth's history. Records of paleomagnetic field direction are the backbone of plate tectonics (Butler, 1992), they provide magnetostratigraphic chronologies for marine and continental sediment sequences, and build a global reference for the geologic timescale (Ogg, 2020). Dipolar geomagnetic field variations recorded in individual sequences are globally synchronized and therefore provide crucial stratigraphical tie-points to correlate sedimentary archives such as deep-sea cores from different ocean basins (Stoner et al., 2002).

High-resolution chronologies (thousand-year timescales) stem from time series of relative paleointensity (RPI) records (Valet, 2003; Channell et al., 2009; Roberts et al., 2013b). Such records are a direct stratigraphic tool, but also contribute to a better understanding of the Earth's magnetic field itself and serve as important boundary conditions for magnetic field models. Because the strength of the Earth's magnetic field also controls the intensity of cosmic radiation that reaches the atmosphere and the Earth's surface, RPI records are also important for calibrating radionuclide based ages e.g. for radiocarbon or surface exposure dating (Gosse and Phillips, 2001; Weninger and Jöris, 2008).

Chapter III details a classic paleomagnetic case study, where I dated terrestrial sediment sequences from from the Tian Shan mountains (Central Asia). Paleomagnetic analysis suggested the rocks carry primary DRMs, from which we deduced magnetic polarity (reversal) sequences. Correlation to the global reference scale of two new and two previously published sequences yielded a nearly complete magnetostratigraphy for the Cenozoic syn-tectonic sediments that fill the Issyk-Kul Basin. The new age constrains allowed to determine sedimentation rates, which together with a general sedimentologic and geologic investigation allowed to reconstruct the uplift history of the surrounding mountain ranges, and to better constrain when Lake Issyk-Kul, the deepest mountain lake in Central Asia, was formed (***Publication III*** tiled "Miocene to Early Pleistocene Depositional History and Tectonic

Evolution of the Issyk-Kul Basin, Central Tian Shan" by Roud, S. C., Wack, M. R., Gilder, S. A., Kudriavtseva, A., & Sobel, E. R. in the journal Geochemistry, Geophysics, Geosystems, 2021).

4. Post-depositional changes in the paleomagnetic record

To obtain reliable, continuous magnetic field records that accord with the age of the sediment, it is crucial that the natural remanence is a DRM and was acquired when the sediments got deposited. Post-depositional processes can however alter, erase, or overprint the primary magnetization. Bioturbation can lead to a realignment of magnetic grains in the sediment and small magnetic grains can remain free to rotate in a coarse unconsolidated sediment matrix, causing small grains to be locked-in at greater depths and therefore smooth the paleomagnetic record. Associated post-depositional remanent magnetization, pDRM is considered common in aquatic sediments. Being usually confined to the surface layer, only minor uncertainties arise from to these processes (Kodama, 2012).

The aforementioned fossil remains of MTB are often considered to carry a primary pDRM, as mixing in the surface layer affects detrital and biogenetic magnetic grains in the same way, although the depth range at which biogenic magnetite can be produced is largely unknown. The narrow grain size range and SD properties make magnetofossils generally ideal paleomagnetic magnetic recorders compared to detrital grains with a broader grain size distribution. Particularly in deep sea sediments that mainly consist of carbonate without major detrital magnetic input, magnetofossils can produce weak but stable and accurate magnetic record (Roberts et al., 2013a).

Detrital and biogenic magnetic minerals, and Fe-oxides in general, are redox-sensitive; they can be reduced or dissolved under anoxic conditions. Weathering, on the other hand, can lead to oxidation of magnetite and the dehydration of goethite. The redox conditions of aquatic sediments are controlled by early diagenesis, i.e. the microbial degradation of organic matter. Microbial sulfate reduction, and in greater depth anaerobic methane oxidation, releases hydrogen sulfide (H_2S) which is highly corrosive to Fe-oxides (Berner, 1981). Karlin and Levi (1983) were the first to show how early diagenesis can affect the magnetism of sediments, and described a characteristic dissolution of magnetic Fe-oxides with increasing depth, as sulfate is metabolized to H_2S and Fe-sulfides precipitate.

The dissolution of Fe-oxides is generally accompanied by the precipitation of authigenic Fe-sulfide. Common sulfides that form during early diagenesis are mackinawite (FeS), greigite

(Fe_3S_4), and pyrite (FeS_2), of which pyrite is the most ubiquitous. It is non-magnetic (weakly paramagnetic) and is often considered the only stable end product of sulfidation (Rickard, 2012). Greigite is ferromagnetic. If it is preserved in sediments, it complicates environmental magnetic interpretations and leads to a secondary remanent magnetization, referred to as a crystallization or chemical remanent magnetization, CRM (Snowball and Thompson, 1990). Secondary CRMs can form by various processes any time after deposition and are, therefore, problematic for paleomagnetism, where it is crucial to know the age of the magnetic remanence. Hence, testing for CRM components is an integral part of every paleomagnetic study. Compared to DRM acquisition, the CRM process is poorly understood, and its identification remains challenging

Chapter IV describes a new method to grow greigite in aqueous sediments under controlled laboratory conditions. By measuring magnetic properties during the growth period, we were able to monitor the process of CRM acquisition in sediments. Magnetic characterization indicated that the grain size spectrum remained unchanged over the growth phase, and samples continuously acquired a chemical magnetic remanence, proportional to the greigite concentration. (***Publication IV*** titled "Greigite (Fe_3S_4) formation in artificial sediments via solid-state transformation of lepidocrocite" by Roud, S.C., Gilder, S. A. & Park S. in the journal Geochemistry, Geophysics, Geosystems).

Chapter V characterizes the CRMs acquired by the synthetic greigite-bearing sediments. Additional re-deposition of these sediments allowed, for the first time, a direct comparison of the CRM and DRM recording efficiencies. The results are in good agreement with a theoretical model based on Néel's thermal relaxation theory (Néel, 1949). DRM and CRM can be distinguished in our samples by their demagnetization behavior and their magnetic recording efficiency, which was 5-6 times higher for CRM than for DRM. The difference in recording efficiencies is consistent with theoretical models and suggests that CRM components in paleomagnetic records can lead to overestimated paleointensity. The results emphasize the importance of detailed rock-magnetic investigations and checks to ensure primary, DRM based magnetization components to obtain reliable paleomagnetic records. The reported CRM characteristics are likely representative for grain-growth CRMs in natural sediments and could help to better recognize CRM overprints in paleomagnetic studies. (***Manuscript V*** titled "Chemical and Depositional Magnetic Recording in Greigite-bearing Sediments" by Roud, S.C. & Gilder, S. A. in preparation for Journal of Geophysical Research: Solid Earth).

Chapter I

Seasonal Variability of Magnetotactic Bacteria in a Freshwater Pond

Summary and Context

The motivation for this study was to gain a better understanding of what governs the natural distribution of MTB and how well the local abundance of magnetotactic bacteria (MTB) in a small (cm-sized) sampling area represents the MTB abundance of an ecosystem. We investigated the living MTB population in a natural freshwater pond by measuring the concentration of three MTB phenotypes over the course of two years to test if temporal changes are coherent between different sampling areas. This information can contribute to better understand how the concentration of magnetofossils in a single sedimentary archive, such as a deep-sea drill core, reflects a general response of that ecosystem to climate forcing contrary to local, small-scale variations in the benthic microbial composition. While a previous study showed that the spatiotemporal distribution of MTB in a laboratory system is highly chaotic (He et al. 2017), this study of a natural system is the first to demonstrate coherent spatiotemporal changes in the abundance of MTB.

Reference

He, K., Roud, S. C., Gilder, S. A., Egli, R., Mayr, C., & Petersen, N. (2018). Seasonal variability of magnetotactic bacteria in a freshwater pond. Geophysical Research Letters, 45(5), 2294-2302.

https://doi.org/10.1002/2018GL077213

Contributions

I contributed to the study design and methodology, sampling of sediment cores, measurement of magnetic properties, data processing, data analysis, and to writing the manuscript.

AGU PUBLICATIONS

Geophysical Research Letters

RESEARCH LETTER
10.1002/2018GL077213

Key Points:
- Our two-year study found coherent relative variations in MTB morphotype abundances among nine sites in a natural ecosystem
- Temporal variations of MTB abundances evolved independently of oxygen and temperature except for spirilla at some sites
- Single-domain magnetite (magnetosome) concentrations in the sediments varied with water depth but did not reflect living MTB abundances

Supporting Information:
- Supporting Information S1

Correspondence to:
S. A. Gilder,
gilder@lmu.de

Citation:
He, K., Roud, S. C., Gilder, S. A., Egli, R., Mayr, C., & Petersen, N. (2018). Seasonal variability of magnetotactic bacteria in a freshwater pond. *Geophysical Research Letters*, *45*, 2294–2302. https://doi.org/10.1002/2018GL077213

Received 22 JAN 2018
Accepted 21 FEB 2018
Accepted article online 28 FEB 2018
Published online 10 MAR 2018

Seasonal Variability of Magnetotactic Bacteria in a Freshwater Pond

Kuang He[1], Sophie C. Roud[1], Stuart A. Gilder[1], Ramon Egli[2], Christoph Mayr[1,3,4], and Nikolai Petersen[1]

[1]Department of Earth and Environmental Sciences, Ludwig-Maximilians-University, Munich, Germany, [2]Division Data, Methods and Models, Central Institute of Meteorology and Geodynamics (ZAMG), Vienna, Austria, [3]Institute of Geography, Friedrich-Alexander-Universität Erlangen-Nürnberg, Erlangen, Germany, [4]GeoBio-Center, Ludwig-Maximilians-Universität München, Munich, Germany

Abstract Magnetotactic bacteria (MTB) synthesize ferrimagnetic crystals that contribute to the remanent magnetization in sediments, yet knowledge of how MTB populations vary in natural environments over time remains limited. We report abundances of three MTB morphotypes from nine sites collected and measured every month over a two-year period from a natural pond near Munich, Germany. Morphotype populations underwent coherent temporal trends among the nine sites—especially at proximal sites with similar water depths. MTB populations varied independently of bottom water oxygen concentrations or temperature over the two-year period, except for spirilla, which flourished during the summer at some sites. Magnetic properties of the sediments did not reflect living MTB abundances, but instead varied with water depth. Deeper sites, which were also lower in organic carbon, nitrogen, and oxygen concentrations than shallower sites, had higher saturation magnetizations and were richer in single-domain particles.

1. Introduction

Magnetotactic bacteria (MTB) are found in most fresh and saline water habitats (Blakemore, 1975; Petermann & Bleil, 1993; Schüler et al., 1999; Simmons & Edwards, 2007; Spring et al., 1993). They are microaerobic to anaerobic organisms that live in the oxic-anoxic transition zone where chemical gradients are high (Frankel et al., 1997). MTB belong to different gram-negative phylogenetic groups (Uebe & Schüler, 2016) and host a wide variety of cell morphotypes including cocci, vibrios, spirilla, ovoids, rods, and multicellular prokaryotes (Lefèvre et al., 2011; Spring & Schleifer, 1995; Wenter et al., 2009). They produce 30 to 120 nm sized crystals of membrane-bound, ferrimagnetic magnetite, and/or greigite magnetosomes that are aligned in chains (Kopp & Kirschvink, 2008). The magnetosome chains are fixed to the cell, which compels MTB to move along magnetic field lines (Blakemore & Frankel, 1981).

It is well established that fossil magnetosomes preserved in sedimentary rocks can serve as recorders of the paleomagnetic field (Petersen et al., 1986; Vasiliev et al., 2008). The morphology and abundance of magnetosomes can also reflect environmental conditions and have been used as paleoenvironmental proxies (Chang & Kirschvink, 1985; Hesse, 1994; Moisescu et al., 2014; Paasche et al., 2004; Roberts et al., 2011; Snowball et al., 2002; Yamazaki, 2012). MTB cells contain 2 to 4% (dry weight) Fe, so they likely influence iron cycles in nature by sequestering Fe in sediments (Chen et al., 2014). Relationships between temperature and MTB abundance have been observed, which could make them potentially useful temperature proxies (Du et al., 2015; Lin, Wang, & Pan, 2012). MTB are also sensitive to local chemical factors such as organic carbon, dissolved iron, and nitrate concentrations (Lin & Pan, 2010; Roberts et al., 2011; Zhou et al., 2013).

Despite their importance to paleomagnetic and environmental studies, few studies have been dedicated to understanding natural environmental factors governing MTB life cycles. Simmons et al. (2004) measured MTB abundances at one site in a chemically stratified coastal salt pond three times over four months. Du et al. (2015) studied MTB at two sites in a brackish water environment every two weeks for 15 months. Although some fairly long-term microcosm studies have been carried out (He et al., 2017; Postec et al., 2012), MTB populations growing in temperature-controlled microcosms versus those in nature are likely quite different (Flies et al., 2005).

A high MTB population density and broad diversity of magnetic microorganisms live in a pond within an isolated forest owned by LMU-Munich (Jogler et al., 2010; Zhao, 2015). Here we report MTB abundances,

Geophysical Research Letters 10.1002/2018GL077213

temperature, bottom-water dissolved O_2, and magnetic properties from nine sites in the pond measured each month over a two-year period. These results are compared against a control beaker kept in a laboratory. Vertical profiles of MTB and magnetic hysteresis loops, as well as carbon and nitrogen concentration of the surface sediments, were also measured at a few discrete places and/or times. The data herein enable us to address (1) how well a random sample of MTB at one site in an ecosystem represents the ecosystem as a whole, (2) the proportion that live MTB contribute to the total magnetic fraction in sediment, and (3) environmental factors that bear on long-term MTB life cycles.

2. Methods

2.1. Study Design and Sampling

The pond, 30 m in length and 7 m in width, lies at the edge of a forest, 80 km northeast of Munich (48°35′15″ N, 12°04′43″E) (Figure 1). A small stream feeds the pond whose source water percolates out of permeable bedrock from several different places in the forest. A golf course abuts one side of the stream for 1.5 km and contributes run off to the stream; no discharge from nearby farms enters the pond. When we began the experiment in January 2015, the water was ~60 cm deep near the pond's outlet and ~30 cm near the inlet (Figure 1b).

A bridge suspends a carriage over the water that allows access to the pond from above with minimal disturbance to the environment. We extracted cores from nine sites (Figures 1b and 1c), with each site comprising an area of 100×60 cm^2 spanning the two-year period ensuring that each extraction did not disturb the sedimentary environment of successive cores. Cores to obtain vertical profiles of MTB and magnetic parameters were collected in June, August, and November 2016 at the sites indicated in Figure 1b.

Before sampling, we measured the height of the sediment and water surfaces relative to a constant reference to obtain sediment accumulation rates and water depth (Figure 2a). Water temperature was measured at each site every 5 cm from the air-water interface until 1–4 cm above the water-sediment interface. For sampling, plastic pipes, 5 cm diameter and 20 cm in height, were inserted ~10 cm deep into the sediment. A rubber stopper sealed the top of the pipe, the pipe was removed from the sediment, and then a second rubber stopper blocked the bottom of the pipe. In January 2015, we also sampled the upper 10 cm layer of the sediment near the inlet of the pond (Figure 1b) and thoroughly mixed it into a 2 L glass beaker. The beaker was stored in the laboratory and studied monthly over the same two-year period as the pond.

2.2. Measurement Protocol: Geochemistry, MTB Counting, and Magnetic Properties

Within 5 min after transporting the cores 100 m to the laboratory with minimal disturbance, dissolved oxygen (O_2) profiles were measured in 1 mm steps starting 10 mm above the water-sediment interface using a Unisense oxygen-50 microsensor (detection limit = 0.3 μM). The sensor was fixed on a computer-driven micromanipulator mounted on a heavy laboratory stand. We used the viable cell count technique to quantify the MTB morphotypes using the instrumentation and methodology of He et al. (2017).

Morphotypes were classified into three categories based on easily recognizable traits: (1) rods that are elongate, mostly opaque, and >5 μm; (2) cocci based on their rounded morphology, fast swimming behavior, and small (~1–4 μm) sizes; and (3) spirilla, which are ~2–3 μm long and slightly concave. Vibrios would be counted as spirilla, as the two cannot be distinguished optically. 16S rRNA sequencing of the pond sediment identified several cocci species and two rod-types (Coskun et al., 2017), but species cannot be distinguished under the microscope, only morphotypes. Two subsamples were prepared from each core, and the control beaker every month and two drops were counted per subsample. The number of MTB morphotypes per site and time was taken as the average of the four drops. For the vertical profiles, only one sample was extracted and one drop was counted for each layer.

Magnetic hysteresis loops and backfield curves were measured with a vibrating sample magnetometer (MicroMag3900) on air-dried sediments (uppermost 1 cm from the cores) from all nine cores taken each month in 2016 to calculate the saturation magnetization (Ms), the remanent magnetization after saturation (Mrs), the coercive force (Bc), and the coercivity of remanence (Bcr). Mass percentage total organic carbon (TOC) and total nitrogen (TN) were measured in the same sediment samples that were used to count MTB in January 2015 and August 2016. Analyses of the freeze-dried, homogenized samples took place at Erlangen University using a Carlo Erba NC 2500 elemental analyzer coupled to a Thermo-Finnigan, Delta

Geophysical Research Letters 10.1002/2018GL077213

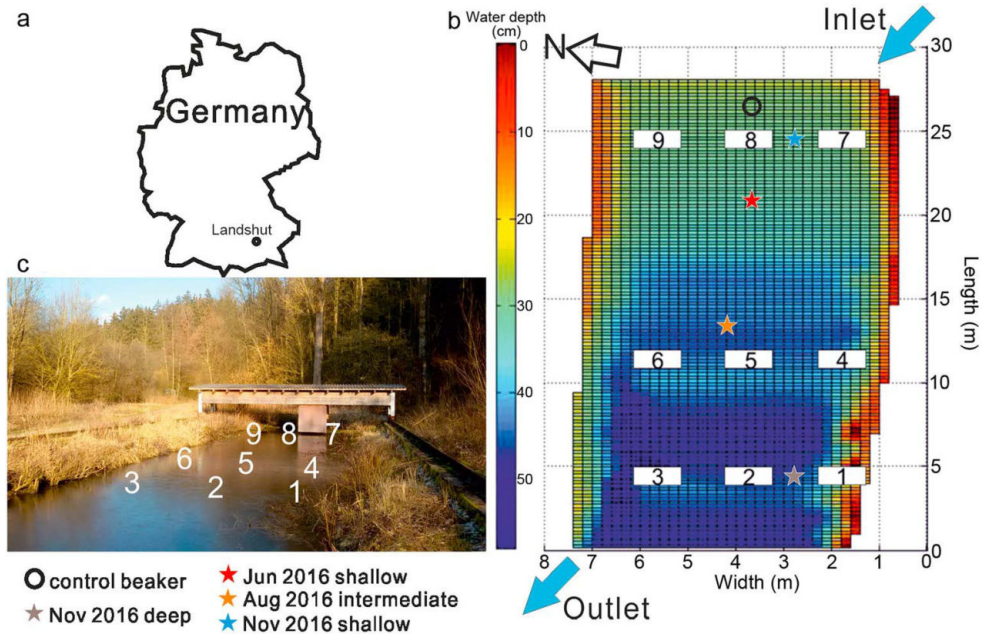

Figure 1. (a) General location map of the pond near Landshut. (b) Water depth (in September 2011) and distribution of the sampling sites. Extraction points for the control beaker (circle) and vertical profiles (stars) are also shown. (c) Photo of the pond with bridge and rails. A cabin suspended on the bridge moves back and forth enabling a single user to access any point in the pond with sampling/analytical equipment.

Plus isotope-ratio-mass spectrometer (Mayr et al., 2011). TOC and $^{13}C/^{12}C$ of organic carbon were measured from samples decalcified with 20% HCl in silver cups; TN and $^{15}N/^{14}N$ were determined from chemically untreated samples. Isotopic ratios are reported in the common delta notation ($\delta^{15}N_{TN}$ and $\delta^{13}C_{TOC}$) versus the international standards AIR and VPDB, respectively. Carbon-to-nitrogen ratios are reported as molar ratios and were calculated from TOC and TN values. Internal standards used for element content determinations were cyclohexanone-2,4-dinitrophenylhydrazone and atropine; for isotope calibration, a peptone laboratory standard was used. The error was less than 5% for TOC and TN determinations and less than 0.2‰ (1σ) for isotope analyses.

3. Results

Figures 2a to 2c show the water depth, bottom water temperature, and dissolved O_2 over the two-year period (Tables S1 and S2). Water level varied throughout the observation period with lowest stands in summer. Bottom water temperatures reached 16–21 °C in summer and ~0 °C in winter. Bottom water O_2 concentrations generally waxed in spring and waned in late summer. A horizontal gradient in O_2 occurred in summer 2016 with hypoxic bottom waters at the deepest sites and O_2 saturated waters at the shallowest sites. The maximum penetration depth where O_2 disappeared in the sediment ranged from ~2 to ~7 mm and correlated well (r = 0.72, n = 24) with the bottom water O_2 concentrations; that is, the higher the bottom water O_2 concentration, the deeper the O_2 penetrated into the sediment. Floating plants (*Lemnoideae* = duckweed) covered the pond's surface from June to September, which reduced the light and limited O_2 production at depth. The beaker in the temperature-controlled environment (between 20 and 25 °C) underwent similar annual trends in O_2 as the pond (Figure 2c), independent of temperature correction, suggesting common O_2 respiration and production mechanisms.

Figures 2d to 2f show the temporal variation of MTB morphotype abundances averaged over the nine sites (Tables S1 and S3). Cocci dominated the MTB community, being 10× on average more abundant than spirilla and 100× more abundant than rods. Generally, the growth and death phases coincided among the different sites in the pond, although the total abundance from site to site varied up to an order of magnitude (Figure S1).

Geophysical Research Letters 10.1002/2018GL077213

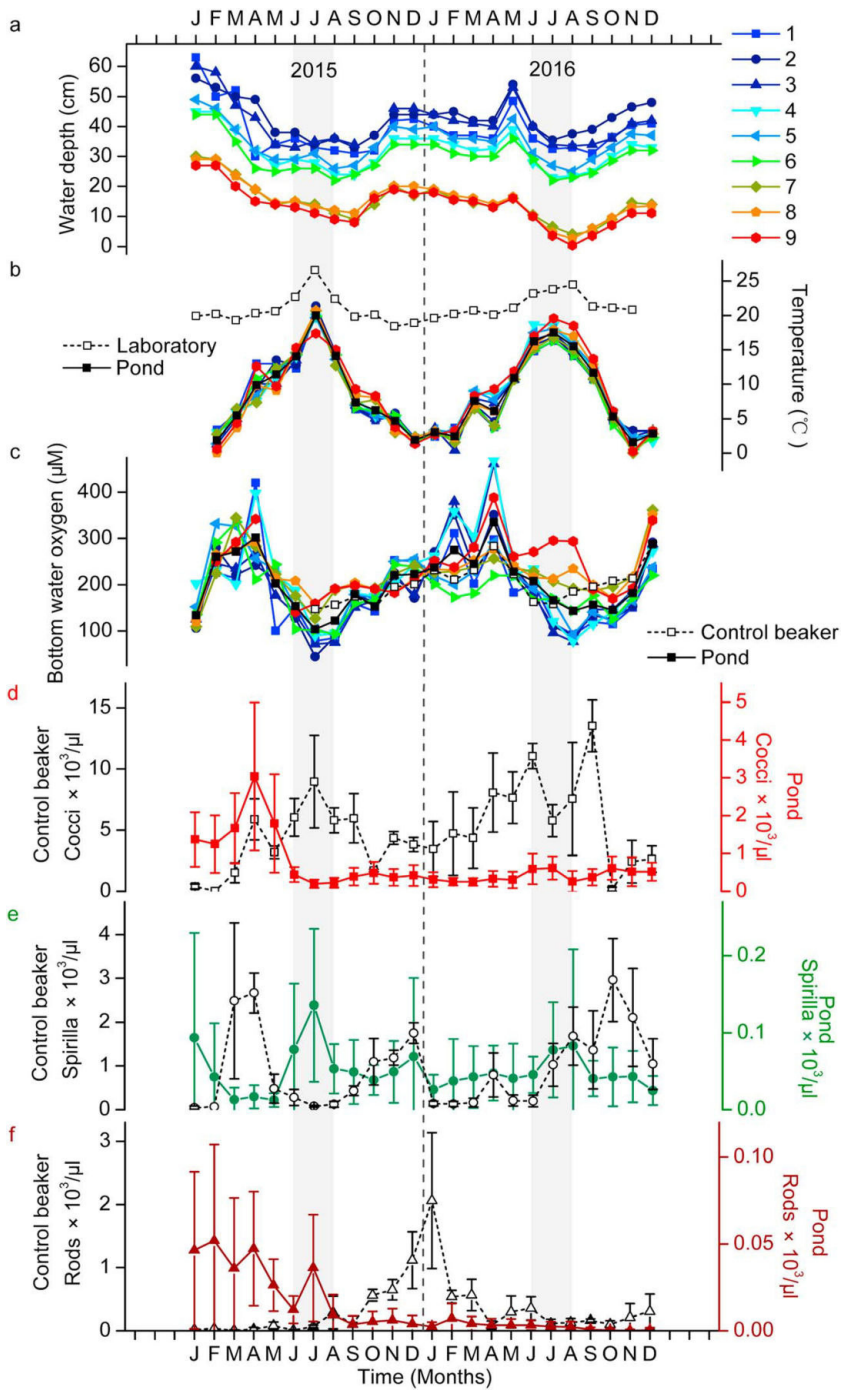

Figure 2. Temporal variation of (a) water depth at sites 1–9, (b) bottom water temperature at each site (legend in a) together with the temperature of the water in the laboratory used for the O_2 calibration measurements, (c) bottom water O_2 concentrations for each site, the average of all sites (solid black line) and the control beaker (dashed black line), (d–f) average and single standard deviation (nine sites) for each of the three MTB morphotype populations. The open symbols with dashed lines are from the control beaker with scale on left. Figure S9 plots the MTB concentrations on a log scale.

Cocci underwent a precipitous decrease after April 2015, then underwent a slight renaissance in the summer of 2016. Like cocci, rods were significantly more abundant at the beginning of the observation period. Their numbers decreased with time, with the exception of a pronounced growth phase in July 2015. Rods were no longer detected at most sites by the end of 2016. Spirilla showed consistent seasonal trends in both years, reaching the highest numbers in the summer months and lowest in spring and autumn, with the

AGU Geophysical Research Letters 10.1002/2018GL077213

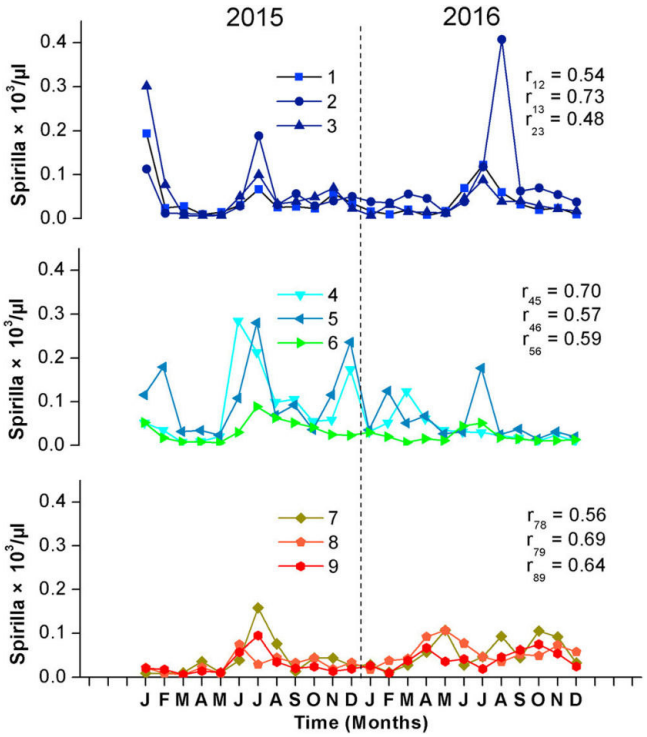

Figure 3. Temporal variation of spirilla at each site separated into rows of similar water depth. Spearman coefficients (r) from each row (1–3, 4–6, and 7–9) are significant at the 0.01 level for each of the tested cases except for r_{23}, which is significant at the 0.05 level (Table S4).

exception of shallow sites 7–9 (Figure 3), which nearly fell dry in August 2016 (Figure 2a). Spirilla underwent a less pronounced growth phase during the winter months at several sites.

MTB populations evolved quite distinctly between the pond and the control beaker (Figure 2). Initially, all morphotypes were less abundant in the control environment relative to the pond. Within several months cocci concentrations in the beaker rose ~10× higher than those in the pond and peaked in the summer of 2015. Rod numbers in the beaker exhibited a peak in winter 2015–2016. Spirilla boomed in spring and late autumn-early winter in contrast to the pond.

Table S4 lists Spearman correlation coefficients for the three MTB morphotypes among the nine sites over the 24 month period (18 months for rods). The correlations are significant at or above the 0.05 level across all sites in 33 of 36 cases for cocci, 35 of 36 cases for rods, but only 15 of 36 cases for spirilla. Remarkable correlations in MTB abundances exist among proximal sites with similar water depth—even for spirilla (e.g., 1–3, 4–6, and 7–9) (Figures 3, S2, and S3). The high degree of correlation in MTB populations among the sites, especially at proximal sites with similar water depth, appears to be a robust result when drawing conclusions concerning MTB evolution in time and space from natural environments. As expected, bottom water O_2 concentrations and temperature were highly consistent among the nine sites (Figures 2b and 2c and Table S5), whereas bottom water O_2 and temperature show insignificant correlation with MTB populations, except spirilla at some sites (Table S6).

Spirilla and cocci numbers in the pond were negatively correlated in 2015 ($r = -0.28$, $p < 0.01$, $n = 108$) and positively correlated in 2016 ($r = 0.38$, $p < 0.01$, $n = 108$), although intersite variability was high (Figure S4). Cocci abundance was positively correlated with O_2 in 2015, but not in 2016 (Figure S5), whereas spirilla exhibited a negative correlation with O_2 in 2015, but not in 2016 (Figure S5). Rods had no significant relationship with O_2 in either year.

Previous work in the pond identified magnetite as the sole ferrimagnetic mineral in the sediment (Zhao, 2015). We corroborated this with low-temperature experiments that revealed a broad Verwey transition around 110 K (Figure S6a), characteristic of oxidized magnetite. The temperature dependence of the magnetic remanence and susceptibility defined Curie temperatures around 575 °C (Figure S6b). First-order reversal curves (FORCs) showed a distinct central ridge diagnostic of noninteracting single-domain (SD) magnetite with no hint of authigenic greigite (Figures S6c and S6d).

The magnetic properties of the pond surface sediments were not related to the number of living MTB, nor did they change through time, but instead varied as a function of water depth (Figures 4a and 4b). Sites from deeper water had higher Ms and were magnetically harder (higher Bcr), being more displaced toward the SD region on the Day et al. (1977) plot than sites from shallow water (Figure 4c). TOC, TN, and bottom water O_2 concentrations were higher at the shallow sites close to the inflow and were higher on average in August 2016 than in January 2015 (Figures 4d to 4f and Table S9). The carbon-to-nitrogen ratio (C:N) was nearly constant in space and time (January 2015: 13.2 ± 0.8; August 2016: 13.8 ± 1.3, 1σ uncertainties). The $\delta^{13}C_{TOC}$ isotopic composition of the sediments was −29.2 ± 0.1‰ and −28.7 ± 0.1‰, while $\delta^{15}N_{TN}$ was 2.1 ± 0.2‰ and 1.9 ± 0.3‰ in January 2015 and August 2016, respectively. The rather homogenous geochemical data indicate that the type of organic matter was similar at all times and locations sampled in the pond.

Depth profiles of MTB counts revealed that cocci and spirilla were bimodally distributed with maximum numbers around 1–2 cm depth and a second less pronounced peak around 4–6 cm depth (Figure S7). Spirilla were generally skewed deeper than cocci, although both were found within the same depth range, as deep as 15 cm. Ms, which serves a proxy for magnetite concentration, and Mrs/Ms, which can indicate

AGU Geophysical Research Letters 10.1002/2018GL077213

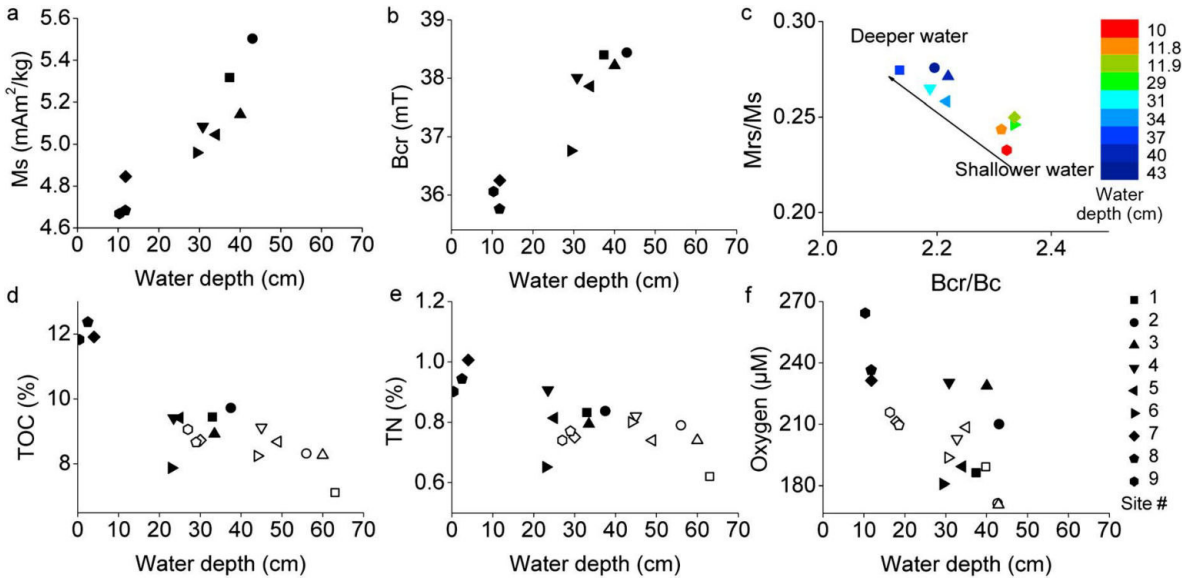

Figure 4. Magnetic and chemical parameters of the upper 1 cm of sediment from the pond (averages from 12 months for each of the nine sites; legend in f). (a) Average saturation magnetization (Ms) for 2016. (b) Coercivity of remanence (Bcr) for 2016. (c) Day plot (Day et al., 1977) from 2016 color coded by average depth. (d) Total organic carbon (TOC) in January 2015 (open symbols) and August 2016 (solid symbols). (e) Total nitrogen (TN) in January 2015 (open symbols) and August 2016 (solid symbols). (f) Average bottom water O_2 concentration in 2015 (open symbols) and 2016 (solid symbols). Data are presented in Tables S2, S7, and S9.

grain size, were uncorrelated with the number of live MTB (Figure S7). The relationship between live MTB abundance and Ms was insignificant (Table S8).

4. Discussion

Two years of observations showed distinct trends in MTB populations in the pond. Despite differences between morphotypes, the relative changes of individual morphotype populations appear coherent from site to site, which indicates an overall sensitivity of MTB populations to the pond's environment (Figures 3 and S1 to S3). Spirilla tended to be more abundant in the summer months when bottom water temperatures peaked and bottom water O_2 concentrations were lowest (Figures 2 and 3). A subsidiary spirilla growth phase occurred in the winter.

Population trends of spirilla were in antipathy with cocci in 2015, when absolute numbers varied strongly, yet coincided in 2016 when temporal variations in cocci abundance were more subdued (Figure S4). Significant anticorrelation in time and space between spirilla and cocci populations was also found by He et al. (2017), who measured MTB abundances at 72 points in two aquaria each month for 198 days. Such antipathy between cocci and spirilla might be related to differences in their magnetotactic behavior (Mao, Egli, Petersen, Hanzlik, & Liu, 2014), or to disparate mechanisms coping in chemical environments, as suggested by the differential depth range where the morphotypes were detected in the vertical profiles, with spirilla being skewed lower in the sediment column than cocci (Figure S7) (Lefèvre et al., 2011). Interestingly, the anticorrelation was significant when both morphotypes correlated distinctly negative (spirilla) or positive (cocci) with bottom water O_2 (Figure S5). We cannot exclude that the observed changes in MTB abundances are related to the changes on the species level of cocci or spirilla, since we can only distinguish morphotypes with the viable cell count technique (Lefèvre & Bazylinski, 2013). Moreover, the three depth profiles suggest that the MTB might have, at times, migrated vertically and escaped detection (Figure S7). This could eventually bear on our measurements and interpretations of the MTB abundances, as the surface samples integrated over the upper 1 cm of the sediment column.

Within the scope of the measured chemical parameters, none can singularly explain the variability in MTB population. That O_2 trends in the control beaker and pond were fairly similar over the two-year period, yet the MTB trends of the two environments did not correlate, suggests that there is no universal relationship between O_2 and MTB concentrations across different ecosystems (Flies et al., 2005; Jogler et al., 2010). Du

AGU Geophysical Research Letters 10.1002/2018GL077213

et al. (2015) found that unicellular MTB abundances at two brackish water sites peaked just after the period with the highest temperatures (~23 °C), similar to our findings for spirilla but opposite of cocci whose lowest abundances occurred in summer 2015 (Figure 2). Excessive warmth will be detrimental, as Lin, Wang, and Pan (2012) found that temperatures of 37 °C reduced cocci abundance to 1% of those living at 26 °C. The more moderate temperature variations during the course of our study likely had little influence on MTB populations in the pond and were negligible in the control beaker. The C:N ratios and isotopic values indicate that the organic matter consists of a rather homogenous mixture of algal and vascular terrestrial organic matter (Meyers, 1994). TOC and TN percentages were rather constant, which suggests that nutrient type or availability did not drive the observed changes in MTB populations.

Ms and Mrs/Ms of the sediments were uncorrelated with live MTB abundance, but instead varied in proportion with water depth, with deeper sites possessing ~15% higher Ms and Mrs/Ms than sites from shallower water (Figure 4). Live MTB abundance did not correlate with water depth, except only slightly for rods whose abundance was minimal (Figure S8). Because the magnetosomes of the living cells represent $<$1% of the total Ms, the magnetization of the sediment should reflect the cumulative magnetofossil concentration. This is in agreement with FORC diagrams that display a central ridge characteristic of noninteracting SD particles that account for ~50% of the magnetization (Mao, Egli, Petersen, Hanzlik, & Zhao, 2014; Figure S6).

The ranges in Mrs/Ms (0.21–0.27) and Bcr/Bc (2.1–2.4) are displaced away from the wholly SD character of pure MTB extracts with Mrs/Ms ~0.5 and Bcr/Bc ~1.0–1.5 (Lin & Pan, 2009; Moskowitz et al., 1988; Pan et al., 2005). Lower than expected values for pure-SD particle distributions can stem from dilution by non-SD detrital magnetite and/or from oxidation. Low-temperature oxidation of SD magnetite lowers Ms (Readman & O'Reilly, 1972). Although higher O_2 concentrations existed in shallower water where Ms was lower (Figure 4), a change in domain state is required to explain the reduction in Mrs/Ms. Reducing Mrs/Ms by low-temperature oxidation of SD grains can be feasible when SD particles close to the SD-superparamagnetic (SP) limit become SP thereby lowering their remanent magnetizations (Mrs). However, the FORC diagrams showed no signature characteristic of magnetic viscosity related to SP particles (Figure S6). Because sediment accumulated more rapidly during the two-year period in the shallow area, greater dilution should be expected there, which would lower Ms. Diluting with material impoverished in SD particles would lower Mrs/Ms preferentially in the shallow sites, and hence, lowering Mrs/Ms can be explained by a mixing trend between SD magnetosomes and non-SD (detrital) magnetite end-members.

That Ms and Mrs/Ms increase with depth in the sediment (Figure S7) may be attributed to an increase in magnetofossil concentration and/or to the reduction of oxidized magnetite back to stoichiometric magnetite in more reducing environments. The former agrees with the higher MTB abundances at the start of the experiment that decreased by a factor of 10 within several months. Less oxidized magnetite at greater depth in the sediment is in agreement with our low-temperature experiments that show a better definition of the Verwey transition with increasing depth (Figure S6). However, reduction of maghemite to magnetite increases Ms by only about 20%, so reversion to stoichiometric magnetite can only account for a limited increase in Ms with depth in the intermediate and deepwater profiles.

Our two-year study shows that environmental factors drive MTB abundance as reflected by coherent trends throughout the pond, but neither dissolved O_2 nor temperature variations can singularly explain changes in MTB populations. Several other factors that were not measured in our study have been shown to affect MTB abundance, such as salinity or sulfur and iron concentration (Lin & Pan, 2009, 2010; Lin, Wang, Li, et al., 2012; Postec et al., 2012; Sobrinho et al., 2011). However, we can conclude that MTB populations in the freshwater pond, particularly spirilla, vary with season, especially at the deeper water sites. Although absolute MTB concentrations differed in space, all three individual morphotypes underwent similar relative changes in the time domain; hence, long-term trends of MTB populations in natural ecosystems are likely indicative of the ecosystem as a whole. This is in distinct contrast to artificial habitats in the laboratory that have not reached steady state conditions (He et al., 2017). Magnetite concentrations and relative grain sizes of the surface sediments do not reflect trends in MTB abundance but are related to water depth, likely due to enhanced dilution of the SD magnetofossil fraction by detrital material at the shallow sites that were situated proximal to the pond's inflow.

AGU Geophysical Research Letters 10.1002/2018GL077213

Acknowledgments
Xiangyu Zhao measured the water depth that contributed to Figure 1b. Manuela Weiß took care of the control beaker. The China Scholarship Council helped support this study. We appreciate helpful comments from Mike Jackson and an anonymous reviewer and editorial handling by Tatiana Ilyina. Data used in this manuscript are in the supporting information.

References

Blakemore, R. (1975). Magnetotactic bacteria. *Science*, *190*(4212), 377–379. https://doi.org/10.1126/science.170679

Blakemore, R. P., & Frankel, R. B. (1981). Magnetic navigation in bacteria. *Scientific American*, *245*(6), 58–65. https://doi.org/10.1038/scientificamerican1281-58

Chang, S.-B. R., & Kirschvink, J. L. (1985). Possible biogenic magnetite fossils from the Late Miocene Potamida clays of Crete. In J. L. Kirschvink, D. S. Jones, & B. J. MacFadden (Eds.), *Magnetite Biomineralization and Magnetoreception in Organisms* (chap. 36, pp. 647–669). US: Springer. https://doi.org/10.1007/978-1-4613-0313-8_36

Chen, A., Berounsky, V., Chan, M., Blackford, M., Cady, C., Moskowitz, B., et al. (2014). Magnetic properties of uncultivated magnetotactic bacteria and their contribution to a stratified estuary iron cycle. *Nature Communications*, *5*, 4797. https://doi.org/10.1038/ncomms5797

Coskun, Ö. K., Roud, S., He, K., Petersen, N., Gilder, S. A., & Orsi, W. D. (2017). Tracking heterotrophic and autotrophic carbon cycling by magnetotactic bacteria in freshwater sediments using DNA stable isotope probing. European Geosciences Union General Assembly, Vienna, Austria, Abstract 15745.

Day, R., Fuller, M., & Schmidt, V. (1977). Hysteresis properties of titanomagnetites: Grain-size and compositional dependence. *Physics of the Earth and Planetary Interiors*, *13*(4), 260–267. https://doi.org/10.1016/0031-9201(77)90108-X

Du, H., Chen, Y., Zhang, R., Pan, H., Zhang, W., Zhou, K., et al. (2015). Temporal distributions and environmental adaptations of two types of multicellular magnetotactic prokaryote in the sediments of Lake Yuehu, China. *Environmental Microbiology Reports*, *7*(3), 538–546. https://doi.org/10.1111/1758-2229.12284

Flies, C. B., Jonkers, H. M., de Beer, D., Bosselmann, K., Böttcher, M. E., & Schüler, D. (2005). Diversity and vertical distribution of magnetotactic bacteria along chemical gradients in freshwater microcosms. *FEMS Microbiology Ecology*, *52*(2), 185–195. https://doi.org/10.1016/j.femsec.2004.11.006

Frankel, R. B., Bazylinski, D. A., Johnson, M. S., & Taylor, B. L. (1997). Magneto-aerotaxis in marine coccoid bacteria. *Biophysical Journal*, *73*(2), 994–1000. https://doi.org/10.1016/S0006-3495(97)78132-3

He, K., Gilder, S. A., Orsi, W. D., Zhao, X., & Petersen, N. (2017). Constant flux of spatial niche partitioning through high-resolution sampling of magnetotactic bacteria. *Applied and Environmental Microbiology*, *83*(20), e01382–e01317. https://doi.org/10.1128/AEM.01382-17

Hesse, P. P. (1994). Evidence for bacterial palaeoecological origin of mineral magnetic cycles in oxic and sub-oxic Tasman Sea sediments. *Marine Geology*, *117*(1-4), 1–17. https://doi.org/10.1016/0025-3227(94)90003-5

Jogler, C., Niebler, M., Lin, W., Kube, M., Wanner, G., Kolinko, S., et al. (2010). Cultivation-independent characterization of 'Candidatus Magnetobacterium bavaricum' via ultrastructural, geochemical, ecological and metagenomic methods. *Environmental Microbiology*, *12*(9), 2466–2478. https://doi.org/10.1111/j.1462-2920.2010.02220.x

Kopp, R. E., & Kirschvink, J. L. (2008). The identification and biogeochemical interpretation of fossil magnetotactic bacteria. *Earth-Science Reviews*, *86*(1-4), 42–61. https://doi.org/10.1016/j.earscirev.2007.08.001

Lefèvre, C. T., & Bazylinski, D. A. (2013). Ecology, diversity, and evolution of magnetotactic bacteria. *Microbiology and Molecular Biology Reviews*, *77*(3), 497–526. https://doi.org/10.1128/MMBR.00021-13

Lefèvre, C. T., Frankel, R. B., Abreu, F., Lins, U., & Bazylinski, D. A. (2011). Culture-independent characterization of a novel, uncultivated magnetotactic member of the Nitrospirae phylum. *Environmental Microbiology*, *13*(2), 538–549. https://doi.org/10.1111/j.1462-2920.2010.02361.x

Lin, W., & Pan, Y. (2009). Uncultivated magnetotactic cocci from Yuandadu park in Beijing, China. *Applied and Environmental Microbiology*, *75*(12), 4046–4052. https://doi.org/10.1128/AEM.00247-09

Lin, W., & Pan, Y. (2010). Temporal variation of magnetotactic bacterial communities in two freshwater sediment microcosms. *FEMS Microbiology Letters*, *302*(1), 85–92. https://doi.org/10.1111/j.1574-6968.2009.01838.x

Lin, W., Wang, Y., Li, B., & Pan, Y. (2012). A biogeographic distribution of magnetotactic bacteria influenced by salinity. *The ISME Journal*, *6*(2), 475–479. https://doi.org/10.1038/ismej.2011.112

Lin, W., Wang, Y., & Pan, Y. (2012). Short-term effects of temperature on the abundance and diversity of magnetotactic cocci. *MicrobiologyOpen*, *1*(1), 53–63. https://doi.org/10.1002/mbo3.7

Mao, X., Egli, R., Petersen, N., Hanzlik, M., & Liu, X. (2014). Magneto-chemotaxis in sediment: First insights. *PLoS One*, *9*(7), e102810. https://doi.org/10.1371/journal.pone.0102810

Mao, X., Egli, R., Petersen, N., Hanzlik, M., & Zhao, X. (2014). Magnetotaxis and acquisition of detrital remanent magnetization by magnetotactic bacteria in natural sediment: First experimental results and theory. *Geochemistry, Geophysics, Geosystems*, *15*, 255–283. https://doi.org/10.1002/2013GC005034

Mayr, C., Försterra, G., Häussermann, V., Wunderlich, A., Grau, J., Zieringer, M., & Altenbach, A. (2011). Stable isotope variability in a Chilean fjord food web: Implications for N-and C-cycles. *Marine Ecology Progress Series*, *428*, 89–104. https://doi.org/10.3354/meps09015

Meyers, P. A. (1994). Preservation of elemental and isotopic source identification of sedimentary organic matter. *Chemical Geology*, *114*(3-4), 289–302. https://doi.org/10.1016/0009-2541(94)90059-0

Moisescu, C., Ardelean, I., & Benning, L. (2014). The effect and role of environmental conditions on magnetosome synthesis. *Frontiers in Microbiology*, *5*, 49. https://doi.org/10.3389/fmicb.2014.00049

Moskowitz, B., Frankel, R. B., Flanders, P., Blakemore, R., & Schwartz, B. B. (1988). Magnetic properties of magnetotactic bacteria. *Journal of Magnetism and Magnetic Materials*, *73*(3), 273–288. https://doi.org/10.1016/0304-8853(88)90093-5

Paasche, Ø., Løvlie, R., Dahl, S. O., Bakke, J., & Nesje, A. (2004). Bacterial magnetite in lake sediments: Late glacial to Holocene climate and sedimentary changes in northern Norway. *Earth and Planetary Science Letters*, *223*(3-4), 319–333. https://doi.org/10.1016/j.epsl.2004.05.001

Pan, Y., Petersen, N., Winklhofer, M., Davila, A. F., Liu, Q., Frederichs, T., et al. (2005). Rock magnetic properties of uncultured magnetotactic bacteria. *Earth and Planetary Science Letters*, *237*(3-4), 311–325. https://doi.org/10.1016/j.epsl.2005.06.029

Petermann, H., & Bleil, U. (1993). Detection of live magnetotactic bacteria in South Atlantic deep-sea sediments. *Earth and Planetary Science Letters*, *117*(1-2), 223–228. https://doi.org/10.1016/0012-821x(93)90128-v

Petersen, N., von Dobeneck, T., & Vali, H. (1986). Fossil bacterial magnetite in deep-sea sediments from the South Atlantic Ocean. *Nature*, *320*(6063), 611–615. https://doi.org/10.1038/320611a0

Postec, A., Tapia, N., Bernadac, A., Joseph, M., Davidson, M., Wu, L.-F., et al. (2012). Magnetotactic bacteria in microcosms originating from the French Mediterranean coast subjected to oil industry activities. *Microbial Ecology*, *63*(1), 1–11. https://doi.org/10.1007/s00248-011-9910-z

Readman, P. W., & O'Reilly, W. (1972). Magnetic properties of oxidized (cation-deficient) titanomagnetites. *Journal of Geomagnetism and Geoelectricity*, *24*(1), 69–90. https://doi.org/10.5636/jgg.24.69

Geophysical Research Letters 10.1002/2018GL077213

Roberts, A. P., Florindo, F., Villa, G., Chang, L., Jovane, L., Bohaty, S. M., et al. (2011). Magnetotactic bacterial abundance in pelagic marine environments is limited by organic carbon flux and availability of dissolved iron. *Earth and Planetary Science Letters*, *310*(3-4), 441–452. https://doi.org/10.1016/j.epsl.2011.08.011

Schüler, D., Spring, S., & Bazylinski, D. A. (1999). Improved technique for the isolation of magnetotactic spirilla from a freshwater sediment and their phylogenetic characterization. *Systematic and Applied Microbiology*, *22*(3), 466–471. https://doi.org/10.1016/S0723-2020(99)80056-3

Simmons, S. L., & Edwards, K. J. (2007). Unexpected diversity in populations of the many-celled magnetotactic prokaryote. *Environmental Microbiology*, *9*(1), 206–215. https://doi.org/10.1111/j.1462-2920.2006.01129.x

Simmons, S. L., Sievert, S. M., Frankel, R. B., Bazylinski, D. A., & Edwards, K. J. (2004). Spatiotemporal distribution of marine magnetotactic bacteria in a seasonally stratified coastal salt pond. *Applied and Environmental Microbiology*, *70*(10), 6230–6239. https://doi.org/10.1128/AEM.70.10.6230-6239.2004

Snowball, I., Zillén, L., & Sandgren, P. (2002). Bacterial magnetite in Swedish varved lake-sediments: A potential bio-marker of environmental change. *Quaternary International*, *88*(1), 13–19. https://doi.org/10.1016/S1040-6182(01)00069-6

Sobrinho, R. L., Lins, U., & Bernardes, M. C. (2011). Geochemical characteristics related to the gregite-producing multicellular magnetotactic prokaryote Candidatus Magnetoglobus multicellularis in a hypersaline lagoon. *Geomicrobiology Journal*, *28*(8), 705–713. https://doi.org/10.1080/01490451.2010.514027

Spring, S., Amann, R., Ludwig, W., Schleifer, K.-H., van Gemerden, H., & Petersen, N. (1993). Dominating role of an unusual magnetotactic bacterium in the microaerobic zone of a freshwater sediment. *Applied and Environmental Microbiology*, *59*(8), 2397–2403.

Spring, S., & Schleifer, K.-H. (1995). Diversity of magnetotactic bacteria. *Systematic and Applied Microbiology*, *18*(2), 147–153. https://doi.org/10.1016/S0723-2020(11)80386-3

Uebe, R., & Schüler, D. (2016). Magnetosome biogenesis in magnetotactic bacteria. *Nature Reviews Microbiology*, *14*(10), 621–637. https://doi.org/10.1038/nrmicro.2016.99

Vasiliev, I., Franke, C., Meeldijk, J. D., Dekkers, M. J., Langereis, C. G., & Krijgsman, W. (2008). Putative greigite magnetofossils from the Pliocene epoch. *Nature Geoscience*, *1*(11), 782–786. https://doi.org/10.1038/ngeo335

Wenter, R., Wanner, G., Schüler, D., & Overmann, J. (2009). Ultrastructure, tactic behaviour and potential for sulfate reduction of a novel multicellular magnetotactic prokaryote from North Sea sediments. *Environmental Microbiology*, *11*(6), 1493–1505. https://doi.org/10.1111/j.1462-2920.2009.01877.x

Yamazaki, T. (2012). Paleoposition of the Intertropical Convergence Zone in the eastern Pacific inferred from glacial-interglacial changes in terrigenous and biogenic magnetic mineral fractions. *Geology*, *40*(2), 151–154. https://doi.org/10.1130/G32646.1

Zhao, X. (2015). Natural remanent magnetization acquisition in bioturbated sediments (PhD thesis). Munich, Germany: Department of Earth and Environmental Sciences, University of Munich.

Zhou, K., Zhang, W. Y., Pan, H. M., Li, J. H., Yue, H. D., Xiao, T., & Wu, L. F. (2013). Adaptation of spherical multicellular magnetotactic prokaryotes to the geochemically variable habitat of an intertidal zone. *Environmental Microbiology*, *15*(5), 1595–1605. https://doi.org/10.1111/1462-2920.12057

Chapter II

Proxy Approach to Unravel Late Pleistocene Sediment Flux and Bottom Water Conditions in the Western South Atlantic Ocean

Summary and Context

This study investigates the magnetic mineral inventory of a 20 m long gravity core from the Santos Plateau, a sedimentary basin offshore SE Brazil. In a multidisciplinary approach, the sediment flux, and redox conditions in the Western South Atlantic during the past ~200 ka were reconstructed, based on rock magnetic and various geochemical and sedimentologic proxy parameters. Systematic variations in fine-grained magnetite, that were unrelated to the terrigenous sediment flux, likely reflect the abundance of magnetofossils (the fossil remains of magnetotactic bacteria). Most notably, the concentration of inferred magnetofossils showed a glacial-interglacial cyclicity. Geochemical analysis indicated coeval variations in the sediment organic matter content as well as in the benthic 13C isotope ratio, which reflects bottom water ventilation. Assuming that magnetite concentration was not affected by reductive dissolution, the co-variation suggested that the abundance of MTB was governed by the bottom water conditions during the past ~200 ka on the Santos Plateau.

Reference

G. L. Mathias, S. C. Roud, C. M. Chiessi, M. C. Campos, B. B. Dias, T. P. Santos, A. L. S. Albuquerque, F. A. L. Toledo, K. B. Costa, and B. A. Maher (2021). A Multi-Proxy Approach to Unravel Late Pleistocene Sediment Flux and Bottom Water Conditions in the Western South Atlantic Ocean. Paleoceanography and Paleoclimatology, 36(4), e2020PA004058.

https://doi.org/10.1029/2020PA004058

Contributions

I contributed to the data analysis and interpretation of the magnetic and major elemental proxy records concerning the sediment provenance, early diagenetic influences on reactive metal species the origin of SD magnetite. I conducted rock magnetic measurements on selected subsamples of the core and carried out all FORC (first order reversal curve) analyses and their interpretation. I contributed to writing the manuscript and prepared the geologic and oceanographic overview of the study area (Figure 1) and the FORC diagrams (Figure 4).

Paleoceanography and Paleoclimatology

RESEARCH ARTICLE
10.1029/2020PA004058

A Multi-Proxy Approach to Unravel Late Pleistocene Sediment Flux and Bottom Water Conditions in the Western South Atlantic Ocean

G. L. Mathias[1,2,3], S. C. Roud[4], C. M. Chiessi[1], M. C. Campos[1], B. B. Dias[5], T. P. Santos[5], A. L. S. Albuquerque[5], F. A. L. Toledo[6], K. B. Costa[6], and B. A. Maher[2]

[1]School of Arts, Sciences and Humanities, University of São Paulo, São Paulo, Brazil, [2]Lancaster Environment Centre, University of Lancaster, Lancaster, UK, [3]Institute of Geosciences, University of São Paulo, São Paulo, Brazil, [4]Department of Earth and Environmental Sciences, Ludwig-Maximilians University of Munich, Munich, Germany, [5]Geochemistry Graduate Program, Fluminense Federal University, Niterói, Brazil, [6]Oceanographic Institute, University of São Paulo, São Paulo, Brazil

Abstract Magnetic signals in deep-sea sediments have the potential to unravel past continental environmental changes, via changes in primary terrigenous magnetic supply, but also record past marine environmental conditions, via in situ formation of secondary magnetic minerals, particularly when complemented by independent proxies. By combining environmagnetic, geochemical, and siliciclastic grain size data, we investigated marine sediment core GL-1090 (24.92°S, 42.51°W, 2,225 m water depth) aiming to unravel changes in terrigenous sediment input and bottom water conditions during the last ~184 ka at the western South Atlantic middepth. The Al/Si, Fe/κ and siliciclastic grain size data show that terrigenous sediments at this core location derived from the Plata River (southeastern South America). This material was transported northwards by the Brazilian Coastal Current and their delivery to our core site was modulated by sea-level oscillations. Periods of low sea-level were characterized by the input of coarser and more abundant terrigenous sediments. Environmagnetic parameters indicate significant downcore variations in the magnetic domain state, which we interpret as changes in the content of biogenic magnetite following glacial-interglacial cycles. Coeval negative excursions in magnetic grain size and benthic $\delta^{13}C$ suggests that concentrations of single domain magnetite (possibly magnetotactic bacterial magnetite) vary in response to middepth water ventilation. We suggest that reduced ventilation in the middepth western South Atlantic bottom waters during peak glaciations triggered a decrease in the production of biogenic magnetite. Peak glaciations were, in turn, linked with increases in the residence time of North Atlantic Deep Water (or its glacial counterpart).

Key Points:

- Multi-proxy approach points to the Plata River as the main lithogenic sediment source to tropical SE South American continental margin, modulated by sea-level
- Reduced biogenic magnetite formation coeval with negative benthic $\delta^{13}C$ anomalies during glaciations
- Biogenic magnetite formation hampered by decreased bottom water ventilation during glaciations

Supporting Information:

- Supporting Information S1

Correspondence to:
G. L. Mathias,
g.mathias@alumni.usp.br

Citation:
Mathias, G. L., Roud, S. C., Chiessi, C. M., Campos, M. C., Dias, B. B., Santos, T. P., et al. (2021). A multi-proxy approach to unravel late Pleistocene sediment flux and bottom water conditions in the western South Atlantic Ocean. *Paleoceanography and Paleoclimatology*, *36*, e2020PA004058. https://doi.org/10.1029/2020PA004058

Received 27 JUL 2020
Accepted 4 FEB 2021

1. Introduction

Combining rock-magnetic proxies with bulk sediment characteristics has been proven useful to unravel the composition of the primary minerals present in the sediment, transport dynamics in different marine settings and sediment provenance (Hounslow & Maher, 1999; Itambi et al., 2009; Just, Dekkers, et al., 2012; Mathias et al., 2014; Razik et al., 2013). In turn, marine sediments are widely used to reconstruct continental paleoclimate, often based on major element composition. Relative changes in major element concentrations provide insights into weathering intensity in the source area (Sheldon & Tabor, 2009), paleoenvironments in the continent (Just, Heslop, et al., 2012), and sediment transport pathways (Mulitza et al., 2008; Portilho-Ramos et al., 2017). Changes in marine sediment may also be recorded in the magnetic as well as bulk mineral assemblies. Care is always needed as sedimentary minerals may have been formed in the source area (primary assembly) and/or after deposition, during early diagenesis (authigenic assembly) (Chang, Bolton, et al., 2016; Funk et al., 2004). In terms of authigenesis, the presence of bacterial magnetosome particles can often be inferred within the sedimentary "haystack" due to some characteristic magnetic "fingerprints", even if they constitute only a minor fraction of the bulk magnetic assemblage (Egli et al., 2010; Roberts et al., 2012). If preserved, this additional biogenic magnetic component may provide unique insights into past benthic microbial activity and bottom water conditions effective when the sediments were deposited.

Paleoceanography and Paleoclimatology 10.1029/2020PA004058

Transported terrigenous magnetic minerals form the primary magnetic assemblage of marine sediments. Their concentration, composition and size distribution are a function of the geologic characteristics of the source area, weathering conditions and transport mechanisms, each potentially leaving characteristic fingerprints on the marine sedimentary magnetic assemblage (Evans & Heller, 2003; Liu et al., 2012; Maher & Thompson, 1999; Thompson & Oldfield, 1986; Verosub & Roberts, 1995). The western South Atlantic is bathed by diverse water masses from remote areas (i.e., Southern Ocean, northern North Atlantic Ocean, and Indian Ocean) and receives terrigenous sediments from multiple drainage basins in South America. In subtropical latitudes, one large (i.e., Plata River) and many small (e.g., Paraíba do Sul River) drainage basins occupy southeastern South America and deliver terrigenous sediments to the western South Atlantic (Razik et al., 2015). Changes in sediment production, transport and delivery over southeastern South America are expected to affect the terrigenous infill of the subtropical western South Atlantic. In mid-depths (~2,000 m), the western South Atlantic is influenced by the southward-flowing Deep Western Boundary Current that transports North Atlantic Deep Water (NADW) (Stramma & England, 1999). During deposition, the terrigenous material can be "diluted" by primary production of carbonate and opal, while the magnetic assemblage can be altered through the production of biogenic magnetic minerals by benthic microorganisms. Additionally, during early diagenesis, all magnetic minerals may undergo chemical alterations (oxidation, reduction, dissolution) depending on the redox conditions of the sediment (Chang, Roberts, et al., 2014; Hounslow & Maher, 1999; Karlin et al., 1987; Lovley et al., 1987; Roberts, Florindo, et al., 2011). Under sulphidic conditions, additional magnetic information can arise through the formation of magnetic sulphide minerals (Roberts, Chang, et al., 2011). Because the complete history of sediments, from source to sink including diagenetic alteration, can leave characteristic marks on the magnetic mineral assemblage, sedimentary magnetic properties comprise a powerful, if sometimes complex, tool to disentangle the driving forces of sediment supply and transformation. Biogenic magnetic particles produced by magnetotactic bacteria (MTB) appear almost ubiquitous in surface sediments (Maher & Hounslow, 1999; Roberts et al., 2012). Such bacteria commonly live near the sediment-water interface in the chemically stratified horizons spanning the oxic to anoxic transition (e.g., Faivre & Schüler, 2008). MTB biomineralize intracellular, membrane-bound magnetic nanoparticles, called magnetosomes, which are composed of magnetite (Fe_3O_4) or greigite (Fe_3S_4) depending on the redox conditions of their habitat (Bazylinski et al., 1995; Chen et al., 2014). The ecological roles of these particles remain unresolved but they are often ideal single-domain (SD) magnets that passively align the microorganisms with the Earth's magnetic field, suggesting some contribution to directed motility. The long intracellular chains of dense magnetite may also provide some cellular structural support (Hanzlik et al., 1996). If preserved in the sedimentary record, the MTB magnetofossils register past microbial activity and sediment chemistry. Their abundance has been linked to paleo-environmental and sedimentary conditions (Hesse, 1994; Kopp & Kirschvink, 2008; Maher & Hounslow, 1999; Roberts, Florindo, et al., 2011). Although it has been demonstrated that the number of living MTB undergoes seasonal changes (Du et al., 2015; He et al., 2018) and that magnetofossil abundance in deep-sea sediments can be modulated by organic carbon and dissolved iron availability (Roberts, Florindo, et al., 2011) or by primary productivity (Savian et al., 2014), our understanding of the conditions responsible for MTB magnetic mineral formation is still limited.

Here we provide new magnetic, geochemical, and siliciclastic grain size data from a core collected from the middepth western South Atlantic (24.92°S, 42.51°W, 2,225 m water depth) covering the last 184 ka. Changes in the concentration of magnetic minerals, major elements, and siliciclastic grain size suggest Plata River as the main source of the terrigenous material deposited in the subtropical western South Atlantic, with a mixing of terrigenous material from Paraíba do Sul River modulated by sea-level oscillations. In addition, we observed relationships among variations in magnetic grain size, benthic foraminifera $\delta^{13}C$ (Santos et al., 2017), and total organic carbon (Figueiredo et al., 2020), which suggest a potential connection between bottom water ventilation and single domain, possibly bacterial magnetite abundance. Magnetic grain size changes in response to glacial and interglacial stages may offer new insights into the influence of NADW (or its glacial counterpart) ventilation on bacterial magnetite abundance.

Paleoceanography and Paleoclimatology 10.1029/2020PA004058

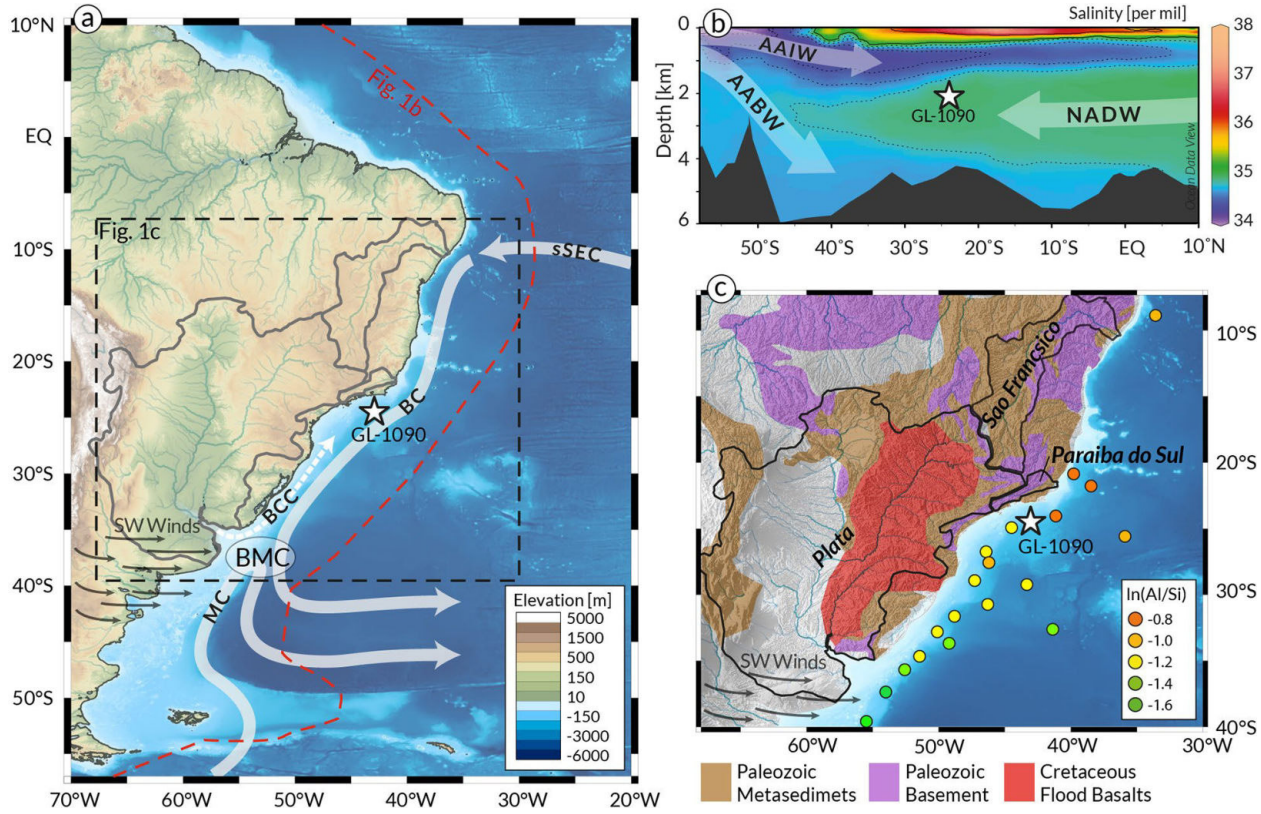

Figure 1. Overview of the study area. The location of marine sediment core GL-1090 is shown in each panel by a white star. (a) Topographic map of South America with the catchment area of rivers of interest that drain into the western South Atlantic outlined in black. The white arrows over the bathymetric map of the South Atlantic schematically depict the surface currents of interest (i.e., Brazilian Coastal Current [BCC], Brazil Current [BC] and Malvinas Current [MC]) as well as the Brazil-Malvinas Confluence (BMC). Thinner gray arrows show the Westerlies. The red and black dashed lines indicate the position of the salinity transect in Figure 1b and the location of Figure 1c, respectively. Topography and bathymetry from ETOPO1 (Amante & Eakins, 2009). (b) Western South Atlantic modern mean annual salinity (color shading; Zweng et al., 2013). Main water masses are depicted by the gray arrows, Antarctic Intermediate Water (AAIW), North Atlantic Deep Water (NADW) and Antarctic Bottom Water (AABW). (c) Simplified geology of the major drainage basins, outlined in black, that represent relevant source areas for terrigenous material in the study area (geology simplified after/adapted from "World CGMW, 1:50M, Geologic Units Onshore" with sedimentary overburden removed) (Commission for the Geological Map of the World). Major tributaries of the Plata River are shown in blue. Colored dots on the adjacent continental margin indicate surface sediment ln(Al/Si) values after Govin et al. (2012). This figure was partially produced using the software Ocean Data View (Schlitzer, 2019).

2. Study Area

2.1. Hydrographic Setting, Sediment Redistribution

Figures 1a and 1b shows the complex oceanographic setting of the western South Atlantic. On the continental shelf (upper 100 m of the water column), Plata River discharge is transported to the north by the Brazilian Coastal Current (BCC) (Piola et al., 2005; Souza & Robinson, 2004). Satellite observations of sea surface salinity and temperature suggest that the modern BCC reaches as far north as 25°S (Souza & Robinson, 2004). Magnetic studies of Holocene sediments, however, suggest that the Plata River plume has delivered sediments further north, up to at least 24°S (Mathias et al., 2014).

Beyond the shelf break, the upper 500 m of the water column is dominated by the southward transport of the Brazil Current (BC) which originates from the southern branch of the South Equatorial Current at about 10°S. The BC transports the warm and saline equatorial waters poleward until it collides with the northward-flowing Malvinas Current and is deflected to the east (Peterson & Stramma, 1991; Stramma & England, 1999). This convergence area, the Brazil-Malvinas Confluence Zone, is located around 33–38°S offshore the Plata River mouth (Figure 1a).

Paleoceanography and Paleoclimatology 10.1029/2020PA004058

From 500 m down to intermediate depths (~1,200–1,500 m water depth), the Intermediate Western Boundary Current (IWBC) transports Antarctic Intermediate Water (AAIW) and Upper Circumpolar Deep Water (UCDW) toward the north (Figure 1b) (Boebel et al., 1999). The southern-sourced AAIW and UCDW are relatively fresh, cold, nutrient-enriched and oxygen-depleted water masses (Tsuchiya et al., 1994). NADW fills the mid-depths of the water column between ~1,200 and 3,000 m water depth (Stramma & England, 1999). NADW, a nutrient-depleted and oxygen-enriched water mass, has a similar temperature but is saltier than its overlying water mass (Tsuchiya et al., 1994). NADW is transported southwards by the Deep Western Boundary Current, and at 25°S reaches maximum salinity (~0.35 psu) in its deepest part (Stramma & England, 1999).

2.2. Geological Setting, Sediment Sources

Southeastern South America is characterized by the presence of the Serra do Mar and Serra da Mantiqueira mountain ranges close to the Atlantic coastline that forces rivers to drain into the hinterland and deviate from this topographic barrier before reaching the western South Atlantic. The narrow coastal plain adjacent to our core location, dominated by Precambrian basement and Fe oxide-rich meta-sediments, is drained by a number of minor rivers with a combined drainage area of $\sim 6 \times 10^5$ km^2 (Figure 1c). Among these rivers, the Paraíba do Sul is closest to our study site (~20°S, 41°W), and drains a small catchment area (5.7×10^4 km^2) of which more than 90% is covered by Precambrian rocks, with predominance of granitoid gneisses, migmatites, biotite-gneiss and biotite schists (Gómes Tapias et al., 2019). The two major basins that drain the hinterland before reaching the western South Atlantic host the São Francisco and Plata rivers. The São Francisco River drains an area of $\sim 6 \times 10^5$ km^2 of Precambrian hinterland into the tropical Atlantic at ~ 10°S (ca. 15° north of our study site). About 10° south of our study site (~35°S, 57°W), the Plata River meets the subtropical Atlantic Ocean. Its tributaries, the Paraná and Uruguay rivers, drain an area five times bigger than the São Francisco Basin ($\sim 3.2 \times 10^6$ km^2). The Plata Basin represents the largest source of terrigenous material to the western South Atlantic and ranges from the Mesozoic-Tertiary Andean Mountains in the west to the Cretaceous Flood Basalts (Paraná-Etendeka igneous province) in the east (Gómes Tapias et al., 2019). With only minor riverine input in close proximity, the sedimentary dynamics at the core site is primarily controlled by sediment redistribution by ocean currents, and primary carbonate production; both modulated by climatic and sea-level changes (Mahiques et al., 2008; Razik et al., 2015).

In addition to riverine transport of detrital material to the continental margin of southeastern South America, the westerlies play an important role in transporting dust from the Andes to the mid-latitudes off southern South America (e.g., Gaiero et al., 2003). During dry glacial climate stages, enhanced generation and transport of aeolian dust increased the transport of terrigenous material to the Argentinean and Uruguayan continental shelves (e.g., Maher et al., 2010).

3. Materials and Methods

3.1. Core GL-1090

Marine sediment core GL-1090 is 1,914 cm long and was collected from the continental slope (2,225 m water depth) of southeastern South America (24.92°S, 42.51°W) (Figure 1), in a region bathed by the NADW. GL-1090 is mostly composed of carbonate mud. According to Santos et al. (2017), greenish to olive sediments somewhat rich in foraminifera-bearing silty clay characterize glacial layers. Carbonate-rich reddish-brown and whitish clays characterize interglacial sediments. At about 30 cm core depth, there is a ~ 2 cm-thick ferruginous crust.

3.2. Age Model

The age model for core GL-1090 was published in Santos et al. (2017) and is based on 10 accelerator mass spectrometer radiocarbon ages from planktonic foraminifera (covering the top 327 cm), combined with 13 benthic foraminifera $\delta^{18}O$ tie-points aligned to two reference curves (Govin et al., 2014; Lisiecki & Raymo, 2005) for the lower part of the core (327–1,914 cm). Core GL-1090 covers the last ~184 ka. The mean sedimentation rate for core GL-1090 is 13 cm/ka. Highest rates were observed during MIS 4 with 24 cm/ka.

Paleoceanography and Paleoclimatology 10.1029/2020PA004058

During MIS 5e, MIS 5d and MIS 1 the sedimentation rates are smaller than 5 cm/ka, with minimum of 3 cm/ka. The complete age model and details on the methodology used to produce it can be found in Santos et al. (2017).

3.3. Rock Magnetism

For the rock magnetic characterization of the sediment core, a series of laboratory magnetization and demagnetization experiments were carried out on unorientated samples in plastic cylinders (16 cm^3 volume). We measured volume magnetic susceptibility (κ) on the whole core with a 2 cm resolution using a 130 mm diameter Bartington loop sensor (MS2C) integrated with a Geotek Multi-Sensor Core Logger system. For 101 of the single samples, we imparted an anhysteretic remanent magnetization (ARM) at 300 mT using a bias field of 0.1 mT. Thereafter, we demagnetized the ARM on these samples using 77 steps up to 300 mT, as suggested by Egli (2004). The ARM was acquired, measured and demagnetized using a 2G Enterprises RAPID magnetometer 755 (noise level 5×10^{-12} Am^2) housed in a magnetically shielded room (ambient field <500 nT) at the Laboratory of Paleomagnetism (USPMag), Institute of Astronomy, Geophysics and Atmospheric Sciences (IAG), University of São Paulo, Brazil. We imparted isothermal remanent magnetization (IRM) to 163 samples in three steps (at 100, 300, and 1,000 mT), and backfields at −100 and−300 mT using a magnetizer Newport 4″ Electromagnet Type A (0–1.5 Tesla) and measured the IRMs with a Molspin fluxgate spinner magnetometer (noise level $\sim 5 \times 10^{-10}$ Am^2) at the Center for Environmental Magnetism and Paleomagnetism (CEMP), University of Lancaster, United Kingdom.

From these measurements, we derived typical environmental magnetic proxies to determine type, size and concentration of the magnetic carriers (e.g., Evans & Heller, 2003; Maher & Thompson, 1999). The susceptibility (κ) measures the induced magnetization of the bulk sediment, and is often dominated by ferrimagnetic materials. Magnetic susceptibility of ferrimagnetic minerals (up to $\sim 57 \times 10^{-6}$ m^3kg^{-1} e.g., magnetite) is orders of magnitude larger than antiferromagnetic ($\sim 0.5 \times 10^{-6}$ m^3kg^{-1}, e.g., hematite), paramagnetic ($\sim 0.4 \times 10^{-6}$ m^3kg^{-1}, e.g., clay minerals) and diamagnetic (-0.005×10^{-6} m^3kg^{-1}, e.g., carbonate) materials (Maher, 1998). Paramagnets and diamagnets have minor contributions to bulk sediment susceptibility in comparison to ferrimagnetic minerals, yet dilution effects may affect the total susceptibility (Hounslow & Maher, 1999). The geochemical/magnetic proxy Fe/κ is a relative measure of how much of the total Fe is bound in magnetic minerals. The IRM is representative of the total concentration of magnetic minerals. Differences between the IRM acquired at 300 mT (IRM_{300}) and 1 T (SIRM) reveal contributions of different magnetic mineral types. The S-Ratio (=(IRM_{300}/SIRM)/2) can track relative mineralogical changes of magnetically “hard” versus “soft” minerals (Bloemendal et al., 1992). HIRM (=(SIRM + IRM_{-300})/2) is useful in quantifying relative concentrations of the high-coercivity (magnetically “hard”) mineral, like hematite (Maher et al., 2004).

The ARM represents mainly the low-coercivity ferrimagnetic mineral fraction (usually magnetite) and is selective toward the stable single domain grains that exhibit ARMs 1–2 orders of magnitude greater than larger grains (Maher, 1988; Peters & Dekkers, 2003). Ratios of ARM/IRM are thus sensitive to relative changes in grain size. Here we use $\chi ARM_{300mT}/IRM_{100mT}$ (χARM/IRM hereafter) to detect changes in magnetite grain size. ARM_{300} was converted to susceptibility of ARM (χARM) by normalizing with the bias field (79.625 A/m).

We further characterized 72 representative sub-samples by measuring hysteresis loops, stepwise IRM acquisition and backfield curves with maximum fields of 1T. We used a Princeton Measurements Corporation MicroMag 3900 Vibrating Sample Magnetometer at both the Laboratory of Paleomagnetism (USPMag), Institute of Astronomy, Geophysics and Atmospheric Sciences (IAG), University of São Paulo, and at the Paleomagnetism and Environmental Magnetism Laboratory, National Oceanography Center (NOC), Southampton, United Kingdom.

From hysteresis loops and backfield curves, we obtained the saturation remanence (Mrs), saturation magnetization (Ms), the coercive field (Bc) and the coercivity of remanence (Bcr). The ratios Mrs/Ms and Bcr/Bc provide information on the magnetite grain size and resultant domain structures of the magnetic particles, indicative of different grain size thresholds: superparamagnetic (SP), single-domain (SD), pseudo-single domain (PSD), and multidomain (MD) (Dunlop & Özdemir, 1997). A cross plot of the two ratios allows

Paleoceanography and Paleoclimatology 10.1029/2020PA004058

some preliminary assessment of the average domain state (i.e., magnetic grain size), identification of relative grain size changes and checking the presence of different types of magnetic minerals (Dunlop, 2002).

For a more detailed characterization of the finest magnetite fraction, we measured high-resolution first-order reversal curves (FORC) of seven subsamples representing horizons of different glacial stages. These measurements were performed in a Princeton Measurements Corporation vibrating sample magnetometer at the Department of Earth and Environmental Sciences, Ludwig-Maximilians, University of Munich, Germany. The measuring protocol was optimized to selectively cover the central ridge area of the FORC diagram that characterizes SD particle distribution. (H_b: −10/+20 mT, H_c: 0–80 mT, H_{Sat}: 300 mT, increment 0.5 mT (N:233), averaging time: 120 ms, sample mass: 0.2 g). The FORC distributions were calculated using VARIFORC (Egli, 2013) by averaging 10 high-resolution measurements per sample, applying variable smoothing and extracting the central ridge feature. Variable smoothing factor was applied to reduce noise in the low amplitude areas of the FORC space and increase the resolution of the central ridge (VARIFORC processing parameters: sc,0 = 4, sc,1 = sb,1 = 5, λc = λb = 0.1).

3.4. Major Elements

X-ray fluorescence (XRF) core scanner data were collected every 5 mm down-core over a 60 mm^2 area (down-core slit size of 5 mm using generator settings of 10 kV, a current of 0.35 mA, and a sampling time of 20 s), directly from the split core surface of u-channels collected from the archive half of core GL-1090. The data were collected using the XRF Core Scanner II (AVAATECH Serial No. 2) at the Center for Marine Environmental Sciences (MARUM), University of Bremen, Germany. The split-core surface was covered with a 4 μm thin SPEXCerti Prep Ultralene1 foil to avoid contamination of the XRF measurement unit and desiccation of the sediment. The element data reported here were acquired by a Canberra X-PIPS Silicon Drift Detector (SDD; Model SXD 15C-150-500) with 150 eV X-ray resolution, the Canberra Digital Spectrum Analyzer DAS 1000, and an Oxford Instruments 50W XTF5011 X-ray tube with rhodium (Rh) target material. Recently, Figueiredo et al. (2020) published XRF core scanner data from core GL-1090 in counts for the elements Ti, Al, Fe, Mn, and Ca. Here we present major element concentrations obtained from bulk sediment samples in order to cross-calibrate the scanner counts. We freeze-dried, powdered, and homogenized 55 samples (~5 g of dry sediment). Major element concentrations were measured by energy dispersive polarization X-ray fluorescence (EDP-XRF) spectroscopy at the Department of Geochemistry, Fluminense Federal University, Brazil. We performed the calibration using a log-ratio approach after Weltje and Tjallingii (2008). The log ratios of major element (Al, Si, K, Ca, Ti, Mn, S, and Fe) and Ca as denominator were calculated. The log-ratios of the core scanner data were then calibrated to the corresponding ratios of the powder measurements through linear regression. Figure S1 shows the comparison between EDP discrete data and calibrated curve with XRF counting.

We show elemental concentrations of Al, Si, K, Ti, and Fe considered to represent terrigenous contributions, and Ca, representing the biogenic calcium carbonate fraction of the bulk sediment (Govin et al., 2012). Assuming that terrigenous Fe and Ti have a common origin (Figure S2a), we used the immobile element Ti as a normalizer for Fe, aiming to assess if the iron distribution in the sediment has been altered after deposition. The terrigenous fraction of the bulk sediment can be further characterized by the elemental ratios, Al/Si, which reflects compositional and/or grain size changes in the siliciclastic mineral fraction, and Fe/K, which responds to changes in the clay mineral composition and reflects weathering intensity (Govin et al., 2012). Since Fe can be remobilized in the sediment after deposition (Reitz et al., 2004), in this study we used K/Ti to identify weathering intensity in the continent, as K derives from minerals characteristic from dry regions, like potassium feldspar and illite (Zabel et al., 2001).

3.5. Siliciclastic Grain Size

Particle size measurements of sediment core GL-1090 were performed in a particle analyzer via laser diffraction (CILAS 1064) in the Department of Geochemistry at Fluminense Federal University, Brazil. The analysis was performed on decalcified and organic matter-free samples, by the addition of HCl 1M and 30% hydrogen peroxide, respectively. The results were calculated following the Wentworth scale for particle size classification.

Paleoceanography and Paleoclimatology 10.1029/2020PA004058

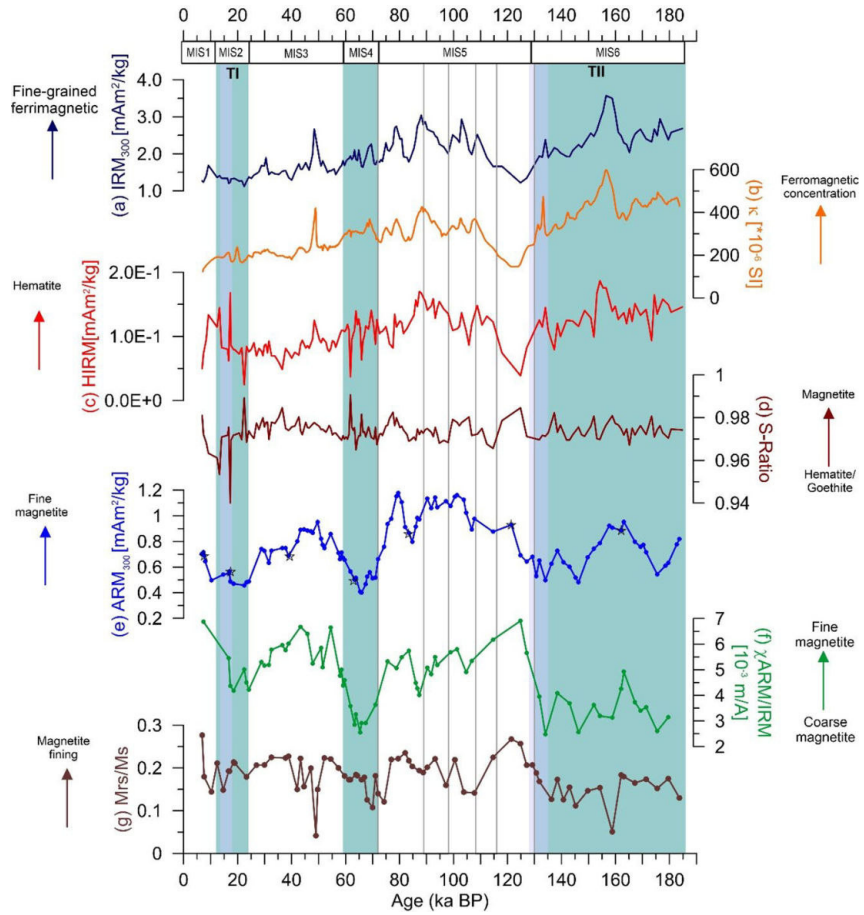

Figure 2. Downcore environmental magnetic parameters (a)–(f), and hysteresis parameter Mrs/Ms (g) from marine sediment core GL-1090. (a) IRM_{300}, (b) magnetic susceptibility (κ), and (c) HIRM, record changes in the concentration of magnetic minerals. (d) S-Ratio, records relative changes in magnetite versus haematite. (e) ARM_{300} reflects changes in the concentration of fine magnetic grains, (f) χARM/IRM, and (g) Mrs/Ms record changes in the relative proportion of fine magnetite *vs*. course magnetite. Black stars in plot (e) show the samples we performed FORC analysis. The main lithological changes vary accordingly with cold/warm stages, blue/white bars, respectively, which represent marine isotope stages (Lisiecki & Raymo, 2005). Gray lines represent the MIS 5 stages (Santos et al., 2017), and gray bars show Terminations II and I (TII and TI, respectively) (Lisiecki & Raymo, 2005).

4. Results

4.1. Magnetic Characterization

4.1.1. Magnetic Mineral Concentration

Magnetic susceptibility (κ) displays highest values (Figure 2b) during marine isotope stage (MIS) 6, reaching a prominent peak (~600 × 10^{-6} SI) at ~157 ka, and then gradually declining (except during MIS 4) through to the present interglacial (MIS 1). Some variability is evident during MIS 5; during the last interglacial (MIS 5e), magnetic susceptibility reaches its lowest values (~122 × 10^{-6} SI), comparable with the low values of MIS 1. At about 48 ka, it rises again (~414 × 10^{-6} SI); magnetic susceptibility is increased during the entire MIS 4, as we observe during MIS 6, but varies within a smaller range. IRM_{300} varies in accordance with magnetic susceptibility throughout the core (Figures 2a and 2b; Figure 6a), ranging between 1 × 10^{-3} and 4 × 10^{-3} Am^2/kg. HIRM follows the general trend of magnetic susceptibility and IRM_{300} (Figure 2c), with values ranging between 1 × 10^{-5} and 4 × 10^{-4} Am^2/kg (Figures 2a–2c). We calculated Pearson (ρ_p) and Spearman (ρ_s) correlation coefficients and a good correlation exists between HIRM and κ (ρ_p = 0.64 and ρ_s = 0.67). From MIS 6 to MIS 2, low but measurable HIRM values display similar variations as IRM_{300}.

Paleoceanography and Paleoclimatology 10.1029/2020PA004058

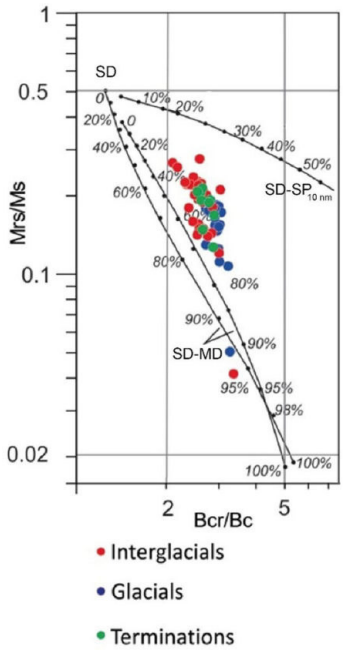

Figure 3. Magnetic hysteresis parameters from marine sediment core GL-1090 represented on a plot of Mr/Ms versus Bcr/Bc (Day et al., 1977). Samples collected in different climate periods are represented by red (interglacial), blue (glacial), and green (termination) circles. The data fields represent areas expected for single domain (SD), pseudo-single domain (PSD), and multi-domain (MD) (titano) magnetite particles. The curves represent theoretical mixing lines for SD–MD and SD-$SP_{10\ nm}$ mixtures (Dunlop, 2002).

Local HIRM maxima in MIS 1, however, indicate selective enrichment of high-coercivity minerals in these interglacial horizons.

4.1.2. Magnetic Mineralogy

The S-ratio mean value (~0.97) is close to the theoretical maximum of 1 for most of the studied period (Figure 2d). It is notable that the lowest S-ratio value (0.94) is observed at ~17 ka, at the same level as the ferruginous crust, and thus likely reflects the increased presence of oxidized magnetic minerals (Figure S7). In IRM acquisition curves, ~95% of the magnetization is saturated before 300 mT (Figure S5), indicative of magnetically soft magnetic minerals. The hysteresis loops all present similar shapes, with a narrow waist and low coercive fields ranging between 10 and 18 mT (Figure S6a). All samples show an important paramagnetic component (~70%) (Figure S6b). We calculated the mean coercivity from ARM demagnetization curve for 10 samples along core GL-1090, and the average value is ca. 27 mT.

4.1.3. Magnetic Grain Size

The hysteresis ratios Mrs/Ms and Bcr/Bc range from 0.1 to 0.3 and from 2.0 to 3.5, respectively (Figures 2g and 3). Using the Day Plot (Day et al., 1977) and following the theoretical SD-MD mixing curve proposed by Dunlop, 2002, our samples fall in the range of 40%–80% coarse MD grains (Figure 3). Grouping the samples into glacial (MIS 6, 4, and 2), transitional (glacial termination) and interglacial horizons (MIS 1, 3, and 5) reveals a trend of relative grain size fining from cold to warm stages. MIS 5, 3, and 1 show higher ARM_{300} values (higher concentration of finer, SD-like magnetic grains) relative to the cold MIS stages, 6, 4, and 2 (Figure 2e). Short-duration (millennial-scale) decreases in ARM can be seen during MIS 5d/5c and MIS 5b/5a transitions, and higher values during MIS 5e, 5c, 5a. Coeval variations both in χARM/IRM and Mrs/Ms further demonstrate a relative coarsening of the magnetic grain size during cold climate stages (Figures 2e–2g).

FORC diagrams for samples from each isotope stage are dominated by a central ridge feature, confirming the presence of non-interacting SD particles in each measured horizon. Separation of the central ridge (CR) from the background (BG) signal allows characterization of the SD and MD fractions (Figures 4 and S9). Figure 4 shows the extracted CR features and their normalized coercivity distributions. The topmost sample (4 cm depth) has the strongest signal, indicating highest SD magnetite concentrations. Its lower coercivity spectrum (average $H_c < 10$ mT) that is connected to the vertical ($H_c = 0$) axis suggests the presence of very fine particles close to the SP-SD threshold. All samples from below 4 cm core depth contain fairly similar CRs, indicative of stable SD grains. The similarity of the curves suggests that the properties (e.g., size and mineralogy) of the SD particles remain fairly constant below 36 cm depth.

4.2. Major Elements

The highest ln(Ti/Ca) values are observed in the first half of MIS 6 and during MIS 4 (Figure 5f). During MIS 5, this ratio shows several peaks between 110 and 106 ka (MIS 5d/5c transition), 91 and 85 ka (MIS 5b/5a transition), and ~79.6 and 77.2 ka (MIS 5a) (Figure 5f). Minima in ln(Ti/Ca) values are observed just after Terminations II (TII) and I (TI), during MIS 5e and MIS 1, respectively. A peak in ln(Fe/Ca) is observed at ~17 ka (not matched in prominence by the ln(Ti/Ca) ratio) (Figures S3a and S3b), which is probably related to the ferruginous crust (Figure S7) observed in this part of the core (for lithology details, see Section 3.1). Since Fe bound in (oxy-) hydroxides is highly reactive, it can be prone to post-depositional dissolution and re-precipitation; whereas Ti is resistant to alteration. Therefore, we use ln(Ti/Ca) as a conservative proxy for terrigenous input. Two significant peaks are also observed in ln(Fe/Ti) (~130 ka, during TII, and at ~17 ka, during TI) and an abrupt decrease during MIS 5e (Figure 5l).

Paleoceanography and Paleoclimatology 10.1029/2020PA004058

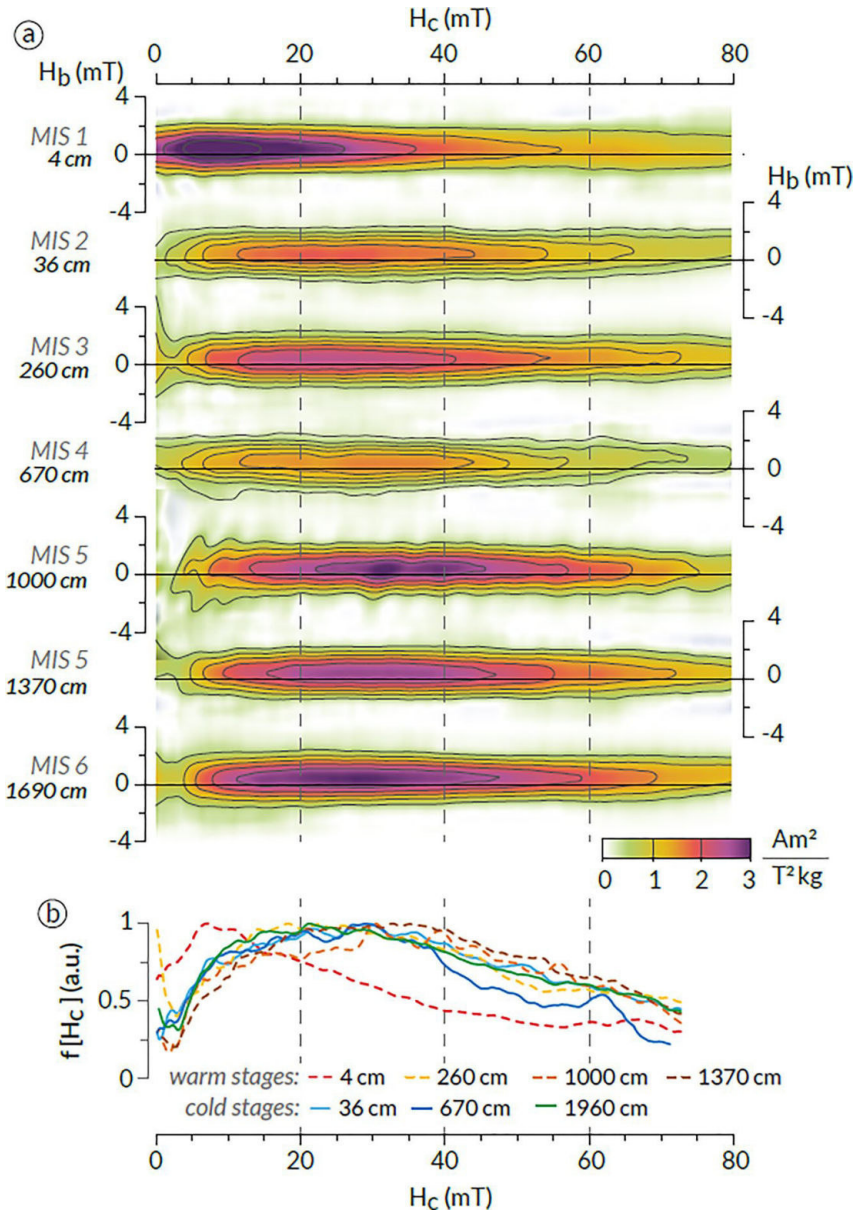

Figure 4. Down core series of FORC diagrams for representative samples from marine sediment core GL-1090. (a) Isolated central ridges, and (b) combined normalized coercivity distributions of the central ridges shown in panel (a). The respective Marine Isotope Stage (MIS) of each sample is indicated in the left-hand side of panel (a). For measurement and analytical detail see Section 3.3 of the text. Black stars in Figure 2e represent the location of the FORC samples along core GL-1090.

Values of ln(Fe/K) display little variability during most of the recorded period, except for two notable peaks (post-depositional feature) during TII and TI (Figure S3c). During TI, ln(Fe/K) values gradually increase, with a sharp drop at the end of the termination, followed by another gradual increase up to MIS 1. To avoid the influence of the outliers we observe in Fe/K (Figure S3c), we used K/Ti instead to examine sediment source. The ln(Al/Si) values show little change during MIS 6, a sharp increase just after TII, a gradual decrease encompassing MIS 5-2, and a sharp increase just after TI (Figure 5j). Aiming to evaluate the marine contribution (i.e., biogenic opal), we also present the ln(Al/Ti), which reflects only the terrigenous input (Figure S3d). The correlation between ln(Al/Ti) and ln(Al/Si) is high ($\rho_p = 0.81$) during MIS 6-4, but after that ln(Al/Ti) shows a smooth decrease during MIS 3, whilst ln(Al/Si) exhibits few variance (Figure S2b).

Paleoceanography and Paleoclimatology 10.1029/2020PA004058

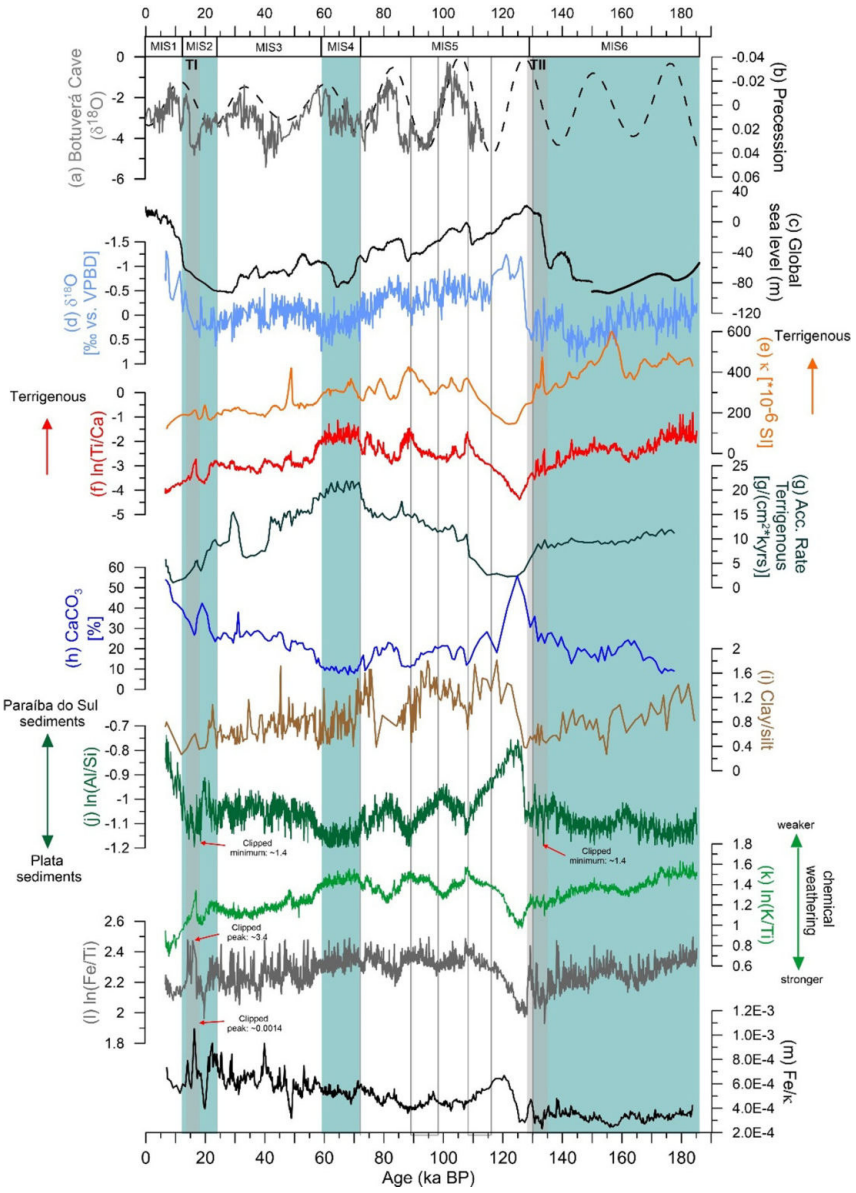

Figure 5. Downcore parameters from marine sediment core GL-1090. External literature: (a) Speleothem $\delta^{18}O$ from Botuverá Cave (Cruz et al., 2006), (b) Precession (Berger & Loutre, 1991), (c) Global Sea Level for the last 150 (Grant et al., 2012) and between 150 and 186 ka (de Boer et al., 2012), (d) *Globigerinoides ruber* $\delta^{18}O$ (Santos et al., 2017), and (h) $CaCO_3$ (%) (Figueiredo et al., 2020); parameters for sediment provenance: (e) magnetic susceptibility, (f) Ti/Ca, (g) accumulation rate of terrigenous, (i) Clay/Silt, (j) Al/Si, (k) K/Ti, and reductive proxies: (l) Fe/Ti and (m) Fe/κ. The main lithological changes vary accordingly with cold/warm stages, blue/white bars, respectively, which represent marine isotope stages (Lisiecki & Raymo, 2005). Gray lines represent the MIS 5 stages (Santos et al., 2017), and gray bars show Terminations II and I (TII and TI, respectively) (Lisiecki & Raymo, 2005).

Notable features of the Fe/κ data are a sharp increase just after Termination II, a marked decrease prior to Termination I, and an increasing trend until MIS 1, when it declines (Figure 5m).

4.3. Redox-Sensitive Elements

Under suboxic to anoxic conditions, Mn, Fe, and S can easily be remobilized in the sediment. Relative enrichment and depletion of Mn and Fe can, therefore, reveal insights into the sediment redox conditions and bottom water oxygen concentration during deposition (Reitz et al., 2004). In core GL-1090, prominent

Paleoceanography and Paleoclimatology 10.1029/2020PA004058

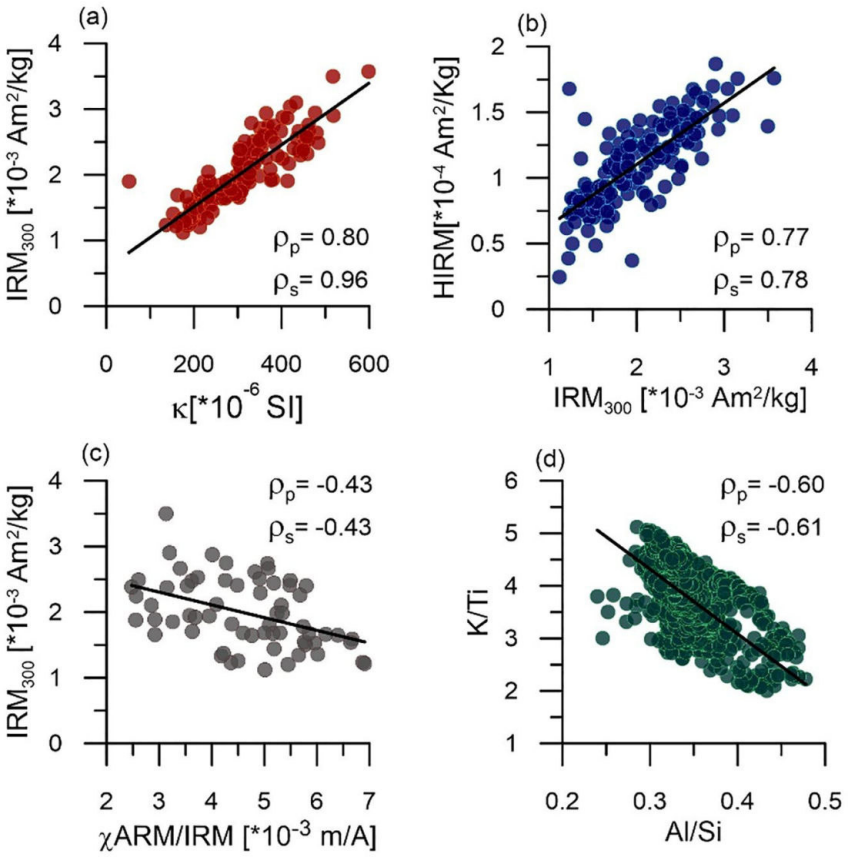

Figure 6. Scatterplots between magnetic and geochemical proxies from marine sediment core GL-1090. The black line represents the linear fit. Pearson Correlation Coefficient (ρ_P) and Spearman Correlation Coefficient (ρ_S) were calculated and are displayed on the plots.

anomalies in ln(Mn/Ti) and ln(Fe/Ti) relative to core-top values reveal a characteristic sequence of Mn and Fe enrichment at two levels (Figure 7). Consecutive peaks of these two trace metals at the end of MIS 2 and MIS 6 for Fe and just after that at MIS 5e and MIS 1 for Mn correspond to the last two glacial terminations (Figure 7). During TII and TI ln(Fe/Ti) peaks likely reflect the post-depositional iron re-precipitation in the ferruginous crust, with no peak seen in the ratio ln(K/Ti) (Figures 5k and 5l). Likewise, an abrupt decrease in ln(Fe/Ti) after TII leading to a pronounced minimum during MIS 5e indicates Fe depletion. In contrast to Mn and Fe, we find only minor variations in relative S concentration (ln(S/Ti), Figure 7).

4.4. Siliciclastic Grain Size

The sediment in core GL-1090 is mainly composed of mixed silt and clay, with minor contribution of sand (<1%) detected only in four samples. The clay/silt ratio ranges between 1.81 and 0.27 (Figure 5i). A gradual reduction in the clay/silt ratio is observed during MIS 6 and from MIS 4 to MIS 1, indicating a decrease in the proportion of the finest particles, reaching a minimum around both TII and TI (0.37 and 0.36, respectively). A marked rise in the clay/silt ratio is observed during MIS 5e; the predominance of fine sediments is maintained during MIS 5d, 5c, 5b, and also during the transition from MIS 5a to MIS 4.

5. Discussion

5.1. Sediment Composition Controlled by Source Area and Sea-Level

The magnetic concentration parameters (IRM_{300} and κ) alongside ln(Ti/Ca) indicate the highest terrigenous inputs during MIS 6 (~160 ka) and transitions MIS 5d/c (~108 ka) and b/a (~90 ka), and the lowest during

Paleoceanography and Paleoclimatology 10.1029/2020PA004058

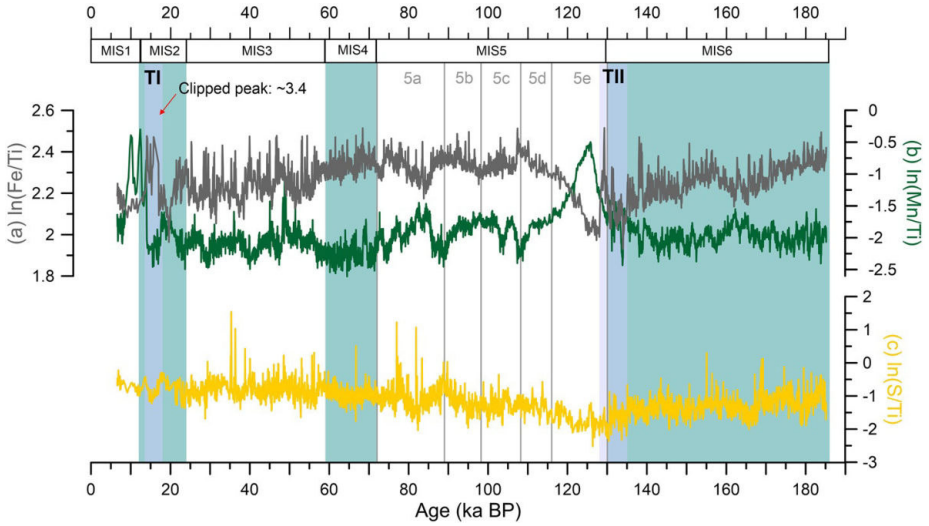

Figure 7. Redox sensitive elements represented by relative iron (Fe/Ti), magnesium (Mn/Ti), and sulphur (S/Ti) concentration compared to the terrigenous "background sedimentation" represented by titanium. The main lithological changes vary accordingly with cold/warm stages, blue/white bars, respectively, which represent marine isotope stages (Lisiecki & Raymo, 2005). Gray lines represent the MIS 5 stages (Santos et al., 2017), and gray bars show terminations II and I (TII and TI, respectively) (Lisiecki & Raymo, 2005).

MIS 5e and 1 (Figures 2a, 5e, and 5f). Both IRM_{300} and κ are dominated by a ferrimagnetic (magnetite-like) mineral component. Comparatively low HIRM and high S-ratio values suggest only minor contributions from antiferromagnetic minerals (hematite and/or, less likely, goethite) (Figures 2c and 2d). Because HIRM follows the general trend of IRM_{300} and magnetic susceptibility its changes may also reflect variations in the concentration of ferrimagnetic particles, instead of variance in the type of magnetic minerals (Figure 6b). The concentration of fine-grained magnetite, represented by ARM_{300} (Figure 2e), does not mirror variations in IRM and susceptibility, but instead exhibits maxima during warm stages MIS 3 and MIS 5. The magnetic grain size proxy χARM/IRM (Figure 2f) varies accordingly, indicating a relative enrichment in single domain magnetite in interglacial stages.

High values of magnetic susceptibility, ln(Ti/Ca) and the accumulation rate of terrigenous material during MIS 6 and 4 reflect an increase in terrigenous supply and a possible response to glacio-eustatic sea-level fall (Figures 5e–5g, 6a, 6b, and S2d). These changes in terrigenous supply are accompanied by compositional changes as evident from variations in ln(Al/Si) and ln(K/Ti) (Figures 5i and 5j, 6d, S2f and S2g). The correlation between ln(K/Ti) and ln(Ti/Ca) demonstrates that the siliciclastic sediment composition is closely linked to the amount of terrigenous material deposited. A more acid geochemical signature (elevated K/Ti and reduced Al/Si) corresponds to a larger terrigenous fraction (Ti/Ca). Notably, the S-ratio is consistently high throughout core GL-1090, and shows no covariation with either proxies sensitive to changes in terrestrial chemical weathering (K/Ti and S-ratio show low correlation and is not shown here; $\rho_p = 0.05$ and $\rho_s = 0.12$) nor with precipitation records from SE South America (Cruz et al., 2005, 2006). Thus, in contrast to the siliciclastic sediment composition, the sediment magnetic mineralogy type has remained constant over time (Figures 2, 5a, and S2h).

Long-term changes in precipitation over SE South America have been attributed to orbital-scale variations in insolation (directly affected by precessional changes) (Figures 5a and 5b). Precipitation over southeastern South America is associated with the mature phase of the South America Monsoon System (Marengo et al., 2012), which is characterized by a well-developed South Atlantic Convergence Zone (Carvalho et al., 2004). The Plata and Paraíba do Sul drainage basins are under the influence of the South America Monsoon System, which produces a see-saw effect: enhanced (decreased) precipitation in its core and the southern Brazilian coast, and drier (wetter) conditions in southern South America (Garreaud et al., 2009). During austral summer, maximum insolation in the Southern Hemisphere (sub)tropics intensified the monsoon system , increasing the relative amount of summer precipitation (Cruz et al., 2005). Changes in

Paleoceanography and Paleoclimatology 10.1029/2020PA004058

terrigenous content (magnetic susceptibility, IRM_{300}, HIRM, ln(Ti/Ca), ln(Al/Ti)) and weathering product (ln(Al/Si) and ln(K/Ti)) of core GL-1090 do not follow changes in precession (Figures 2, 5, and S2g, S2i, S2j). Thus, we exclude precipitation as a controller for terrigenous input in our study site.

Variations in ln(Al/Si) have been used to track changes in siliciclastic particle size (Mulitza et al., 2008), in circumstances where there have been no major changes in terrestrial chemical weathering conditions or the flux of biogenic opal (Chiessi et al., 2010). The siliciclastic particle size distribution in GL-1090 gradually changes from clay- to silt-dominated from early to late MIS 6, reaching its maximum coarseness during Termination II and I (Figure 5m). After TII, and in association with maximum sea-level (i.e., MIS 5e), particle size becomes finer, until clays dominate the record. Notwithstanding a similar trend in siliciclastic grain size and ln(Al/Si) across Termination II, overall, the correlation between both parameters is not significant (Figure S2e); thus, siliciclastic grain size appears not to be the main driver of variations in the Al/Si ratio in core GL-1090. Concerning biogenic opal, some authors have suggested an increase in silicic acid content and primary productivity in the southern Brazilian margin during cold stages (Portilho-Ramos et al., 2019). However, the concentration of biogenic opal at ~2,000 m water depth, the depth of our core site, is small (<1%) according to Romero and Hensen (2002).

The parameter Fe/κ varies coevally with ln(Al/Si) and with sea-level changes (Figures 5c, 5j, and 5m; $\rho_p = 0.85$, scatterplot not presented). Changes in Fe/κ may reflect post-depositional Fe remobilization (Funk et al., 2004; Reitz et al., 2004), as seen in the Fe enrichment, in association with the ferruginous crust in core GL-1090 (Figure S7), and/or changes in terrigenous source materials, with differing proportions of para- and ferromagnetic Fe-bearing minerals (Itambi et al., 2009). Because of the covariation of Fe/κ with the redox independent parameter (Al/Si), we infer that overall Fe/κ reflects changes in the primary Fe-oxide mineralogy. Coeval minima in ln(Al/Si) and Fe/κ suggests that relatively more Fe was bound in ferromagnetic minerals of the sediment delivered to our core site (Figures 5j and 5m).

Temporal changes in Al/Si may indicate variation in the source weathering conditions. Al enrichment, recorded during interglacial periods (MIS 1 and 5e), thus points to either enhanced weathering in the source area and/or to a shift in sediment source toward more humid areas in proximity to the core location. A typical weathering product in tropical regions is the Al-rich clay mineral, kaolinite. Originating predominantly from NE Brazil, kaolinite constitutes more than 80% of the clay mineral fraction at ~20°S (off the Paraiba do Sul River mouth) and to less than 10% off the Plata River, south of ~30°S (Petschick et al., 1996). In arid regions, weathering can lead to potassium (K) enrichment (from illite or K-feldspar); in the surface sediments of the western South Atlantic, K enrichment is expressed as a strong south-north gradient in ln(K/Ti) values (Figure S4c). The observed anti-correlation between ln(Al/Si) and ln(K/Ti) in GL-1090 further supports a shift between more humid weathering products deposited during interglacial periods and more arid weathering products deposited during glacial periods.

There is very little riverine input to the continental margin off southeastern Brazil, thus contributions from more distal areas with higher runoff seem likely. Several studies have shown that at sea level lowstand, a substantial fraction of the terrigenous material from the Plata River plume reaches as far north as 24°S (Gyllencreutz et al., 2010; Mathias et al., 2014; Piola et al., 2000, 2005). Magnetic characterization of modern Plata River sediments identified the presence of ultrafine and fine (4–16 μm) detrital magnetite in the Plata mud belt, that would be transported up to 24°S by the BCC (Razik et al., 2015). The influence of Plata River sediments at this latitude was also suggested for the mid-Holocene based on environmagnetic parameters (Mathias et al., 2014). In addition, the elemental composition of suspended sediment from the Plata River exhibits the same Al/Si values as measured in sediments from the south Brazilian margin (24°S) (Depetris et al., 2003). Paraíba do Sul River is another potential source area to the Southeastern South America adjacent margin. In the surface sediments of the Western South Atlantic, the Al/Si ratio (as well as the kaolinite concentration) exhibits a strong latitudinal gradient (Govin et al., 2012; Petschick et al., 1996) (Figure 1c). Govin et al. (2012) have found comparable Ti/Al values between south Brazil (24°S–38°S) and Plata River sediments. We observe a good correlation between ln(Al/Si) and ln(Al/Ti) in MIS 6-2 ($\rho_p = 0.84$ and $\rho_s = 0.73$) in core GL-1090 (Figure S2b), which may suggest an enhanced supply of Plata River-sourced sediment during glacial stages. As biogenic opal does not affect Al/Ti, we assume that the influence of biogenic opal on the ln(Al/Si) record is negligible. Mn/Ti ratios along core GL-1090 show a peak in Termination I that clearly reflects changes in the redox condition, since it happens just after the Fe peak (Figures 7a and

Paleoceanography and Paleoclimatology 10.1029/2020PA004058

7b). In TII, there is a less clear peak, possibly reflecting a mixing signal; redox conditions plus sediment from volcanic rock in Paraná Basin. After TII and TI, sudden increases in ln(Al/Si) likely reflect decreased delivery of Plata River sediments to our study site. Transgressive sea-level events drowned the Plata River estuary, decreasing the northwards transport of Plata River sediments by the BCC. During these periods, the reduction in Al-rich siliciclastics indicates a changed and/or additional sediment source, producing a mixture of sediments from the Plata and Paraíba do Sul rivers. We therefore suggest that relative Al depletion and K enrichment during full glacial stages MIS 6, 4 and 2 (and, to a lesser degree at the MIS 5d/5c and MIS 5b/5a transitions) reflect the northward extent of the Plata River plume, modulated by glacio-eustatic sea-level changes. Minimum ln(Al/Si) and maximum ln(K/Ti) values in GL-1090 indicate that terrigenous sediments delivered to our study site during glacial periods were similar in composition to present day surface sediments deposited off the Plata River mouth. We therefore infer that the Plata plume was the dominant source of terrigenous sediment to our study site during glacial maxima. A reduced northward transport of the Plata plume during interglacial sea-level high stands led to an overall decrease in terrigenous input to the study site, promoting a higher relative contribution from Paraíba do Sul River.

Additional to the suspended sediments from the Plata and Paraíba do Sul rivers, another potential source of terrigenous sediments is aeolian dust transported by the westerlies to the Argentinean and Uruguayan continental shelves (e.g., Maher et al., 2010). Prospero et al. (2002) characterized three main dust sources in South America: one located in the Bolivian Altiplano (20°S, 67°W) and two in Argentina: Patagonia (38–48°S) and Santa Cruz (46–48°S). These authors identified a modern active dust area in the southern Pampas and northern Patagonia. According to Gaiero et al. (2003), about 90% of the present day material deposited in the SW South Atlantic is delivered by the atmospheric pathway and comes from Patagonia. The magnetic characterization of sediments from the southeastern Brazil margin (24°S) indicates the Argentinean loess as the possible source of fine magnetite (PSD) between 6 and 4.7 ka BP (Mathias et al., 2014). In addition to the Plata Plume sediment, Razik et al. (2015) suggested that material delivered to the Southern Atlantic margin from the Argentinean Pampas by westerly winds is transported further north (24°S) as well. These authors reported magnetic concentrations in surface sediments that are widely different from the magnetic data from core GL-1090 (Figure S8). Especially the magnetic grain size parameter (χARM/IRM) from core GL-1090 is one order of magnitude higher than the surface sediment data from Southern Atlantic margin, whereas the other magnetic parameters present similar values with the Pampean Shelf magnetic material, which is mostly composed of aeolian dust transported by the westerlies.

5.2. Terrigenous versus Biogenic Signals

Similar to the geochemical proxies for terrigenous sediment input (Ti/Ca and K/Ti), the magnetic mineral concentration (as indicated by IRM_{300} and κ) is greatest during MIS 6 (~160 ka) and transitions MIS 5d/c (~108 ka) and b/a (~90 ka), and lowest during MIS 5e and 1 (Figures 2a–2c and 5e, 5f, 5k). In contrast, the concentration of the magnetic fine fraction (ARM and χARM/IRM, Figures 2e and 2f) shows low correlation with total terrigenous flux to our study site (Figures 6c and S2c). Continuous S-ratio values close to 1 throughout the core (Figure 2d), together with >95% IRM acquisition at fields smaller than 300 mT (Figure S5), indicate that the sediment magnetization is carried by a magnetically soft material like magnetite (or potentially greigite). Substantive contributions from greigite, a common authigenic magnetic Fe-sulphide, can however be excluded because of the absence of its characteristic signatures from the FORC diagrams (Figures 3 and 4) (Roberts et al., 2006). Thus, it appears that the magnetic remanence is dominantly carried by magnetite throughout core GL-1090.

Alongside ARM, both magnetic grain size-dependent parameters (χARM/IRM and Mrs/Ms) indicate enrichment of SD magnetite in the warm stages MIS 1, 3, and 5 and depletion in the cold stages MIS 2, 4 and 6 (Figures 2e–2g). Considering domain state estimates from the Day plot (Day et al., 1977) our data fall in two clusters in the area characteristic for PSD particles or of SD-MD mixtures of ~40%–80% MD particles (Day et al., 1977; Dunlop, 2002). HIRM and S-ratio show no correlation, which suggest that minor hematite inputs observed along core GL-1090 are independent from magnetite enrichment (Figures 2c, 2d, and S2d). Magnetic grain size (χARM/IRM) plotted against the concentration parameter IRM_{300} shows anti-correlation, implying that the SD magnetite fraction changes independent of terrigenous flux (Figures 2

Paleoceanography and Paleoclimatology 10.1029/2020PA004058

and 6c). This indicates either an additional source of SD magnetite during warm stages and/or selective dissolution of the fine fraction during cold stages.

FORC diagrams of all samples of core GL-1090 are dominated by a central ridge, which indicates the presence of non-interacting SD particles (Egli et al., 2010) throughout the core (Figure 4a). The low Hc central ridge in the 4 cm sample (MIS 1) may suggest an assemblage of nanometre-sized less stable particles close to the SP-SD threshold (10–15 nm), possibly extracellular magnetite (Lovley et al., 1987; Roberts et al., 2000). Potentially this particle fraction is absent below 4 cm depth because of reductive dissolution (Hounslow & Maher, 1999). The coercivity range (30–40 mT) of the central ridge from our samples below 4 cm depth has been reported previously as a typical signal of bacterial magnetite (Egli et al., 2010; Roberts et al., 2012). Low (32–44 mT) and restricted coercivity range has been attributed to uniform grain size assembly of MTB magnetite (Abrajevitch & Kodama, 2011). Similar coercivity has been observed also in silicate crystals with magnetite inclusions (Chang, Roberts et al., 2016). The presence of fine magnetite (SD) from clayey silt weathered from La Plata Drainage Basin was detected up to 24°S along the Brazilian coast (Razik et al, 2015). Yet, a comparison between these data and our magnetic parameters shows that the concentration parameters κ, HIRM, and IRM_{300} from core GL-1090 are lower than most of the data from Razik et al. (2015), whereas some samples from the Plata Shelf display similar values (Figures S8a and S8b). In addition, our magnetic grain size parameter is an order of magnitude higher than the finest fraction identified by Razik et al. (2015), suggesting finer magnetic particles in core GL-1090 (Figure S8c). Regarding a partial dissolution of SD magnetite, it cannot be ruled out entirely. However the two facts that ARM minima are not restricted to the narrow horizons of Fe and Mn-mobilization and that we see no indication of enhanced sulfidization of the sediments (see 5.3), lead us to infer that reductive dissolution of the detrital magnetic mineral assembly was not important in core GL-1090. Greigite magnetosomes also have a central ridge, but typically show a lower coercivity range (maximum intensity~20 mT) (Chang, Vasiliev, et al., 2014; Chen et al., 2014; Reinholdsson et al., 2013). Hence, the SD particles detected here are consistent with magnetite magnetofossils.

The intensity of the FORCs central ridge varies following ARM intensity, suggesting that ARM primarily reflects the concentration of non-interacting SD magnetite (Figures 2e and 4a). If reductive dissolution would have affected the SD magnetite assemblage in some horizons selectively, one could expect an impact on the grain size distribution where SD concentrations are lowest. Identical coercivity distributions below 4 cm depth however suggest a uniform size distribution of the SD particles, further supporting the assumption of an ARM signal that was not affected by early diagenesis. The "background" FORC distributions with the central ridge removed are typical for PSD-MD ferrimagnetic particle assemblages (Roberts, 2006; Roberts et al., 2000). With highest intensities around H_C = 10 mT, we attribute the background FORCs to the detrital magnetite fraction (Figure S9). The uniform coercivity distribution among the background FORCs for GL-1090 samples suggests a consistent detrital magnetite component throughout the core.

Our environmagnetic parameters show that detrital magnetite is the dominant magnetic mineral in GL-1090 and variations in the magnetite concentration correspond to changes in the terrigenous flux. In contrast, the concentration of SD magnetite appears to be decoupled from the terrigenous flux. Significantly higher SD contribution in comparable surface sediments along the western South Atlantic (Razik et al, 2015) and the lack of evidence for selective dissolution of the fine fraction indicate that SD magnetite in core GL-1090 is derived from an independent, possibly post-depositional, process. Although not unique, the magnetic properties of the SD fraction are consistent with the presence of biogenic magnetite formed by magnetotactic bacteria.

5.3. Redox Conditions and Early Diagenesis Processes

To better understand the impact of any post-depositional alterations on core GL-1090 and its rock magnetic properties, we look at the distribution of reactive metal species that can give insights into the early diagenetic redox processes in the sediment. The redox conditions of sediments are driven by the microbial oxidation of organic matter (early diagenesis), as controlled by the balance between organic matter supply and the availability of oxidants. When oxygen is depleted, different types of microorganisms will utilize successively less efficient oxidants: nitrate, Mn-oxides, Fe-oxides and sulphate (e.g., Canfield & Thamdrup, 2009). Thereby, dissolved Mn^{2+} and Fe^{2+} can then migrate within the sediment column and

Paleoceanography and Paleoclimatology 10.1029/2020PA004058

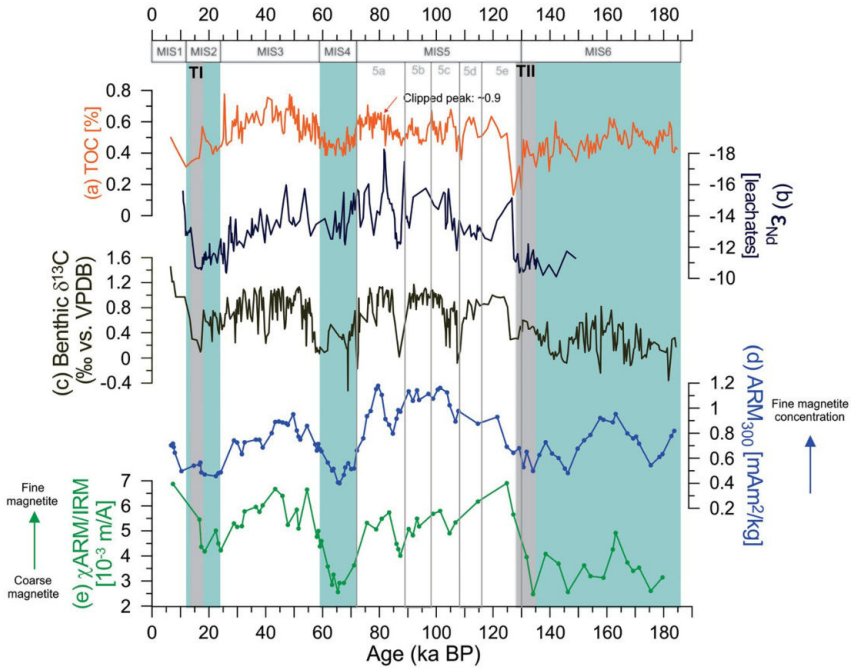

Figure 8. Association between SD biogenic magnetite and NADW ventilation via magnetic parameters, total organic carbon (TOC), stable carbon isotopic composition ($\delta^{13}C$) of benthic foraminifera and ε_{Nd} record. (a) TOC (Figueiredo et al., 2020), (b) ε_{Nd} record from Bermuda Rise ODP site 1,063 (Bohm et al., 2015) (c) benthic *Cibicides wuellerstorfi* $\delta^{13}C$ (Santos et al., 2017), and (d)–(e) magnetic grains size parameters from GL-1090. The main lithological changes vary accordingly with cold/warm stages, blue/white bars, respectively, which represent marine isotope stages (Lisiecki & Raymo, 2005). Gray lines represent the MIS 5 stages (Santos et al., 2017), and gray bars show terminations II and I (TII and TI, respectively) (Lisiecki & Raymo, 2005).

rapidly re-precipitate in the presence of oxygen or dissolved sulphide. Sudden changes in the availability of involved substances can cause an imbalance in the early diagenetic sequence. Such nonsteady state conditions can lead to the prolonged fixation of sediment redox zones and to localized accumulation of authigenic precipitates (Reitz et al., 2004).

Successive Mn and Fe enrichments associated with both glacial terminations in GL-1090 (Figure 7) are characteristic for a prolonged fixation of sub-oxic redox boundaries and indicate repeated non-steady state conditions (Reitz et al., 2004). Non-steady state conditions can be caused by a decrease in sedimentation rates, a decrease of bottom water oxygenation and/or an increase in bioavailable organic matter buried in the sediment (e.g., due to increase in primary productivity). The glacial terminations in GL-1090 are both associated with a drop in sedimentation rates (Santos et al., 2017), relative increase in carbonate (low ln(Ti/Ca), Figures 5f, 5g, and 5h) and minima in the TOC content (Figure 8a, Figueiredo et al., 2020). We thus suggest that the fixation of redox horizons at our study site was driven by the sudden decline of terrigenous sediment flux during glacial terminations. Reduced TOC concentrations at these horizons may be related to enhanced in situ carbon degradation during these times. Notably, Figueiredo et al. (2020) have reported anomalies in mercury (Hg) concentration in GL-1090 associated with the glacial terminations. They attributed these anomalies to changes in organic carbon cycling and, in case of TII, to the presence of an active redox boundary.

The maximum depth of the Fe peak at TI corresponds to the visually observed reddish-brown ferruginous crust (Figure S7) and likely represents the position of the present-day Fe-redox boundary (Fe^{2+}/Fe^{3+}). The successive Mn and Fe peaks at TII are less well defined than those around TI (Figures 7a and 7b). They likely represent a relic of non-steady state diagenesis during the rapid transitions from glacial conditions in MIS 6 to interglacial conditions in MIS 5e, analogous to the last glacial termination. The correlation between Al/Si and Mn/Ti is intermediate ($\rho_p = 0.58$ and $\rho_s = 0.54$; Figure S2i). Hence, the use of Mn/Ti as a proxy for sediment provenance is not reliable. Instead, we use Al/Si and K/Ti.

Paleoceanography and Paleoclimatology 10.1029/2020PA004058

Local peaks in Fe/κ, that match anomalous ln(Fe/Ti) values during TII and TI, point to additional Fe remobilization effects (Figures 5l and 5m). The paramagnetic Fe component in these sediments is contributed by the clay minerals, biotite and nontronite. Notable is that the magnetic concentration-based parameters (IRM_{300} and HIRM) do not exhibit anomalies during TII and TI, suggesting that, notwithstanding some evidence of post-depositional Fe mobilization, the ferromagnetic signal along core GL-1090 appears to be preserved (Figure 2). In order to evaluate if the ferromagnetic signal has not been erased, and hence still reflects changes in sediment supply/provenance, we used elemental ratios excluding iron, ln(K/Ti) and ln(Al/Ti) (Figures 5k and S3d). Indeed, both of these ratios also undergo substantial changes during and after TII and TI, supporting an important shift in sediment provenance through the transitions MIS 6/5e and MIS 2/1.

The absence of sulphur enrichments at these horizons (associated with both glacial terminations) furthermore demonstrates the oxic character of the Fe-precipitates (Figure 7). The general absence of localized S enrichments in the core indicates that either suboxic (nonsulfidic) reduction prevailed in the sampled horizons or that the sulfidic zone has not been fixed at a certain depth interval. This assumption is further supported by the observation that none of our rock magnetic proxies show depletion zones, even in horizons where there is evidence for Fe-mobilization. Possibly, an excess of more readily soluble Fe-oxyhydroxides played a role in the preservation of magnetite. Ferrihydrite, for instance, has been suggested to be more reactive toward sulphide than iron oxides (Canfield, 1989). Such minerals may have been preferentially dissolved and remobilized leaving the distribution of the more crystalline magnetic Fe-oxide fraction intact.

Given that Fe remobilization is limited and does not appear to control the preservation of the ferromagnetic signal (Figures 2 and 5e), we suggest that our SD magnetite-sensitive parameters reflect climatically modulated changes in the rate of biogenic magnetite formation (Figures 8d and 8e). We cannot exclude the alternative possibility of selective biogenic magnetite dissolution/preservation but some observations argue against magnetite dissolution in the cold stages when SD magnetite concentration is low. The redox sensitive proxies, Fe/Ti and Fe/κ, indicate that horizons associated to glacial terminations experienced Fe remobilization, which likely involved the local dissolution of Fe-oxides. However, minima in SD magnetite are not restricted to these narrow horizons but occur throughout the entire cold stages MIS 6, 4 and 2. As we find no indication for the systematic dissolution of magnetite in these cold stages, it appears reasonable to assume that variations in SD magnetite reflect the primary concentration of SD magnetite.

5.4. Magnetite Formation Induced by Mid-depth Ventilation

ARM is very sensitive to the presence of SD magnetite particles (Evans & Heller, 2003; Maher, 1988; Schmidbauer & Veitch, 1980). SD magnetite exhibits ARM 1–2 orders of magnitude higher than the larger MD magnetite (Dunlop, 1981; Hartstra, 1982; Maher, 1988; Peters & Dekkers, 2003). Within sedimentary sequences, the presence of biogenic intracellular magnetite records the past activity of MTB (Funk et al., 2004; Kirschvink & Chang, 1984; Kopp & Kirschvink, 2008; Korff et al., 2016; Petersen et al., 1986; Stolz et al., 1986; Vali et al., 1987). MTB actively form well-ordered chains of magnetite (or more rarely, greigite), often as uniform SD particles (Bazylinski, 1999; Bazylinski et al., 1995; Blakemore et al., 1985; Matsuda et al., 1983). Upon deposition and preservation within sediments, these particles, released by lysis of the host magnetosomes, form a fossil record of past MTB activity, physical characteristics that allow them to be identified by their strong and distinctive magnetization (Egli et al., 2010; Maher & Hounslow, 1999; Roberts et al., 2012, 2013). The magnetofossil concentration depends on (i) the MTB abundance, thus magnetite production during sediment deposition, and (ii) the degree of preservation of SD magnetite crystals released from magnetosomes after burial. Reductive dissolution of iron oxides includes the removal of authigenic magnetic minerals (including biogenic magnetite) from the sediment and may eliminate the magnetofossils (Chang, Bolton, et al., 2016; Korff et al., 2016; Lippert, 2008; Maher & Hounslow, 1999). Thus, water column conditions, early diagenesis and all post-depositional processes that may affect the microbial metabolism (i.e., surface primary productivity, carbon exported to the seafloor, organic matter decomposition) can all play a role in the preservation or dissolution of these magnetofossils.

The concentration of biogenic magnetite in sediments can mirror the past abundance of MTB during the time the sediment formed. However, due to their small size, magnetofossils are also susceptible to reduc-

Paleoceanography and Paleoclimatology 10.1029/2020PA004058

tive dissolution and their abundance may respond to post-depositional redox processes. As outlined above, we find no indication for glacial-stage dissolution of SD magnetite in GL-1090. Korff et al. (2016) reported characteristic coarsening of magnetite in pelagic sediments affected by dissolution, with correlation between magneto-granulometric parameters (ARM_{300}, χARM/IRM) and concentration-dependent parameters (κ and IRM), and with Fe. Core GL-1090 displays no such correspondence between these parameters, suggesting that little or no dissolution effects took place (Figures 7c and S2c). Further, the interplay between MTB production/preservation and organic carbon flux can provide valuable insights into diagenetic conditions in the sediment. Roberts et al. (2011) have shown that higher organic carbon concentration is associated with greater MTB abundance. Here, TOC changes are generally coeval with magnetic grain size fining, with low (high) values during the glacial (interglacial) horizons (Figures 8a, 8d, and 8e). The correlation between TOC and benthic $\delta^{13}C$ shows intermediate values, due to the different trends in TII and TI (Figures 8a and S2k). Without these outliers, represented by low TOC (%) values, the TOC/benthic $\delta^{13}C$ correlation increases to $\rho_p = 0.56$ and $\rho_s = 0.58$. Hence, it seems likely that the middepth site of core GL-1090 in the subtropical western South Atlantic was propitious for MTB production under interglacial and glacial conditions during the last ~184 ka, with enhanced (decreased) MTB production during warm stages (glaciations), but no cessation of bacterial magnetite formation during the lower-oxygen glacials (Figures 8a, 8d, and 8e).

Association between scavenging of reactive species of metal and physical/chemical conditions of NADW has been found recently by Figueiredo et al. (2020), supporting the idea of bottom water ventilation affecting sediment redox conditions in the subtropical western South Atlantic. The negative excursions in benthic $\delta^{13}C$ in core GL-1090 core suggest that bottom water ventilation changed at this site during the last ~184 ka. Notably, the concentration of fine-grained magnetite (ARM_{300}) and the grain size-dependent parameter (χARM/IRM) co-vary with $\delta^{13}C$ of epibenthic foraminifera *Cibicides wuellerstorfi* (Santos et al., 2017), indicating that common processes may have controlled these parameters (Figures 8c–8e and S2l). It is notable that both our SD magnetite record and $\delta^{13}C$ anomalies from core GL-1090 (Santos et al., 2017) vary synchronously with ε_{Nd} from Bermuda Rise sediments (Bohm et al., 2015) (Figure 8b) reinforcing the notion that middepth ventilation plays a key role in ocean variability over different timescales through changes in the Atlantic Meridional Overturning Circulation strength. Changes in in the abundance of benthic microbes, like MTB, may also be related to varying conditions in the overlying bottom water. Since $\delta^{13}C$ of *C. wuellerstorfi* reflects the $\delta^{13}C$ of the bottom water dissolved inorganic carbon with no pore water effects (Mackensen et al., 1993; Mackensen & Schmiedl, 2019), we suggest that MTB magnetite production was at least partially controlled by changes in the overlying bottom water. Negative $\delta^{13}C$ excursions in the western South Atlantic are frequently associated with periods of weak Atlantic Meridional Overturning Circulation (e.g., glacial stages and Heinrich stadials) (Campos et al., 2020; Lund et al., 2015; Santos et al., 2017; Schmittner & Lund, 2015). During these periods of reduced ventilation, increased NADW residence time allowed the accumulation of respired carbon at Atlantic mid-depths (Campos et al., 2020; Howe et al., 2016; Schmittner & Lund, 2015; Voigt et al., 2017). The carbon accumulated as a result of increased microbial respiration at the expense of oxygen. Seawater $[O_2]$ reconstruction from the North Atlantic also points to a decrease in the oxygen availability of bottom waters during cold events (Hoogakker et al., 2016). The coeval trends in magnetic domain state (ARM_{300}, χARM/IRM), *C. wuellerstorfi* $\delta^{13}C$ negative excursions, and TOC around the end of the penultimate and last glacial cycles (i.e., during MIS 6 and 2), as well as during MIS 4 (Figures 8c–8e) support an association between our magnetic record and changes in the NADW ventilation. Hence, we hypothesize a decrease in the biogenic magnetite production during periods of reduced ventilation.

Notably, between 175 and 145 ka BP, the ARM_{300} intensity and χARM/IRM in our core exhibit values similar to those recorded during MIS 3 and $\delta^{13}C$ shows a positive excursion (Figures 8c–8e). Santos et al (2017) noticed higher variability in $\delta^{13}C$ from early- to mid-MIS 6 in comparison to MIS 3 (Figure 8c). The same study, using Mg/Ca analysis in *G. ruber* shells for core GL-1090, recorded high sea surface temperature variability in the same period (during early-MIS 6). The positive values observed in magnetic grain size parameters and $\delta^{13}C$ during early-MIS 6 may suggests that, exceptionally during this glaciation, biogenic magnetite formation increased in response to ventilation change, which during this period resembles its interglaciation mode, with decreased NADW residence time.

Paleoceanography and Paleoclimatology 10.1029/2020PA004058

6. Conclusions

In core GL-1090 from the subtropical western South Atlantic mid-depth, magnetic concentration-dependent parameters and major element ratios dominantly reflect glacio-eustatic-modulated changes in the delivery of terrigenous detrital particles. In contrast, changes in magnetic grain-size, likely driven by the concentration of biogenic magnetite, may reflect variations in oceanographic environment during the last ~184 ka. Changes in ln(Al/Si) and Fe/κ indicate that, during periods of low sea-level, sedimentation at this location was dominated by coarser (silt and clay) detrital input from the Plata River, and more Fe was bound to ferromagnetic terrigenous magnetic minerals. Coeval changes in ln(Al/Ti) and ln(K/Ti) support this sediment source interpretation. Conversely, during periods of high sea level, transgressive drowning of the Plata River estuary diminished the northward transport of Plata River sediments by the BCC. During these periods, a mixture between Plata and Paraíba do Sul rives takes place. Decoupled from changes in the terrigenous sources, glacial/interglacial changes in the magneto-granulometric parameters, χARM/IRM and Mrs/Ms together with the SD magnetite concentration parameter ARM_{300}, may reflect variations in the post-depositional formation of biogenic magnetite. The continuous presence of SD magnetite throughout the core suggests that bottom water conditions were favorable both for bacterial magnetite formation and the preservation of magnetofossils. However, coeval declines in SD magnetite concentrations and negative $\delta^{13}C$ values during glacial stages suggest that the reduced ventilation of NADW (or its glacial counterpart) hampered the production of MTB-formed magnetite. In this interpretation, during cold marine isotopic stages, magnetofossil concentrations are lower, directly co-varying with epibenthic foraminifera $\delta^{13}C$ and TOC. Independent, quantitative examination of sediment magnetic extracts would be required in order to test this hypothesis.

Acknowledgments
We thank Stefanie Brachfeld (reviewer), two anonymous reviewers and the anonymous associate editor for constructive comments. This work was supported by CAPES (grants 88882.151090/2017-0, 88881.196484/2018-01 and 88887.177256/2018-00). Cristiano Mazur Chiessi acknowledges financial support from FAPESP (grant 2018/15123-4), CAPES (grants 564/2015 and 88881.313535/2019-01), CNPq (grants 302607/2016-1 and 422255/2016-5) and the Alexander von Humboldt Foundation. M.C. Campos acknowledges the financial support from FAPESP (grant 2016/10242-0). A.L.S. Albuquerque is a senior CNPq researcher (grants 302521-2017-8 and 429767/2018-8), and acknowledges the financial support from CAPES (Finance Code 001, PRINT 88881.310302-2018/01). Sophie C. Roud acknowledges financial support from the Deutsche Forschungsgemeinschaft (grant GI712-16/1). Bruna B. Dias appreciates financial support from CAPES/FAPERJ (grant 202.134/2015). Grasiane L. Mathias acknowledges Prof. Andy Biggin from School of Environmental Sciences, University of Liverpool, UK, and Chuang Xuan and Jin Yuxi from National Oceanography Center (NOC), Southampton, UK, for providing laboratory facilities and friendly receiving me. Janna Just from MARUM, Center for Marine Environmental Sciences, University of Bremen, Germany is thanked for kindly calibrating the EDP-XRF data. This study has benefited from detailed reviews by Prof. Wilbor Poletti, UFVJM, Brazil.

Data Availability Statement

Germany is thanked for kindly calibrating the EDP-XRF data. New data presented herein are archived in Pangaea (https://doi.pangaea.de/10.1594/PANGAEA.922302).

References

Abrajevitch, A., & Kodama, K. (2011). Diagenetic sensitivity of paleoenvironmental proxies: A rock magnetic study of Australian continental margin sediments. *Geochemistry, Geophysics, Geosystems*, *12*. https://doi.org/10.1029/2010GC003481

Amante, C., & Eakins, B. W. (2009). *ETOPO1 1 arc-minute global relief model: Procedures, data sources and analysis* (pp. 1–19). National Geophysical Data Center, NOAA, NOAA Technical Memorandum NESDIS NGDC-24.

Bazylinski, D. A. (1999). Synthesis of the bacterial magnetosome: the making of a magnetic personality. *International Microbiology*, *2*, 71–80.

Bazylinski, D. A., Frankel, R. B., Heywood, B. R., Mann, S., King, J. W., Donaghay, P. L., Hanson, A. K. (1995). Controlled Biomineralization of Magnetite (Fe (inf3) O (inf4)) and Greigite (Fe (inf3) S (inf4)) in a Magnetotactic Bacterium. *Applied and Environmental Microbiology*, *61*, 3232–3239.

Berger, A., & Loutre, M. F. (1991). Insolation values for the climate of the last 10 million years. *Quaternary Science Reviews*, *10*, 297–317.

Blakemore, R., Short, K., Bazylinski, D., Rosenblatt, C., & Frankel, R. B. (1985). Microaerobic conditions are required for magnetite formation within Aquaspirillum magnetotacticum. *Geomicrobiology Journal*, *4*, 53–71.

Bloemendal, J., King, J. W., Hall, F. R., & Doh, S.-J. (1992). Rock magnetism of Late Neogene and Pleistocene deep-sea sediments: Relationship of sediment source, diagenetic processes, and sediment lithology. *Journal of Geophysical Research*, *97*, 4361–4375.

Boebel, O., Davis, R. E., Ollitrault, M., Peterson, R. G., Richardson, P. L., Schmid, C., & Zenk, W. (1999). The intermediate depth circulation of the western South Atlantic. *Geophysical Research Letters*, *26*, 3329–3332.

Bohm, E., Lippold, J., Gutjahr, M., Frank, M., Blaser, P., Antz, B., et al. (2015). Strong and deep Atlantic meridional overturning circulation during the last glacial cycle. *Nature*, *517*, 73–76. https://doi.org/10.1038/nature14059

Campos, M. C., Chiessi, C. M., Venancio, I. M., Pinho, T. M. L., Crivellari, S., Kuhnert, H., et al. (2020). Constraining millennial-scale changes in northern component water ventilation in the western tropical South Atlantic. *Paleoceanography and Paleoclimatology*, e2020PA003876. https://doi.org/10.1029/2020PA003876

Canfield, D. E. (1989). Reactive iron in marine sediments. *Geochimica et Cosmochimica Acta*, *53*, 619–632.

Canfield, D. E., & Thamdrup, B. (2009). Toward a consistent classification scheme for geochemical environments, or, why we wish the term 'suboxic' would go away. *Geobiology*, *7*, 385–392. https://doi.org/10.1111/j.1472-4669.2009.00214.x

Carvalho, L. M. V., Jones, C., & Liebmann, B. (2004). The South Atlantic convergence zone: Intensity, form, persistence, and relationships with intraseasonal to interannual activity and extreme rainfall. *Journal of Climate*, *17*, 88–108. https://doi.org/10.1175/1520-0442(2004)017<0088:TSACZI>2.0.CO;2

Chang, L., Bolton, C. T., Dekkers, M. J., Hayashida, A., Heslop, D., Krijgsman, W., et al. (2016a). Asian monsoon modulation of nonsteady state diagenesis in hemipelagic marine sediments offshore of Japan. *Geochemistry, Geophysics, Geosystems*, *17*, 4383–4398. https://doi.org/10.1002/2016GC006344

Chang, L., Roberts, A. P., Heslop, D., Hayashida, A., Li, J., Zhao, X., et al. (2016b). Widespread occurrence of silicate-hosted magnetic mineral inclusions in marine sediments and their contribution to paleomagnetic recording. *Journal of Geophysical Research: Solid Earth*, *121*, 8415–8431. https://doi.org/10.1002/2016JB013109

Paleoceanography and Paleoclimatology 10.1029/2020PA004058

Chang, L., Roberts, A. P., Winklhofer, M., Heslop, D., Dekkers, M. J., Krijgsman, W., et al. (2014a). Magnetic detection and characterization of biogenic magnetic minerals: A comparison of ferromagnetic resonance and first-order reversal curve diagrams. *Journal of Geophysical Research: Solid Earth*, *119*, 6136–6158. https://doi.org/10.1002/2014JB011213

Chang, L., Vasiliev, I., Baak, C. V., Krijgsman, W., Dekkers, M. J., Roberts, A. P., et al. (2014b). Identification and environmental interpretation of diagenetic and biogenic greigite in sediments: A lesson from the Messinian Black Sea. *Geochemistry, Geophysics, Geosystems*, *15*, 3612–3627.

Chen, A. P., Berounsky, V. M., Chan, M. K., Blackford, M. G., Cady, C.,Moskowitz, B. M., et al. (2014). Magnetic properties of uncultivated magnetotactic bacteria and their contribution to a stratified estuary iron cycle. *Nature Communications*, *5*, 4797. https://doi.org/10.1038/ncomms5797

Chiessi, C. M., Mulitza, S., Pätzold, J., & Wefer, G. (2010). How different proxies record precipitation variability over southeastern South America. *IOP Conference Series: Earth and Environmental Science*, *9*, 1–6. https://doi.org/10.1088/1755-1315/9/1/012007

Commission for the Geological Map of the World, (CGMW). *Maps for understanding the Earth*. CGMW. Retrieved from https://ccgm.org/

Cruz, F. W., Burns, S. J., Karmann, I., Sharp, W. D., & Vuille, M. (2006). Reconstruction of regional atmospheric circulation features during the late Pleistocene in subtropical Brazil from oxygen isotope composition of speleothems. *Earth and Planetary Science Letters*, *248*, 495–507. https://doi.org/10.1016/j.epsl.2006.06.019

Cruz, F. W., Burns, S. J., Karmann, I., Sharp, W. D., Vuille, M., Cardoso, A. O., et al. (2005). Insolation-driven changes in atmospheric circulation over the past 116,000 years in subtropical Brazil. *Nature*, *434*, 63–65. https://doi.org/10.1038/nature03365

Day, R., Fuller, M., & Schmidt, V. A. (1977). Hysteresis properties of titanomagnetites: Grain size and compositional dependence. *Physics of the Earth and Planetary Interiors*, *13*, 260–267.

de Boer, B., van de Wal, R. S. W., Lourens, L. J., Bintanja, R., & Reerink, T. J. (2012). A continuous simulation of global ice volume over the past 1 million years with 3-D ice-sheet models. *Climate Dynamics*, *41*, 1365–1384. https://doi.org/10.1007/s00382-012-1562-2

Depetris, P. J., Probst, J.-L., Pasquini, A. I., & Gaiero, D. M. (2003). The geochemical characteristics of the Paraná River suspended sediment load: An initial assessment. *Hydrological Processes*, *17*(7), 1267–1277. https://doi.org/10.1002/hyp.1283

Du, H. J., Chen, Y. R., Zhang, R., Pan, H. M., Zhang, W. Y., Zhou, K., et al. (2015). Temporal distributions and environmental adaptations of two types of multicellular magnetotactic prokaryote in the sediments of Lake Yuehu, China. *Environmental Microbiology Reports*, *7*, 538–546. https://doi.org/10.1111/1758-2229.12284

Dunlop, D. J. (1981). The rock magnetism of fine particles. *Physics of the Earth and Planetary Interiors*, *26*, 1–26.

Dunlop, D. J. (2002). Theory and application of the Day plot (Mrs/Ms versus Hcr/Hc) 1. Theoretical curves and tests using titanomagnetite data. *Journal of Geophysical Research*, *107*(B3). https://doi.org/10.1029/2001JB000486

Dunlop, D. J., & Özdemir, Ö. (1997). *Rock magnetism, fundamentals and frontiers* (p. 573). Cambridge Studies in Magnetism.

Egli, R. (2004). Characterization of individual rock magnetic components by analysis of remanence curves, 1. Unmixing natural sediments. *Studia Geophysica et Geodaetica*, *48*, 391–446. https://doi.org/10.1023/B:SGEG.0000020839.45304.6d

Egli, R. (2013). VARIFORC: An optimized protocol for calculating non-regular first-order reversal curve (FORC) diagrams. *Global and Planetary Change*, *110*, 302–320. https://doi.org/10.1016/j.gloplacha.2013.08.003

Egli, R., Chen, A. P., Winklhofer, M., Kodama, K. P., & Horng, C.-S. (2010). Detection of noninteracting single domain particles using first-order reversal curve diagrams. *Geochemistry, Geophysics, Geosystems*, *11*(1), 1–22. https://doi.org/10.1029/2009GC002916

Evans, M. E., & Heller, F. (2003). *Environmental Magnetism Principles and Applications of Enviromagnetics*. International Geophysics Series (86, p. 304). Academic Press.

Faivre, D., & Schüler, D. (2008). Magnetotactic bacteria and magnetosomes. *Chemical Reviews*, *108*, 4875–4898. https://doi.org/10.1021/cr078258w

Figueiredo, T., Santos, T. P., Costa, K. B., Toledo, F., Albuquerqu, A. L. S., Smoak, J. M., et al. (2020). Effect of deep Southwestern Subtropical Atlantic Ocean circulation on the biogeochemistry of mercury during the last two glacial/interglacial cycles. *Quaternary Science Reviews*, *239*. https://doi.org/10.1016/j.quascirev.2020.106368

Funk, J. A., Von Dobeneck, T., & Reitz, A. (2004). Integrated rock magnetic and geochemical quantification of redoxomorphic iron mineral diagenesis in Late Quaternary sediments from the equatorial Atlantic. In G. Wefer, S. Mulitza, & V. Ratmeyer, Eds., *The South Atlantic in the Late Quaternary: Reconstruction of material budgets and current systems* (pp. 237–260). Springer.

Gaiero, D. M., Probst, J. L., Depetris, P. J., Bidart, S. M., & Leleyter, L. (2003). Iron and other transition metals in Patagonian riverborne and windborne materials: geochemical control and transport to the southern South Atlantic Ocean. *Geochimica et Cosmochimica Acta*, *67*(19), 3603–3623. https://doi.org/10.1016/S0016-7037(03)00211-4

Garreaud, R. D., Vuille, M., Compagnucci, R., & Marengo, J. (2009). Present-day South American climate. *Palaeogeography, Palaeoclimatology, Palaeoecology*, *281*, 180–195. https://doi.org/10.1016/j.palaeo.2007.10.032

Gómes Tapias, J., Schobbenhaus, C., & Montes Ramírez, N. E. (2019). *Geological map of south America*. https://doi.org/10.32685/10.143.2019.929

Govin, A., Chiessi, C. M., Zabel, M., Sawakuchi, A. O., Heslop, D., Hörner, T., et al. (2014). Terrigenous input off northern South America driven by changes in Amazonian climate and the North Brazil Current retroflection during the last 250 ka. *Climate of the Past*, *10*, 843–862. https://doi.org/10.5194/cp-10-843-2014

Govin, A., Holzwarth, U., Heslop, D., Keeling, L. F., Zabel, M., Mulitza, S., et al. (2012). Distribution of major elements in Atlantic surface sediments (36°N-49°S): Imprint of terrigenous input and continental weathering. *Geochemistry, Geophysics, Geosystems*, *13*, 1–23. https://doi.org/10.1029/2011GC003785

Grant, K. M., Rohling, E. J., Bar-Matthews, M., Ayalon, A., Medina-Elizalde, M., Bronk Ramsey, C., et al. (2012). Rapid coupling between ice volume and polar temperature over the past 150,000 years. *Nature*, *491*, 744–747. https://doi.org/10.1038/nature11593

Gyllencreutz, R., Mahiques, M. M., Alves, D. V. P., & Wainer, I. K. C. (2010). Mid- to late Holocene paleoceanographic changes on the southeastern Brazilian shelf based on grain size records. *The Holocene*, *20*, 863–875. https://doi.org/10.1177/0959683610365936

Hanzlik, M., Winklhofer, M., & Petersen, N. (1996). Spatial arrangement of chains of magnetosomes in magnetotactic bacteria. *Earth and Planetary Science Letters*, *145*, 125–134.

Hartstra, R. L. (1982). A comparative study of the ARM and Isr os some natural magnetites of MD and PSD grain size. *Geophys. Journal RAS*, *71*, 497–518.

He, K., Roud, S. C., Gilder, S. A., Egli, R., Mayr, C., & Petersen, N. (2018). Seasonal variability of magnetotactic bacteria in a freshwater pond. *Geophysical Research Letters*, *45*, 2294–2302. https://doi.org/10.1002/2018GL077213

Hesse, P. (1994). Evidence for bacterial palaeoecological origin of mineral magnetic cycles in oxic and sub-oxic Tasman Sea sediments. *Marine Geology*, *117*, 1–17.

Paleoceanography and Paleoclimatology 10.1029/2020PA004058

Hoogakker, B. A. A., Thornalley, D. J. R., & Barker, S. (2016). Millennial changes in North Atlantic oxygen concentrations. *Biogeosciences*, *13*, 211–221. https://doi.org/10.5194/bg-13-211-2016

Hounslow, M. W., & Maher, B. A. (1999). Source of the climate signal recorded by magnetic susceptibility variations in Indian Ocean sediments. *Journal of Geophysical Research*, *104*, 5047–5061.

Howe, J. N. W., Piotrowski, A. M., Noble, T. L., Mulitza, S., Chiessi, C. M., & Bayon, G., et al. (2016). North Atlantic deep water production during the Last Glacial Maximum. *Nature Communications*, *7*, 1–8. https://doi.org/10.1038/ncomms11765

Itambi, A. C., von Dobeneck, T., Mulitza, S., Bickert, T., & Heslop, D. (2009). Millennial-scale northwest African droughts related to Heinrich events and Dansgaard-Oeschger cycles: Evidence in marine sediments from offshore Senegal. *Paleoceanography*, *24*. https://doi.org/10.1029/2007PA001570

Just, J., Dekkers, M. J., von Dobeneck, T., van Hoesel, A., & Bickert, T. (2012a). Signatures and significance of aeolian, fluvial, bacterial and diagenetic magnetic mineral fractions in Late Quaternary marine sediments off Gambia, NW Africa. *Geochemistry, Geophysics, Geosystems*, *13*. https://doi.org/10.1029/2012GC004146

Just, J., Heslop, D., Tilo, D., Bickert, T., Mark, J. D., Thomas, F., et al. (2012b). Multiproxy characterization and budgeting of terrigenous end-members at the NW African continental margin. *Geochemistry, Geophysics, Geosystems*, *13*. https://doi.org/10.1029/2012GC004148

Karlin, R., Lyle, M., & Ross Heath, G. (1987). Authigenic magnetite formation in suboxic marine sediments. *Letters to Nature*, *326*, 490–493.

Kirschvink, J. L., & Chang, S.-B. R. (1984). Ultrafine-grained magnetite in deep-sea sediments: Possible bacterial magnetofossils. *Geology*, *12*, 559–562.

Kopp, R. E., & Kirschvink, J. L. (2008). The identification and biogeochemical interpretation of fossil magnetotactic bacteria. *Earth-Science Reviews*, *86*, 42–61. https://doi.org/10.1016/j.earscirev.2007.08.001

Korff, L., Dobeneck, T. V., Frederichs, T., Kasten, S., Kuhn, G., Gersonde, R., Diekmann, B. (2016). Cyclic magnetite dissolution in Pleistocene sediments of the abyssal northwest Pacific Ocean: Evidence for glacial oxygen depletion and carbon trapping. *Paleoceanography and Paleoclimatology*, *31*, 600–624. https://doi.org/10.1002/2015PA002882

Lippert, P. C. (2008). Big discovery for biogenic magnetite. *Proceedings of the National Academy of Sciences of the United States of America*, *105*, 17595–17596. https://doi.org/10.1073/pnas.0809839105

Lisiecki, L. E., & Raymo, M. E. (2005). A Pliocene-Pleistocene stack of 57 globally distributed benthic δ18O records. *Paleoceanography*, *20*. https://doi.org/10.1029/2004PA001071

Liu, Q., Andrew, P. R., Juan, C. L., Subir, K. B., Yohan, G., Lisa, T., & Frank, O. (2012). Environmental magnetism: Principles and applications. *Reviews of Geophysics*, *50*. https://doi.org/10.1029/2012RG000393

Lovley, D. R., Stolz, J. F., Gordon, L., Nord, J., & Phillips, E. J. P. (1987). Anaerobic production of magnetite by a dissimilatory iron-reducing microorganism. *Nature*, *330*, 252–254.

Lund, D. C., Tessin, A. C., Hoffman, J. L., & Schmittner, A. (2015). Southwest Atlantic water mass evolution during the last deglaciation. *Paleoceanography*, *30*, 477–494. https://doi.org/10.1002/2014PA002657

Mackensen, A., Hubberten, H.-W., Bickert, T., Fischer, G., & Fütterer, D. K. (1993). The δ13C in benthic foraminiferal tests of Fontbotia wuellerstorfi (Schwager) Relative to the δ13C of dissolved inorganic carbon in Southern Ocean Deep Water: Implications for glacial ocean circulation models. *Paleoceanography*, *8*, 587–610.

Mackensen, A., & Schmiedl, G. (2019). Stable carbon isotopes in paleoceanography: Atmosphere, oceans, and sediments. *Earth-Science Reviews*, *197*, 102893. https://doi.org/10.1016/j.earscirev.2019.102893

Maher, B. A. (1988). Magnetic properties of some synthetic sub-micron magnetites. *Geophysical Journal International*, *94*, 83–96.

Maher, B. A. (1998). Magnetic properties of modern soils and Quaternary loessic paleosols: paleoclimatic implications. *Palaeogeography, Palaeoclimatology, Palaeoecology*, *137*, 25–54.

Maher, B. A., & Hounslow, M. W. (1999). The significance of magnetotactic bacteria for the palaeomagnetic and rock magnetic record of Quaternary sediments and soils. In D. H. Tarling, & P. Turner, Eds., *Palaeomagnetism and diagenesis in sediments geological society* (pp. 43–46). Special Publications.

Maher, B. A., Karloukovski, V. V., & Mutch, T. J. (2004). High-field remanence properties of synthetic and natural submicrometre haematites and goethites: significance for environmental contexts. *Earth and Planetary Science Letters*, *226*, 491–505. https://doi.org/10.1016/j.epsl.2004.05.042

Maher, B. A., Prospero, J. M., Mackie, D., Gaiero, D., Hesse, P .P., Balkanski, Y. (2010). Global connections between aeolian dust, climate and ocean biogeochemistry at the present day and at the last glacial maximum. *Earth-Science Reviews*, *99*, 61–97. https://doi.org/10.1016/j.earscirev.2009.12.001

Maher, B. A., & Thompson, R. (1999). *Quaternary climates, environments and magnetism* (p. 390). Cambridge University Press.

Mahiques, M. M., Tassinari, C. C. S., Marcolini, S., Violante, R. A., Figueira, R. C. L., Silveira, I. C. A., et al. (2008). Nd and Pb isotope signatures on the Southeastern South American upper margin: Implications for sediment transport and source rocks. *Marine Geology*, *250*, 51–63. https://doi.org/10.1016/j.margeo.2007.11.007

Marengo, J. A., Liebmann, B., Grimm, A. M., Misra, V., Silva Dias, P. L., Cavalcanti, I. F. A., et al. (2012). Recent developments on the South American monsoon system. *International Journal of Climatology*, *32*, 1–21. https://doi.org/10.1002/joc.2254

Mathias, G. L., Nagai, R. H., Trindade, R. I. F., & de Mahiques, M. M. (2014). Magnetic fingerprint of the late Holocene inception of the Río de la Plata plume onto the southeast Brazilian shelf. *Palaeogeography, Palaeoclimatology, Palaeoecology*, *415*, 183–196. https://doi.org/10.1016/j.palaeo.2014.03.034

Matsuda, T., Endo, J., Osakabe, N., Tonomura, A., & Arii, T. (1983). Morphology and structure of biogenic magnetite particles. *Nature*, *302*, 411–412.

Mulitza, S., Prange, M., Stuut, J. B., Zabel, M., Dobeneck, T. V., Itambi, A. C., et al. (2008). Sahel megadroughts triggered by glacial slowdowns of Atlantic meridional overturning. *Paleoceanography*, *23*(4). https://doi.org/10.1029/2008PA001637

Peters, C., & Dekkers, M. J. (2003). Selected room temperature magnetic parameters as a function of mineralogy, concentration and grain size. *Physics and Chemistry of the Earth*, *28*(16), 659–667. https://doi.org/10.1016/S1474-7065(03)00120-7

Petersen, N., von Dobeneck, T., & Vali, H. (1986). Fossil bacterial magnetite in deep-sea sediments from the South Atlantic Ocean. *Nature*, *320*, 611–615.

Peterson, R. G., & Stramma, L. (1991). Upper-level circulation in the South Atlantic Ocean. *Progress in Oceanography*, *26*, 1–73.

Petschick, R., Kuhn, G., & Gingele, F. (1996). Clay mineral distribution in surface sediments of the South Atlantic: sources, transport, and relation to oceanography. *Marine Geology*, *130*, 203–229.

Piola, A. R., Campos, E. J. D., Möller, O. O., Charo, M., & Martinez, C. (2000). Subtropical Shelf Front off eastern South America. *Journal of Geophysical Research*, *105*, 6565.

Paleoceanography and Paleoclimatology 10.1029/2020PA004058

Piola, A. R., Matano, R. P., Palma, E. D., Möller, O., Jr, & Campos, E. J. D. (2005). The influence of the Plata River discharge on the western South Atlantic shelf. *Geophysical Research Letters*, *32*. https://doi.org/10.1029/2004GL021638

Portilho-Ramos, R. C., Chiessi, C. M., Zhang, Y., Mulitza, S., Kucera, M., Siccha, M., et al. (2017). Coupling of equatorial Atlantic surface stratification to glacial shifts in the tropical rainbelt. *Scientific Reports*, *7*, 1561. https://doi.org/10.1038/s41598-017-01629-z

Portilho-Ramos, R. D. C., Pinho, T. M. L., Chiessi, C. M., & Barbosa, C. F. (2019). Understanding the mechanisms behind high glacial productivity in the southern Brazilian margin. *Climate of the Past*, *15*, 943–955. https://doi.org/10.5194/cp-15-943-2019

Prospero, J. M., Ginoux, P., Torres, O., Nicholson, S. E., & Gill, T. E. (2002). Environmental characterization of global sources of atmospheric soil dust identified with the Nimbus 7 total ozone mapping spectometer (TOMS) absorbing aerosol product. *Reviews of Geophysics*, *40*(1), 1002. https://doi.org/10.1029/2000RG000095

Razik, S., Chiessi, C. M., Romero, O. E., & von Dobeneck, T. (2013). Interaction of the South American Monsoon System and the Southern Westerly Wind Belt during the last 14kyr. *Palaeogeography, Palaeoclimatology, Palaeoecology*, *374*, 28–40. https://doi.org/10.1016/j.palaeo.2012.12.022

Razik, S., Govin, A., Chiessi, C. M., & von Dobeneck, T. (2015). Depositional provinces, dispersal, and origin of terrigenous sediments along the SE South American continental margin. *Marine Geology*, *363*, 261–272. https://doi.org/10.1016/j.margeo.2015.03.001

Reinholdsson, M., Snowball, I., Zillén, L., Lenz, C., & Conley, D. J. (2013). Magnetic enhancement of Baltic Sea sapropels by greigite magnetofossils. *Earth and Planetary Science Letters*, *366*, 137–150. https://doi.org/10.1016/j.epsl.2013.01.029

Reitz, A., Hensen, C., Kasten, S., Funk, J. A., & de Lange, G. J. (2004). A combined geochemical and rock-magnetic investigation of a redox horizon at the last glacial/interglacial transition. *Physics and Chemistry of the Earth, Parts A/B/C*, *29*, 921–931. https://doi.org/10.1016/j.pce.2004.03.013

Roberts, A. P. (2006). High-resolution magnetic analysis of sediment cores: Strengths, limitations and strategies for maximizing the value of long-core magnetic data. *Physics of the Earth and Planetary Interiors*, *156*, 162–178. https://doi.org/10.1016/j.pepi.2005.03.021

Roberts, A. P., Chang, L., Heslop, D., Florindo, F., & Larrasoaña, J. C. (2012). Searching for single domain magnetite in the "pseudo-single-domain" sedimentary haystack: Implications of biogenic magnetite preservation for sediment magnetism and relative paleointensity determinations. *Journal of Geophysical Research*, *117*. https://doi.org/10.1029/2012JB009412

Roberts, A. P., Chang, L., Rowan, C. J., Horng, C.-S., & Florindo, F. (2011a). Magnetic properties of sedimentary greigite (Fe3S4): An update. *Reviews of Geophysics*, *49*. https://doi.org/10.1029/2010RG000336

Roberts, A. P., Florindo, F., Chang, L., Heslop, D., Jovane, L., Larrasoaña, J. C. (2013). Magnetic properties of pelagic marine carbonates. *Earth-Science Reviews*, *127*, 111–139. https://doi.org/10.1016/j.earscirev.2013.09.009

Roberts, A. P., Florindo, F., Villa, G., Chang, L., Jovane, L., Bohaty, S. M., et al. (2011b). Magnetotactic bacterial abundance in pelagic marine environments is limited by organic carbon flux and availability of dissolved iron. *Earth and Planetary Science Letters*, *310*(3–4), 441–452. https://doi.org/10.1016/j.epsl.2011.08.011

Roberts, A. P., Liu, Q., Rowan, C. J., Chang, L., Carvallo, C., Torrent, J., Horng, C. S. (2006). Characterization of hematite (α-Fe2O3), goethite (α-FeOOH), greigite (Fe3S4), and pyrrhotite (Fe7S8) using first-order reversal curve diagrams. *Journal of Geophysical Research*, *111*. https://doi.org/10.1029/2006JB004715

Roberts, A. P., Pike, C. R., & Verosub, K. L. (2000). First-order reversal curve diagrams: A new tool for characterizing the magnetic properties of natural samples. *Journal of Geophysical Research*, *105*, 28461–28475.

Romero, O., & Hensen, E. (2002). Oceanographic control of biogenic opal and diatoms in surface sediments of the Southwestern Atlantic. *Marine Geology*, *186*(3–4), 263–280. https://doi.org/10.1016/S0025-3227(02)00210-4

Santos, T. P., Lessa, D. O., Venancio, I. M., Chiessi, C. M., Mulitza, S., Kuhnert, H., et al. (2017). Prolonged warming of the Brazil Current precedes deglaciations. *Earth and Planetary Science Letters*, *463*, 1–12. https://doi.org/10.1016/j.epsl.2017.01.014

Savian, J. F., Jovane, L., Frontalini, F., Trindade, R. I. F., Coccioni, R., Bohaty, S. M., et al. (2014). Enhanced primary productivity and magnetotactic bacterial production in response to middle Eocene warming in the Neo-Tethys Ocean. *Palaeogeography, Palaeoclimatology, Palaeoecology*, *414*, 32–45. https://doi.org/10.1016/j.palaeo.2014.08.009

Schlitzer, R. (2019). *Ocean Data View*. Retrieved from https://odv.awi.de

Schmidbauer, E., & Veitch, R. (1980). Anhysteretic remanent magnetization of small multidomain Fe3O4 particles dispersed in various concentrations in a non magnetic matrix. *Journal of Geophysics*, *48*, 148–152.

Schmittner, A., & Lund, D. C. (2015). Early deglacial Atlantic overturning decline and its role in atmospheric CO_2 rise inferred from carbon isotopes ($\delta^{13}C$). *Climate of the Past*, *11*, 135–152. https://doi.org/10.5194/cp-11-135-2015

Sheldon, N. D., & Tabor, N. J. (2009). Quantitative paleoenvironmental and paleoclimatic reconstruction using paleosols. *Earth-Science Reviews*, *95*, 1–52. https://doi.org/10.1016/j.earscirev.2009.03.004

Souza, R. B., & Robinson, I. S. (2004). Lagrangian and satellite observations of the Brazilian Coastal Current. *Continental Shelf Research*, *24*, 241–262. https://doi.org/10.1016/j.csr.2003.10.001

Stolz, J. F., Chang, S.-B. R., & Kirschvink, J. L. (1986). Magnetotactic bacteria and single-domain magnetite in hemipelagic sediments. *Nature*, *321*, 849–851.

Stramma, L., & England, M. (1999). On the water masses and mean circulation of the South Atlantic Ocean. *Journal of Geophysical Research*, *104*, 20863–20883.

Thompson, R., & Oldfield, F. (1986). *Environmental magnetism* (p. 228). Allen & Unwin.

Tsuchiya, M., Talley, L. D., & McCartney, M. S. (1994). Water-mass distributions in the western South Atlantic; A section from South Georgia Island (54S) northward across the equator. *Journal of Marine Research*, *52*, 52–81.

Vali, H., Förster, O., Amarantidis, G., & Petersen, N. (1987). Magnetotactic bacteria and their magnetofossils in sediments. *Earth and Planetary Science Letters*, *86*, 389–400.

Verosub, K. L., & Roberts, A. P. (1995). Environmental magnetism- Past, present, and future. *Journal of Geophysical Research*, *1000*, 2175–2192.

Voigt, I., Cruz, A. P. S., Mulitza, S., Chiessi, C. M., Mackensen, A., Lippold, J., et al. (2017). Variability in mid-depth ventilation of the western Atlantic Ocean during the last deglaciation. *Paleoceanography*, *32*, 948–965. https://doi.org/10.1002/2017PA003095

Weltje, G. J., & Tjallingii, R. (2008). Calibration of XRF core scanners for quantitative geochemical logging of sediment cores: Theory and application. *Earth and Planetary Science Letters*, *274*, 423–438. https://doi.org/10.1016/j.epsl.2008.07.054

Zabel, M., Schneider, R. R., Wagner, T., Adegbie, A. T., Vries, U. D., Kolonic, S. (2001). Late Quaternary climate changes in Central Africa as inferred from terrigenous input to the Niger fan. *Quaternary Research*, *56*(2), 207–217.

Zweng, M. M., Reagan, J. R., Antonov, J. I., Locarnini, R. A., Mishonov, A. V., Boyer, T. P., et al. (2013). *World Ocean Atlas 2013, Volume 2: Salinity*. (S. Levitus, Ed., A. Mishonov Technical Ed.). NOAA Atlas NESDIS 74, p. 39.

Chapter III

Miocene to Early Pleistocene Depositional History and Tectonic Evolution of the Issyk-Kul Basin, Central Tian Shan

Summary and Context

In this study we analyzed terrigenous deposits of an intermountain sediment basin in the Tian Shan Mountains, which hosts the deepest mountain lake of Central Asia. Up to 4 km of Cenozoic sediments record the tectonic and climatic history of the area. The study area is a key locality to investigate the influence of tectonics (mountain building related to the Indian-Asia collision) and climate induced weathering on erosion and sediment accumulation. I joined the research team to date the fossil-poor late Neogene sediments exposed around the lake via magnetostratigraphy. Through a combination of paleomagnetic analyses and regional geologic interpretations indicate that mountain building and syn-tectonic deposition in the Issyk-Kul Basin began at ~22 Ma and increased at ~7 Ma, concurrent with accelerated uplift in the mountain ranges to the south. A change in deformation style around 5 Ma suggested the closure of the basin, facilitating the formation of a deep lake, as is presently observed. The study provides a valuable new basal age (3-5 Ma) for the lake sediments, which are an interesting target for future sedimentologic investigations.

Reference

Roud, S. C., Wack, M. R., Gilder, S. A., Kudriavtseva, A., & Sobel, E. R. (2021). Miocene to early Pleistocene depositional history and tectonic evolution of the Issyk-Kul Basin, central Tian Shan. Geochemistry, Geophysics, Geosystems, 22, e2020GC009556.

https://doi.org/10.1029/2020PA004058

Contributions

I contributed to all aspects of this study: field work, data acquisition and analysis, magnetostratigraphic correlations, geologic mapping based on aerial and satellite images, and interpretation of the geology. I wrote the original draft of the manuscript and prepared all figures.

Geochemistry, Geophysics, Geosystems

RESEARCH ARTICLE
10.1029/2020GC009556

Miocene to Early Pleistocene Depositional History and Tectonic Evolution of the Issyk-Kul Basin, Central Tian Shan

Sophie C. Roud[1], Michael R. Wack[1], Stuart A. Gilder[1], Anna Kudriavtseva[2], and Edward R. Sobel[2]

[1]Department of Earth and Environmental Sciences, Ludwig-Maximilians-Universität München, Munich, Germany, [2]Institute of Geosciences, Universität Potsdam, Potsdam-Golm, Germany

Key Points:

- Mountain building and syn-tectonic deposition in the Issyk-Kul Basin began at ~22 Ma and accelerated at ~7 Ma
- Deformation propagated northward at ~5 Ma, initiating the closure of the basin and facilitating the formation of a deep Lake Issyk-Kul
- Comparable depositional ages of equivalent strata throughout the central Tian Shan suggest regionally synchronized geologic processes

Supporting Information:

Supporting Information may be found in the online version of this article.

Correspondence to:

S. C. Roud,
sophie.roud@lmu.de

Citation:

Roud, S. C., Wack, M. R., Gilder, S. A., Kudriavtseva, A., & Sobel, E. R. (2021). Miocene to early Pleistocene depositional history and tectonic evolution of the Issyk-Kul Basin, central Tian Shan. *Geochemistry, Geophysics, Geosystems*, *22*, e2020GC009556. https://doi.org/10.1029/2020GC009556

Received 20 NOV 2020
Accepted 22 FEB 2021

Abstract The Issyk-Kul Basin (Kyrgyzstan), situated in the central Tian Shan Mountains, hosts the largest and deepest mountain lake in Central Asia. Erosion of the surrounding Terskey and Kungey ranges led to the accumulation of up to 4 km of sediment in the adjacent depression. Creation of the basin from regional shortening and uplift likely initiated around the Oligocene-Miocene, yet precise age control is sparse. To better understand the timing of these processes, we obtained magnetostratigraphic age constraints on fossil-poor, fluvio-lacustrine sediments exposed south of Lake Issyk-Kul, that agree well with previous age constraints of the equivalent strata outside the Issyk-Kul Basin. Two 500–650 m thick sections comprised mainly of Chu Group sediments were dated at 6.3–2.8 Ma and 7.0–2.4 Ma (late Miocene to early Pleistocene). Together with reinterpreted magnetostratigraphic constraints from underlying strata, we find that syn-tectonic deposition commenced at ~22 Ma with average sedimentation rates <10 cm/ka. Sedimentation rates increased to 10–30 cm/ka at 7 Ma, concurrent with accelerated uplift in the Terskey Range to the south. A deformation event in one section (Kaji-Say) between 5 and 3 Ma together with concurrent shifts of depositional centers throughout the basin signal the onset of substantial uplift of the Kungey Range to the north at ~5 Ma. This uplift and deformation transformed the Issyk-Kul area into a closed basin that facilitated the formation of a deep lake. Lacustrine facies deposited around 3 Ma mark the existence of Lake Issyk-Kul by that time.

Plain Language Summary In this study, we investigated how and when the sedimentary basin that contains the deepest mountain lake in central Asia (Lake Issyk-Kul) formed. The sediments originated from the surrounding Tian Shan Mountains that were exhumed by tectonic forces related to the collision between the Indian and Eurasian plates. Sediments accumulated in the Issyk-Kul Basin as the nearby mountains eroded. By determining detailed records of sedimentation ages and deposition rates, we found that the oldest sediments stemming from mountain building are 22 Myr old, suggesting that uplift initiated then. Around 7 Ma, sedimentation rates increased 2–3 times, thereby signifying a time of accelerated uplift and erosion. After 5 Ma, sedimentary layers south of the lake were strongly deformed, while sedimentation patterns shifted throughout the basin, likely caused by the uplift of mountains farther north. This transformed the Issyk-Kul area into a closed basin, thereby facilitating the formation of a deep lake. Carbonate-rich facies became widespread around 3 Ma, further confirming the existence of Lake Issyk-Kul.

1. Introduction

1.1. Regional Geology

The Tian Shan Mountains comprise a 2,500 km long orogenic belt in central Asia. Ongoing uplift of the range is driven by the India-Asia collision. Although located 1,500 km north of the India-Asia plate boundary, the Tian Shan currently accommodate about 20 mm/yr of north-south shortening, which is equivalent to nearly two-thirds of the total convergence between India and Asia (Zubovich et al., 2010). Mountain building in central Asia initiated along reactivated Paleozoic structures in the late Oligocene, creating vast basins that were subsequently dissected by younger ranges (Buslov et al., 2003; Macaulay et al., 2014; Sobel & Dumitru, 1997).

Geochemistry, Geophysics, Geosystems 10.1029/2020GC009556

The Issyk-Kul Basin is one of the largest intermountain basins in the Tian Shan realm, bounded by the Kungey Range to the north and the Terskey Range to the south (Figure 1) with maximum peak heights of 4.8 and 5.2 km, respectively. The basin contains up to 4 km of Cenozoic sediments (Buslov et al., 2003; Turchinskiy, 1970) that record the uplift and erosion history of the surrounding mountain ranges. Unroofing of the Terskey range commenced around the Oligocene-Miocene boundary between 26 and 20 Ma based on thermochronologic cooling ages (De Grave et al., 2013; Macaulay et al., 2013, 2014) and on the onset of sediment deposition in the adjacent Issyk-Kul Basin (Wack et al., 2014). The initial uplift phase was followed by a second phase of rapid basement cooling after 10 ± 5 Ma when deformation of the Terskey range propagated northward, creating the Issyk-Kul Broken Foreland (Macaulay et al., 2013, 2014). Uplift of the youngest ranges initiated in the Plio-Pleistocene. Unroofing of the Kungey Range that led to the closure of the Issyk-Kul Basin is loosely estimated to ca. 7–4 Ma based on sediment provenance data (Selander et al., 2012).

To better resolve the uplift history of the central Tian Shan around the Issyk-Kul Basin, we collected Cenozoic sediments at two sections, Ak-Terek and Kaji-Say (Figure 1), in the southern rim of the basin in 2016 and 2017 to constrain the age, sedimentation rate and the depositional environment. Here, we describe the geologic setting, the rock magnetism and magnetostratigraphy of the sections. We then discuss the new and existing magnetostratigraphic age constraints from the Issyk-Kul Basin, and place our results in the larger context of the tectonic evolution of the area.

1.2. Local Geology and Stratigraphy

Cenozoic sediments in the central Tian Shan can be divided into four main lithologic groups. These are, from oldest to youngest, the Kokturpak, Shamsi, Chu, and Sharpyldak groups (Abdrakhmatov et al., 2001). All four groups are exposed in the southern Issyk-Kul Basin, where we mapped their extent with satellite images (Bing Maps and Sentinel 2, Bands 12-4-2) using QGIS software (Figure 1). Outside our study area, we also referred to Soviet geological maps (Pomazkov, 1971; Turchinskiy, 1970) and the PhD thesis of Burgette (2008).

The Kokturpak Group represents pre-orogenic sediments. It comprises deeply weathered paleosols, thin lacustrine deposits and reddish sandstones that formed in shallow, low-relief areas above the Paleozoic basement or above locally preserved Jurassic deposits (Fortuna et al., 1994). In the Issyk-Kul Basin, the Kokturpak Group reaches up to 100 m in thickness (Selander et al., 2012). The age is loosely constrained as late Cretaceous to Eocene (Fortuna et al., 1994; Sobel & Arnaud, 2000). Kokturpak and Jurassic sediments were combined in our geologic maps (Figure 1, J-Pg); these are identified as white and yellow layers that cover basement rocks and/or by resistant red horizons that crop out in the cores of anticlines (Figures 1d and 1e).

The Shamsi Group represents the basal, syn-orogenic sediments (locally called the Kyrgyz or Dzhety Oguz Formation) overlying the Kokturpak Group. In the Issyk-Kul Basin, these deposits consist of poorly sorted sandstone and conglomerate with a characteristic red pigment near the base that fades toward the top. In the vicinity of the Terskey Range (CK and JO in Figure 1a), the ~1 km thick sections were magnetostratigraphically dated between 26 and 11 Ma (Wack et al., 2014). We mapped the Shamsi unit in Figure 1 based on its distinctive red color and strong reflectance in the Sentinel bands 12 and 4. In the eastern part of the basin, the Shamsi Group can be subdivided into a lower (N_1-S_1, red) and upper (N_1-S_2, light red) unit based on a characteristic decrease in red pigment (Figure 1e). The similar appearance of lower Shamsi and upper Kokturpak groups made it sometimes ambiguous to distinguish them on the aerial images.

The Shamsi Group grades upward into lighter, more fine-grained strata of the Chu group, which consists of white to tan sandstone and siltstone, intercalated with conglomerate. The Chu Group is often described as the main basin-filling unit, with thicknesses up to 2.5 km reported in the Naryn Basin (Goode et al., 2011), 1.5 km in the Chu Basin (Bullen et al., 2001) and 3 km in the At-Bashi Basin (Abdrakhmatov et al., 2001). In the latter two, the Chu Group was magnetostratigraphically dated between 7.5 and 3.0 Ma (Abdrakhmatov et al., 2001; Bullen et al., 2001). Selander et al. (2012) reported a maximum thickness of 600 m in the northern Issyk-Kul Basin. This unit was mapped based on its tan color at the base that fades toward the top and possesses alternating lighter and darker horizons. Where possible, we differentiated between lower Chu (dominantly darker tones; mapped as N_1C_1) and upper Chu (highly reflective, grayish beds; mapped as N_1C_2; Figures 1b–1d).

Geochemistry, Geophysics, Geosystems 10.1029/2020GC009556

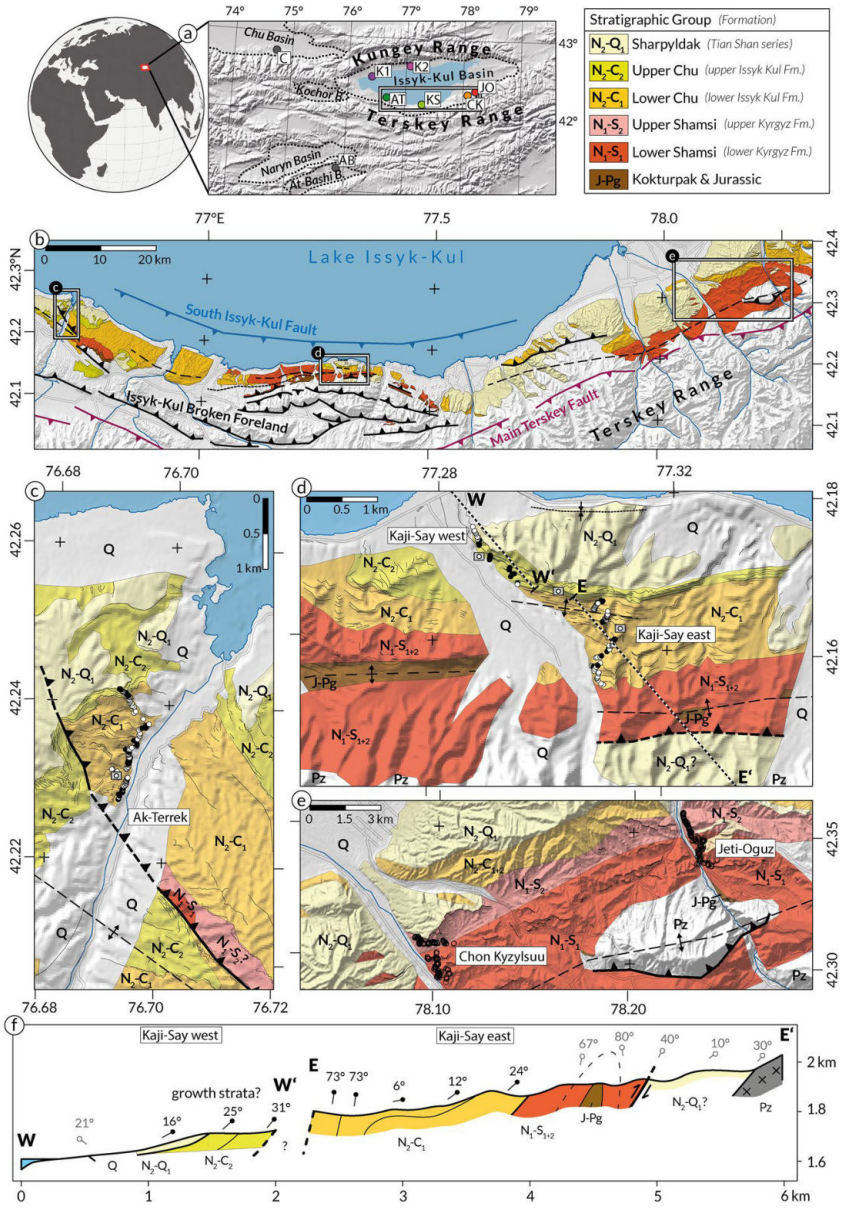

Figure 1. Geologic overview of the study area at Lake Issyk-Kul (Central Tian Shan, Kyrgyzstan). (a) General location map. Names and abbreviations in white boxes denote locations of new and previously studied stratigraphic sections as follows: (c) Chu, (AB) At-Bashi, (K1) Toru-Aygir, (K2) Cholpon-Ata, (AT) Ak-Terek, (KS) Kaji-Say, (CK) Chon Kyzylsuu and (JO) Jeti-Oguz. (b) Geology of the southern Issyk-Kul Basin with mapped sedimentary units (see legend and text for details), major faults (thick lines) and folds (thin lines, anticlines dashed, synclines dotted). Geologic and structural information were mapped from satellite images, a digital elevation model, Burgette (2008), Macaulay et al. (2013; 2014; 2016) and Korzhenkov and Deev (2017). Rectangles show locations of maps (c)–(e); units corresponding to the legend: Q, Quaternary; N, Neogene; 1, lower, 2, upper; Pg, Paleogene, J, Jurassic; Pz, Paleozoic basement. Filled circles in (c) and (d) indicate paleomagnetic sample locations of this study (black = normal polarity and white = reversed polarity). Circles in (e) show sample locations from Wack et al. (2014). Projection (b)–(e): Pulkovo 1942/Gauss-Kruger zone 14. (f) Cross-section through the western (W-W′) and eastern transect (E-E′) at Kaji-Say (2:1 vertical exaggeration); bedding attitudes outside the magnetostrigraphic section from Burgette (2008). Camera symbols show locations where the field photos in Figure 2 were taken.

Geochemistry, Geophysics, Geosystems 10.1029/2020GC009556

Poorly sorted, coarse conglomerates of the Sharpyldak Group overlie the Chu group, with the contact being sometimes gradual and sometimes unconformable, indicating that locally, deformation has occurred prior to deposition of the conglomerates. The basal age of the Sharpyldak Group was dated to ca. 5–3 Ma in adjacent basins (Abdrakhmatov et al., 2001; Bullen et al., 2001). We mapped the Sharpyldak deposits (N_2-Q_1) based on their bright gray appearance without visible bedding structures. The Sharpyldak conglomerates are locally covered by lacustrine deposits and river terraces that formed in response to lake level variations and glaciation events during the Quaternary (Burgette et al., 2017). We did not map these youngest features (Q in Figures 1c–1e) in detail. The distinction between Sharpyldak conglomerates and Quaternary terraces in Figure 1 was primarily based on topography.

The major tectonic structures in Figure 1 were adapted from Burgette (2008), Macaulay et al. (2013, 2014, 2016), and Korzhenkov and Deev (2017) and mapped on a 30″ (arcsec) digital surface model (Tadono et al., 2015) that is shown as topographic shading in all maps. The two major thrust faults are the north-vergent South Issyk-Kul Fault and the Main Terskey Fault. The Issyk-Kul Broken Foreland, north of the Main Terskey Fault, is dominated by secondary south-vergent reverse faults that thrust Cenozoic sediments over basement rocks (Burgette, 2008; Korzhenkov & Deev, 2017; Macaulay et al., 2014), thereby producing E-W striking folds in the southern Issyk-Kul Basin. Anticlines with gently tilted northern and steep southern limbs are typically thrust up along reverse faults (Buslov et al., 2003; Figure 1f).

2. Sections and Sampling

2.1. Ak-Terek Section

The Ak-Terek section was sampled on the west side of the Ak-Terek river valley, spanning 500 m in stratigraphic height (Figures 1c, 2a, and 3a). Figure 3a includes a stratigraphic column of the section that can be subdivided into three lithologic units (AT-1 to AT-3). The lower part (AT1) contains alternating sand and silt layers intercalated with conglomerate. Above ~230 m, fine massive sandstones become dominant (AT2). Above 324 m, the number of conglomerate layers, sporadic calcareous deposits and paleosols increase (AT3). A 30 cm-thick gypsum layer was found at 430 m. Massive conglomerates above ~500 m mark the conformable transition from Chu to Sharpyldak deposits. Bedding dips gradually flatten from 21° at the base to 5° at the top, reflecting regional scale folding or growth strata. No major discontinuity, unconformity, or fault was observed in the section.

We collected two oriented paleomagnetic cores per horizon (302 in total), generally selecting fine-grained mud or silt layers. The lower 200 m of the section were sampled along the Ak-Terek river valley in ~2 m intervals. The coarser grained upper 300 m of the section were sampled every 7 m on average, following tributaries away from the river valley. Samples were obtained using a battery-powered, water or air-cooled drill; poorly lithified strata were sampled with a handheld push corer that we manufactured for this purpose. The corer injects the extracted, oriented sediment directly into plastic cylinders of the same dimension as standard paleomagnetic specimens (2.5 cm diameter, 2.2 cm height). All samples were oriented with a magnetic and, when possible, with a sun compass using a Pomeroy orientation tool. The average anomaly from 58 sun compass readings was 4.0° ± 2.5°, in good agreement with the International Geomagnetic Reference Field (IGRF) declination anomaly of 4.6°, which we used to correct the declination azimuths of all samples.

2.2. Kaji-Say Section

The Kaji-Say section is located 10 km northeast of Kaji-Say village and spans 650 m in stratigraphic height. We sampled the section along two transects, west and east (Figures 1d and 1f). Bedding dips in the eastern transect are ~25° (N) at the base of the section (0 m) and flatten to horizontal at around 225 m height. After 245 m the beds abruptly dip ~75° (N), defining an asymmetric anticline with its axis striking E-W (Figure 2b). The beds remain steeply dipping (~75°) until the top of the eastern transect at 464 m. Farther north of these sites, the steeply dipping beds disappear under Sharpyldak conglomerates. Following 1 km along strike to the west (western transect), the Chu beds dip more gently around 30° (N) (Figure 2d) shallowing to ~15° (N) toward the top of the section. The beds thicken to the northwest and pinch out to the southeast, which could indicate the presence of growth strata.

Geochemistry, Geophysics, Geosystems 10.1029/2020GC009556

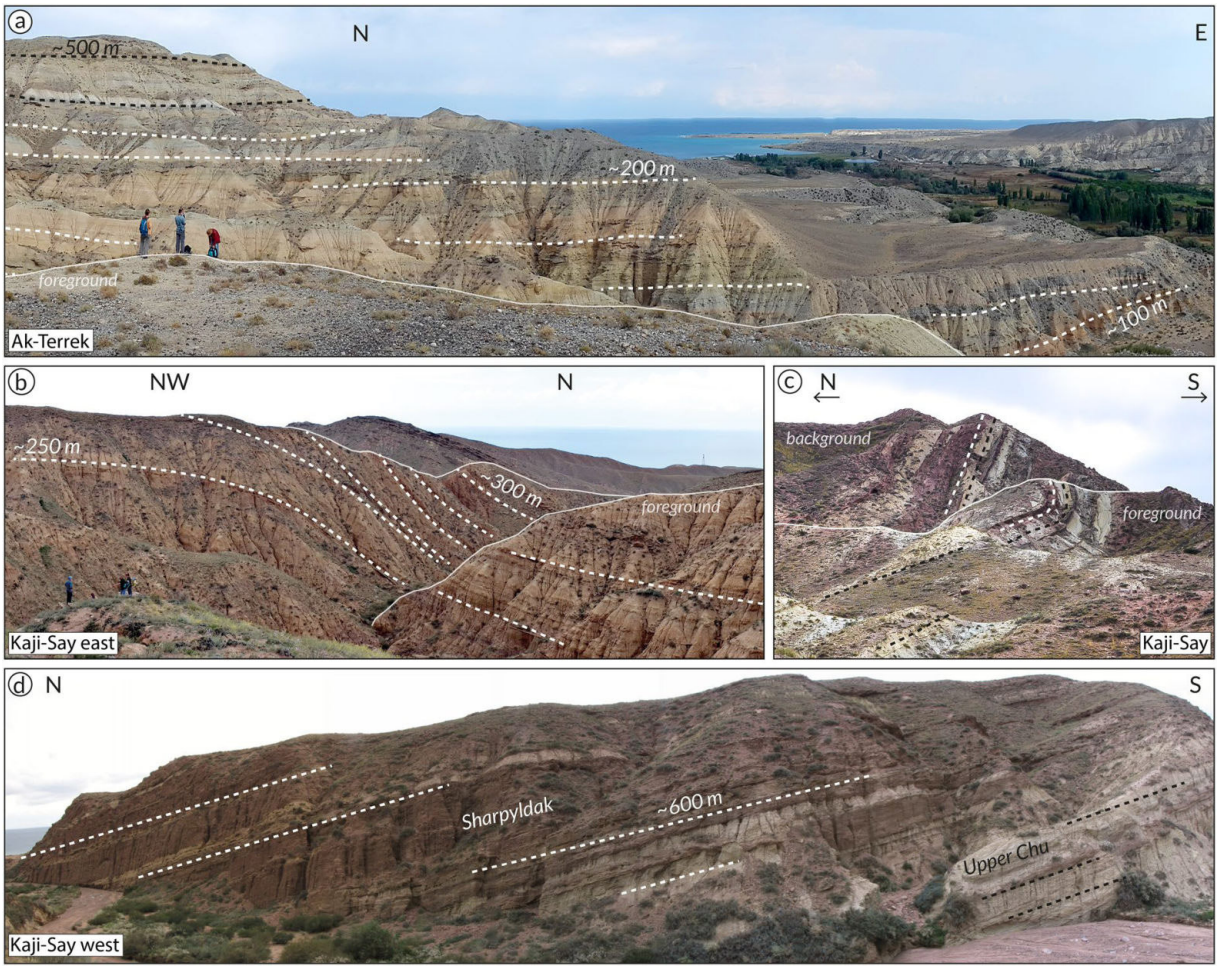

Figure 2. Field photos of the Ak-Terek (AT) and Kaji-Say (KS) sections. (a) Upper ~400 m of the AT section; view to the north with Lake Issyk-Kul in the background; dashed lines highlight bedding structures and numbers indicate approximate stratigraphic heights. (b) Panorama of the eastern part of the KS section with bedding attitudes steepening from nearly horizontal to >70° above ~250 m. (c) Syncline structure between the eastern and western parts of KS (d) Panorama of the Chu-Sharpyldak contact in the western part of the KS section. See Figure 1 for the locations where the photos were taken.

We could not follow individual beds between the eastern and western transects. The change in dip from ~75° in the eastern section to ~30° in the western section could signal an unconformable surface thereby suggesting the section was folded prior to the deposition of the upper unit, with a hiatus between the two. The postulated unconformable surface likely strikes E-W, parallel to the strike of the strata, which would explain why we did not identify it on the ground or in aerial images. An alternate interpretation that we cannot rule out is that a syncline observed between the two transects (Figure 2c) connects the steeply dipping (~75°) units in the east to the shallow-dipping (~30°) units in the west.

Fluvial deposits of alternating sand, silt, and mudstone layers intercalated with conglomerates characterize the lower, eastern part of the section (Figure 3b, KS-1). At the top of this transect, between 440 and 460 m, we identified two, <0.5 m thin calcareous interbeds. Along the western transect, the sediments consist mostly of fine-grained calcareous silt, and carbonates that alternate with laminated silt or mudstone, and rippled or cross-bedded sandstone (Figure 3b, KS-2). The up to 9 m thick calcareous, partially laminated beds indicate lacustrine deposition. The number and thickness of interbedded coarse conglomerates increases above ~550 m, marking the transition between Chu and Sharpyldak style deposits (Figure 2d); above 600 m the section is dominated by Sharpyldak conglomerates.

Paleomagnetic samples were collected in approximately 2 m intervals, taking two oriented cores per horizon (312 in total) and selecting fine grained mud or silt when possible. In contrast to Ak-Terek, most strata

Geochemistry, Geophysics, Geosystems 10.1029/2020GC009556

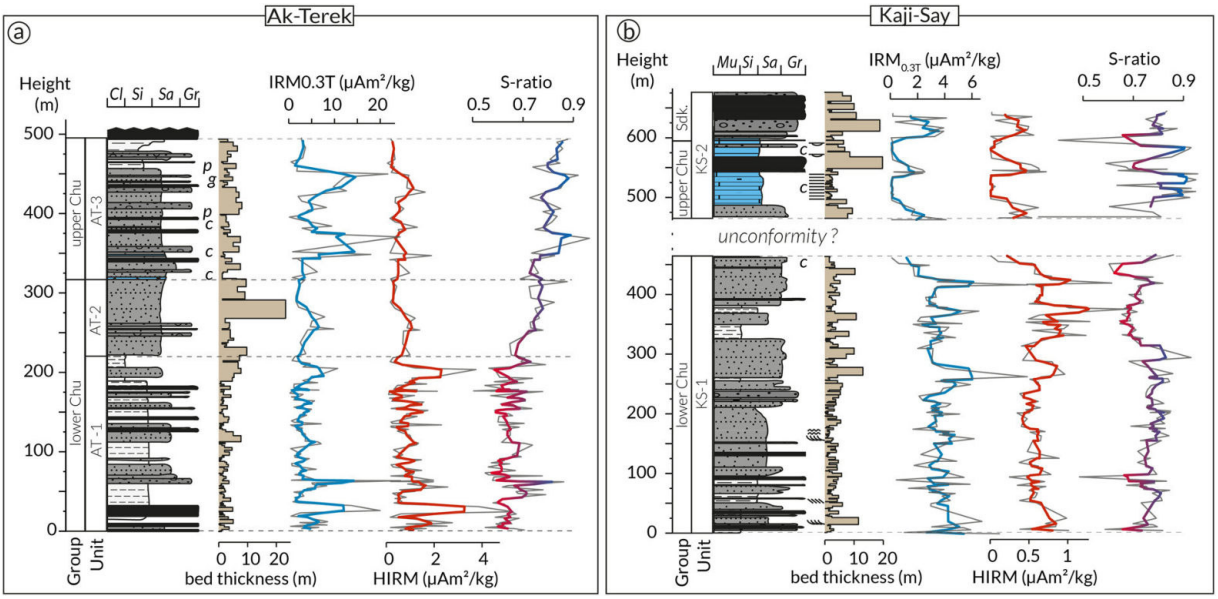

Figure 3. Summary of sedimentologic and rock magnetic data of the Ak-Terek (a) and Kaji-Say (b) sections. Lithologic columns show fluvial beds in gray scale; lacustrine carbonates in blue, with dominant grain size of clay (Cl), mud (Mu), silt (Si), sand (Sa) and gravel (Gr). Letters indicate: p, paleosol; c, carbonate; g, gypsum. Groups correspond to the lower and upper Chu and Sharpyldak (Sdk.) groups mapped in Figure 1; Units (AT-1 to AT-3 and KS-1 to KS-2) defined based on prominent changes in the lithologic and rock magnetic parameters. Parameters left to right: bed thickness, $IRM_{0.3T}$ reflecting magnetite concentration, HIRM reflecting hematite concentration and S-ratio reflecting relative magnetite to hematite proportions.

in this section were poorly lithified. We obtained drill cores from 15 horizons, while 297 horizons were sampled with the push corer. Therefore, samples from Kaji-Say were predominantly contained within plastic cylinders. The average anomaly from 156 Sun compass readings was 4.2° ± 2.3°, again in good agreement with the IGRF declination anomaly of 4.5°.

3. Paleo and Rock Magnetic Characterization

3.1. Laboratory Methods

Because the majority of the samples were contained in plastic cylinders that prevented thermal treatment, we subjected one sample of each horizon to stepwise alternating field (AF) demagnetization. In case of unstable trajectories, or if polarity intervals were defined by a single specimen, a second sample was AF demagnetized. In addition, samples from all 15 drilled horizons from Kaji-Say and from 23 of the drilled sites from Ak-Terek were thermally demagnetized using 14 heating steps to compare against the AF demagnetization data. AF demagnetization (16 steps up to 90 mT) and magnetic moment measurements were conducted inside a magnetically shielded room (~500 nT) using an automated measurement system (SushiBar) based on a 2G Enterprises, three-axis superconducting magnetometer (Wack & Gilder, 2012). Characteristic remanent magnetizations were determined by principal component analysis (Kirschvink, 1980) and mean directions were calculated with Fisher statistics (Fisher, 1953) using the software PaleoMac (Cogné, 2003).

Rock magnetic parameters were measured on at least one sample per horizon to determine magnetic mineralogy and grain size variations throughout both sections. We measured magnetic susceptibility (χ), anhysteretic remanent magnetization (ARM) with a peak alternating field of 90 mT and a 0.1 mT bias field and calculated the ARM/χ ratio as a proxy for grain size and/or mineralogic changes (King et al., 1982). Subsequently, a 1 T isothermal magnetic remanence (IRM) followed by a back field IRM of −0.3 T were measured in order to calculate the S-ratio (Bloemendal et al., 1992), which is a proxy for the relative hematite to magnetite concentration. We further determined the low coercivity component ($IRM_{0.3T}$) and the high coercivity component (HIRM) representative of the magnetite and hematite concentrations, respectively (e.g., Liu et al., 2012).

Geochemistry, Geophysics, Geosystems 10.1029/2020GC009556

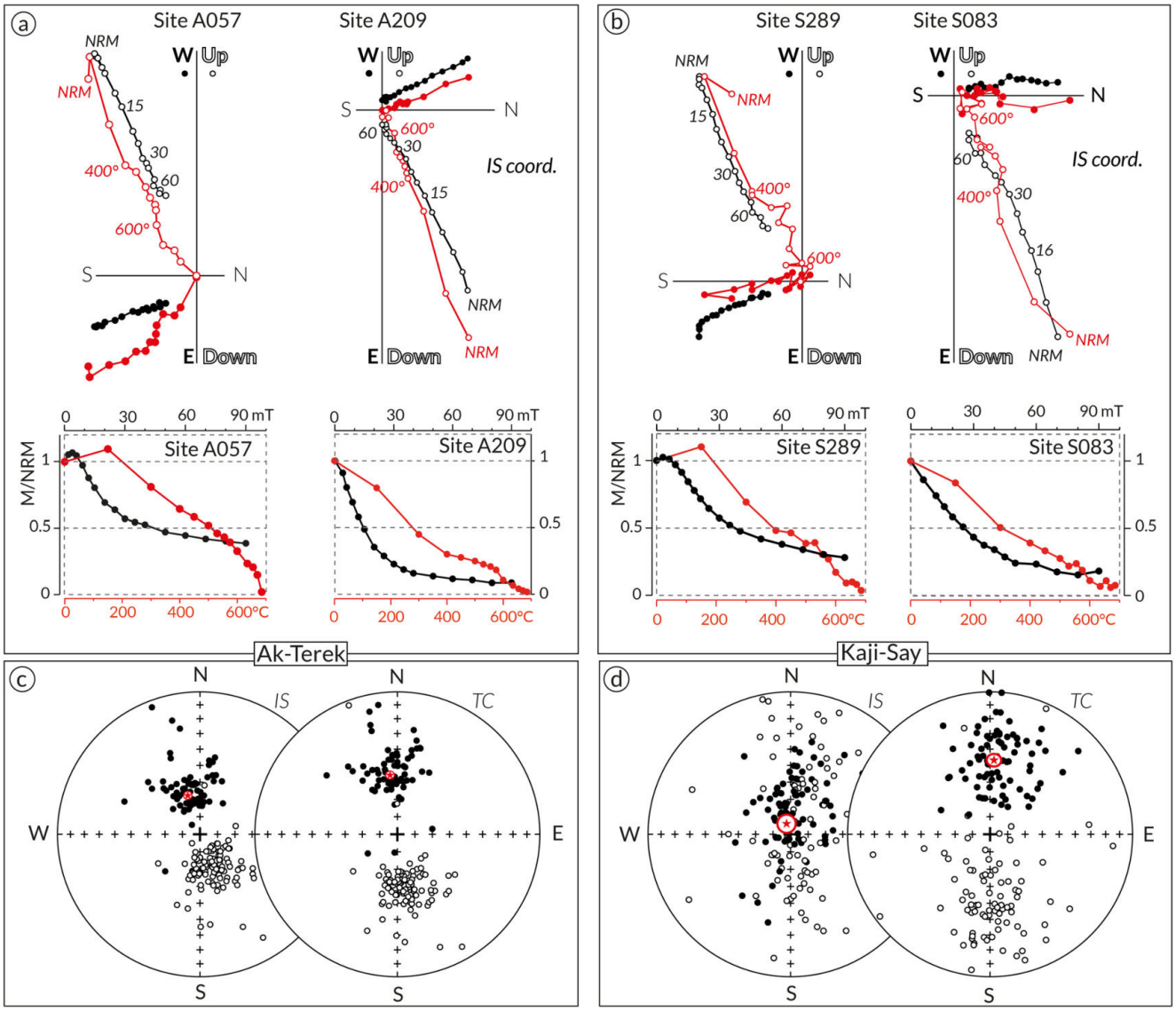

Figure 4. Summary of paleomagnetic data. (a)–(b) Comparison of stepwise thermal (red) and AF (black) demagnetization trajectories showing selected demagnetization steps (values in °C and mT, respectively). A normal and reversed polarity sample pair from the same horizons are shown for (a) Ak-Terek and (b) Kaji-Say. Further examples shown in Figures S1 and S2. (c)–(d) Stereographic projections of the best-fit line components in in-situ (IS) and tilt corrected (TC) coordinates for both sections; mean directions and 95% confidence ellipsoids shown in red.

3.2. Rock Magnetic Analyses

Thermal demagnetization experiments indicated that both sections contain two magnetic phases: one that unblocks between 300°C and 580°C, suggestive of magnetite with variable titanium concentrations and another whose magnetic remanence persists to ~680°C, indicative of hematite (Figures 4a, 4b, S1 and S2). At Ak-Terek, the magnetic mineralogy changes midsection, as indicated by an increase in the S-ratio from an average of 0.65 below 200 m (AT1) to 0.82 above 300 m (AT3) (Figure 3a), signifying a decrease in relative hematite contribution with increasing stratigraphic height. HIRM and $IRM_{0.3T}$ show that this trend is linked to a decrease in hematite concentration above 200 m and an increase in magnetite above 350 m.

At the Kaji-Say section, $IRM_{0.3T}$ and HIRM indicate that hematite and magnetite concentrations are significantly lower above the hypothetical unconformity at 464 m (KS-2) compared to below (KS-1) (Figure 3b). In unit KS-2, the magnetic properties correlate with lithology, where calcareous lacustrine horizons have an order of magnitude lower $IRM_{0.3T}$ and HIRM than coarser grained, fluvial deposits. Substantially lower

Geochemistry, Geophysics, Geosystems 10.1029/2020GC009556

Table 1
Average Paleomagnetic Directions From This study

	n	Dg	Ig	k	α_{95}	Ds	Is	k	α_{95}
Ak-Terek (42.2°N, 76.7°E)									
All samples	188	341.6	67.0	24.9	2.1	352.4	56.0	24.3	2.1
Reversed-only	110	157.5	−68.8	29.5	2.5	170.3	−58.3	30.8	2.5
Normal-only	78	346.5	64.2	21.5	3.5	355.0	52.6	19.8	3.7
Kaji-Say (42.2°N, 77.3°E)									
All samples	163	335.2	85.7	5.9	5.0	2.9	48.0	11.5	3.4
Reversed-only	83	42.4	−80.5	4.7	8.1	178.0	−50.3	10.5	5.0
Normal-only	80	10.2	76.2	11.0	5.0	7.4	45.5	13.4	4.5

Note. Precise GPS coordinates are given for each sample in the on-line data.
Abbreviations: n, number of samples; D, declination; I, inclination; g, geographic (in-situ) coordinates, s, stratigraphic (tilt-corrected) coordinates; k, best estimate of the precision parameter; α95, radius that the mean direction lies within 95% confidence.

magnetite and hematite concentrations in the lacustrine sediments likely reflect the dilution of detrital particles by diamagnetic carbonate. Sharpyldak conglomerates are characterized by elevated HIRM and low S-ratios, reflecting higher proportions of hematite. A slightly reddish color of the Sharpyldak Group at Kaji-Say (Figure 2c) further suggests the presence of hematite pigment in these layers.

3.3. Paleomagnetic Analyses

AF demagnetization removed 70%–80% of the natural remanent magnetization (NRM) on average, suggesting that at least 20%–30% of the NRM is carried by hematite. Most samples had a single magnetization component that decayed toward the origin or close to it, and demagnetization trajectories from thermal and AF treatment of samples from the same horizon yielded compatible demagnetization components (Figures 4a, 4b, and S2).

Best-fit directions from AF demagnetized samples were derived using an average of nine steps between 20 and 80 mT, and thermally demagnetized samples were mostly fit between 400°C and 680°C. For Ak-Terek, we retained 188 magnetization directions out of 216 demagnetized samples (Figure 4c). For Kaji-Say, 163 magnetization directions were retained from 235 demagnetized samples (Figure 4d). At both sections, the McFadden and McElhinny (1990) reversals test is negative. For Ak-Terek, the angle between the two polarity populations is 6.3°, which exceeds the critical angle of 4.3°; for Kaji-Say, the angle between the two means is 7.9° with a critical angle of 6.7° (Table 1 and Figures 4c and 4d). The bootstrap reversals test of Tauxe (2010) shows that the Y and Z components overlap at 95% confidence but not X for Ak-Terek and overlap for the X and Z components but not Y for Kaji-Say. Incompletely removed recent field components can explain the differences between the two polarities. For Kaji-Say, the fold test is positive at 95% confidence limits McFadden (1990) ($Xicrit_{95}$: 14.85, Xi_{1g}: 23.27, Xi_{1s}: 6.39), with the Fisher (1953) precision parameter (k) being maximized at 96 ± 32% unfolding when considering no uncertainty on bedding attitudes or at 90 ± 18% unfolding with 5° uncertainty on bedding attitudes (Watson & Enkin, 1993). Only minor differences in bedding attitudes at Ak-Terek lead to an insignificant change in k, hence an inconclusive/indeterminate fold test.

4. Magnetostratigraphy

To establish a magnetic polarity sequence for each section we converted the magnetization component directions into virtual geomagnetic poles (VGPs; Figures 5a and 5b). At least two successive horizons of the same VGP polarity were used to define polarity intervals. The obtained polarity sequence was then correlated to the Neogene geomagnetic polarity time scale (GPTS2012) of Gradstein et al. (2012). Because both sections mostly contain Chu Group sediments, our correlations assumed the sections must be younger than

Geochemistry, Geophysics, Geosystems 10.1029/2020GC009556

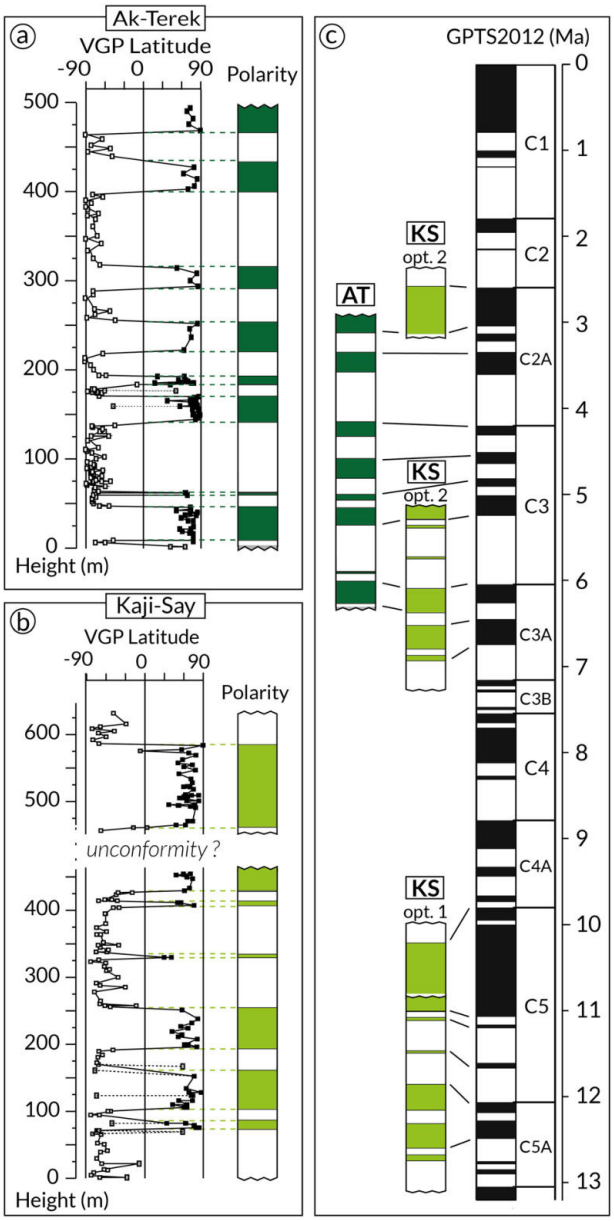

Figure 5. Magnetostratigraphy of Ak-Terek and Kaji-Say. (a)–(b) Virtual geomagnetic pole (VGP) latitude versus stratigraphic height and assigned polarity sequences (green: normal polarity, white: reversed polarity). (c) Magnetostratigraphic correlation of Ak-Terek (AT) and Kaji-Say (KS) with the geomagnetic polarity time scale (GPTS2012) of Gradstein et al. (2012). Two options are shown for Kaji-Say assuming either continuous (Opt. 1) or discontinuous (Opt. 2) deposition between the eastern and western transects. AT, Ak-Terek; KS, Kaji-Say; VGP, Virtual geomagnetic pole.

the top of the underling Shamsi Group, which was previously dated to 11 or 13 Ma (Wack et al., 2014) in the Issyk-Kul Basin. We therefore took 13 Ma as the maximum possible age for both sections.

4.1. Ak-Terek

Based on 188 tilt-corrected VGP directions, we established 15 polarity intervals for Ak-Terek (Figure 5a). Visual correlation of the polarity sequence with the GPTS yields the best match between 6.3 and 2.8 Ma (Figure 5c). This correlation includes a missing normal polarity subchron (C2An.2n) at ca. 3.2 Ma (450 m) and a normal polarity interval at 5.9 Ma (60 m) that has no equivalent with the reference scale. The former lasted ca. 90 ka, which corresponds to about 10 m in thickness. With an average sampling interval of 7 m in this part of the section, the subchron could have been missed given fluctuations in the sedimentation process. The normal polarity interval at ~60 m is restricted to a 2.5 m thin conglomerate layer of anomalously high IRM values (Figure 4a), so it likely represents an isolated aberration in the magnetic recording process.

4.2. Kaji-Say

The magnetic polarity sequence for Kaji-Say was based on 165 tilt-corrected directions (Figure 5b), which identified 13 polarity intervals. A normal polarity interval spans ~150 m across the potential unconformity between the eastern and western transect. However, the base of the upper section contains a single reversed and two transitional samples, which may indicate that a reversed polarity interval lies below. Two possibilities were considered when correlating the obtained polarity sequence with the global reference scale. Option 1 assumes continuous sedimentation between the eastern and western transects, where a correlation can be found between 12.7 and 9.5 Ma (Figure 5c). This solution includes one reversed polarity interval at ~100 m that does not exist in the reference scale and misses two short subchrons at the top of the section (580–620 m). Option 2 assumes a hiatus exists between the eastern and western transects at 464 m. The stratigraphically higher, western section spans ~200 m in thickness but contains only two polarity intervals. However, assuming the sedimentation rates are similar in the lower unit, restricts the possible correlations with the GPTS. Moreover, the transition between Chu and Sharpyldak deposits between 550 and 600 m can serve as a tentative tie point to the equivalent transition at the Ak-Terek section. When respecting these criteria, the 160 m normal polarity interval, followed by a 50 m reversed polarity interval of the upper section, best match the reference scale between 3.0 and 2.4 Ma (Figure 5c).

Correlating the lower part of the section (eastern transect) individually to the GPTS yields two plausible matches. One possibility is to correlate the lower section in the same way as in Option 1, from 12.7 to 10.9 Ma (Figure 5c). However, this correlation results in an 8 Myr hiatus within the section and a ~4 Myr age gap between the Chu Group at Kaji-Say and Ak-Terek. The other possible correlation to the reference scale lies between 7.0 and 5.1 Ma, which overlaps our age estimate for the base of the Ak-Terek section and reduces the hiatus to 2 Myr (Figure 5c). This correlation involves two normal polarity zones around 320 and 400 m height that are not matched to the reference scale. Considering their short duration, the unmatched intervals are likely explained by local magnetic recording aberrations in our sections but could also represent true subchrons that were too short to be recognized in the global polarity scale.

Geochemistry, Geophysics, Geosystems 10.1029/2020GC009556

5. Depositional History of the Issyk-Kul Basin

5.1. Depositional Age at Ak-Terek

The magnetostratigraphic correlation of the 500 m thick Ak-Terek section yields a robust correlation to the reference scale, suggesting that the Chu sediments were deposited between 6.3 and 2.8 Ma with an average sedimentation rate of 14 cm/ka. The conformable transition to conglomerate at the top of the section dates the Chu-Sharpyldak transition at 2.8 Ma. We did not observe a lithologic transition at the base of the section; however, along strike to the east, Shamsi deposits are exposed by a reverse fault (Figure 1c). Together with the observation of slightly reddish layers at the base of the section (Figure 2a) that are rich in hematite (Figure 3a), this points to a Shamsi-Chu transition close to 6.3 Ma at Ak-Terek.

5.2. Depositional Age at Kaji-Say

Of the two plausible magnetostratigraphic correlations for Kaji-Say, Option 1 assumes quasi-continuous sedimentation between the eastern and western transects, thereby dating the ca. 650 m thick section to between 12.7 and 9.5 Ma, with an average sedimentation rate of 25 cm/ka and places the Chu-Sharpyldak transition at ca. 10 Ma. Based on more reddish strata south of the sampled section, suggestive of Shamsi type deposits (Figure 1d), we assume that the base of our section represents approximately the base of the Chu Group at Kaji-Say. A basal age of ca. 13 Ma for the Chu Group is consistent with previous age estimates from the eastern Issyk-Kul Basin that dated the top of the Shamsi Group to 13–11 Ma (Wack et al., 2014). On the other hand, this age model implies a 4 Myr hiatus between the Chu sediments deposited at Kaji-Say and Ak-Terek. It also suggests that the stratigraphic boundary between the Chu and Sharpyldak groups at Kaji-Say predates the equivalent transition at Ak-Terek by more than 7 Myr.

Option 2 dates the lower unit to 7.0–5.1 Ma and the upper unit to 3.0–2.4 Ma with average sedimentation rates of 23 and 30 cm/ka, respectively. This places the Shamsi-Chu transition at around 7 Ma and the Chu-Sharpyldak transition at 2.8–2.6 Ma, which agrees well with the stratigraphic boundaries inferred for Ak-Terek. Although average sedimentation rates of the two age models are similar, Option 2 involves less variability within the section (20–30 cm/ka, Figure 7a) compared to Option 1 (16–43 cm/ka). The presence of calcareous lacustrine deposits in the upper part of Kaji-Say (Figure 3b) yields an additional age constraint that points to the younger age of Option 2, as it implies the existence of a lake (Lake Issyk-Kul) at the time of deposition. A precondition for lake formation was the closure of the Issyk-Kul Basin, caused by uplift of the Kungey Range, which was estimated to post-date 7 Ma (Macaulay et al., 2014; Selander et al., 2012).

A conformable transition to Sharpyldak conglomerates in the upper section also argues for the younger ages implied by Option 2. Deposition of Sharpyldak-type conglomerates marks a prominent transition from a low to high energy depositional regime, a widely recognized phenomenon throughout the Tian Shan, with Sharpyldak equivalents identified in China as the Xiyu Formation (e.g., Zhou et al., 2020) and the Polizak Formation in Tajikistan (e.g., Dedow et al., 2020). Commonly, these formations are late Plio-Pleistocene in age and have been linked to the onset of northern hemispheric glaciation (e.g., Peizhen et al., 2001; Zhao et al., 2020). However, other authors described the Xiyu conglomerates as a time-transgressive prograding gravel wedge with depositional ages ranging from ca. 15 to 2 Ma (Charreau et al., 2009; Heermance et al., 2007), therefore, regional correlation of the formations should be made with caution.

In the Chu Basin (Noruz section, 150 km west of AT, Figure 1a), the transition between the Shamsi equivalent (Saryagach Formation) and the 1.5 km thick Chu Formation was dated magnetostratigraphically to ~7.5 Ma, while the Chu-Sharpyldak transition was dated to ca. 3 Ma (Bullen et al., 2001) and 4.5 Ma (Abdrakhmatov et al., 2001; C1 and C2 in Figure 6). Based on similar depositional ages inferred for a ~3.5 km thick Chu Group in the At-Bashi Basin (AB in Figure 6) and on further preliminary magnetostratigraphic studies from the Kochor and Naryn basins, Abdrakhmatov et al. (2001) suggested that the transitions between the main stratigraphic groups occurred coevally from basin to basin in the central Tian Shan. Their proposed Shamsi-Chu and Chu-Sharpyldak transition ages around 8 and 4 Ma, respectively, generally agree with the depositional ages we determined for Ak-Terek and with the age model of Option 2 at Kaji-Say (Figure 6).

Geochemistry, Geophysics, Geosystems 10.1029/2020GC009556

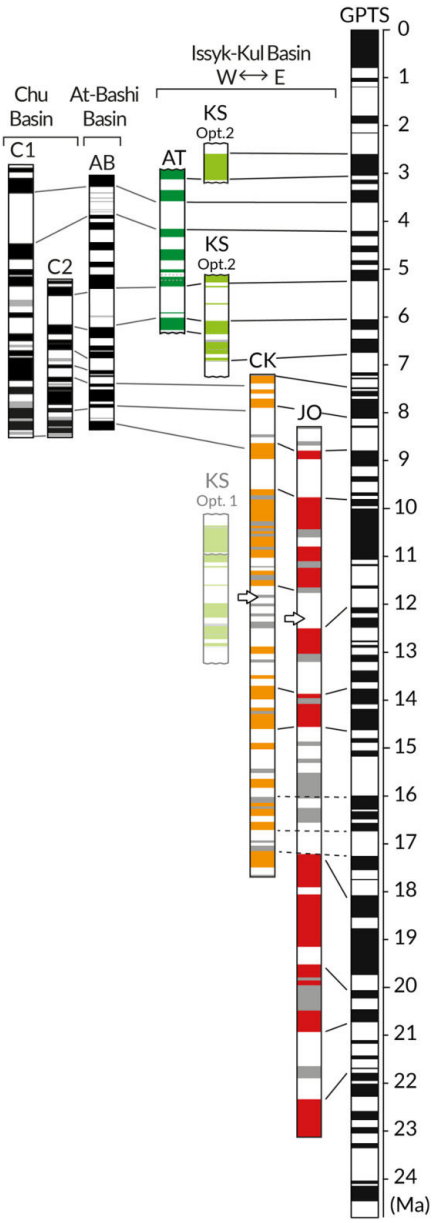

Figure 6. Magnetostratigraphic correlations of sections from the central (Krygyz) Tian shan. Abbreviations above the polarity sequences indicate name and location of the sections from Figure 1. New and reinterpreted magnetostratigraphies from the Issyk-Kul Basin are shown in color (this study). Polarity sequences of CK and JO after Wack et al. (2014); arrows indicate tie points based on a prominent change in magnetic properties (see also Figure 8). C1 and C2 represent the Naryn section from the Chu Basin after Bullen et al. (2001) and Abdrakhmatov et al. (2001), respectively; AB is from the At-Bashi Basin (Abdrakhmatov et al., 2001). CK, Chon Kyzylsuu; JO, Jeti-Oguz.

Taking into account all local and regional age constrains from the Chu and Sharpyldak-equivalent formations supports Option 2 at Kaji-Say, suggesting a depositional age of ca. 7.0–2.4 Ma, with a hiatus between ca. 5 and 3 Ma.

5.3. The Shamsi Group, Eastern Issyk-Kul Basin

The new age constraints for the Chu Group at Ak-Terek and Kaji-Say with a tentative Shamsi-Chu transition age close to 7 Ma led us to reevaluate the magnetostratigraphy of the Shamsi Group in the eastern Issyk-Kul Basin (Figure 1e), previously dated between 26 and 11 Ma (Wack et al., 2014). Owing to its lower sedimentation rate and poorer magnetic recording than the Chu group, the magnetizations in the Shamsi Group were less stable and their polarity sequence yielded ambiguously defined polarity intervals, leading to inconclusive magnetostratigraphic age estimates (Wack et al., 2014). The polarity sequence of Chon Kyzylsuu (CK) was assigned to two age models (A) and (B), with model A yielding 26–16 Ma and model B yielding 25–11 Ma. Re-correlating this section with the GPTS2012 (Gradstein et al., 2012) to the period from 26 to 7 Ma, by considering all inconclusive horizons as unknown polarities, yields a plausible match between 17.3 and 7.5 Ma (Figure 6), with an average sedimentation rate of 9 cm/ka.

The polarity sequence of Jeti-Oguz (JO) was originally correlated between ca. 23 and 13 Ma or 23 and 11 Ma (Wack et al., 2014). The lower 400 m of the section are robustly defined as 23–18 Ma in both age models they considered. Polarity intervals were more ambiguously defined above 400 m. However, a tie-point exists between the two sections based on a characteristic change in magnetic properties (up-section increase in ARM) observed at around 550 and 700 m stratigraphic height in the CK and JO sections, respectively (arrows in Figures 6 and 7; Wack et al., 2014). Respecting this tie point, the whole section yields a plausible correlation to the GPTS2012 as well as to the CK polarity sequence between 22.4 and 8.5 Ma with an average sedimentation rate of 8 cm/ka (Figure 6).

Geologic mapping based on satellite images further supports the proposed tie-point between the two sections (Figure 1e). In both sections, the levels characterized by increasing ARM values, reflecting an increase in fine grained magnetite (Figures 7c and 7d), mark a prominent color transition from intense dark red beds below (lower Shamsi) to lighter, pale red beds above (upper Shamsi; Figure 1e), indicating a decrease in pigmentary hematite. The difference in basal ages (22.4 Ma vs. 17.3 Ma) of the two sections appears reasonable, considering that the Shamsi deposits extend significantly farther below the base of the CK section. In contrast, the base of JO lies above white (lower) Kokturpak or Jurassic strata (observed on satellite images and in the field) that onlap on up-thrusted basement rocks (Figure 1e). The transition from Shamsi to Chu type deposits is unconformably overlain by Sharpyldak conglomerates at both sections and was therefore not identified in the field. However, our satellite image mapping further supports that the top of both sections lies within the uppermost Shamsi Group (Figure 1e). Good agreement between the here suggested age of the Shamsi group, the new age constraints for the Chu Group, and geologic mapping between the studied sections, leads us to conclude that the Shamsi Group was likely deposited throughout the Miocene, between ca. 22 and 7 Ma in the Issyk-Kul Basin.

Geochemistry, Geophysics, Geosystems 10.1029/2020GC009556

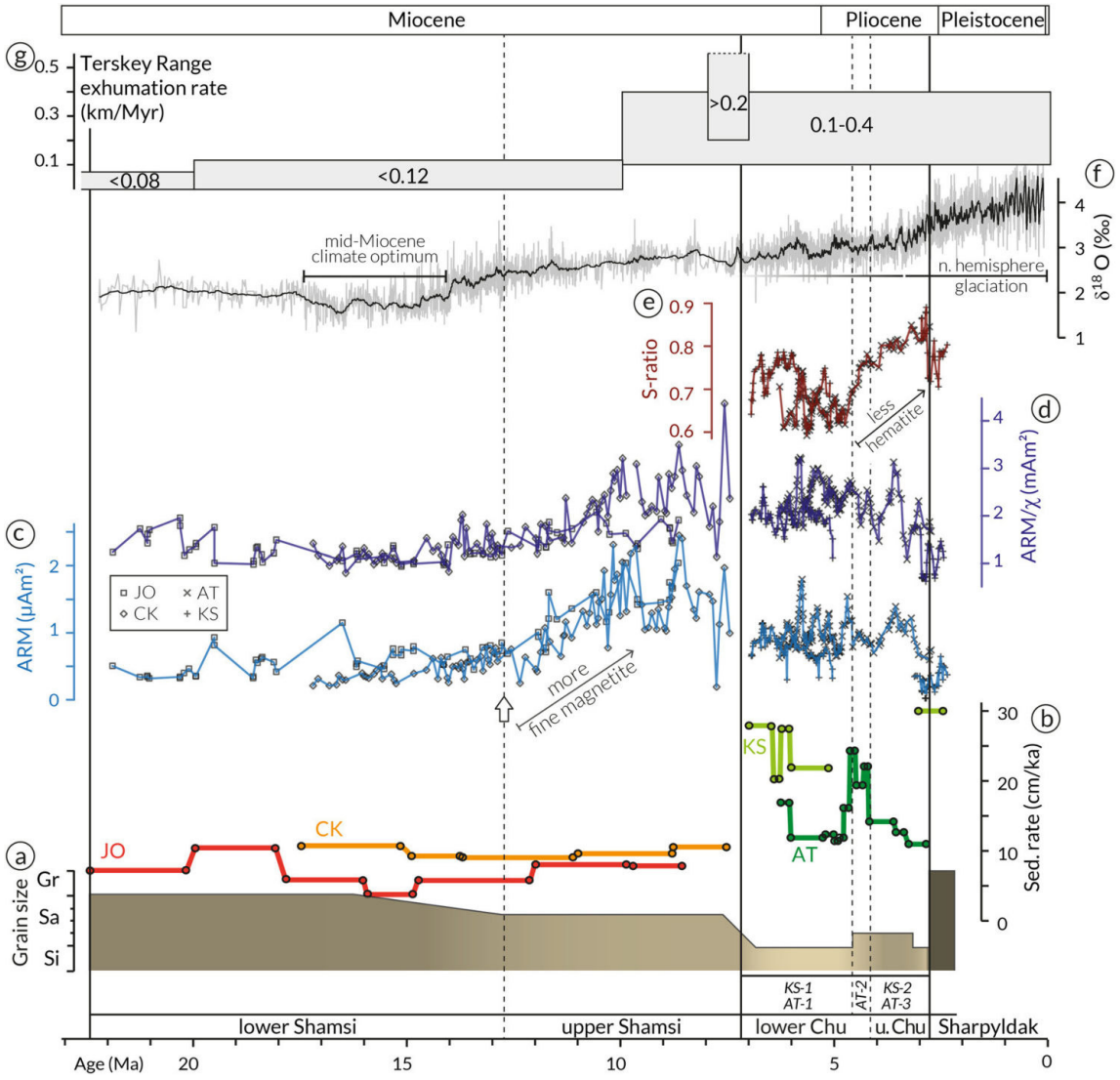

Figure 7. Characterization of the Mio- to early Pleistocene sediments from the southern Issyk-Kul Basin. From bottom to top: (a) Dominant average grain size; data for the Shamsi group after Macaulay et al. (2016). (b) Sedimentation rates determined from the magnetostratigraphic age models; JO, CK, KS, and AT indicate section name/location from Figure 1. Option 2 is shown for KS. (c)–(e) Rock magnetic parameters ARM, ARM/Xχ, and S-ratio; symbols denote the section as shown in (c); arrow indicates tie point between sections; data for the Shamsi Group from Wack et al. (2014), data for the Chu Group (this study) were smoothed using a 5 point moving average. (f) Global climate trends represented by compiled deep-sea oxygen isotope ($d^{18}O$) record from Zachos et al. (2001) using a 90 point moving average. (g) Exhumation rates of the Terskey Range in 10 Ma bins determined from thermochronologic data (Macaulay et al., 2013). Vertical lines indicate transitions between stratigraphic groups and lithologic units (solid and dashed lines, respectively). AT, Ak-Terek; CK, Chon Kyzylsuu; JO, Jeti-Oguz; K1, Toru-Aygir; K2, Cholpon-Ata; KS, Kaji-Say.

6. Tectonic Implications of the Syn-orogenic Sedimentary Record

6.1. Uplift of the Terskey Range

Taken together, the age constraints from four different sedimentary sections yield a nearly complete record of the Neogene to early Pleistocene depositional history of the southern Issyk-Kul Basin. These sediments accumulated in response to the exhumation and successive erosion of the Terskey Range (Macaulay et al., 2016), thus the sedimentation rate and lithologic characteristics of these units hold information concerning the uplift- and climate-history of the area. The Shamsi group, deposited between 22.4 and 7.5 Ma, consists dominantly of coarse-medium sized sandstone (Figure 7a) with relatively low sedimentation rates of 4–11 cm/ka (Figure 7b). A prominent increase in fine grained magnetite (higher ARM and ARM/Sus, Figures 7c and 7e) and a decrease in pigmentary hematite mark the transition from lower to upper Shamsi

Geochemistry, Geophysics, Geosystems 10.1029/2020GC009556

Group at ca. 12 Ma and coincide with a grain size fining from coarse to medium sand (Figure 7a). Assuming that the oldest sediments from the Jeti-Oguz section represent the base of the Shamsi Group, implies that syn-tectonic sedimentation in the Issyk-Kul Basin, and therefore uplift in the Terskey range, commenced by 22.4 Ma, which is compatible with the estimated onset of deformation in the range at 26-20 Ma (Macaulay et al., 2013, 2014). Relatively constant and low sedimentation rates throughout the Shamsi Group imply that erosion rates were comparatively low and did not change significantly until 7.5–7.0 Ma. However, changes in magnetic mineralogy may indicate a change in source material around 12 Ma. The timing of these changes generally coincides with the onset of global cooling after the mid-Miocene climate optimum (Figure 7f); consequently, a climatically driven change in erosion cannot be excluded. Exhumation rates inferred from thermochronologic data (Figure 7g) point to a slight increase in exhumation during the early to middle Miocene from <0.08 to <0.12 km/Myr (Macaulay et al., 2013), which is, however, not mirrored by an increase in sedimentation rate.

The transition from Shamsi to Chu-type deposits between 7.5 and 7.0 Ma is linked to a fining in grain size from medium sand to dominantly fine sand and silt deposits and an overall increase in sedimentation rates (Figures 7a and 7b). Up to three-fold higher sedimentation rates of the Chu compared to the Shamsi Group indicate an increase in erosion rate after 7 Ma. Thermochronologic data point to accelerated unroofing of the Terskey Range after 10 Ma with exhumation rates of 0.1–0.4 km/Myr and of >0.2 km/Myr between 8 and 7 Ma (Figure 7g) (Macaulay et al., 2013, Figure 7f). A good agreement between the increase in exhumation and sedimentation rates suggests that the stratigraphic boundary between the Shamsi and Chu groups at ca. 7 Ma marks the onset of accelerated uplift of the Terskey Range.

Based on local and temporal variations in lithology and sedimentation rates, the Chu Group can be subdivided into two distinctly different deposition stages. Stage 1, between 7 and 5 Ma, is characterized by comparatively high sedimentation rates (on average 23 cm/ka) in the central part of the basin (at Kaji-Say) and low sedimentation rates (~13 cm/ka) at Ak-Terek further west. It comprises the lithologic units KS-1 and AT-1. Stage 2 between 5 and 3 Ma is characterized by a hiatus at Kaji-Say, while sedimentation rates nearly doubled at Ak-Terek between 5 and 4 Ma (AT-2, Figure 7b) and the lithology changed to more massive and uniform sandstone beds (Figure 3a). After ca. 4 Ma sedimentation rates decreased again, and a more frequently changing lithology includes sporadic carbonates and a gypsum layer that indicate still water deposition (AT-3), while laminated limestones deposited after 3 Ma imply lacustrine deposition (KS-2). The hiatus together with strongly folded strata (dip > 70°) of the lower Chu Group at Kaji-Say likely reflect the onset of deformation and uplift within the foreland basin, which shifted the local depocenter farther north. The concurrent changes in sedimentation rates, lithology and magnetic mineralogy at Ak-Terek (Figures 7c and 7e) may signal a change of source material in the western side of the basin at ca. 4.5 Ma. The transition from Stage 1 to 2, between 4.5 and 5.0 Ma, therefore, marks a prominent change in the deposition dynamics in the Issyk-Kul Basin. The associated northward propagation of the locus of deformation at Kaji-Say indicates that the formation of the Issyk-Kul Broken Foreland initiated around 5 Ma.

Uplift of the mountain ranges to the north may have influenced the depositional dynamics throughout the basin. Thermochronologic data suggest an onset of exhumation of the northern Tian Shan (Zaili Range) between 29 and 15 Ma (De Grave et al., 2013). However, paleocurrent and provenance data from the Kungey Range in the northern Issyk-Kul Basin attest that sediments from the Terskey Range in the south persisted until ca. 7–4 Ma, suggesting that substantial uplift north of the lake commenced only after 7 Ma (Selander et al., 2012).

6.2. Uplift of the Kungey Range and Formation of Lake Issyk-Kul

A shift in sediment provenance within the Chu Group exposed north of Lake Issyk-Kul, from the lower Terskey member to the upper Kungey member, marks the onset of substantial uplift in the Kungey Range (Selander et al., 2012). Although no precise age constraints are available for the sediments in the northern part of the basin, our new age constraints for the Chu Group at Ak-Terek and Kaji-Say (7.0–2.8 Ma) likely apply to the entire Issyk-Kul Basin, yielding an average sedimentation rate of 14 cm/ka for the up to 600 m thick Chu Group in the northern basin. Assuming a constant sedimentation rate dates the transition from the Terskey member (up to 200 m thickness) to the Kungey member (up to 400 m thickness) to ca. 5.5 Ma. Consideration of the evidence for major spatio-temporal shifts of depocenters during this time interval in

Geochemistry, Geophysics, Geosystems 10.1029/2020GC009556

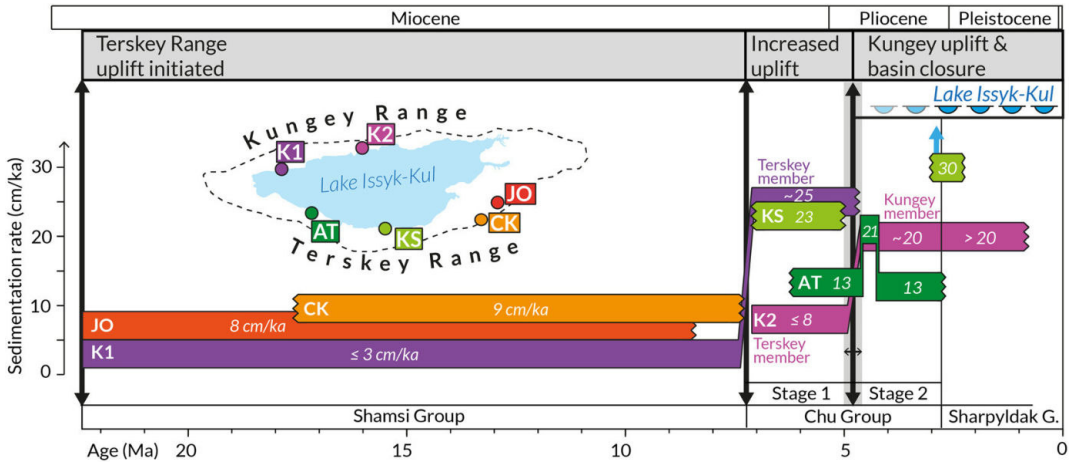

Figure 8. Depositional history of the Issyk-Kul basin with implications for mountain building and lake formation. Sedimentation rates and depositional ages of four magnetostratigraphic sections located in the southern side of the Issyk-Kul Basin (Terskey area; JO, CK, KS, AT) and two stratigraphic sequences from the northern part of the basin (Kungey areas K1 and K2). Sedimentation rates in the Terskey area were based on the magnetostratigraphic age models of this study and average values were determined for the whole Shamsi Group and for the lithologic sub-units (see also Figure 3) of the Chu Group. The respective average sedimentation rates for the Kungey area were estimated based on stratigraphic thicknesses reported by Selander et al. (2012) and the stratigraphic boundaries dated in the southern part of the basin (black arrows). Site locations in inset (see also Figure 1). AT, Ak-Terek; CK, Chon Kyzylsuu; JO, Jeti-Oguz; K1, Toru-Aygir; K2, Cholpon-Ata; KS, Kaji-Say.

the southern and in the northern part of the Issyk-Kul Basin points to a link between the change in deformation style around 5 Ma in the southern basin and the shift from Terskey to Kungey-sourced Chu deposits in the northern basin. We therefore propose that the unconformity at Kaji-Say and the doubling of sedimentation rates at Ak-Terek at ca. 5 Ma coincide with the initiation of substantial uplift in the Kungey range.

To further test this hypothesis, we dated the available stratigraphic columns of the northern side of the Issyk-Kul Basin (Selander et al., 2012; K1 and K2 in Figure 1a), based on the depositional record of the southern basin, by assuming synchronous transitions between equivalent stratigraphic groups (Figure 8). Based on the stratigraphic thicknesses of ca. 500 m for the Shamsi and Sharpyldak groups and ca. 600 m for the Chu Group reported by Selander et al. (2012) and assuming Shamsi, Chu, and Sharpyldak were deposited between ca. 22–7, 7–3, and <3 (Figure 7), we infer a progressive increase in average sedimentation rates over time from ≤3 to ≤12 to ≥20 cm/ka, respectively. Assuming further that the transition from Terskey (10–200 m at K1; 600 m at K2) to Kungey-derived Chu Group sediments (400 m at K1, absent at K2) coincides with the transition from Stage 1 to Stage 2 in the southern side of the basin at ~5 Ma, yields a sedimentation rate of ~25 cm/ka for the Terskey member at location K1 in the northwest and suggests an increase from <8 to ~20 cm/ka after 5 Ma at K2 in the central Kungey area (Figure 8).

The proposed sedimentation rates compare well with the values determined in the southern part of the basin (Figure 8). Comparing Kaji-Say and K2 both located in the central basin, more sediment was deposited at Kaji-Say (up to 28 cm/ka), in proximity to the Terskey Range, than at K2 (<8 cm/ka) between 7 and 5 Ma. However, comparing Ak-Terek and K1, in the western side of the basin, indicates that here sedimentation rates were twice as high at the more distal location K1 (~25 cm/ka) than at Ak-Terek (~13 cm/ka) before 5 Ma. Together, this suggests that between 7 and 5 Ma in the western part of the basin, deposition was located farther north from the Terskey Range than in the central part of the basin. This pattern may be applicable for the entire Miocene, as indicated by the westward thickening of the Shamsi Group in the northern side of the basin (Selander et al., 2012) and an apparent eastward thickening of the Shamsi Group on the southern side (Figure 1b). Uplift of the Kungey Range would shift the deposition of Terskey sourced sediments southward to more proximal areas, which is consistent with the observed doubling of sedimentation rates around 4.5 Ma at Ak-Terek. This uplift event may be associated with a change in the direction of compression from NW-SE to N-S reported for the central Tian Shan around the Miocene-Pliocene transition (Buslov et al., 2003).

Geochemistry, Geophysics, Geosystems 10.1029/2020GC009556

Mountain building north of the basin transformed the Issyk-Kul area from a foreland to an intermountain basin, thereby facilitating the formation of a deep lake within it. Two thin limestone layers at the top of the eastern transect at Kaji-Say, corresponding to ~5 Ma according to Option 2, as well as sporadic calcareous horizons and a gypsum layer deposited between 4 and 3 Ma at Ak-Terek, may point to the expansion and retreat of an early lake. Up to 50 m thick sequences of mostly calcareous lacustrine strata in the western section at Kaji-Say signify the existence of Lake Issyk-Kul at 3 Ma.

7. Conclusions

New and reinterpreted magnetostratigraphic age constraints of continental sediments from the Issyk-Kul Basin yield a near-continuous stratigraphic record of the Mio- to early Pleistocene, syn-tectonic depositional history in one of the largest sedimentary basins in the central Tian Shan. From these, we draw the following main conclusions:

(1) The Shamsi group, which represents the basal syn-tectonic unit, was deposited between 22.4 and 7.5 Ma. This unit is found in the southeastern and northwestern parts of the basin, with maximum thicknesses of ca. 1,000 and 500 m, respectively, implying average sedimentation rates of 8–9 cm/ka and ~3 cm/ka, respectively. Slight fining in grain size and changes in magnetic mineralogy after the middle Miocene (ca. 13 Ma) may reflect a gradual shift in sediment source or transport conditions
(2) A major grain size fining between 7.5 and 7 Ma marks the stratigraphic boundary between the Shamsi and Chu groups. Overall higher sedimentation rates after 7 Ma (11–28 cm/ka) indicate that erosion rates increased, linked to accelerated uplift of the Terskey Range around this time. It is interesting to note the inverse relationship between grain size and sedimentation rate across the Shamsi-Chu transition, which may be related to longer sediment transport or increased subsidence of the basin
(3) Spatio-temporal shifts in the deposition centers documented north and south of Lake Issyk-Kul indicate that the locus of deformation propagated from the Terskey Range into the basin around 5 Ma, forming the Issyk-Kul Broken Foreland. This change in deformation style likely coincides with the initiation of uplift in the Kungey Range to the north, which led to the closure of the basin, a precondition for the formation of Lake Issyk-Kul. Lacustrine deposits dated at ~3 Ma demonstrate that a substantial lake must have existed by that time
(4) Equivalent stratigraphic boundaries around 7 and 3 Ma in nearby basins suggest that the driving mechanisms that controlled sediment accumulation and the lithology of the three main syn-tectonic units were regionally synchronized throughout the central (Kyrgyz) Tian Shan

Data Availability Statement

Data produced during this study are available in the open-access online database Zenodo (https://doi.org/10.5281/zenodo.4548968). The interpreted paleomagnetic directions used for the magnetostratigraphy are provided in the supplementary information. Further data sets for this research are included in Wack et al. (2014), Macaulay et al. (2014), and Zachos et al. (2001).

Acknowledgments
The authors thank Kanatbek Abdrakhmatov and Alexander Mikolaichuk and Nina Andre for scientific discussions and logistical help. This work was supported by the Deutsche Forschungsgemeinschaft (GI 712/10-1, GI 712/16-1 and SO 436/9-1). Editorial handling by Joshua Feinberg and helpful reviews by Ken Kodama and "anonymous" are greatly appreciated. Open access funding enabled and organized by Projekt DEAL.

References

Abdrakhmatov, K. Y., Weldon, R. J., Thompson, S. C., Burbank, D. W., Rubin, C. M., Miller, M., & Molnar, P. (2001). Onset, style and current rate of shortening in the central Tien Shan, Kyrgyz Republic. *Russian Geology and Geophysics*, *42*(10), 1585–1609.

Bloemendal, J., King, J. W., Hall, F. R., & Doh, S.-J. (1992). Rock magnetism of Late Neogene and Pleistocene deep-sea sediments: Relationship to sediment source, diagenetic processes, and sediment lithology. *Journal of Geophysical Research*, *97*(B4), 4361–4375. https://doi.org/10.1029/91jb03068

Bullen, M. E., Burbank, D. W., Garver, J. I., & Abdrakhmatov, K. Y. (2001). Late Cenozoic tectonic evolution of the northwestern Tien Shan: New age estimates for the initiation of mountain building. *The Geological Society of America Bulletin*, *113*(12), 1544–1559. https://doi.org/10.1130/0016-7606(2001)113<1544:lcteot>2.0.co;2

Burgette, R. J. (2008). *Uplift in response to tectonic convergence: The Kyrgyz tien Shan and Cascadia subduction zone*. PhD Thesis, Oregon. 242 pp.

Burgette, R. J., Weldon, R. J., Abdrakhmatov, K. Y., Ormukov, C., Owen, L. A., & Thompson, S. C. (2017). Timing and process of river and lake terrace formation in the Kyrgyz Tien Shan. *Quaternary Science Reviews*, *159*, 15–34. https://doi.org/10.1016/j.quascirev.2017.01.003

Geochemistry, Geophysics, Geosystems 10.1029/2020GC009556

Buslov, M. M., Klerkx, J., Abdrakhmatov, K., Delvaux, D., Batalev, V. Y., Kuchai, O. A., et al. (2003). Recent strike-slip deformation of the northern Tien Shan. *Geological Society, London, Special Publications*, *210*(1), 53–64. https://doi.org/10.1144/gsl.sp.2003.210.01.04

Charreau, J., Gumiaux, C., Avouac, J.-P., Augier, R., Chen, Y., Barrier, L., et al. (2009). The Neogene Xiyu Formation, a diachronous prograding gravel wedge at front of the Tianshan: Climatic and tectonic implications. *Earth and Planetary Science Letters*, *287*(3–4), 298–310. https://doi.org/10.1016/j.epsl.2009.07.035

Cogné, J. P. (2003). PaleoMac: A Macintosh™ application for treating paleomagnetic data and making plate reconstructions. *Geochemistry, Geophysics, Geosystems*, *4*(1), 1007. https://doi.org/10.1029/2001gc000227

Dedow, R., Franz, M., Szulc, A., Schneider, J. W., Brückner, J., Ratschbacher, L., et al. (2020). Tajik Basin and Southwestern Tian Shan, Northwestern India-Asia collision zone: 3. Preorogenic to synorogenic retro-foreland basin evolution in the eastern Tajik depression and linkage to the Pamir hinterland. *Tectonics*, *39*(5). e2019TC005874. https://doi.org/10.1029/2019tc005874

De Grave, J., Glorie, S., Buslov, M. M., Stockli, D. F., McWilliams, M. O., Batalev, V. Y., & van den haute, P. (2013). Thermo-tectonic history of the Issyk-Kul basement (Kyrgyz Northern Tien Shan, Central Asia). *Gondwana Research*, *23*(3), 998–1020. https://doi.org/10.1016/j.gr.2012.06.014

Fisher, R. (1953). Dispersion on a sphere. *Proceedings of the Royal Society A: Mathematical, Physical & Engineering Sciences*, *217*(1130), 295–305. https://doi.org/10.1098/rspa.1953.0064

Fortuna, A. B., Kerimbekov, C. K., Kuzikov, S. I., & Mikolaichuk, A. V. (1994). Litostratigraphy and palynologic data on Cenozoic deposits of the Tessyk-Sarybulak depression. In *Geology of Cenozoic and seismotectonics of the tien Shan [in Russian]* (pp. 26–40). Bishkek, Kyrgyzstan: Ilim.

Goode, J. K., Burbank, D. W., & Bookhagen, B. (2011). Basin width control of faulting in the Naryn Basin, south-central Kyrgyzstan. *Tectonics*, *30*(6). TC6009. https://doi.org/10.1029/2011tc002910

Gradstein, F. M., Ogg, J. G., Schmitz, M. D., & Ogg, G. M. (Eds.), (2012). *The geologic time scale 2012*. Elsevier.

Heermance, R. V., Chen, J., Burbank, D. W., & Wang, C. (2007). Chronology and tectonic controls of Late Tertiary deposition in the southwestern Tian Shan foreland, NW China. *Basin Research*, *19*(4), 599–632. https://doi.org/10.1111/j.1365-2117.2007.00339.x

King, J., Banerjee, S. K., Marvin, J., & Özdemir, Ö. (1982). A comparison of different magnetic methods for determining the relative grain size of magnetite in natural materials: Some results from lake sediments. *Earth and Planetary Science Letters*, *59*(2), 404–419. https://doi.org/10.1016/0012-821x(82)90142-x

Kirschvink, J. L. (1980). The least-squares line and plane and the analysis of paleomagnetic data. *Geophysical Journal International*, *62*(3), 699–718. https://doi.org/10.1111/j.1365-246x.1980.tb02601.x

Korzhenkov, A. M., & Deev, E. V. (2017). Underestimated seismic hazard in the south of the Issyk-Kul Lake region (northern Tian Shan). *Geodesy and Geodynamics*, *8*(3), 169–180. https://doi.org/10.1016/j.geog.2017.03.012

Liu, Q., Roberts, A. P., Larrasoaña, J. C., Banerjee, S. K., Guyodo, Y., Tauxe, L., & Oldfield, F. (2012). Environmental magnetism: Principles and applications. *Reviews of Geophysics*, *50*(4), RG4002. https://doi.org/10.1029/2012rg000393

Macaulay, E. A., Sobel, E. R., Mikolaichuk, A., Kohn, B., & Stuart, F. M. (2014). Cenozoic deformation and exhumation history of the Central Kyrgyz Tien Shan. *Tectonics*, *33*(2), 135–165. https://doi.org/10.1002/2013tc003376

Macaulay, E. A., Sobel, E. R., Mikolaichuk, A., Landgraf, A., Kohn, B., & Stuart, F. (2013). Thermochronologic insight into late Cenozoic deformation in the basement-cored Terskey Range, Kyrgyz Tien Shan. *Tectonics*, *32*(3), 487–500. https://doi.org/10.1002/tect.20040

Macaulay, E. A., Sobel, E. R., Mikolaichuk, A., Wack, M., Gilder, S. A., Mulch, A., et al. (2016). The sedimentary record of the Issyk Kul basin, Kyrgyzstan: Climatic and tectonic inferences. *Basin Research*, *28*(1), 57–80. https://doi.org/10.1111/bre.12098

McFadden, P. L. (1990). A new fold test for palaeomagnetic studies. *Geophysical Journal International*, *103*(1), 163–169. https://doi.org/10.1111/j.1365-246X.1990.tb01761.x

McFadden, P. L., & McElhinny, M. W. (1990). Classification of the reversal test in palaeomagnetism. *Geophysical Journal International*, *103*(3), 725–729. https://doi.org/10.1111/j.1365-246x.1990.tb05683.x

Peizhen, Z., Molnar, P., & Downs, W. R. (2001). Increased sedimentation rates and grain sizes 2–4 Myr ago due to the influence of climate change on erosion rates. *Nature*, *410*(6831), 891–897. https://doi.org/10.1038/35073504

Pomazkov, K. D. (1971). *Geological map of the USSR of 1:200,000 scales: Northern Tien-Shan series. Sheet K-43-XVII*. Russian Geological Research Institute. (VSEGEI).

Selander, J., Oskin, M., Ormukov, C., & Abdrakhmatov, K. (2012). Inherited strike-slip faults as an origin for basement-cored uplifts: Example of the Kungey and Zailiskey ranges, northern Tian Shan. *Tectonics*, *31*(4). https://doi.org/10.1029/2011tc003002

Sobel, E. R., & Arnaud, N. (2000). Cretaceous–Paleogene basaltic rocks of the Tuyon basin, NW China and the Kyrgyz Tian Shan: The trace of a small plume. *Lithos*, *50*(1–3), 191–215. https://doi.org/10.1016/s0024-4937(99)00046-8

Sobel, E. R., & Dumitru, T. A. (1997). Thrusting and exhumation around the margins of the western Tarim basin during the India-Asia collision. *Journal of Geophysical Research*, *102*(B3), 5043–5063. https://doi.org/10.1029/96jb03267

Tadono, T., Takaku, J., Tsutsui, K., Oda, F., & Nagai, H. (2015). Status of "ALOS World 3D (AW3D)" global DSM generation. In *2015 IEEE international geoscience and remote sensing symposium (IGARSS)* (pp. 3822–3825).

Tauxe, L. (2010). *Essentials of paleomagnetism*. University of California Press. 489 pp.

Turchinskiy, V. P. (1970). *Geological map of the USSR of 1:200 000 scales: Northern Tien Shan series. Sheet K-43-XVIII*. Moscow, Russia: Russian Geological Research Institute (VSEGEI), Nedra.

Wack, M. R., & Gilder, S. A. (2012). The SushiBar: An automated system for paleomagnetic investigations. *Geochemistry, Geophysics, Geosystems*, *13*(3), a. https://doi.org/10.1029/2011gc003985

Wack, M. R., Gilder, S. A., Macaulay, E. A., Sobel, E. R., Charreau, J., & Mikolaichuk, A. (2014). Cenozoic magnetostratigraphy and magnetic properties of the southern Issyk-Kul basin, Kyrgyzstan. *Tectonophysics*, *629*, 14–26. https://doi.org/10.1016/j.tecto.2014.03.030

Watson, G. S., & Enkin, R. J. (1993). The fold test in paleomagnetism as a parameter estimation problem. *Geophysical Research Letters*, *20*(19), 2135–2137. https://doi.org/10.1029/93gl01901

Zachos, J., Pagani, M., Sloan, L., Thomas, E., & Billups, K. (2001). Trends, rhythms, and aberrations in global climate 65 Ma to present. *Science*, *292*(5517), 686–693. https://doi.org/10.1126/science.1059412

Zhao, X., Zhang, H., Lv, H., Lü, Y., Li, X., Liu, K., et al. (2020). Signatures of tectonic-climatic interaction during the Late Cenozoic orogenesis along the northern Chinese Tian Shan. *Basin Research*, *33*(1), 291–311. https://doi.org/10.1111/bre.12466

Zhou, Y., Wu, C., Yuan, B., Wang, J., Zhou, T., Wang, Y., & Tang, X. (2020). Cenozoic tectonic patterns and their controls on growth strata in the northern Tianshan fold and thrust belt, northwest China. *Journal of Asian Earth Sciences*, *198*. https://doi.org/10.1016/j.jseaes.2020.104237

Zubovich, A. V., Wang, X., Scherba, Y. G., Schelochkov, G. G., Reilinger, R., Reigber, C., et al. (2010). GPS velocity field for the Tien Shan and surrounding regions. *Tectonics*, *29*(6). TC6014. https://doi.org/10.1029/2010tc002772

Chapter IV

Greigite (Fe_3S_4) formation in artificial sediments via solid-state transformation of lepidocrocite

Manuscript accepted for publication in Geochemistry, Geophysics, Geosystems

Reference

Roud, S.C., Gilder, S. A. and Park S. (2022). (in press) Greigite (Fe_3S_4) formation in artificial sediments via solid-state transformation of lepidocrocite. Geochemistry, Geophysics, Geosystems.

https://doi.org/10.1029/2022GC010376

Contributions

I designed the study, carried out all magnetic measurements and SEM imaging, analyzed and interpreted the data, and wrote the manuscript.

Key Points

- We present a new method to grow greigite in aqueous sediments and create a chemical remanent magnetization under controlled conditions
- Greigite grain sizes of 20-50 nm span the superparamagnetic to single domain threshold, consistent with theoretical predictions
- Our experimental hysteresis data coincide with calculated mixing curves allowing better quantification of greigite particle sizes in nature

Abstract

Greigite (Fe_3S_4) is a ferrimagnetic iron-sulfide mineral that forms in sediments during diagenesis. Greigite growth can occur diachronously within a stratigraphic profile, complicating or overprinting environmental and paleomagnetic records. An important objective for paleo- and rock-magnetic studies is to identify the presence of greigite and to discern its formation conditions. Greigite detection remains, however, challenging and its magnetic properties obscure due to the lack of pure, stable material of well-defined grain size. To overcome these limitations, we report a new method to selectively transform lepidocrocite to greigite via the intermediate phase mackinawite (FeS). In-situ magnetic characterization was performed on discrete samples with different sediment substrates. Susceptibility and chemical remanent magnetization increased proportionally over time, defining two distinct greigite growth regimes. Temperature dependent and constant initial growth rates indicate a solid-state FeS to greigite transformation with an activation energy

of 78-90 kJ/mol. Low and room temperature magnetic remanence and coercivity ratios match with calculated mixing curves for superparamagnetic (SP) and single domain (SD) greigite and suggest ~25% and ~50% SD proportions at 300 K and 100 K, respectively. The trend coincides with empirical data reported for natural greigite-bearing sediments, suggesting a common SP endmember size of 5-10 nm that is likely inherited from mackinawite crystallites. The average particle size of 20-50 nm determined by X-ray powder diffraction and electron microscopy accords with theoretical predictions of the SP/SD threshold size in greigite. The method constitutes a novel approach to synthesize greigite and to investigate its formation in sediments.

Plain Language Summary

Sediments provide continuous records of Earth's ancient magnetic field, which lend insights into the workings of the geodynamo and help to establish the geologic time scale through global magnetostratigraphic correlation. Greigite is a magnetic iron sulfide mineral that commonly forms after deposition, thereby remagnetizing the sediment and complicating interpretation of the magnetic record. Understanding greigite formation and detecting its presence is fundamental for obtaining reliable records of the paleomagnetic field, yet knowledge of how greigite grows and how its magnetic properties evolve during growth remains limited. This article outlines a novel approach to form greigite in sediments and to monitor its growth kinetics, grain size and magnetic remanence acquisition. The magnetic properties of the synthetic sediments resemble those of natural greigite-bearing sediments and match well with theoretical calculations, which can help quantify grain sizes in sedimentary greigite. The reported method and our results contribute to a better understanding of greigite formation and chemical magnetic remanence acquisition in sediments.

1. Introduction

Greigite, the sulfide analog of magnetite, is a common authigenic magnetic mineral that forms at the expense of existing iron-rich mineral phases during diagenetic processes in sediments. Formation of greigite is of interest for paleomagnetic studies, because it can lead to a secondary chemical remanent magnetization (CRM) that is younger than the stratigraphic age of the sediment and can bias or overprint the primary paleomagnetic record (Hallam and Maher, 1994; Jiang et al., 2001; Roberts et al., 2005; Sagnotti et al., 2005; Rowan and Roberts, 2006; Larrasoaña et al., 2007; Ron et al., 2007; Just et al., 2019; Nowaczyk et al., 2020). Multiple generations of greigite can grow at any time after deposition if favorable conditions exist in a sediment (Roberts and Weaver, 2005). Understanding, greigite formation conditions, its magnetic properties and the characteristics of a CRM are crucial for paleomagnetic studies to determine whether the magnetic remanence is primary, secondary or a mix of the two.

Aside from remagnetizing sediments, greigite is relevant as a potential catalyst for the emergence of life (White et al., 2015) and plays a role in geochemical sulfur and iron cycles as an intermediate phase in the pyritization process (Hunger and Benning, 2007). Greigite is, however, not a necessary precursor of pyrite (FeS_2), as originally proposed (Schoonen, 2004) and its preservation is now thought to inhibit pyrite formation. Greigite formation requires preexisting mackinawite (FeS), which oxidizes to Fe_3S_4 in a solid-state transformation, whereas pyrite forms from dissolved sulfide species (Rickard, 2012). Compared to pyrite, natural greigite concentrations are typically low and the conditions under which it accumulates in sediments are not fully understood. One factor for the limited understanding of natural greigite abundances is the lack of analytical geochemical techniques to identify and quantify the mineral in the bulk sediment. This arises from its low concentrations and because it is geochemically indistinguishable from similarly reactive sulfide compounds that are part of the acid volatile sulfide fraction, such as nanoparticulate pyrite and mackinawite.

Rock magnetic methods are ideal for characterizing small, dilute concentrations of magnetic minerals like greigite. Authigenic greigite can exhibit magnetic characteristics such as gyroremanence, multiaxial crystalline anisotropy, and strong magnetostatic interactions, which facilitate its identification, especially in the single domain (SD) state. Reliably detecting its presence and distinguishing greigite from other magnetic minerals remains challenging because proxy-parameters are often non-unique and depend on factors such as magnetic domain state, metal substitution and magnetic interactions, so that the ranges of possible

values overlap, particularly between greigite and magnetite (Roberts et al., 2011a). Our understanding of the magnetic properties of greigite remains incomplete; obstacles are a scarcity of pure, well characterized reference material and that greigite readily oxidizes under typical laboratory conditions. Moreover, it is still elusive how greigite acquires a CRM in sediments because the process has not been recreated nor investigated under controlled laboratory conditions.

To overcome these limitations, we report a novel method to synthesize greigite in sediments by a two-step transformation of lepidocrocite via the intermediate phase FeS. Greigite growth and CRM acquisition are monitored during the FeS to greigite transformation using bulk magnetic remanence and susceptibility measurements. Based on magnetic measurements, scanning electron microscopy (SEM) observations and X-ray powder diffraction (XRD) analysis we characterize the transformation process including the growth rate, evolution of mineral phases, and their average grain sizes. The Magnetic domain state, grain size and SD proportions of the synthetic greigite are determined using low and room temperature magnetic measurements, which we compare to theoretical models and empirical data for natural sedimentary greigite distributions. The objectives of this study are to document the growth process of greigite and especially the evolution in magnetic properties during its growth; remanence-related aspects will be treated separately.

2. Greigite synthesis and experimental setup

2.1. Synthesis

Synthetic greigite samples (45 in total) were prepared by a two-step transformation of lepidocrocite. Our synthesis method partially follows the solid-gas transformation of Fe-oxides by Igarashi et al. (2016) and uses the "iron sulfide switch" of Rickard et al. (2001) for preferential transformation of FeS to greigite under controlled aqueous conditions. All reactions were performed in crimp-sealed, 10 ml glass vials (Ø22 x 40 mm) prepared under argon atmosphere within a glovebox.

2.1.1. Dry sulfidation of lepidocrocite (Step I)

Synthetic lepidocrocite (γ–FeOOH, grain size < 200 nm, Bayferrox® 943) was sulfidized by exposure to hydrogen sulfide gas. To achieve this, 22 mg (0.25 mmol) of dry, nanocrystalline γ–FeOOH powder was placed into sample vials together with a quartz glass tube containing 0.5 ml of 1M Na_2S. After the vials were sealed with rubber stoppers, 0.5 ml of 2M HCl were

injected into the tubes, neutralizing the Na_2S solution and releasing H_2S gas. This led to an immediate blackening (sulfidation) of the initially yellow lepidocrocite powder. The concentration of reactants was chosen to produce an excess of sulfide (0.5 mmol) over iron (0.25 mmol). After aging the samples in a H_2S atmosphere at room temperature for 15 h, the vials were briefly opened inside the glove box to remove the quartz glass tube and weigh the transformation product.

2.1.2. Aging in aqueous solution (Step II)

The aging solution was prepared in 250 ml glass bottles from degassed, demineralized water supplemented with resazurin as a redox indicator. The redox potential was poised below E_h = -51 mV (as indicated by the reduction of blue resazurin to purple resorufin) by adding sodium sulfide (Na_2S) to a final concentration of 20 mM, which resulted in a dissolved sulfide amount of 0.1 mmol per 5 ml sample. Formaldehyde (HCHO) was added to a concentration of 50 mM to promote greigite and inhibit pyrite formation in the sulfidic solution (Rickard et al., 2001). The pH was adjusted to 5.5 with HCl.

Freshly prepared reaction products from Step I were either directly suspended in 5 ml aging solution or initially dispersed in a non-magnetic silica substrate and then suspended in the aging solution. For the latter, two grain sizes were used: either 5 g of 100-400 µm quartz sand (Carl Roth GmbH) or 3 g of 2-40 µm SiO_2 powder (Alfa Aesar), respectively, that are referred to as sand and silt. After mixing and settling overnight, matrix-bearing samples had a sediment volume of 3 cm^3. Based on the bulk and grain densities, ρ (ρ_{sand} = 1.67 g/cm^3, ρ_{silt} = 1.00 g/cm^3 and ρ_{silica} = 2.65 g/cm^3), porosities of 37% and 67% were estimated for the sand and silt samples, respectively. In silt samples the Fe-fraction and matrix grains formed a homogenous sediment slurry, whereas in sand samples most of the Fe-fraction deposited on top of sand grains.

The vials were placed in a non-magnetic incubator at 75°C that was housed in Helmholtz coils to control the strength and direction of the magnetic field during aging. The incubator consisted of a thermally insulated aluminum block with cavities that accommodated 16 vials. Temperature was monitored with a thermometer placed inside one dedicated vial. The setup provided uniform magnetic field and temperature conditions in which the samples reached the set temperature within a few minutes. Three separate experiments were carried out in magnetic field strengths of 100 µT, 50 µT, and 25 µT (batch #100, #50, and #25) with a constant field direction of declination, D = 0° and inclination, I = 45°. Each experiment

consisted of 15 vials: seven with a sand matrix, seven with a silt matrix and one without matrix (Table 1).

2.2. Analytical Methods

Powder X-ray diffraction (XRD) was performed with a STOE diffractometer (STADI P) with Mo-$K_{\alpha 1}$ radiation (wavelength = 0.7093 Å; Ge[111] monochromator). Wet synthesis products were freeze-dried and sealed between layers of Kapton tape under argon atmosphere to prevent oxidation. Phase identification of the XRD data was based on the Crystallography Open Database (Gražulis et al., 2012) using the Match! v3.11 software package (Crystal Impact).

Table 1. Mass balance for Step I, the anhydrous transformation of lepidocrocite (γ–FeOOH) to FeS+H_2O (Product I), together with aging conditions and magnetic susceptibility data for Step II, the transformation of Product I to greigite and mackinawite (Product II).

		Step I		**Step II**					
		Reactant	**Product I**	**Substrate**		**Aging conditions**		**Product II**	
Sample ID	**n**	γ–FeOOH (mg)	FeS+H_2O (mg)	V (cm^3)	Grain size	t (h)	B_0 (μT)	κ_{lf} (1E-5)	κ_{fd} (%)
#100-03 to #100-09	7	22	29.8 (1.7)	3	sand	7	100	105.8 (4.9)*	7.5 (0.7)*
#100-10 to #100-16	7	22	30.3 (1)	3	silt	7	100	103.4 (6.2)*	7.4 (0.5)*
#100-02	1	22	30.3	-	-	7	100	99.1	6.5
#50-17 to #50-23	7	22	29.8 (1.2)	3	sand	6	50	99.0 (6.5)	7.7 (0.7)
#50-24 to #50-30	7	22	31 (1.2)	3	silt	6	50	88.5 (8.1)	7.6 (1.3)
#50-31	1	22	32.3	-	-	6	50	107.9	7.8
#25-33 to #25-39	7	22	30 (0.7)*	3	sand	7.5	25	122.4 (13.0)	7.1 (0.5)
#25-41 to #25-47	7	22	30.1 (0.3)*	3	silt	7.5	25	110.6 (6.2)	7 .0 (0.4)
#25-48	1	22	30	-	-	7.5	25	136.8	6.1

Mean values and standard deviation (in parentheses) of sample masses, low frequency bulk susceptibility (κ_{lf}) and frequency-dependent susceptibility (κ_{fd}) for groups of equally treated samples; n = 7 unless otherwise stated; * indicates n = 6. #100, #50, and #25 in the sample IDs indicate the applied magnetic field value in μT for the sample batch.

Secondary electron and backscattered electron images were acquired using a Hitachi SU5000 field emission scanning electron microscope (SEM) operating at 10 kV. SEM samples were prepared in an argon atmosphere from the same bulk materials used for X-ray diffraction analysis; dry powder was placed on carbon pads and was carbon coated (8 nm-thick). Particle sizes were determined from 12.5 μm² images using the software ImageJ (Schneider et al., 2012). The particle area, A was measured at 50,000-fold magnification; the average grain diameter, d was estimated as assuming a circular footprint.

Room temperature magnetic susceptibility, κ, was measured before and after 75°C aging with a MS2B Bartington Instruments susceptibility meter at two frequencies (low-frequency,

lf = 465 Hz and high-frequency, hf = 4650 Hz) to calculate the frequency-dependence of susceptibility. Low-frequency susceptibility was monitored in 20 min intervals during the heating experiment on a subset of four samples. For these four, the vials were briefly removed from the heat and immediately measured without cooling to room temperature (measurement temperature 50-70°C). The remanent magnetization was measured on the same subset of samples in 1-2 h intervals during the aging process using a vertical 2G Enterprises Inc., three axis, superconducting magnetometer housed in a magnetically shielded room (residual field <500 nT). Each of the four sample vials was measured in two positions using a custom, manual sample handler and then returned to the aging set-up within minutes. The manual hander allowed careful lowering of the vials into the magnetometer and to rotate them about a vertical axis between consecutive measurements with minimal disturbance of the sediment slurry.

Hysteresis loops, backfield demagnetization, and first-order reversal curves (FORCs) were measured with a Princeton Measurements Corporation vibrating sample magnetometer (VSM) at both 300 K and 100 K in a nitrogen atmosphere. To monitor magnetic properties during progressive sample oxidation, a series of 20 room temperature FORCs was measured in air (sample #100-10) over 12 h. VSM sub-samples were prepared in an argon atmosphere from freeze-dried bulk materials; dry sand and silt samples (#100-03 and #100-10) were pressed into gel caps and pure sulfide powder (#50-31) was fixed with Kapton tape. Saturation fields of 300 mT were used for all experiments. FORC settings were optimized for short measurement times to minimize drift and sample oxidation (B_u = -50/+30 mT, B_c = 0-100 mT, B_{sat} = 300 mT, 1 or 2 mT increment [N = 93 or 173], 150 ms averaging time). FORC data were processed using FORCinel v3.06 (Harrison and Feinberg, 2008) with subtraction of the lower branch of the hysteresis envelop and using VARIFORC smoothing (Egli, 2013). Hysteresis, backfield and FORC measurements were used to calculate the ratio of saturation remanent magnetization over saturation magnetization M_{rs}/M_s and the coercivity of remanence over coercivity B_{cr}/B_c as proxies for magnetic domain state.

Day plot (Day et al., 1977) mixing curves for SD and superparamagnetic (SP) greigite were calculated following Dunlop (2002, eq. 5-6) with $M_{rs}/M_s = f_{SD}(M_{rs}/M_s)_{SD}$ and $B_{cr}/B_c = (B_{cr})_{SD}/(B_c)_{SD}[f_{SD}\chi_{SD}/(f_{SD}\chi_{SD} + f_{SP}\chi_{SP})]$ using greigite room temperature SD endmember values of $(M_{rs}/M_s)_{SD}$ = 0.866 (Winklhofer et al., 2014), $(B_{cr})_{SD}$ = 90 mT and $(B_c)_{SD}$ = 75 mT (Chang et al., 2009, Fig. 1). M_s = 272 kA/m (Li et al., 2014) applies to the greigite SD and SP state, while B_{cr}, B_c and M_{rs} are zero for SP grains. f_{SD} and f_{SP} are the fractions of SD and SP grains, respectively,

and χ_{SD} and χ_{SP} are the respective initial susceptibilities, where $\chi_{SD} = (M_{rs})_{SD}/(B_c)_{SD}$. $\chi_{SP} = \mu_0 V M_s^2/3k_bT$, where μ_0 is vacuum permeability, and k_b the Boltzmann constant, was calculated for temperature, T = 300 K and volume, V for cubic grains of diameters, d = 5 nm and 10 nm.

3. Results

3.1. Transformation reactions and material characterization

3.1.1. Starting material

XRD data confirm that the starting material consisted mainly of nano-crystalline lepidocrocite with minor goethite impurities (α–FeOOH, strongest peak at 2θ = 9.6°, Fig. 1a). An average crystallite size of 60 nm was estimated from the full width at half maximum (FWHM) of lepidocrocite reflections (2θ = 6-20°) using the Scherrer equation (Scherrer, 1912). SEM images of the synthetic lepidocrocite sample contain elongated platelets of crystalline aggregates with an average size of 110±37 nm (N = 50 grains) (Fig. 1b).

3.1.2. Transformation Step I

Exposing lepidocrocite to H_2S gas at room temperature led to a blackening of the initially yellow powder, which is indicative of sulfidation. Like the starting material, the black transformation product after 15 h was not attracted to a neodymium magnet and the magnetic susceptibility was below detection limits (within $\pm 1\times10^{-5}$ SI), which indicates transformation to a non-magnetic Fe-sulfide. The average sample weight increased by 8±1 mg (± single standard deviation) after the transformation (N = 45). If that sulfidation caused the weight increase, this suggests an added sulfur amount of 0.25 mmol per sample, i.e. the addition of one mole of sulfur per mole of FeOOH. XRD data for the transformation product lack well-defined diffraction-peaks (Fig. 1a, middle row), which points to a complete transformation of the Fe-oxyhydroxide to an X-ray amorphous phase. SEM images of the transformation product indicate agglomerates of platy, 100-200 nm particles, slightly larger and more rounded than the starting material (Fig. 1b). Image analysis indicates an average grain diameter of 155±43 nm (N = 50 grains).

3.1.3. Transformation Step II

After the dry black transformation product of Step I was suspended in the aging solution, the initially pink solution became transparent over time, indicating a reduction of resorufin and concomitant lowering of the redox potential to below E_h = -110 mV. In samples where the black powder was in direct contact with the solution (samples without matrix and with sand

matrix), the pink color began fading immediately and the solution turned transparent within 1 h. In silt samples, where the black powder was embedded in the silica matrix, the color change was noticeably slower (the solution became transparent overnight). This suggests that the initial reaction kinetics depend on the exposure of the Fe-fraction to the aging solution.

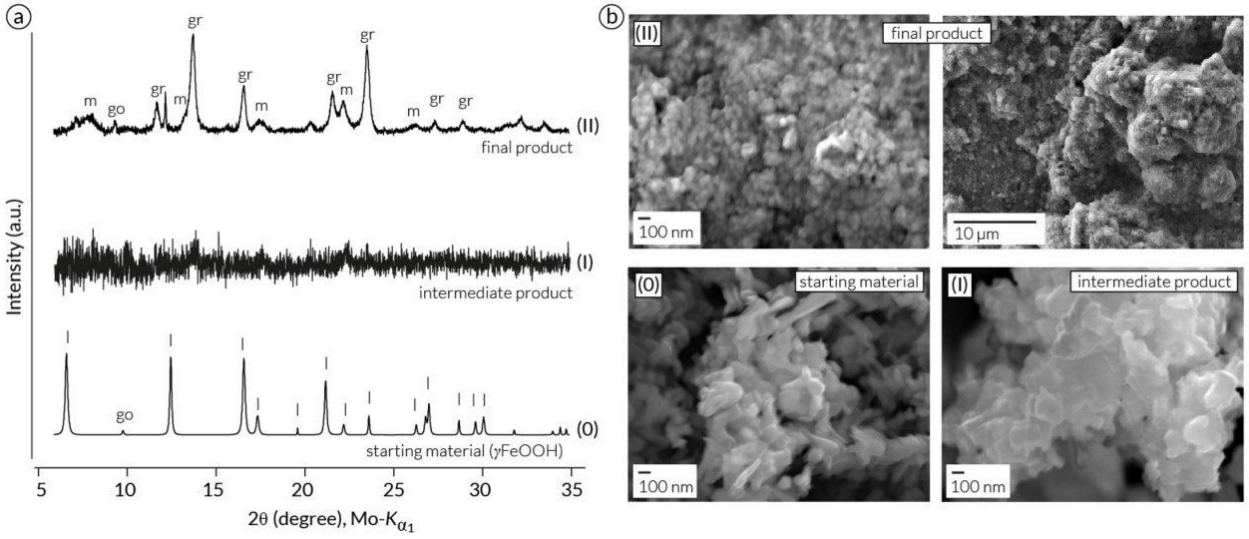

Figure 1. Starting material and transformation products. (a) XRD data and **(b)** SEM images of the starting material γ–FeOOH (0), the intermediate product (Step I) and the final product (Step II). The XRD pattern of the starting material indicates that lepidocrocite (l) is the main phase along with trace amounts of goethite (go). The XRD pattern for the sample from Step II has reflections indicative of greigite (gr) and mackinawite (m) as the main phases.

Approximately 1 h after sample preparation at room temperature, the magnetic susceptibility of all samples from batch #100 increased slightly to 2.4 (±1.0)×10^{-5} (dimensionless SI unit, normalized by the vial volume of 10 cm^3; n = 15). The susceptibility more than doubled to 5.7 (±1.5)×10^{-5} within 15 h aging. In total, 29 of 45 samples had susceptibilities above the noise level after 15 h at room temperature (= 9.2 (±4.6)×10^{-5}, n = 12; = 2.0 (±1.0)×10^{-5}, n = 2). The overall average susceptibility at this stage was 6.9 (±3.8)×10^{-5} with an average frequency dependency of 21±6% (n = 29).

The susceptibility increase during aging experiments at 75°C is shown in Figure 2a for representative sand and silt samples (#100-03, -04, -10 and -11). For all samples, rose immediately upon heating and kept increasing throughout the experiment, reaching a value of 96.6 (±4.8) ×10^{-5} after 6 h. In Figure 2b, normalized and averaged growth curves

demonstrate a consistent time-dependent behavior among the samples (single standard deviation < 4%) with a distinct change in growth rate at 2 h aging time.

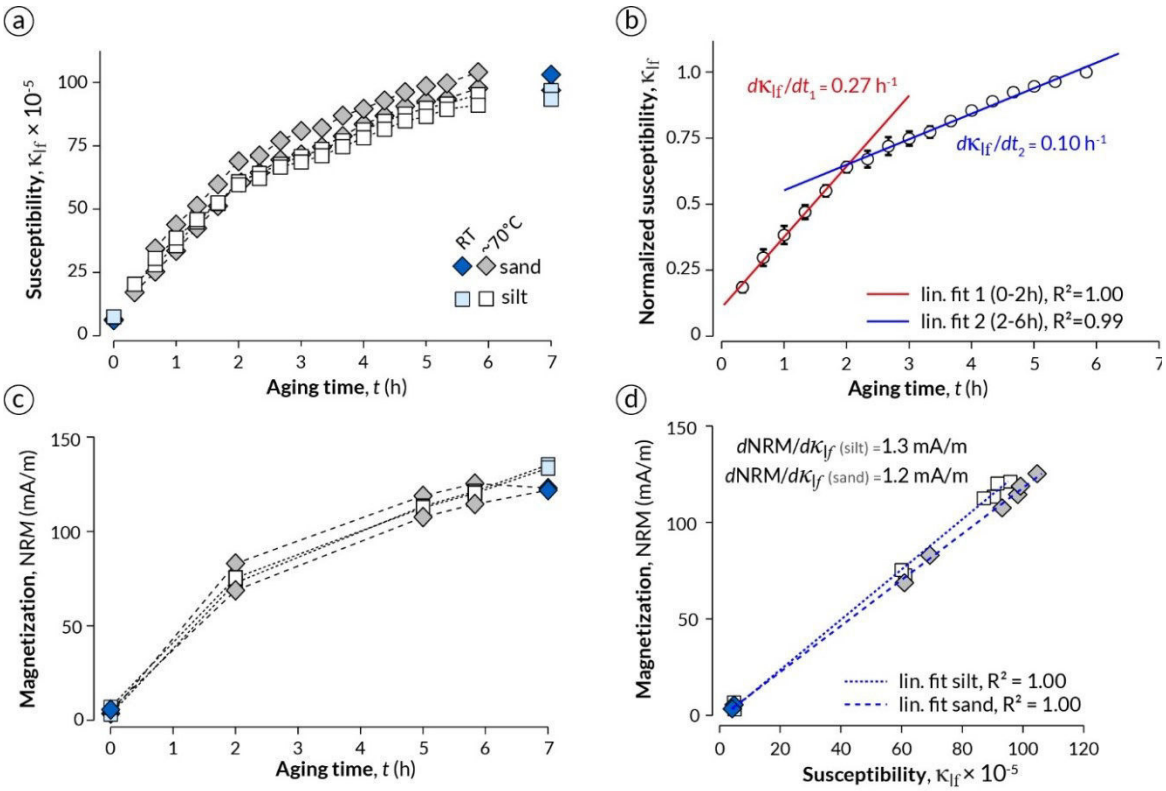

Figure 2. Greigite growth and grain size characterization. (a) Low-frequency magnetic susceptibility against aging time (t, in hours). Measurements during the experiment (gray and open symbols) were performed on samples close to 70°C; the initial and final data points (blue) were measured at room temperature. **(b)** Mean and standard deviation (n = 4) of normalized curves with average susceptibility growth rates . **(c)** Natural remanent magnetization, NRM against aging time (*t*, in hours). **(d)** NRM against demonstrating a linear correlation (R^2 = 1.00) among sand and silt samples. A magnetic field of 100 µT was applied in all cases. Diamonds and squares represent sand (#100-03 and -04) and silt samples (#100-10 and -11), respectively.

Like susceptibility, the natural remanent magnetization (NRM) of the same four samples increased over time, reaching 130 (±10) mA/m (normalized to the vial volume of 10 cm^3) after 7 h (Fig. 2c). The magnetization changed less than 3% after storing the samples in a magnetically shielded room for 12 h and remeasuring the NRM. Magnetization and susceptibility increased linearly with time (Fig. 2d) thereby indicating a high degree of proportionality during greigite growth; NRM/κ_{lf} is 1.3 mA/m for silt samples and 1.2 mA/m for sand samples.

XRD patterns for a sample aged for 6 h at 75°C (sample #50-31 without silica matrix) indicate the presence of nano-crystalline greigite and mackinawite (FeS) with minor contributions of goethite and a hydrous iron sulfate (powder diffraction file 00-009-0006; highest peak at 2θ = 12.13) (Fig. 1a, upper row). Quantitative analysis based on the peak intensities and molecular weight of the two main phases yields mass fractions of 62% Fe_3S_4 and 38% FeS_m. Semi-quantitative analysis of the aging solutions (QUANTOFIX® Iron 100 test swabs) suggests total dissolved iron concentrations >100 mg/l (2 mM) at the end of Step II heating experiments. 100 mg/l was the upper detection limit of the test swabs, which, from the solution volume of 5 ml, is equivalent to 0.5 mg or 4% of the total iron per sample.

From diffraction-peak broadening in sample #50-31, we estimate respective average crystallite sizes of about 20 nm and 10 nm for Fe_3S_4 and FeS. SEM images of the sample (Fig. 1b) taken at the highest possible resolution indicate that individual grains are close to or below the resolution limit and substantially smaller than the lepidocrocite starting material. Image analysis yields an average grain diameter of 51±14 nm (N = 200 grains). However, as smaller grains could not be resolved in detail, the estimate is likely biased toward larger grain sizes. SEM images at lower magnifications indicate that the particles cluster into clumps with sizes up to ~10 µm.

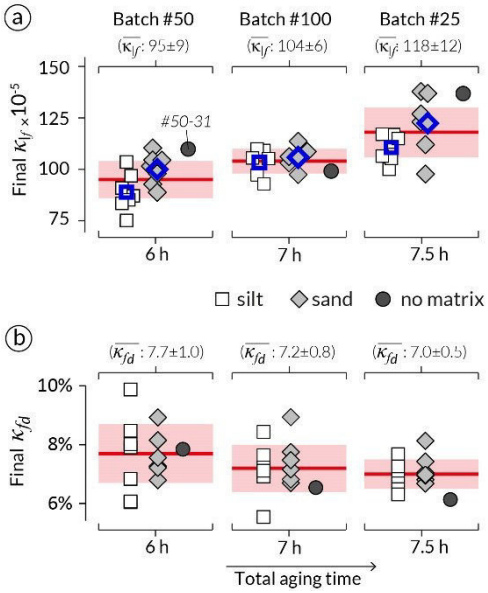

Figure 3. Final bulk susceptibility values. (a) Low frequency susceptibility and **(b)** frequency-dependent susceptibility with respect to the final (75°C) aging time for each batch and grouped by matrix type: sand (□), silt (◇) and no matrix (●). Mean values for and their standard deviations are indicated in red for each batch. Blue symbols in (a) indicate individual group means.

3.2. Final bulk magnetic susceptibility

The final (room temperature) susceptibility averaged 105.6 (±13.8)×10^{-5} with a frequency dependence of 7.3±0.8% (n = 43). The average susceptibility values for different matrix types

are shown in Figure 3. Systematic differences in susceptibility and its frequency dependence among batches correlate with aging time (Pearson correlations: ~ aging time: R = 0.71, p<.001; ~ aging time: R = -0.33, p<.01) but not with the applied magnetic field strength. Samples with sand matrices tended to have higher susceptibilities than those with silt for each batch; however, independent t-tests suggest that the difference is only statistically significant for batch #50 (t[2.4] = 11, p = .02, = 99±7 ×10^{-5}, = 88±9 ×10^{-5}).

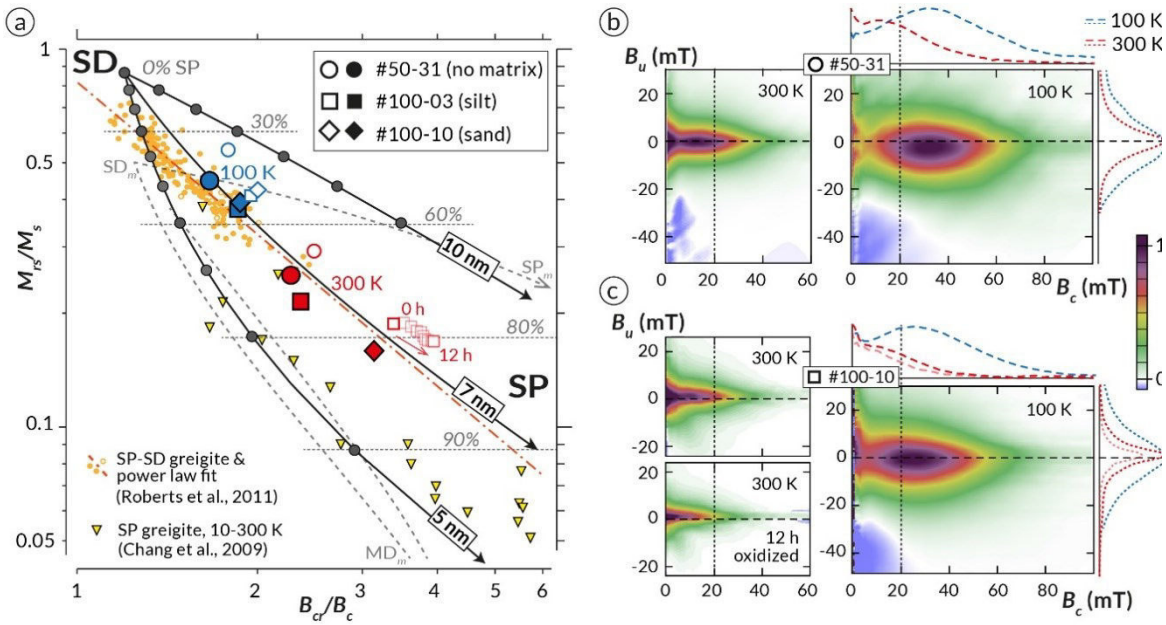

Figure 4. Magnetic properties of representative samples at 300 K and 100 K. (a) Remanence (M_{rs}/M_s) versus coercivity (B_{cr}/B_c) ratios determined from hysteresis and backfield curves (filled symbols) and FORCs (open symbols); pink squares indicate the progressive oxidation in air over ~12 h. Solid black lines represent calculated single domain (SD) and superparamagnetic (SP) mixing curves for greigite (Section 2.2). For reference, the SD to multidomain (MD) and SP(10 nm)-SD mixing curves for uniaxial magnetite (Dunlop, 2002) are shown as gray dashed lines. Yellow symbols indicate data for natural SP-SD greigite-bearing sediments (solid circles), synthetic samples (open circles Dekkers and Schoonen, 1996) and a power law fit (Roberts et al. 2011); yellow triangles represent natural SP greigite measured between 5 and 300 K (Fig. 1 of Chang et al. 2009, samples NR08 and NR27). **(b and c)** FORC diagrams for sample #50-31 (no matrix) and #100-10 (silt matrix) at 300 K (left) and 100 K (right). Colored lines (blue = 100 K, red = 300 K) represent the horizontal and vertical distribution of FORC amplitudes along B_u = 0 mT and B_c = 20 mT, respectively (black dashed lines). Pink dashed lines for sample #100-10 represent measurements after exposing the sample to air for 12 h.

3.3. Magnetic characterization at low and room temperature

To better characterize the magnetic domain state of the material, the remanence and coercivity ratios, M_{rs}/M_s and B_{cr}/B_c, were determined for one sample of each sediment type (#100-03 and #100-10) and a pure sulfide sample (#50-31, which was also analyzed by XRD

and SEM) at 300 and 100 K. The results are shown in Fig. 4a together with theoretical SP-SD mixing lines for greigite that were calculated as described in Section 2.2. Our measured data lie within an envelope confined by SP endmembers of 5 and 10 nm. Their distribution roughly coincides with a 7 nm SP mixing line as well as with an empirical greigite mixing line reported by Roberts et al. (2011). The latter represents a power-law fit to the compiled experimental data from the literature for greigite-bearing sediments (n = 181) and synthetic (n = 9) samples. Hysteresis ratios reported for natural SP greigite between 5-300 K (Chang et al. 2009) have a similar temperature dependency and follow our calculated 5 nm SP mixing line. M_{rs}/M_s ratios for our samples correspond to calculated SP volume fractions of 76±4% (n = 3) at 300 K and are shifted toward the SD endmember with SP proportions of 53±3% (n = 3) at 100 K.

FORC diagrams measured at 300 K (Fig. 4b) contain horizontal signatures with a bimodal coercivity distribution. Peak amplitudes at $B_c = 0$ indicate thermally activated grains close to the SP-SD threshold (Pike et al., 2001). A wider maximum at 12 mT is characteristic of more stable SD grains (coercivity distributions along $B_u = 0$ are shown for 300 and 100 K in Fig. 4b). The vertical spread of the FORC distribution indicates magnetostatic interactions among grains (Pike et al., 1999). The amount of vertical spread is strongest close to the origin and generally scales with the FORC amplitude along the ridge. Room temperature oxidation of the silt sample shifts the FORC distribution toward the origin and reduces the intensity and vertical spread. Remanence and coercivity ratios extracted from the FORC data are comparable to those determined from hysteresis and backfield curves, although values from the FORC data are offset upward and to the right on the Day diagram (Fig. 4a). Day plot ratios for the silt sample left in an open-air atmosphere at 300 K shift progressively toward more SP-like values over time (Fig. 4a).

FORCs at 100 K also have bimodal coercivity distributions with one narrow maximum close to the origin and a broader maximum at 25-30 mT (Bc) (Fig. 4b, right). Lowering the temperature from 300 to 100 K, increases the coercivity. The vertical spread defined by the FWHM (full width at half-maximum) of the vertical FORC distributions at Bc = 20 mT increased from 10 mT at 300 K to 24 mT at 100 K (Fig. 4b), which indicates stronger magnetostatic interactions at 100 K. More negative Bu distributions at 100 K compared to 300 K (shift from 0 to -2 mT in #50-32 and from +2 to 0 mT in #100-10) (Fig. 4b) indicate a change in the mean interaction field (Pike et al., 1999).

4. Discussion

4.1. Greigite formation pathway

Exposing lepidocrocite to H_2S gas during Step I produced a black, non-magnetic, X-ray amorphous material. These characteristics together with an average mass increase of one sulfur equivalent per mol of iron suggests that the iron-oxyhydroxide was reduced and sulfidized by H_2S to X-ray amorphous iron-monosulfide. The absence of well-defined diffraction peaks is common in freshly precipitated FeS and is characteristic of nanocrystalline mackinawite with ~5 nm particle sizes (Ohfuji and Rickard, 2006). In contrast to the apparently minute crystallite size of FeS, SEM images of the material indicate an average particle size of ~150 nm, representing a ~40% increase with respect to the γ–FeOOH stating material. This suggests that the solid-state transformation (i.e. dehydroxylation) led to internal fragmentation of the particles, and that the seemingly larger particles seen in SEM images represent aggregates of smaller FeS regions. Similar observations were reported for the dehydroxylation of lepidocrocite to Fe-oxides by Till et al. (2014).

$$2\mathrm{FeOOH} + 2\mathrm{H_2S} \rightarrow 2\mathrm{FeS} + 2\mathrm{H_2O} + \mathrm{H_2}. \quad (1)$$

Reduction of the aging solution during Step II was coupled to the availability of FeS (the reaction was slower when the sulfide was entirely embedded in the matrix), which points to a reaction that involved FeS oxidation. Presence of dissolved iron in the aging solution at the end of Step II indicates partial dissolution of FeS and Fe release. Both observations are consistent with a solid-state transformation of the precursor FeS via loss of iron, rather than by addition of sulfur (Wilkin and Barnes, 1996) and partial oxidation of Fe^{2+} to form the mixed-valence Fe-sulfide greigite, where two-thirds of the iron is oxidized to Fe^{3+}. Although the electron acceptor (oxidizing agent) remains unclear, the respective mass balance for the transformation of FeS to Fe_3S_4 can be expressed as:

$$4\mathrm{Fe^{2+}S} \xrightarrow{-2e^-} \mathrm{Fe^{2+}}Fe_2^{3+}S_4 + \mathrm{Fe^{2+}}. \quad (2)$$

The released iron fraction is expected to reprecipitate rapidly as FeS in the presence of dissolved sulfide (Rickard, 1995). Buildup of millimolar dissolved iron concentrations in the aging solution could, therefore, suggest that dissolved sulfide was consumed by the end of the experiment. Greigite formation occurred throughout the experiment at constant rates; therefore, H_2S was likely not involved in the oxidation of FeS, at least not in the later stage of the experiments, which may point to the autooxidation of FeS by H_2O. In preliminary experiments, identical to those described above but with pH buffered aging solutions, it was observed that FeS only transformed to a magnetic phase (i.e. greigite) when the solution was

briefly exposed to air or when the dry FeS was exposed to the glovebox atmosphere (0.5-1% O_2) for several minutes. An absence of formaldehyde in the aging solution led, on the other hand, to a magnetic susceptibility decrease after some time, consistent with greigite dissolution and concomitant pyrite formation, as has been reported previously (Rickard et al., 2001; Hunger and Benning, 2007).

Our greigite synthesis method demonstrates that lepidocrocite can be readily sulfidized to greigite by a solid-state transformation via the precursor FeS. A similar solid-state sulfidation of hematite has been reported in methanogen archaea cultures, which produce extracellular bioactive greigite; moreover, equivalent abiotic transformation reactions have been reported for goethite and magnetite (Igarashi et al., 2016). The direct sulfidation of various Fe-(oxyhydr)oxide without prior dissolution of the precursor could represent a relevant process for greigite formation in nature when dissolved sulfide concentrations are low.

Exposing lepidocrocite to H_2S gas during Step I produced a black, non-magnetic, X-ray amorphous material. These characteristics together with an average mass increase of one sulfur equivalent per mol of iron suggests that the iron-oxyhydroxide was reduced and sulfidized by H_2S to X-ray amorphous iron-monosulfide. The absence of well-defined diffraction peaks is common in freshly precipitated FeS and is characteristic of nanocrystalline mackinawite with ~5 nm particle sizes (Ohfuji and Rickard, 2006). In contrast to the apparently minute crystallite size of FeS, SEM images of the material indicate an average particle size of ~150 nm, representing a ~40% increase with respect to the γ–FeOOH stating material. This suggests that the solid-state transformation (i.e. dehydroxylation) led to internal fragmentation of the particles, and that the seemingly larger particles seen in SEM images represent aggregates of smaller FeS regions. Similar observations were reported for the dehydroxylation of lepidocrocite to Fe-oxides by Till et al. (2014).

$$2\mathrm{FeOOH} + 2\mathrm{H_2S} \rightarrow 2\mathrm{FeS} + 2\mathrm{H_2O} + \mathrm{H_2}. \quad (1)$$

Reduction of the aging solution during Step II was coupled to the availability of FeS (the reaction was slower when the sulfide was entirely embedded in the matrix), which points to a reaction that involved FeS oxidation. Presence of dissolved iron in the aging solution at the end of Step II indicates partial dissolution of FeS and Fe release. Both observations are consistent with a solid-state transformation of the precursor FeS via loss of iron, rather than by addition of sulfur (Wilkin and Barnes, 1996) and partial oxidation of Fe^{2+} to form the mixed-valence Fe-sulfide greigite, where two-thirds of the iron is oxidized to Fe^{3+}. Although the

electron acceptor (oxidizing agent) remains unclear, the respective mass balance for the transformation of FeS to Fe_3S_4 can be expressed as:

$$4\mathrm{Fe}^{2+}\mathrm{S} \xrightarrow{-2\mathrm{e}^-} \mathrm{Fe}^{2+}Fe_2^{3+}S_4 + \mathrm{Fe}^{2+}. \quad (2)$$

The released iron fraction is expected to reprecipitate rapidly as FeS in the presence of dissolved sulfide (Rickard, 1995). Buildup of millimolar dissolved iron concentrations in the aging solution could, therefore, suggest that dissolved sulfide was consumed by the end of the experiment. Greigite formation occurred throughout the experiment at constant rates; therefore, H_2S was likely not involved in the oxidation of FeS, at least not in the later stage of the experiments, which may point to the autooxidation of FeS by H_2O. In preliminary experiments, identical to those described above but with pH buffered aging solutions, it was observed that FeS only transformed to a magnetic phase (i.e. greigite) when the solution was briefly exposed to air or when the dry FeS was exposed to the glovebox atmosphere (0.5-1% O_2) for several minutes. An absence of formaldehyde in the aging solution led, on the other hand, to a magnetic susceptibility decrease after some time, consistent with greigite dissolution and concomitant pyrite formation, as has been reported previously (Rickard et al., 2001; Hunger and Benning, 2007).

Our greigite synthesis method demonstrates that lepidocrocite can be readily sulfidized to greigite by a solid-state transformation via the precursor FeS. A similar solid-state sulfidation of hematite has been reported in methanogen archaea cultures, which produce extracellular bioactive greigite; moreover, equivalent abiotic transformation reactions have been reported for goethite and magnetite (Igarashi et al., 2016). The direct sulfidation of various Fe-(oxyhydr)oxide without prior dissolution of the precursor could represent a relevant process for greigite formation in nature when dissolved sulfide concentrations are low.

4.2. Final greigite concentration

Magnetic susceptibility reflects the total greigite concentration in our samples given that the susceptibilities of FeS and the silica matrix are negligible with respect to greigite. Comparable final susceptibilities (Fig. 3), therefore, demonstrate that the experiments consistently facilitated greigite formation and a reproducible greigite yield, independent of the preparation method (with or without matrix). The final greigite concentration was also independent of the applied (Earth-like) magnetic field strength. Studies of hematite precipitated from ferric solutions or formed by aging ferrihydrite reported a correlation with applied magnetic field intensity (Stokking and Tauxe, 1990; Jiang et al., 2016), whereas no

field dependency was reported for magnetite formation by the aging of green rust (Pick and Tauxe, 1991).

XRD analysis indicates that the crystalline solid phase of sample #100-31 consists of 62 wt% Fe_3S_4 and 38 wt% FeS (66 and 34 vol%, respectively). From the Fe_3S_4 weight fraction, equation (2) and the initial FeS budget of 0.25 mmol per sample, a greigite mass of 13 mg is estimated for sample #100-31. The susceptibility of this sample (107.9×10^{-5}) is close to the overall mean of 105.6 (±13.8)$\times10^{-5}$ (Fig. 3a), so it is assumed that its greigite yield is representative of the entire sample set. Considering that the relative standard deviation of magnetic susceptibility is 13%, the average greigite mass in our samples is 13±2 mg. For samples with a sediment matrix this converts to a greigite concentration of 1.1±0.2‰ and a SD greigite concentration of 0.26±0.4‰ based on the SD proportion from the Day plot (Fig. 4a). The fraction of SD greigite relative to the total sulfide concentration is estimated to 16±3 vol% at 300 K and 31±2 vol% at 100 K.

4.3. Greigite growth rate

The observed reduction of the aging solution, together with a 60% susceptibility increase after the initial 15 h aging phase at room temperature, suggests that greigite formation began as soon as FeS was submerged in the solution. Relative to the final susceptibility after the heating experiments, the susceptibility of batch #100 samples increased by 3.2 (±1.1)% between 1 h and 15 h of aging at room temperature, which can be expressed as a relative greigite growth rate of 2.3 (±0.8)$\times10^{-3}$ h^{-1}.

The temporal evolution of susceptibility in the 75°C aging experiment (Fig. 2a) has two distinct stages with a change in slope (i.e. growth rate) at 2 h. From the nearly linear slopes of the two segments, we determined relative greigite growth rates of 0.27 h^{-1} and 0.09 h^{-1} for regimes 1 and 2, respectively (Fig. 2b). Linear growth rates in both stages suggest that greigite formation did not depend on the concentration of a reactant, consistent with a solid-state transformation process and with reported FeS to greigite transformation kinetics at aging temperatures above 125°C (Hunger and Benning, 2007). In their 125°C experiments, Hunger and Benning (2007) reported a single constant greigite growth rate; however, greigite converted to pyrite shortly after its formation, which may explain why a second, slower growth period was not observed. The marked (factor of 3) rate change in our experiments could point to two distinct formation pathways or oxidizing agents, possibly related to H_2S depletion or increased FeS crystallinity. A decrease in susceptibility and NRM growth rate

may also be related to enhanced magnetostatic interactions between greigite particles, since interactions that increase with particle concentration can influence weak field magnetization processes (Muxworthy, 2001; Egli, 2006).

The room temperature growth rate was two orders of magnitude slower than the initial growth rate at 75°C. Following Hunger and Benning (2007), the initial greigite growth rates, k^{+}_{grei} determined at 25°C and 75°C were used to estimate the activation energy, E_a for the mackinawite to greigite transformation from the slope of $\ln(k^{+}_{grei})$ against $1/T$, which yields $-E_a/R$, where R is the ideal gas constant. Considering the 35% relative standard deviation of the room temperature growth rate, our E_a estimates range from 78 to 90 kJ/mol. The lower limit is in good agreement with 67.5±10.6 kJ/mol as determined from the mackinawite destruction rate, k^{-}_{mack} between 100-200°C (Fig. 4a of Hunger and Benning, 2007). Agreement between mackinawite destruction and greigite growth kinetics is expected, given a solid-state transformation between the two mineral phases. The relative growth rates and activation energy interpreted from magnetic susceptibility, thus, lie within uncertainty of those determined by XRD analyses (Hunger and Benning, 2007).

4.4. Greigite grain size

Average crystallite sizes determined by XRD of ~20 nm for greigite and ~10 nm for mackinawite should be considered lower limits for the physical grain size because crystallite size is equal to or smaller than particle size. Minimum sizes of 10 and 20 nm accord with the average sulfide particle size of ~50 nm that was determined from SEM image analysis. The average grain size of our greigite samples, therefore, lies between 20 and 50 nm. The Fe-sulfide particle size is significantly smaller compared to the lepidocrocite starting material, for which XRD and SEM analyses yield average sizes of ~60 nm and ~100 nm, respectively. A smaller size of the sulfide grains is consistent with internal fracturing of lepidocrocite during the initial dihydroxylation and transformation to FeS.

Greigite grain size can be deduced indirectly from magnetic properties, which depend on magnetic domain state. Magnetic particles are in the SP state when they are too small to hold a stable magnetic remanence. Theoretical threshold sizes between the SP and SD states (relaxation time > 1 min at room temperature) for greigite have been estimated to ~20 nm for interacting grain ensembles (chains of aligned, touching grains) and to ~40 nm for non-interacting ensembles (Muxworthy, 2003; Winklhofer et al., 2014; Valdez-Grijalva et al., 2018). With an average grain size between 20-50 nm, our samples are expected to encompass

the SP/SD threshold, which is universally supported by their magnetic properties (Figs. 2-4). For example, continuous acquisition of remanent magnetization during greigite growth in an applied magnetic field (Fig. 2c) demonstrates the presence of stable SD grains, while the frequency dependence of susceptibility (Fig. 3b) indicates that part of the greigite population is in the SP state.

SP grains, detected by bulk susceptibility measured at two frequencies (465 and 4650 Hz) have relaxation times of 0.2-2 ms. The proportion of this SP fraction relative to larger grains (with longer relaxation times) decreased from ~20% when grown at room temperature to 7% upon completion of the 75°C aging experiments (Fig. 3b). This suggests that the grain size increased over time and/or that the growth temperature influenced the final grain size. Also an increase in magnetostatic interactions, as greigite concentration increased over time, may have contributed to lowering κ_{fd} (Muxworthy, 2001). Frequency-dependent susceptibility was not measured during the 75°C experiments; however, final κ_{fd} values for the three batches correlate with total aging time (Fig. 3b). Differences between the means are small (0.7% between 6 and 7.5 h) and are not statistically significant at the 0.05 level. A relative change of SP contributions over time is also expected to affect the NRM/susceptibility ratio. Consistent with the proportional increase of the two parameters over time (Fig. 2d), the average NRM/κ_{lf} ratio was constant within one standard deviation between 2 and 6 h aging time (NRM/κ_{lf} after 2 h was 1.21×10^{-8} (±4%) A/m and 1.25×10^{-8} (±5%) A/m after 6 h). These observations suggest that the SP to SD ratio, and thus the average greigite particle size, did not change substantially during the 75°C aging experiments. Differences in SP contributions before and after the 75°C experiments were, therefore, restricted to the earliest growth phase and are possibly related to growth temperature.

4.5. Domain state and SD threshold size

FORC and hysteresis properties determined at ambient and low temperatures help to further characterize the domain state and SP/SD threshold size of our samples. Room temperature FORC diagrams are dominated by low coercivity horizontal signatures (Fig. 4b) that are characteristic of moderately interacting distributions of thermally activated SD grains close to the SP/SD threshold (Pike et al., 2001; Egli, 2021) and resemble FORC distributions of SP-dominated synthetic and natural greigite bearing samples (Roberts et al., 2006; Rowan and Roberts, 2006). Cooling to 100 K increases the coercivity and vertical spread of the FORC distributions and shifts them to lower B_{u} values, consistent with a decrease in thermal activation and increase in magnetic interactions (Pike et al., 2001). Overall, our 100 K FORC

diagrams resemble those of natural SD greigite-bearing sediments, albeit with lower coercivities (Roberts et al., 2006; 2011). The absence of significant multi- or pseudo single domain (vortex state) signatures in the FORC diagrams indicates that the samples contain mainly SP and SD grains, which makes the calculated SP-SD mixing lines, in Figure 4a applicable to our greigite particle system. This suggests the presence of 70-80% SP contributions at ambient temperature and approximately equal SP and SD contributions at 100 K. Cooling, thus, shifts the SP/SD threshold toward smaller grain sizes (i.e., it brings the greigite particle distribution closer to a stable SD state) as expected.

To better assess the influence of temperature on the proportions of SP and SD grains, we compared the theoretical SP/SD threshold (relaxation time, τ = 1 minute) for non-interacting greigite particles at 350 K (the growth temperature), 300 K and 100 K. Following Winklhofer et al. (2014) and using $\tau = \tau_0 \exp\left[\left(\frac{-K_1}{12} - \frac{-K_2}{27}\right)\frac{V_b}{k_b T}\right]$ with anisotropy constants K_1 and K_2 of -16, and -6 kJ/m³ respectively, we calculated the blocking volumes, V_b and respective SP/SD threshold sizes. For spherical grains the estimated SP/SD threshold at 350, 300, and 100 K decreases from 53 to 50 to 35 nm, and for cubic grains it decreases from 43 to 40 nm to 28 nm, respectively. Differences in the stable SD grain population between growth and room temperatures are minimal. Between 300 and 100 K the SD threshold size is lowered by ~30%, which generally agrees with the increase in stable SD grains between 300 and 100 K (Fig. 4a). The grain size spectrum that is blocked between 300 and 100 K was estimated as 30-50 nm, which is consistent with our measured average grain size (20-50 nm) and approximate SP proportions of 75% at room temperature and 50% at 100 K. Magnetostatic interactions may additionally lower the SP/SD threshold to smaller sizes (Muxworthy, 2001; Muxworthy et al., 2013); stronger interactions at 100 K than at 300 K could, therefore, amplify the shift from SP to SD behavior.

4.6. Day plot mixing trends

Day plot distribution of our synthetic samples overlaps and continues the trend defined by natural SD-dominated greigite (Roberts et al., 2011a) (Fig. 4a), which points to a common SP endmember size close to 7 nm. This size roughly coincides with our inferred crystallite size for FeS, which was estimated to $\lesssim$ 5 nm after Step I and to 10 nm after Step II. Greigite forms by a solid-state transformation of FeS, so a similar particle size of the two phases should be expected. The SP endmember in our samples, thus, likely originates from transformation of single FeS crystallites whereas larger greigite grains may have developed from FeS

aggregates. A similar SP endmember size for natural greigite from diverse locations is consistent with the typical nanoparticulate nature of its precursor FeS (Ohfuji and Rickard, 2006). The well-defined greigite trend along a single mixing line suggests that the smallest grains (5-10 nm) dominate the SP greigite fraction, which likely has a continuous size distribution, similarly as was reported for diagenetic SP-SD magnetite in remagetized carbonates (Jackson and Swanson-Hysell, 2012).

Overlap between the Day plot trends of SP-SD greigite and SD-MD magnetite (Dunlop et al. 2002) suggests that authigenic greigite with more than 40% SP contributions is difficult to distinguish from typical primary magnetite-bearing sediments, which tend to plot close to the SD-MD mixing curves. An overlap between SP-SD greigite and magnetite dominated sediments in the Day plot was shown, for example, in Quaternary marine sediments from the Gulf of Mexico (Fu et al., 2008).

4.7. Grain arrangement and magnetostatic interactions

Magnetostatic interactions are primarily governed by the distance between magnetic particles. Higher concentration and/or local enrichment of magnetic particles within clusters, thus, lead to stronger interactions. The degree of interactions in a sample can be assessed by the vertical spread of its FORC distribution. FORC analysis indicate that the degree of interactions is similar for the matrix free (pure sulfide) sample #50-31 (Fig. 4b) and for silt sample #100-10 (Fig. 4c), in which the sulfide concentration is diluted to 0.1% by the sediment substrate. This implies that for all our samples interactions are independent of the greigite concentration and arise mainly from clustering. A dense clustering of the sulfides can be inferred from the SEM images of the non-matrix sample #50-31 (Fig. 1b, final product). The magnetic fraction in a cluster can be expressed as the packing fraction, p, which is given by the net volume of magnetic particles relative to the total volume, when assuming a uniform cluster composition. In our samples, interactions increase with lower temperature (FWHM increase from 10 mT at 300 K to 24 mT at 100 K), consistent with an increase in the SD fraction, which was estimated to 16±3 vol% at 300 K and 31±2 vol% at 100 K (section 4.2).

Numeric FORC models for uniaxial and cubic magnetite indicate that the vertical spread (FWHM of the B_u distribution) is proportional to the packing fraction and nearly independent of anisotropy type (Harrison and Lascu, 2014). Normalized by the mineral specific saturation magnetization, the FWHM is expected to be independent of magnetic mineralogy. With $\mu_0 M_s \approx 0.34$ T for greigite, our samples yield FWHM/$\mu_0 M_s$ values of 0.29 for 300 K and of 0.70

for 100 K. Comparison to the FWHM/$\mu_0 M_s$ values reported for modeled magnetite FORC distributions (Fig. 9 of Harrison and Lascu, 2014) suggests packing fractions of $p_{300K} \approx 0.07$ (7 vol% magnetic fraction) and $p_{100K} \approx 0.27$ (27 vol%) in our samples.

General agreement between the estimated packing fraction of magnetic minerals and the SD greigite fraction relative to the total sulfide concentration further supports the interpretation that magnetostatic interactions arise predominantly from the proportion of SD greigite within densely packed sulfide clusters. Magnetostatic interactions can bias M_{rs}/M_s ratios to lower values and B_{cr}/B_c to higher values (Muxworthy, 2003; Harrison and Lascu, 2014). Hence SD proportions inferred from the Day plot mixing lines likely underestimate the true SD contributions, particularly at 100 K. This could partially account for the discrepancy between a nearly fourfold difference in estimated packing fraction between 300 and 100 K versus a twofold difference in estimated SD-proportions. Similarly, magnetic interactions may explain why measured M_{rs}/M_s values of sedimentary greigite are generally lower than the expected value for SD grains dominated by cubic magnetocrystalline anisotropy (Roberts et al., 2011a).

4.8. Sample alteration in air

When the samples were exposed to air after aging, yellow patches appeared in the sediment, which increased in number and size over time, thereby suggesting that Fe-sulfides were oxidized partially to a yellow Fe-oxyhydroxide, likely lepidocrocite and/or goethite. Observed changes in FORC distributions over a 12 h period for sample #100-10 (Fig. 4c) demonstrate that the greigite concentration (FORC amplitude) and magnetostatic interactions (vertical spread) decreased, and that thermal activation of the SD fraction increased (shift to lower B_c and higher B_u values). Room temperature FORC diagrams for sample #100-10 have a weak diagonal feature in the lower left half-plane, which is particularly expressed after oxidation. This feature, which is absent at 100 K and in both FORC diagrams of sample #50-3, resembles vortex state signatures associated with flux-closure among clustered SD grains (Egli, 2021). A gradual change in remanence and coercivity ratios marks a relative increase of the SP fraction (Figure 4a).

Taken together, these results suggest that oxidation led to an effective magnetic grain size reduction, where greigite particles were oxidized progressively to a non- or weakly-magnetic phase, which is consistent with a partial transformation to lepidocrocite and/or goethite. Reduced magnetic interactions point to a lower moment and/or to a larger distance between

the remaining greigite particles, consistent with a grain size reduction by surface oxidation and an overall decrease in greigite concentration.

5. Conclusions

5.1. Greigite formation and CRM acquisition

We report a two-step synthesis method to transform lepidocrocite via mackinawite to greigite inside sealed non-magnetic vials. First lepidocrocite powder is transformed to nanoparticulate FeS in an anhydrous H_2S atmosphere at room temperature. FeS is then preferentially oxidized to greigite under aquatic conditions at 75°C via a solid-state transformation, presumably involving the loss of iron ($4FeS \rightarrow Fe_3S_4$) although the involved electron acceptor and the fate of the released iron are not identified.

Through bulk magnetic measurements during greigite growth in a defined magnetic field the growth process and CRM acquisition can be monitored in real-time. Greigite was grown in different water saturated sediment substrates, which stabilized the greigite mechanically but did not influence the greigite growth kinetics. During sample aging at 75°C, we observed a continuous increase in magnetic susceptibility and in CRM intensity. Nearly linear growth rates, which decreased by a factor of three after 2 h, point to two distinct growth regimes. Two thirds of the precursor FeS transformed to greigite after 7 h, leading to a final greigite concentration of ~0.1 vol% in samples with a sediment matrix.

Using magnetic susceptibility growth rates at room temperature and 75°C, the activation energy for the FeS to greigite transformation was estimated at 78-90 kJ/mol, which agrees within uncertainty with previous estimates based on direct analytical measurements (Hunger und Benning 2007). Growth and particularly dissolution rates of greigite have been notoriously difficult to constrain partially due to a lack of pure greigite sample material and because direct in-situ phase analyses are difficult. Magnetic susceptibility measurements represent a valuable alternative to track in-situ greigite concentration in real-time. This indirect method is rapid, simple, and independent of the presence of a growth medium or other non-magnetic mineral phases like mackinawite and pyrite. Moreover, susceptibility can be calibrated with respect to greigite concentration by direct analysis of the studied material. Magnetic measurements, hence, could help to better constrain the solubility of greigite which is a relevant, yet poorly understood variable in sedimentary Fe-S cycles.

5.2. Greigite preservation

Greigite is metastable with respect to pyrite when dissolved sulfide concentrations are high. Rock magnetic studies, however, frequently identify greigite in marine sediments, where pyritization and pervasive diagenetic dissolution of detrital magnetite indicate high sulfide concentrations during diagenesis (Roberts and Weaver, 2005; Roberts et al., 2018). It remains unclear when, and under which conditions greigite accumulates, and how it becomes preserved. Our experiments indirectly confirm that the presence of trace amounts of aldehydes inhibit greigite dissolution and pyrite formation. This "sulfide-switch", originally reported by Rickard et al. (2001), could play a role in preserving greigite in sulfidic microenvironments associated with aldehyde-bearing organic matter. The microbial community involved in the sulfidation process may also influence greigite preservation, as greigite is stable in the presence of certain strains of hyperthermophilic archaea and magnetotactic bacteria (Posfai, 2006; Gorlas et al., 2018). Combining organic and sulfide chemistry with rock magnetic methods in future studies may help to better understand the environmental conditions that promote greigite accumulation in marine sediments.

5.3. Magnetic properties, grain size and domain state

In our experiments, the SP-SD ratio, and hence the average grain size of greigite, remained constant as its concentration increased continuously at 75°C. Individual greigite grains reached a final size within minutes, consistent with a solid-state transformation where grain size is inherited from the precursor phase. This suggests that greigite grains form quasi-instantaneously, and that their size is fixed on geological timescales. Different domain states observed in natural sedimentary greigite may therefore reflect different paleoenvironmental growth conditions. However, progressively increasing greigite concentrations can enhance magnetostatic interactions, which potentially lowers the SP/SD threshold size, leading to more SD-like properties.

The average greigite grain size in our samples lies between 20-50 nm and spans the SP/SD threshold, consistent with theoretical estimates for the greigite blocking volume. SD fractions are estimated to ~25% at room temperature and ~50% at 100 K. Comparison of M_S normalized FORC distributions of our samples to numerical FORC models (Harrison und Feinberg 2008) suggests SD greigite packing fractions of 7% at room temperature and of 27% at 100 K.

Temperature-dependent Day plot distributions for our samples follow the trend of theoretical SP-SD mixing lines calculated for an SP greigite endmember of 7 nm, in accord

with the crystallite size of the precursor FeS. Our data overlap with an empirical mixing trend defined by diverse greigite-bearing sediments, which together suggest a characteristic, common SP endmember size that likely dominates the SP greigite fraction volumetrically. An SP endmember between 5-10 nm agrees with the typical size of precipitated FeS. Our results suggests that the mixing model, based on binary SP and SD fractions, provides a realistic representation of the domain state and physical grain size of SP-SD greigite distributions. Although clustering and associated magnetostatic interactions in authigenic greigite potentially lead to underestimated SD proportions, the model can help quantify the grain size of sedimentary greigite, which is typically in a SP-SD state.

Open Research

All data mentioned in this study are available online at the open-access data repository Zenodo via https://doi.org/10.5281/zenodo.6521653.

Acknowledgements

We thank Dr. Erika Griesshaber for her support using the scanning electron microscope. This work was supported by the Deutsche Forschungsgemeinschaft (GI712/16-1). Editorial handling by Joshua Feinberg and helpful reviews by Andrew Roberts and one anonymous reviewer are greatly appreciated.

Chapter V

Chemical and Depositional Magnetic Recording in Greigite-bearing Sediments

Manuscript in preparation for the Journal of Geophysical Research: Solid Earth

Reference

Roud, S.C. and Gilder, S. A. (2022). Chemical and Depositional Magnetic Recording in Greigite-bearing Sediments [In preparation for Journal of Geophysical Research: Solid Earth]

Contributions

I designed this study, developed the methodology, carried out all measurements, analysis and interpretation and prepared the manuscript including all figures.

Abstract

How and when sediments record the Earth's magnetic field has been long debated. Most studies assume a stratigraphically continuous, time progressive lock-in mechanism through torque alignment of detrital magnetic grains (depositional remanent magnetization, DRM). However, magnetic minerals can also form in-situ at any time after deposition, recording the magnetic field by a grain-growth mechanism (chemical remanent magnetization, CRM). Through novel experiments, we have synthesized greigite (Fe_3S_4) in different magnetic fields and substrates to show, for the first time, a direct comparison between the recording efficiency of grain-growth and depositional magnetizations. CRM intensities were up to six times higher than torque aligned DRMs. The results demonstrate that if CRM components remain unrecognized in paleomagnetic records, paleointensity estimates of the magnetic field can be significantly overestimated. Alternating field demagnetization of the original magnetization in rocks compared to demagnetization of a laboratory-imposed magnetization can distinguish the two recording mechanisms.

1. Introduction

The natural remnant magnetization (NRM) of sedimentary rocks provides quasi-continuous archives of the Earth's magnetic field history. Such records provide magnetostratigraphic chronologies from thousand-year to million-year time scales that help to establish the geologic time scale (Butler, 1992; Tauxe, 1993; Gradstein et al., 2020). Dipolar geomagnetic field variations provide crucial stratigraphically tie-points to globally correlate sedimentary archives (Stoner et al., 2002) and provide information on the geometry and strength of the magnetic field though Earth's history (Valet, 2003; Channell et al., 2009). Geomagnetic field intensity governs cosmogenic nuclide production in the atmosphere (e.g., ^{10}Be and ^{14}C) (Frank et al., 1997; Simon et al., 2016), reconstruction of paleomagnetic intensity variations, thus, bears on a wide range of topics in the Earth and environmental sciences. An important precondition to derive paleointensity information from sediment sequences, is a stratigraphically continuous magnetic recording mechanism with constant recording efficiency (Tauxe, 1993; Roberts et al., 2013).

Sediments typically acquire a magnetization during deposition: as particles settle through the water column, the Earth's magnetic field exerts a torque on magnetic grains, which tends to align them parallel to the magnetic field. Grain alignment is preserved and locked-in during deposition and compaction of the sediment and produces a net magnetization that is referred to as detrital or depositional remanent magnetization (DRM). DRM is not only parallel to the earth's magnetic field but also proportional to the magnetic field strengths (Kodama, 2012). The efficiency of DRM acquisition at a given field strengths depends on numerous factors, including the mineralogy, grain size and concentration of magnetic minerals, flocculation processes during setting, sedimentation rate and bioturbation (Tauxe et al., 2006; Shcherbakov and Sycheva, 2010; Roberts et al., 2013b; Zhao et al., 2016). The complexity of these processes cannot be recreated in laboratory redeposition experiments, which prevents absolute paleointensity estimates from sedimentary records. Assuming, however, that relevant factors remained constant, except for small variations in the concentration of magnetic minerals, then the relative paleointensity (RPI) can be deduced from the natural remanent magnetization (NRM) normalized by a laboratory magnetization (e.g. anhysteretic magnetic remanence, ARM, as proxy for magnetic mineral concentration).

Even if DRM acquisition remained constant, the magnetic record can be compromised by diagenetic processes that lead to formation of authigenic magnetic minerals and the acquisition of secondary magnetic remanence—a chemical, or crystallization remanent

magnetization (CRM). CRM can form any time after deposition. It is therefore not stratigraphically continuous and usually unrelated to the depositional age of the sediment. If a sedimentary CRM is acquired shortly after deposition, it may be parallel to the primary DRM and not affect the interpretation of paleomagnetic directions (Snowball and Thompson, 1990). Potential influences on the paleointensity record have however remained elusive (Roberts et al., 2013b) and thus largely ignored. The mechanisms by which DRM and CRM are acquired differ substantially, so different magnetic recording efficiencies and associated biases in RPI records should be expected.

A common mechanism to produce CRM in reducing sedimentary environments is formation of the magnetic Fe-sulfide greigite (Fe_3S_4) (Snowball and Thompson, 1990; Roberts, 2015). The mineral can form shortly and log after deposition—greigite bearing horizons are therefore often excluded from paleomagnetic interpretations (Nowaczyk et al., 2020), as is generally the case for CRM components, if they are recognized as such, e.g. through inconsistent NRM directions. If a recoded CRM is parallel to the primary DRM, its identification relies on rock-magnetic analysis to detect changes in magnetic mineralogy. However, magnetic proxies are often nun-unique and the properties of greigite and its oxide analog magnetite (Fe_3O_4), a typical magnetic mineral in natural materials, overlap so that distinguishing the two minerals can be difficult (Roberts et al., 2011a). Hence, distinguishing DRM and CRM components in sediments remains challenging. A better understanding of the underlying recording mechanisms, particularly how they differ and how they influence the paleomagnetic signal may yield additional tools that can help to improve the reliability of paleointensity records.

To study the CRM recording mechanism under controlled conditions, we developed a method to recreate the greigite growth process in artificial sediments under controlled magnetic field conditions (*Chapter IV*). Here we report the magnetic remanence-based aspects of the CRMs acquired in 42 discrete samples and characterize their bulk magnetic properties. Redeposition experiments with the same set of samples are reported to compare DRMs and CRMs acquired by the same grains in the same magnetizing fields. The relative CRM and DRM intensities are discussed in relation to basic, fundamental models of the two recording processes.

1.1. Theory of DRM acquisition

DRM recording requires the physical alignment of particles with a fixed magnetic moment. Alignment of magnetic particles that are settling in a viscous medium results from torque exerted by the magnetic field on the settling particle (Nagata, 1961). The time required for alignment with the magnetic field (t~6μ/mB) of a suspended, submicron magnetic grain is typically on the order of seconds or less, so that full alignment should be expected in the deposited sediment. The NRM of sediments is, however, usually far from saturation and linearly dependent on the magnetic field intensity (Johnson et al., 1948). This observation has been linked to various randomizing mechanisms including thermal agitation due to Brownian motion (Collinson, 1965) flocculation of magnetic and nonmagnetic grains, which reduces the effective moment of the settling particles (Shcherbakov and Shcherbakova, 1983; Vreumingen, 1993; Tauxe et al., 2006), particle collisions during settling, as well as rolling and slipping of grains on the sediment surface (Shcherbakov and Sycheva, 2010; Bilardello et al., 2013). Neglecting the latter processes the relative DRM intensity of isolated submicron particles results from the balance between magnetic alignment and thermal agitation, which can be expressed as

$$\frac{M_{\mathrm{DRM}}(B_0)}{M_{\mathrm{DRM-max}}} = L\left(\frac{mB_0}{kT}\right), \quad (1)$$

where L is the Langevin equation, m is the magnetic moment of a grain, B_0 is the applied magnetic field intensity and kT represents thermal anergy given by the Boltzmann constant, k and the absolute temperature, T. $M_{\mathrm{DRM}}(B_0)$ is the volume normalized magnetization of the sample and $M_{\mathrm{DRM-max}}$ is the maximum magnetization. For small B_0, the expression can be approximated by

$$\frac{M_{\mathrm{DRM}}(B_0)}{M_{\mathrm{DRM-max}}} = \frac{m_{\mathrm{max}}B_0}{6kT}, \quad (2)$$

where $m_{\mathrm{max}} = V_{max}\mu_0$ is the maximum moment of a particle ensemble with a uniform moment distribution (Stacey, 1972), defined by the maximum grain volume V_{max} and the material specific saturation magnetization, μ_0.

1.2. Theory of CRM acquisition

In contrast to the physical alignment of grains to obtain a DRM, CRM acquisition is considered a Néel thermal relaxation process (Néel, 1949) governed by the alignment and blocking of magnetic moments of (physically fixed) grains in the presence of a weak magnetic field, analogous to acquisition of thermoremanent magnetization (TRM) (Haigh, 1958). During grain growth, particles are initially too small to hold a magnetic remanence—they are in a

thermally relaxed state referred to as superparamagnetic (SP). In this state the magnetization is in equilibrium with the external magnetic field intensity and can be expressed as a function of $tanh(\mathrm{E}_b/\mathrm{E}_t)$, where , $E_b = mB_0$ is the barrier energy (necessary to flip a magnetic moment between easy axis) and $E_t = kT$ is the thermal energy (Néel, 1949).

As grains grow larger than the blocking volume, V_b the equilibrium magnetization is locked-in as CRM (Haigh, 1958). The CRM intensity of a sample, $M_{CRM}(B_0)$ acquired at the growth temperature, T_g by an ensemble of non-interacting single domain (SD) grains with their easy axis aligned parallel to the applied field is then given by

$$M_{CRM}(B_0) = M_s(T_\mathrm{g})\ tanh\left(\frac{V_b \mu_s(T_\mathrm{g}) B_0}{kT_g}\right). \quad (3)$$

$M_s = c\mu_s$ is the saturation magnetization of the samples, where c is the magnetic mineral concentration. Continued grain growth after blocking increases the remanent magnetization proportionally to the increase in grain volume, for as long as the grains remain in a SD state. If T_g is larger than room temperature, the grain assemblage can additionally acquire a partial TRM when cooled in a magnetic field (McClelland, 1996; Fabian, 2009).
For large B_0 values $tanh\left(\frac{VM_sB_0}{kT}\right) \longrightarrow 1$ so that the CRM intensity approaches the saturation value M_s. The saturation CRM, of randomly oriented SD particle distributions cannot exceed the saturation remanent magnetization M_{rs}, hence eq. (1) can be generalized for randomly oriented SD grain assemblages with final grain volume, V_{fin} as:

$$M_{CRM}(B_0) = M_{rs}(T_g)\ tanh\left(\frac{V_{fin} \mu_s(T_g) B_0}{kT_\mathrm{g}}\right). \quad (4)$$

In weak magnetic fields, so that $V_b M_s(T_\mathrm{g}) B_0 \ll kT_g$ eq. (4) can be simplified to

$$\frac{M_{CRM}(B_0)}{M_{rs}(T_\mathrm{g})} = \frac{V_{fin} \mu_s(T_\mathrm{g}) B_0}{kT_\mathrm{g}}, \quad (5)$$

describing the relative CRM intensity acquired in earth-like magnetic fields by the growth of randomly aligned SD ensembles. Eq. (5) indicates that the CRM depends linearly on the final grain volume and the magnetic field intensity.

Neglecting differences in CRM and DRM acquisition temperatures and assuming $M_{\mathrm{DRM-max}} = M_{rs}$ and $m_{\max} = V_{fin} M_s$ then equations (2) and (5) can be combined and simplified to

$$M_{\mathrm{CRM}}(B_0) = 6\, M_{\mathrm{DRM}}(B_0), \quad (6)$$

suggesting that for identical ensembles of submicron SD grains the CRM recording mechanism is 6 times more efficient than DRM acquisition, given the grains are subject to Brownian motion, while settling in the same magnetizing field.

2. Material and Methods

2.1. Samples

Preparation of 42 greigite-bearing, artificial sediment samples used in this study was described in detail in *Chapter IV*. In brief: every sample is contained in a sealed, 10 ml glass vial of 4 cm height and was prepared from 22 mg of FeOOH powder that was sulfidized to FeS in H_2S atmosphere. FeS was then mixed with non-magnetic silica substrate of either sand (100-400 µm) or silt size (2-40 µm) and 5 ml of an anoxic solution were added. The sediment slurries were thoroughly mixed and allowed to settle at room temperature, before they were aged at 75°C under controlled magnetic field conditions for ~7 h for transform FeS to greigite. Samples were treated in three batches, each containing 7 sand and 7 silt samples. Batch #100, #50, and #25 were aged in uniform magnetic fields of declination, D = 0° and inclination, I = 45° and field intensities of 100, 50 and 25 µT, respectively. At the end of the experiments approximately two thirds of the FeS had transformed to greigite, indicating that the samples contained on average 13±2 mg (± one standard deviation) greigite, equivalent to 0.1 vol% relative to the total sediment volume of 3 cm^3. The average magnetic susceptibility, κ_{lf} normalized by the sediment volume was 352×10^{-5}±13% (± relative standard deviation, unitless SI unit) and the average frequency-dependent susceptibility, κ_{fd} was 7.3±0.8% (n = 43). The average greigite grain size lies between 20-50 nm and the samples are predominantly in a SP state at room temperature with an SP:SD ratio of approximately 3:1, suggesting a SD-greigite concentration of ~0.03%. Despite the initial dispersion of the (non-magnetic) FeS powder in the silica matrix, the sulfide particles remained clustered and moderate magnetostatic interactions suggest an approximate SD-greigite packing fraction within the sulfide clusters of 7 vol% at room temperature (*Chapter IV*).

2.2. Experimental protocol

After the aging experiments the samples were cooled from 75°C to room temperature in a magnetically shielded room (<500 nT) to avoid partial TRM acquisition. The magnetic remanence was measured directly after cooling of the samples and remeasured after 12 h using a vertical 2G Enterprises Inc., three axis, superconducting magnetometer housed in the

shielded room. Each sample vial was measured in two positions using a custom, manual sample handler that allowed careful lowering of the vials into the magnetometer and to rotate them about a vertical axis between consecutive measurement steps with minimal disturbance of the sediment slurry.

Selective samples were then stepwise demagnetized in alternating magnetic fields (AF) in 5-10 mT steps along three orthogonal axes (last AF direction: I=35°, D=270°) until 90% of the remanence was eliminated at peak fields of 30-40 mT. Select samples were AF demagnetized up to 100 mT to test for acquisition of gyroremanent magnetization (GRM)—an increase in magnetization perpendicular to the last AF-field direction that is considered common for SD greigite (Snowball, 1997; Hu et al., 1998).

All samples were then redeposited at room temperature by thoroughly shaking the vials and allowing the substrate to settle overnight under the identical, uniform magnetic field conditions at which they had acquired a CRM: D = 0°, I = 45° and B_0= 100, 50 or 25 μT. Each sample was placed at the same location inside the Helmholtz coil setup as during the CRM experiments (two pairs of square coils with ca. 1 m diameter placed inside a partially magnetically shielded environment with a residual field <9 μT). The resulting magnetic remanence was measured the next day after ca. 17 h of magnetic field exposure. Samples of batch #25 were subsequently returned to the magnetizing field and their magnetic remanence was repeatedly measured after 1, 5, and 10 days of field exposure. The samples were then stored in the magnetically shielded room and remeasured after 1 day. For select samples of each batch the DRM was stepwise AF demagnetization as described above.

All samples were imparted an ARM in peak AF fields of 100 mT using bias fields equivalent to the magnetizing fields each sample was exposed to during the precious experiments (100, 50 or 25 μT for batch #100, #50, and #25 respectively). For samples of batch #50 we measured ARMs before and after their redeposition to compare ARM properties of the CRM and DRM state. For two silt and two sand samples both ARMs (imparted before and after their redeposition) were stepwise demagnetized. Additionally, we measured stepwise acquisition of isothermal remanent magnetization (IRM) up to 300 mT, ARM imparted in different bias fields (25, 50 and 100 μT), and viscous decay of ARM within one day for subsets of 6-12 samples of batch #25 using a Mag-Instruments slow spinning magnetometer.

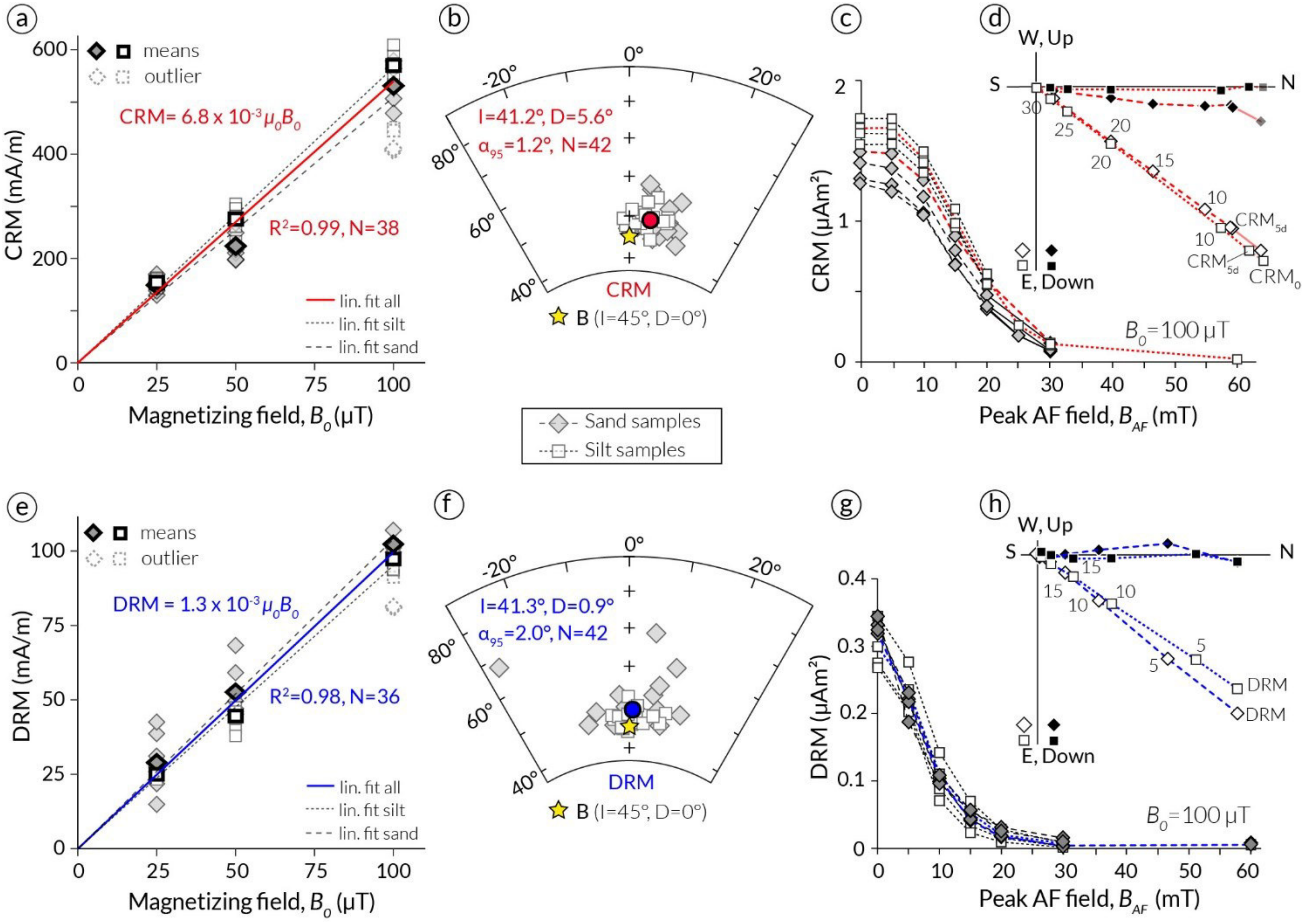

Figure 1. Chemical (upper row) and depositional (lower row) remanent magnetizations. Diamonds and dashed lines indicate samples with sand matrix; squares and dotted lines represent silt matrix samples. **(a, e)** CRM and DRM intensities as a function of field strength. Lines show linear fits of the same sediment type, with slope and R^2) values as shown, p<.000 for all cases; batch#1 outliers were omitted (see text). **(b, f)** Equal area stereographic projection of CRM and DRM directions; yellow stars indicate the applied field direction, colored dots show the (Fisher, 1953) mean directions; α_{95} ellipses are too small to be visible. **(c, g)** Intensity decay as a function of peak AF-field for batch#1 samples (100μT), red and blue lines correspond to data shown in **d** and **h**, respectively. **(d, h)** Representative vector endpoint diagrams of **s**tepwise AF-demagnetization trajectories of CRM and DRM for one sand and one silt sample from batch#1; AF values in mT; CRM_0 refers to the initial CRM and CRM_{5d} to the remaining CRM after 5 days of zero-field storage.

3. Results

3.1. Chemical remanent magnetization

Remanent magnetizations acquired during the greigite growth experiments ranged from 0.1-0.6 A/m (normalized by the sediment volume of 3 cm^3) and were proportional to the intensity of the applied magnetic field (Figure 1a). Two sand and two silt samples from batch #100 that were repeatedly removed from the heat and magnetizing field during the growth phase (*Chapter IV*) had ~20% lower magnetizations than the remaining 10 samples of the same batch. These samples are treated as outliers and excluded from further statistical analyses.

Linear regression (including the origin) yielded an average CRM susceptibility of CRM/($\mu_0 B_0$) = 6.8×10^{-3} (R^2 = 0.99, p<.001), where μ_0 is the vacuum permeability. Among samples of the same batch and sediment type the CRM intensities agreed within 4-12% relative standard deviation (Table 1). Among sand samples the scatter was generally larger, and the CRM susceptibility was on average 13% weaker than for silt samples.

Remeasuring the magnetization after the samples were stored in a shielded room for 12 h indicated that the CRM intensity of silt samples was stable, decreasing by less than 1% (n=18) on average (Fig. 2a). Sand samples lost on average 5±4% (n=19) of the initial CRM, which could point to a viscous magnetization decay. However, the unconsolidated sand samples were more susceptible to physical disturbance than silt samples, and random physical disturbance during sample handling is consistent with the highly variable loss in remanence, ranging from 1-17% among the sand samples. Remeasuring four silt and four sand samples after additional 4 days of storage in a magnetically shielded room, showed a loss in magnetization of ca. 6% and 12% respectively (Fig. 1d), supporting a viscous CRM decay over these timescales. Both stronger physical disturbances and viscous decay in sand samples can partially account for their on average lower CRM intensity and a larger error.

The mean CRM direction (D = 5.6°, I = 41°, α_{95} = 1.2°) agreed well with the applied magnetic field direction (Fig. 1b, Table 1) and there was no systematic difference in inclination between sand and silt samples. For sand samples the declination deviated more from the applied field, and the CRM directions were generally more scattered (Table 1), which could be a related to physical disturbance of the sediment when rotating the samples during the measurements.

Three-axis AF demagnetization yielded univectorial magnetization components that coincided with the samples initial CRM directions (Fig. 1d). The median destructive field (MDF_{CRM}) was 18 mT on average (Table 1) and peak AF fields of 30 mT demagnetized at least 90% of the initial CRM (Fig. 1c). Silt samples (and a sand sample stored for 5 days before demagnetization) tended to have slightly higher MDFs and were less susceptible to 5 mT AF fields than sand samples (Fig. 4c and 5). AF treatment up to 100 mT did not lead to acquisition of gyroremanent magnetization.

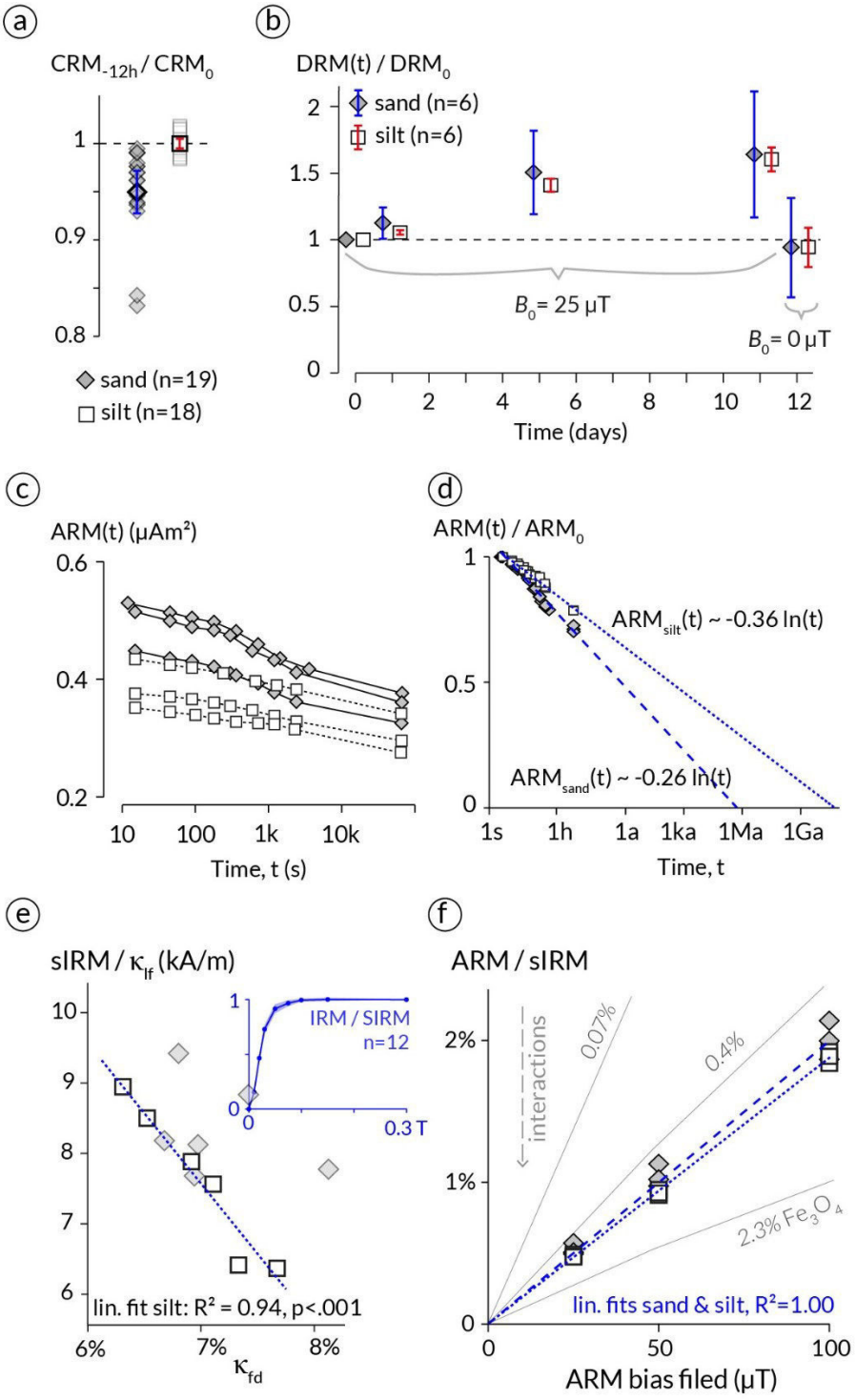

Figure 2. (a) Loss of CRM after sample storage in zero-field (<500nT) for 12 h normalised by the inicial magnetisation, CRM_0. **(b)** Acquisition of magnetisation during sample storage in a 25 µT field after sediment deposition (days 1-11) and magnetisation decy in zero-field (day 11-12). **(c)** Decay of ARM monents as a function of time (log scale). **(d)** ARM decay normalised by the inicial value, ARM_0. **(e)** ARM/sIRM as a function of ARM bias field; equivalend data for synthetic samples with variable SD-PSD magnetite concentrations (Sugiura 1979) are shown in the backround.

Table 1. Grouped mean CRM and DRM intensity and mean directions.

Sample groups			NRM Intensity			NRM mean direction					NRM coercivity	
NRM	**B_0 (μT)**	**matrix**	**M (μAm²)**	**RSD (%)**	**N**	**D (°)**	**I (°)**	**N**	**a95 (°)**	**k**	**MDF (mT)**	**N**
CRM	25	sand	0.45	8.7	7	7.3	38.0	7	4.0	225.5	17.4	4
CRM	25	silt	0.46	4.4	7	5.4	39.7	7	2.9	426.3	18.4	4
CRM	50	sand	0.67	11.8	7	7.7	43.9	7	2.9	437.0	19.6	4
CRM	50	silt	0.83	8.5	7	5.8	40.4	7	2.7	493.6	19.7	4
CRM	100	sand	1.59	7.7	5	5.5	42.6	7	2.9	431.7	16.6	4
CRM	100	silt	1.71	5.5	5	2.1	42.4	7	1.5	1577.0	17.4	4
CRM	all	all				0.9	41.3	42	2.0	118.0	18.2	24
DRM	25	sand	0.09	32.9	7	6.1	40.6	7	3.8	251.7	9.2	2
DRM	25	silt	0.08	5.5	7	0.1	42.6	7	2.7	497.8	11.1	2
DRM	50	sand	0.16	16.0	7	-3.3	41.8	7	3.4	323.9	9.0	2
DRM	50	silt	0.13	10.5	7	-0.2	44.1	7	1.9	1007.6	8.4	2
DRM	100	sand	0.31	3.2	4	-0.6	34.7	7	10.6	33.2	7.1	4
DRM	100	silt	0.29	4.3	4	3.1	43.6	7	2.8	471.3	8.2	4
DRM	all	all				5.6	41.2	42	1.2	340.3	8.5	16

B_0, applied magnetic field strength; M, mean magnetic moment; RSD, relative standard deviation; N, number of samples; D, declination; I, inclination; a95, radius that the mean direction lies within 95% confidence; k, best estimate of the precision parameter; MDF, median destructive field.

3.2. Detrital remanent magnetization

The settling behavior during redeposition experiments strongly depended on the grain size of the silica substrate. The sand substrate deposited within a second, as expected. The sulfide fraction of sand samples remained suspended for a longer time, gradually forming a black layer that covered the surface of the sand substrate. Lager sulfide aggregates deposited within seconds to minutes and the supernatant turned entirely clear within 5 h. In silt samples mixing of the slurry produced a gel-like homogenous suspension that gradually compacted over several hours: at 5 h the slurry had a height of 1.4 cm and at 17 h a relatively stable sediment height of 1 cm was reached (3 cm² sediment volume). The sediment kept gradually compacting at a slower rate, decreasing in volume by ~10% over the course of several weeks.

The remanent magnetizations after deposition ranged from 0.02 to 0.11 A/m. High reproducibility within each batch (Table 1) and a linear dependency with the applied magnetic field intensity indicates the systematic acquisition of DRM in all samples with minor dependency on the sediment type (Fig. 1e). Based on linear regression including the origin and excluding the outliers of batch #100 (see above) the DRM susceptibility, $DRM/\mu_0 B_0$ was 1.3×10^{-3} (R^2 = 99%, p<.000, n=36). The DRM susceptibility was on average 10% stronger in sand (1.35×10^{-3} ± 23%) than silt samples (1.21×10^{-3} ± 10%). Although the dispersion, particularly among sand samples was high, a Welch two-sample t-test showed that the difference between sand and silt DRMs is significant ($t[20.7] = 2.1$, $p = .05$).

Samples that were stored in the magnetizing field after deposition kept acquiring a magnetization over time (Fig. 2b). Within 10 days the magnetization increased by ~60% (n=10) compared to the initial value (DRM_0 measured after 17 h) and appeared to approach a saturation value. When stored in a zero-field, the magnetizations quickly decayed retaining on average 94% of DRM_0 after one day, both in sand and silt samples. Overall, the temporal changes in magnetization were consistent among both sample types, although the variability was larger among sand samples (Fig. 2b). The observed changes could indicate that part of the magnetic fraction remained free to rotate in the pore spaces of the water saturated sediments, leading to acquisition of a post-depositional magnetization (pDRM). The effects could, however, also be attributed to thermally activated magnetic moments of grains close to the blocking volume, i.e. the acquisition and decay of viscous remanent magnetization (VRM). Rapid viscous decay during the measurements could account for the observed DRM differences between sample types: sand samples were generally measured before the silt samples, so that the time for a potential viscous decay was on average 15 min longer in silt samples.

The overall mean DRM direction (D=0.9, I=41.3, α_{95}=2.0, N=42) agreed with the applied field direction (Fig. 1f) and stepwise demagnetization yielded mostly univectorial magnetization components that agreed with the initial DRM (Fig. 1h). DRMs were highly susceptible to AF demagnetization (Fig. 1g) with an average MDF_{DRM} of 9 mT (Table 1). Pronounced demagnetization in weak AF-fields further points the presence of viscous magnetization components. Sand samples were more susceptible to 5 mT AF fields and had ca. 1 mT lower MDFs than silt samples.

3.3. Anhysteretic and isothermal remanent magnetization

ARM intensities imparted at 25, 50, and 100 µT DC bias fields were proportional to the applied bias field with an average susceptibility of ARM, κ_{ARM} of 636×10^{-5}±13% (N=36); there was no significant difference in κ_{ARM} between the two sample types. Timed magnetization measurements for 3 sand and 3 silt samples indicated that ARMs were subject to pronounced viscous decay (Fig. 2c). Within one day silt and sand samples lost on average 21±0% (n=3) and 29±1% (n=3), respectively, of their initial magnetization (ARM_0). The decay rate was approximately logarithmic and highly consistent among samples with same sediment type. Extrapolating normalized decay curves ($ARM(t)/ARM_0$) based on logarithmic regression ($R^2\geq0.97$) suggests ARM half-lives on the order of 1 and 1000 years, and maximum relaxation times of ~ 1 Ma and > 4 Ga for sand and silt samples, respectively (Fig. 2d).

Stepwise IRM acquisition of 6 silt and 6 sand samples of batch #25 showed that all samples saturated in fields of 100 mT (inset Fig. 2e). The average saturation IRM (sIRM) was 27.8±4.5 A/m (n=12). sIRM was on average 19% higher in sand (30.6±4.0 A/m, n=6) than in silt samples (24.9±2.8 A/m, n=6). For this specific samples set, also the ARMs were on average 16% higher in sand than in silt samples, whereas over the whole sample set no significant difference was observed in ARM intensity between sample types. sIRM/κ_{lf} ratios ranged from 6-9 kA/m (Fig. 2e). The ratio is a typical rock-magnetic proxy to detect greigite in sediments, where for SD greigite sIRM/κ_{lf} often exceeds 50 kA/m (Snowball and Thompson, 1990). Although greigite is the only magnetic mineral in our samples, sIRM/κ_{lf} ratios are lower than 10 kA/m, a frequently used threshold of to discriminate between greigite and magnetite dominated sediments (Nowaczyk et al., 2020). Low sIRM/κ_{lf} values may relate to substantial SP contributions in our samples (*Chapter IV*), considering that SP grains just below the room temperature blocking volume can significantly increase κ_{lf} (Worm, 1998) but do not contribute to magnetic remanence (i.e. SIRM). Plotting sIRM/κ_{lf} against κ_{fd} (frequency dependency of susceptibility), a proxy for relative SP contributions, shows a significant negative correlation for silt samples (Fig. 2e), supporting that lower sIRM/κ_{lf} values are related to higher SP contributions. Data for sand samples exhibit no significant correlation, but generally overlapped with the trend observed for silt samples.

Ratios of ARM(B_0)/sIRM determined for 6 samples of batch #25 for B_0 = 25, 50 100 µT were linearly dependent on B_0, as expected (R^2=1.00) (Fig. 2f). The ARM recording efficiency (thus, the ARM/sIRM ratio) of SD particle ensamples is strongly dependent on the degree of magnetostatic interactions, which relate to the concentration of magnetic particles in a non-magnetic matrix or their packing fraction within clusters (Sugiura, 1979; Egli, 2006). A general overlap between sand and silt samples, therefore, indicates a similar degree of interactions between the greigite particles in both sample types. Comparison of ARM/sIRM ratios of our samples and those reported for synthetic magnetite bearing samples (Sugiura, 1979), suggest that our data correspond to magnetite concentrations of 0.4% and 2.3% Fig. 2f. The reference values for magnetite likely underestimate greigite concentration, considering that the saturation magnetization of magnetite (and thus its interaction fields) is roughly twice as high as for greigite (Chang et al., 2008). Moreover, Sugiura (1979) reported contributions of pseudosingledomain grains, which lower ARM. The overlap between our data with those for 0.4%-2.3% magnetite bearing samples is, therefore, consistent with the reported 7% SD greigite packing fraction in sulfide clusters of our samples (*Chapter IV*).

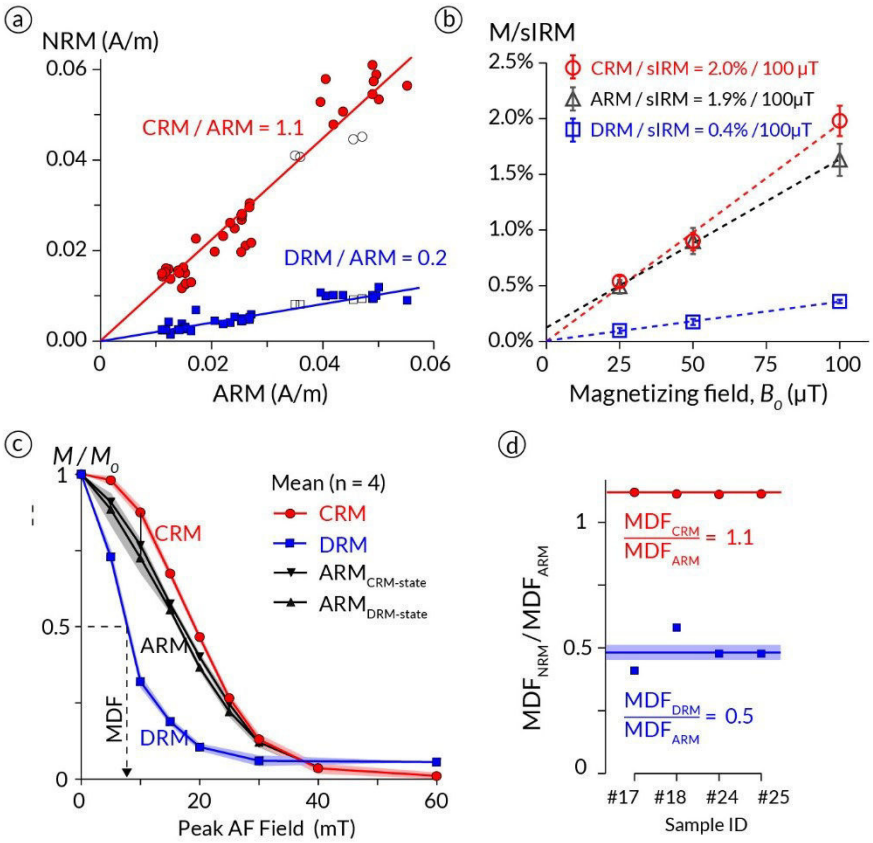

Figure 3. Comparison of CRM and DRM. **(a)** CRM vs. DRM moments for magnetizing fields of 25-100 µT. **(b)** Normalized AF demagnetization of CRM, DRM and ARM imparted after and before re-deposition; mean values of 4 samples (#6.17, #6.18, #6.24, #6.25) are shown, shading indicated standard deviation. **(c)** Ratio of median destructive fields (MDF) of NRM over MDF of ARM determined from the individual demagnetization spectra. A magnetizing field of 50 µT was applied in all cases.

4. Discussion

4.1. CRM intensity and recording efficiency

Our CRM results indicate that the magnetization acquired during greigite formation tracks the applied magnetic field direction and intensity, as is generally expected for growth of SD grains in weak magnetic fields. Linear proportionality of the absolute CRMs with the applied magnetic field intensity and good agreement (within 12% RSD) among samples grown in the same field, further indicate similar magnetic recording characteristics, i.e. similar greigite concentration and grain size distributions for all samples. Absolute CRM intensities were similar to ARMs acquired in the same magnetizing fields, although slightly higher for most samples (Fig. 3a). The average difference of 7% is significant on the 0.05 level, based on a paired t-test. Due to the ca. 50°C higher acquisition temperature for CRM, lower magnetizations than for ARM should be expected. Observation of the opposite suggests that

the temperature difference had no major influence on the magnetizations. However, acquisition temperature could account for the marked difference in remanence-loss, where CRM decayed by on average 0-5% and ARM by 20-30% within one day after acquisition. The smallest, most vicious grain fraction that is responsible for the pronounced decay of ARM was likely unblocked at 50°C and did not acquire a CRM, which is consistent with CRM being more resistant to weak AF fields of 5-10 mT than ARM (Fig. 3c).

Figure 3b compares the average weak-field magnetizations acquired at each field intensity, normalized by the average sIRM of batch#25 (27.8±4.5 A/m, n=12), to better evaluate the relative recording efficiencies. Low ARM/sIRM ratios, also shown in Figure 2f, indicate the damping of ARM due to magnetostatic interactions. Values obtained for our samples, point to stronger interactions than would be expected for a uniform greigite distribution with an overall SD concentration of ~ 0.03%. The results are generally consistent with a clustering of the sulfide particles and with the estimated SD-greigite packing fraction of 7% in the clusters. Numeric modeling results suggest a ~90% reduced ARM intensity for magnetite packing fractions of 3.5% (Egli, 2006), which, considering the ca. two times lower magnetic moment of greigite, is assumed equivalent to the interactions among greigite grains with a 7% packing fraction. It should therefore be expected that interactions lower the ARM intensity in our samples by ~90%.

Both ARM and CRM acquisition are controlled by weak-field thermal relaxation processes, interactions likely influence both remanence types in a similar way, which is supported by comparable CRM and ARM recording efficiencies in our experiments. For the CRM, however, interactions should be negligible in the beginning of the formation process and increase over time, proportional with concentration of magnetic minerals. Because CRMs were only slightly higher than ARMs, this effect had seemingly no major influence on the CRM intensities in our experiments, but it could account for the minor difference between the two remanence types. Potentially, a higher CRM recording efficiency in the beginning of the greigite growth process compensated for the smaller fraction of SD grains due to the 50°C higher acquisition temperature.

To compare the experimental relative CRM intensities to the CRM model, magnetostatic interactions should be accounted for in eq. (5). Interactions effectively reduce the magnetizing field B_0, which should therefore be substituted by $B_{\mathrm{eff}} = B_0 - B_{\mathrm{int}}$, where B_{int} is the interaction field. B_{int} depends on the sample magnetization, which, for weak

magnetizing fields, increases linearly with B_0, so that $B_{\text{eff}} = B_0 f_{\text{int}}$, where f_{int} is a damping factor ranging from 0-1 that describes to which degree the recording efficiency is reduced. The relative CRM intensity for interacting SD grain ensembles is then given by:

$$\frac{M_{CRM}(B_0,V)}{M_{rs}(T_{\text{g}})} = \frac{V_{fin}\mu_s B_0 f_{int}}{kT_{\text{g}}}. \quad (7)$$

Similarity of ARM and CRM recording efficiencies and comparison of our ARM/sIRM results to numeric ARM modelling results (Egli, 2006) suggests interactions could have lowered the CRMs by ~90%, so that $f_{\text{int}} \approx 0.1$.

Neglecting the inferred minor differences in remanent magnetization between 75°C and room temperature, so that $M_{rs}(T_{\text{g}}) \approx sIRM$ allows to directly compare eq. (7) to our experimental $\frac{CRM}{sIRM}$ values. M_s can, likewise, be approximated by the room temperature value 270 kA/m (Li et al., 2014). The temperature dependency of M_s for greigite has, to our knowledge, not been determined above 300 K, however, reported differences between 5-300 K are small (5-7%) (Chang et al., 2008; Li et al., 2014). The final volume, V_{fin} is not identical for all grains in a sample but rather a volume distribution—for simplicity, it can be approximated by the average grain volume of the SD-greigite distribution. The average size of all (SP+SD) greigite particles lies between 20-50 nm. Considering that only the largest ~25% of grains were in a stable SD state at room temperature, suggests that the average SD size lies closer to the upper limit of 50 nm. Assuming spherical grains, this size corresponds to the theoretical SP/SD threshold (relaxation time of 1 minute) of greigite at room temperature (*Chapter IV*). The actual SD grain size in our samples may, however, be smaller than the estimated threshold, particularly if the grains are not equidimensional, since larger aspect ratios and magnetostatic interactions can reduce the blocking volume, i.e. lower the SP/SD threshold (Muxworthy et al., 2013). Taken together these constraints allow to calculate the theoretical relative CRM for a range of grain volumes $V_{fin}=4/3 \text{ pi } (d_{fin}/2)^3$ with d_{fin} = [20-50] nm, and for different damping factors. Figure 4 compares the modeling results for $f_{\text{int}} = [1, 0.1, 0.05]$. Without interactions ($f_{\text{int}} = 1$), the CRM model nearly overlaps with our data for d_{fin}=20 nm but significantly overestimates the measured relative CRM intensity for larger grain sizes (Fig. 4a). Since we expect a reduced recording efficiency and grains of 20 nm are likely smaller than the blocking volume, this model cannot explain our experimental CRM results. For the expected f_{int} value of 0.1, the CRM

model overlaps with our data for d_{fin} = 40 nm (Fig. 4b), which lies within a plausible range for SD greigite in our samples assuming a minor reduction of the SD threshold compared to the theoretical value for spherical non-interacting grains. Fitting f_{int} so that the CRM model for d_{fin} = 50 nm overlaps our data, yields $f_{\mathrm{int}} = 0.05$, i.e. requires a 95% reduced recording efficiency (Fig. 4c).

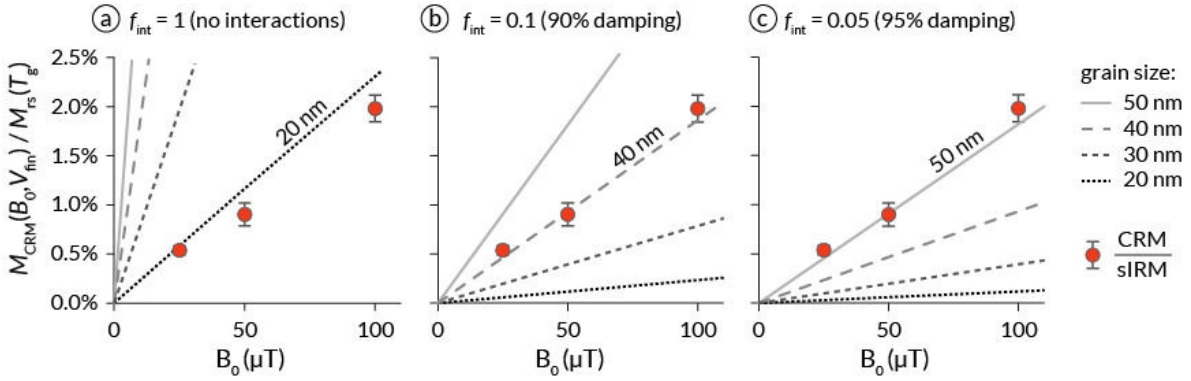

Figure 4. Comparison of experimental and modeled relative CRM intensities. Red circles indicate average values and standard deviations for experimental CRM/sIRM ratios and grey lines represent modelled curves using eq. (7) for spherical grains of 20, 30, 40, and 50 nm diameter and different f_{int} values. (a) $f_{\mathrm{int}} = 1$, (b) $f_{\mathrm{int}} = 0.1$, (c) $f_{\mathrm{int}} = 0.05$.

The results indicate that eq. (7) yields a realistic representation of the relative CRM intensity acquired by our samples. For a plausible range of f_{int} and d_{fin} values, corresponding to a 90-95% reduced CRM recording efficiency and an average SD-greigite grain size of 40-50 nm the calculated values match the empirical data within one standard deviation. Considering the number of approximations used in our calculation, the good agreement is striking and suggests, that the CRM acquisition process in greigite is equivalent to a grain growth CRM and obeys the Néel thermal relaxation theory.

4.2. Comparison of CRM and DRM

Redeposition of the samples in the same weak magnetic fields lead to the acquisition of magnetic remanences that were consistent for each field strength and showed a linear dependency the applied field intensity, indicating acquisition of DRM in all samples. Differences between sand and silt samples were negligible, particularly considering the large differences in settling behavior: the sulfide fraction of sand samples deposited from within seconds to up to 5 hours whereas in silt samples the sulfides and matrix formed a dense suspension that slowly compacted over 17 hours. Comparable final remanences, therefore, imply that neither differences in settling time, flocculation of sulfide and matrix grains, nor

particle collisions during settling in the gel-like suspension of silt samples influenced the acquisition process substantially.

Comparison of the absolute and relative DRM and CRM and ARM intensities (Fig. 3a and b) indicates that the CRM recording efficiency was significantly higher than the DRM recording efficiency. The difference was greater for silt than sand samples with average CRM/DRM ratios of 5.0±1.4 and 6.1±0.3, respectively (n=18). Both estimates agree within one standard deviation with theoretical factor of 6 difference, predicted by eq. (6). The prediction was derived for non-interacting, submicron SD particles. As shown above, the CRM recording process in our samples was substantially affected by magnetostatic interactions. ARM acquisition and demagnetization of four samples before and after redeposition, thus, in the CRM and DRM state, gave the reproducible results (Fig. 3c). This indicates that the degree of interactions and the grain arrangement were equal for CRM and DRM. The settling greigite particles were therefore embedded in sulfide aggregates of various sizes and their alignment with the magnetic field (i.e. the DRM recording efficiency) is controlled by the net moment of the aggregates. This concept is similar to the DRM flocculation theory, where aggregation of non-magnetic matrix and magnetic minerals reduces the effective magnetization of the settling objects (Tauxe et al., 2006; Shcherbakov and Sycheva, 2010). Clustering of the sulfides, therefore, reduced the both the CRM and DRM recording efficiencies, albeit via different mechanisms.

Eq. (6) further assumes the settling of sub-micron particles that are subject to Brownian motion. Sulfide clusters that settled within seconds where likely too large to be influence by Brownian motion and on the other hand settled to quickly to align with magnetic field, and therefore may not have contributed to DRM. Moreover, DRM appears to be preferentially recorded by the most viscous grain fraction, as indicated by stronger demagnetization in weaker AF-peak fields, with average MDFs of 9 mT and 18 mT for DRM and CRM respectively (Fig. 3c and d). Longer exposure to the magnetizing field for DRM than CRM (7 vs. 17 h), in combination with a lower acquisition temperature likely led to partial VRM acquisition during and after deposition, which could have reduced the CRM/DRM ratio.

Slight differences in the grain fractions that contributed to DRM vs. those that contributed to CRM and ARM in our samples manifest in the demagnetization behavior. The differences were consistent among all samples, so that the ratio of the MDF_{NRM} / MDF_{ARM} can distinguish

between the type of NRM, where values close to 1 were characteristic for CRM and values around 0.5 characteristic for DRM (Fig. 3d).

In summary, our experimental CRMs and DRMs can be distinguished by their recording efficiencies, and their AF-demagnetization behavior. The relative "paleointensity" NRM/sIRM and NRM/ARM was 5-6 times higher for CRMs than for DRMs, consistent with theoretical predictions. Although the CRM intensity could be accurately reproduced by thermal relaxation theory and a damping factor to account for magnetostatic interactions, the DRM recording process in our samples remains less well contained. Given that the settling sulfide clusters are primarily randomized by Brownian motion and that VRM contributions to DRM are negligible, the good agreement between the observed and predicted difference in DRM and CRM recording efficiency could suggest that sulfide clustering reduced the DRM intensity to a similar extent as it reduced CRM and ARM due to magnetostatic interactions.

The observed differences in our experiments may not be directly applicable to natural sediments, where DRM and CRM are carried by different grain fractions that usually differ in mineralogy and/or grain size. Moreover, the DRM recording efficiency in natural sediments is governed by multiple processes and different variables, so that our redeposition experiments are likely not representative for most sedimentary environments. CRM acquisition, in contrast, is primarily controlled by grain growth and the strength of the ambient field, so that the CRM characteristics of our samples, specifically NRM/ARM and MDF_{NRM}/MDF_{ARM} ratios close to 1, should apply to a wide range of natural CRM bearing sediments. Values close to 1 not unique to CRM, however, positive anomalies in both ratios could point to the presence of CRM components.

5. Conclusions

Greigite growth in 42 discreate samples in different Earth-like magnetizing fields led to the systematic acquisition of CRMs that tracked the magnetic field direction and intensity. With a theoretical CRM model, based on thermal relaxation and a damping factor that accounts for magnetostatic interactions we could reproduce our experimental results. Good agreement of the CRM model and data further indicate that CRM, acquired during greigite growth, which is a solid-state transformation of preexisting FeS, is equivalent to a grain-growth CRM, that is governed by thermal relaxation processes analogous to TRM acquisition. Similar recording efficiencies of CRM and ARM suggests that if CRM-bearing greigite is the only magnetic mineral in a sediment, NRM/ARM ratios can be representative of the absolute paleointensity.

It was shown that authigenic greigite can hold a reliable record of the Earth's magnetic field direction, given that the timing of greigite formation can be sufficiently constrained.

Redeposition experiments with the same samples in the same magnetizing fields produced DRMs that were parallel and proportional to the applied magnetic field. DRM intensities were 5-6 lower than CRM intensities, which is compatible with the theoretical difference in recording efficiencies. Additionally, the DRMs differed from CRMs in their AF-demagnetization behavior, being more susceptible to weak AF fields than CRM and ARM.

In contrast to DRM recording, which is highly variable in different sedimentary environments, CRM depends mainly on the growth process and the magnetic field strengths, so that the reported CRM characteristics are likely representative for natural sediments. High recording efficiency of CRM, with CRM/ARM ratio close to 1 may lead to an overestimation of paleointensity where DRM and CRM components coexist, and CRM remains undetected. Our results indicate that positive anomalies in paleointensity that are coupled to positive MDF_{NRM}/MDF_{ARM} anomalies can be indicative of paleointensity biases due to CRM. A combination of the two proxies, which are both based on standard parameters that often determined in paleo- and rock-magnetic studies, can help distinguishing DRM and CRM in natural sediments.

Acknowledgements

We thank Dr. Przemysław Kryczka from Mag-Instruments for providing a portable spinning magnetometer. This work was supported by the Deutsche Forschungsgemeinschaft (GI712/16-1).

References

Berner, R.A., 1981. A New Geochemical Classification of Sedimentary Environments. Journal of Sedimentary Research Vol. 51 (2), 359–365.

Bilardello, D., Jezek, J., Gilder, S.A., 2013. Role of spherical particles on magnetic field recording in sediments: Experimental and numerical results. Physics of the Earth and Planetary Interiors 214, 1–13.

Butler, R.F., 1992. Paleomagnetism: magnetic domains to geologic terranes. American Library Association.

Chang, L., Roberts, A.P., Rowan, C.J., Tang, Y., Pruner, P., Chen, Q., Horng, C.-S., 2009. Low-temperature magnetic properties of greigite (Fe_3S_4). Geochemistry, Geophysics, Geosystems 10 (1).

Chang, L., Roberts, A.P., Tang, Y., Rainford, B.D., Muxworthy, A.R., Chen, Q., 2008. Fundamental magnetic parameters from pure synthetic greigite (Fe_3S_4). J. Geophys. Res. 113 (B6).

Channell, J., Xuan, C., Hodell, D.A., 2009. Stacking paleointensity and oxygen isotope data for the last 1.5 Myr (PISO-1500). Earth and Planetary Science Letters 283 (1-4), 14–23.

Day, R., Fuller, M., Schmidt, V.A., 1977. Hysteresis properties of titanomagnetites: Grain-size and compositional dependence. Physics of the Earth and Planetary Interiors 13 (4), 260–267.

Dekkers, M.J., Schoonen, M.A.A., 1996. Magnetic properties of hydrothermally synthesized greigite (Fe_3S_4)—I. Rock magnetic parameters at room temperature. Geophysical Journal International 126 (2), 360–368.

Dunlop, D.J., 2002. Theory and application of the Day plot (M_{rs}/M_s versus H_{cr}/H_c) 1. Theoretical curves and tests using titanomagnetite data. Journal of Geophysical Research 107 (B3).

Dunlop, D.J., Özdemir, Ö., 1997. Rock magnetism: Fundamentals and frontiers. Cambridge University Press, Cambridge, 573 pp.

Egli, 2021. Magnetic characterization of geologic materials with first-order reversal curves, in: Victorino, F., Dodrill, B. (Eds.), Magnetic Measurement Techniques for Materials Characterization. Springer, pp. 455–604.

Egli, R., 2006. Theoretical considerations on the anhysteretic remanent magnetization of interacting particles with uniaxial anisotropy. J. Geophys. Res. 111 (B12S18).

Egli, R., 2013. VARIFORC: An optimized protocol for calculating non-regular first-order reversal curve (FORC) diagrams. Global and Planetary Change 110, 302–320.

Evans, M.E., Heller, F., 2003. Environmental magnetism: Principles and applications of enviromagnetics. Academic Press, Amsterdam, Boston, 299 pp.

Fabian, K., 2009. Thermochemical remanence acquisition in single-domain particle ensembles: A case for possible overestimation of the geomagnetic paleointensity. Geochemistry, Geophysics, Geosystems 10 (Q6).

Fisher, R., 1953. Dispersion on a Sphere. Proceedings of the Royal Society A: Mathematical, Physical and Engineering Sciences 217 (1130), 295–305.

Frank, M., Schwarz, B., Baumann, S., Kubik, P.W., Suter, M., Mangini, A., 1997. A 200 kyr record of cosmogenic radionuclide production rate and geomagnetic field intensity from 10Be in globally stacked deep-sea sediments. Earth and Planetary Science Letters 149 (1-4), 121–129.

Fu, Y., Dobeneck, T. von, Franke, C., Heslop, D., Kasten, S., 2008. Rock magnetic identification and geochemical process models of greigite formation in Quaternary marine sediments from the Gulf of Mexico (IODP Hole U1319A). Earth and Planetary Science Letters 275 (3-4), 233–245.

Gorlas, A., Jacquemot, P., Guigner, J.-M., Gill, S., Forterre, P., Guyot, F., 2018. Greigite nanocrystals produced by hyperthermophilic archaea of Thermococcales order. PloS One 13 (8), e0201549.

Gosse, J.C., Phillips, F.M., 2001. Terrestrial in situ cosmogenic nuclides: theory and application. Quaternary Science Reviews 20 (14), 1475–1560.

Gradstein, F.M., Ogg, J.G., Schmitz, M.D., Ogg, G.M. (Eds.), 2020. Geologic Time Scale 2020. Elsevier, Amsterdam, 1 Online-Ressource 2 Bände.

Gražulis, S., Daškevič, A., Merkys, A., Chateigner, D., Lutterotti, L., Quirós, M., Serebryanaya, N.R., Moeck, P., Downs, R.T., Le Bail, A., 2012. Crystallography Open Database (COD): an open-access

collection of crystal structures and platform for world-wide collaboration. Nucleic acids research 40, D420-7.

Haigh, G., 1958. The process of magnetization by chemical change. Philosophical Magazine 3 (27), 267–286.

Hallam, D.F., Maher, B.A., 1994. A record of reversed polarity carried by the iron sulphide greigite in British early Pleistocene sediments. Earth and Planetary Science Letters 121 (1-2), 71–80.

Harrison, R.J., Feinberg, J.M., 2008. FORCinel: An improved algorithm for calculating first-order reversal curve distributions using locally weighted regression smoothing. Geochemistry, Geophysics, Geosystems 9 (Q5).

Harrison, R.J., Lascu, I., 2014. FORCulator: A micromagnetic tool for simulating first-order reversal curve diagrams. Geochemistry, Geophysics, Geosystems 15 (12), 4671–4691.

Hesse, P.P., 1994. Evidence for bacterial palaeoecological origin of mineral magnetic cycles in oxic and sub-oxic Tasman Sea sediments. Marine Geology 117 (1-4), 1–17.

Hu, S., Appel, E., Hoffmann, V., Schmahl, W.W., Wang, S., 1998. Gyromagnetic remanence acquired by greigite (Fe_3S_4) during static three-axis alternating field demagnetization. Geophys J Int 134 (3), 831–842.

Hunger, S., Benning, L.G., 2007. Greigite: a true intermediate on the polysulfide pathway to pyrite. Geochemical Transactions 8 (1), 1.

Igarashi, K., Yamamura, Y., Kuwabara, T., 2016. Natural synthesis of bioactive greigite by solid–gas reactions. Geochimica et Cosmochimica Acta 191, 47–57.

Jackson, M., Swanson-Hysell, N.L., 2012. Rock magnetism of remagnetized carbonate rocks: another look. Geological Society, London, Special Publications 371 (1), 229–251.

Jiang, W.-T., Horng, C.-S., Roberts, A.P., Peacor, D.R., 2001. Contradictory magnetic polarities in sediments and variable timing of neoformation of authigenic greigite. Earth and Planetary Science Letters 193 (1-2), 1–12.

Jiang, Z., Liu, Q., Dekkers, M.J., Barrón, V., Torrent, J., Roberts, A.P., 2016. Control of Earth-like magnetic fields on the transformation of ferrihydrite to hematite and goethite. Scientific Reports 6, 30395.

Johnson, E.A., Murphy, T., Torreson, O.W., 1948. Pre-history of the Earth's magnetic field. J. Geophys. Res. 53 (4), 349.

Just, J., Sagnotti, L., Nowaczyk, N.R., Francke, A., Wagner, B., 2019. Recordings of fast paleomagnetic reversals in a 1.2 Ma greigite-rich sediment archive from Lake Ohrid, Balkans. Journal of Geophysical Research: Solid Earth 124 (12), 12445–12464.

Karlin, R., Levi, S., 1983. Diagenesis of magnetic minerals in Recent haemipelagic sediments. Nature 303 (5915), 327–330.

Kodama, K.P., 2012. Paleomagnetism of sedimentary rocks: Process and interpretation. John Wiley & Sons, Chichester West Sussex, Hoboken NJ, 157 pp.

Kopp, R.E., Raub, T.D., Schumann, D., Vali, H., Smirnov, A.V., Kirschvink, J.L., 2007. Magnetofossil spike during the Paleocene-Eocene thermal maximum: Ferromagnetic resonance, rock magnetic, and electron microscopy evidence from Ancora, New Jersey, United States. Paleoceanography 22 (4).

Larrasoaña, J.C., Roberts, A.P., Musgrave, R.J., Gràcia, E., Piñero, E., Vega, M., Martínez-Ruiz, F., 2007. Diagenetic formation of greigite and pyrrhotite in gas hydrate marine sedimentary systems. Earth and Planetary Science Letters 261 (3-4), 350–366.

Lefèvre, C.T., Bazylinski, D.A., 2013. Ecology, diversity, and evolution of magnetotactic bacteria. Microbiol Mol Biol Rev 77 (3), 497–526.

Li, G., Zhang, B., Yu, F., Novakova, A.A., Krivenkov, M.S., Kiseleva, T.Y., Chang, L., Rao, J., Polyakov, A.O., Blake, G.R., Groot, R.A. de, Palstra, T.T.M., 2014. High-purity Fe_3S_4 greigite microcrystals for magnetic and electrochemical performance. Chemistry of Materials 26 (20), 5821–5829.

Maher, B.A., Thompson, R., 1999. Quaternary Climates, Environments and Magnetism. Cambridge University Press.

McClelland, E., 1996. Theory of CRM acquired by grain growth, and its implications for TRM discrimination and palaeointensity determination in igneous rocks. Geophysical Journal International 126 (1), 271–280.

Muxworthy, A., 2003. Effect of magnetostatic interactions on the hysteresis parameters of single-domain and pseudo-single-domain grains. Journal of Geophysical Research 108 (B11).

Muxworthy, A.R., 2001. Effect of grain interactions on the frequency dependence of magnetic susceptibility. Geophysical Journal International 144 (2), 441–447.

Muxworthy, A.R., Williams, W., Roberts, A.P., Winklhofer, M., Chang, L., Pósfai, M., 2013. Critical single domain grain sizes in chains of interacting greigite particles: Implications for magnetosome crystals. Geochemistry, Geophysics, Geosystems 14 (12), 5430–5441.

Nagata, T., 1961. Rock magnetism. Maruzen Company.

Néel, L., 1949. Théorie du traînage magnétique des ferromagnétiques en grains fins avec application aux terres cuites. Annales de géophysique 5, 99-136.

Nowaczyk, N.R., Liu, J., Arz, H.W., 2020. Records of the Laschamps geomagnetic polarity excursion from Black Sea sediments: magnetite versus greigite, discrete sample versus U-channel data. Geophysical Journal International 224 (2), 1079–1095.

Ogg, J.G., 2020. Chapter 5 - Geomagnetic Polarity Time Scale, in: Gradstein, F.M., Ogg, J.G., Schmitz, M.D., Ogg, G.M. (Eds.), Geologic Time Scale 2020. Elsevier, Amsterdam, pp. 159–192.

Ohfuji, H., Rickard, D., 2006. High resolution transmission electron microscopic study of synthetic nanocrystalline mackinawite. Earth and Planetary Science Letters 241 (1-2), 227–233.

Pick, T., Tauxe, L., 1991. Chemical remanent magnetization in synthetic magnetite. Journal of Geophysical Research 96 (B6), 9925.

Pike, C.R., Roberts, A.P., Verosub, K.L., 1999. Characterizing interactions in fine magnetic particle systems using first order reversal curves. Journal of Applied Physics 85 (9), 6660–6667.

Pike, C.R., Roberts, A.P., Verosub, K.L., 2001. First-order reversal curve diagrams and thermal relaxation effects in magnetic particles. Geophysical Journal International 145 (3), 721–730.

Posfai, M., 2006. Sulfides in Biosystems. Reviews in Mineralogy and Geochemistry 61 (1), 679–714.

Rickard, D., 1995. Kinetics of FeS precipitation: Part 1. Competing reaction mechanisms. Geochimica et Cosmochimica Acta 59 (21), 4367–4379.

Rickard, D., 2012. Sedimentary Sulfides, in: Rickard, D.T. (Ed.), Sulfidic sediments and sedimentary rocks, vol. 65. Elsevier Science Ltd, Oxford, pp. 543–604.

Rickard, D., Butler, I.B., Oldroyd, A., 2001. A novel iron sulphide mineral switch and its implications for Earth and planetary science. Earth and Planetary Science Letters 189 (1-2), 85–91.

Roberts, A.P., 2015. Magnetic mineral diagenesis. Earth-Science Reviews 151, 1–47.

Roberts, A.P., Chang, L., Heslop, D., Florindo, F., Larrasoaña, J.C., 2012. Searching for single domain magnetite in the "pseudo-single-domain" sedimentary haystack: Implications of biogenic magnetite preservation for sediment magnetism and relative paleointensity determinations. Journal of Geophysical Research 117 (B8).

Roberts, A.P., Chang, L., Rowan, C.J., Horng, C.-S., Florindo, F., 2011a. Magnetic properties of sedimentary greigite (Fe_3S_4): An update. Reviews of Geophysics 49 (1).

Roberts, A.P., Florindo, F., Chang, L., Heslop, D., Jovane, L., Larrasoaña, J.C., 2013a. Magnetic properties of pelagic marine carbonates. Earth-Science Reviews 127, 111–139.

Roberts, A.P., Florindo, F., Villa, G., Chang, L., Jovane, L., Bohaty, S.M., Larrasoaña, J.C., Heslop, D., Fitz Gerald, J.D., 2011b. Magnetotactic bacterial abundance in pelagic marine environments is limited by organic carbon flux and availability of dissolved iron. Earth and Planetary Science Letters 310 (3-4), 441–452.

Roberts, A.P., Jiang, W.-T., Florindo, F., Horng, C.-S., Laj, C., 2005. Assessing the timing of greigite formation and the reliability of the Upper Olduvai polarity transition record from the Crostolo River, Italy. Geophysical Research Letters 32 (5).

Roberts, A.P., Liu, Q., Rowan, C.J., Chang, L., Carvallo, C., Torrent, J., Horng, C.-S., 2006. Characterization of hematite (α-Fe_2O_3), goethite (α-FeOOH), greigite (Fe_3S_4), and pyrrhotite (Fe_7S_8) using first-order reversal curve diagrams. Journal of Geophysical Research 111 (B12).

Roberts, A.P., Tauxe, L., Heslop, D., 2013b. Magnetic paleointensity stratigraphy and high-resolution Quaternary geochronology: successes and future challenges. Quaternary Science Reviews 61, 1–16.

Roberts, A.P., Weaver, R., 2005. Multiple mechanisms of remagnetization involving sedimentary greigite (Fe_3S_4). Earth and Planetary Science Letters 231 (3-4), 263–277.

Roberts, A.P., Zhao, X., Harrison, R.J., Heslop, D., Muxworthy, A.R., Rowan, C.J., Larrasoaña, J.-C., Florindo, F., 2018. Signatures of reductive magnetic mineral diagenesis from unmixing of first-order reversal curves. Journal of Geophysical Research: Solid Earth 123 (6), 4500–4522.

Ron, H., Nowaczyk, N.R., Frank, U., Schwab, M.J., Naumann, R., Striewski, B., Agnon, A., 2007. Greigite detected as dominating remanence carrier in Late Pleistocene sediments, Lisan formation, from Lake Kinneret (Sea of Galilee), Israel. Geophysical Journal International 170 (1), 117–131.

Rowan, C.J., Roberts, A.P., 2006. Magnetite dissolution, diachronous greigite formation, and secondary magnetizations from pyrite oxidation: Unravelling complex magnetizations in Neogene marine sediments from New Zealand. Earth and Planetary Science Letters 241 (1-2), 119–137.

Sagnotti, L., Roberts, A.P., Weaver, R., Verosub, K.L., Florindo, F., Pike, C.R., Clayton, T., Wilson, G.S., 2005. Apparent magnetic polarity reversals due to remagnetization resulting from late diagenetic growth of greigite from siderite. Geophysical Journal International 160 (1), 89–100.

Scherrer, P., 1912. Bestimmung der inneren Struktur und der Größe von Kolloidteilchen mittels Röntgenstrahlen, in: Zsigmondy, R. (Ed.), Kolloidchemie Ein Lehrbuch. Springer, Berlin, Heidelberg, pp. 387–409.

Schneider, C.A., Rasband, W.S., Eliceiri, K.W., 2012. NIH Image to ImageJ: 25 years of image analysis. Nature Methods 9 (7), 671–675.

Schoonen, M.A., 2004. Mechanisms of sedimentary pyrite formation, in: Amend, J.P., Edwards K. J., Lyons, T.W. (Eds.), Sulfur Biogeochemistry - Past and Present, vol. 379. Geological Society of America, pp. 117–134.

Shcherbakov, V., Sycheva, N., 2010. On the mechanism of formation of depositional remanent magnetization. Geochemistry, Geophysics, Geosystems 11 (Q2).

Shcherbakov, V.P., Shcherbakova, V.V., 1983. On the theory of depositional remanent magnetization in sedimentary rocks. Geophysical Surveys 5 (4), 369–380.

Simon, Q., Thouveny, N., Bourlès, D.L., Valet, J.-P., Bassinot, F., Ménabréaz, L., Guillou, V., Choy, S., Beaufort, L., 2016. Authigenic 10Be/9Be ratio signatures of the cosmogenic nuclide production linked to geomagnetic dipole moment variation since the Brunhes/Matuyama boundary. Journal of Geophysical Research: Solid Earth 121 (11), 7716–7741.

Snowball, I., Thompson, R., 1990. A stable chemical remanence in Holocene sediments. Journal of Geophysical Research 95 (B4), 4471.

Snowball, I.F., 1997. Gyroremanent magnetization and the magnetic properties of greigite-bearing clays in southern Sweden. Geophysical Journal International 129 (3), 624–636.

Stacey, F.D., 1972. On the role of Brownian motion in the control of detrital remanent magnetization of sediments. Pure and Applied Geophysics 98 (1), 139–145.

Stacey, F.D., Banerjee, S.K., 1974. The physical principles of rock magnetism. Elsevier Scientific Pub. Co, Amsterdam, New York, 195 pp.

Stokking, L.B., Tauxe, L., 1990. Properties of chemical remanence in synthetic hematite: Testing theoretical predictions. Journal of Geophysical Research 95 (B8), 12639.

Stoner, J., Laj, C., Channell, J., Kissel, C., 2002. South Atlantic and North Atlantic geomagnetic paleointensity stacks (0–80ka): implications for inter-hemispheric correlation. Quaternary Science Reviews 21 (10), 1141–1151.

Sugiura, N., 1979. ARM, TRM and magnetic interactions: Concentration dependence. Earth and Planetary Science Letters 42 (3), 451–455.

Tauxe, L., 1993. Sedimentary records of relative paleointensity of the geomagnetic field: Theory and practice. Reviews of Geophysics 31 (3), 319.

Tauxe, L., Steindorf, J.L., Harris, A., 2006. Depositional remanent magnetization: Toward an improved theoretical and experimental foundation. Earth and Planetary Science Letters 244 (3-4), 515–529.

Till, J.L., Guyodo, Y., Lagroix, F., Ona-Nguema, G., Brest, J., 2014. Magnetic comparison of abiogenic and biogenic alteration products of lepidocrocite. Earth and Planetary Science Letters 395, 149–158.

Valdez-Grijalva, M.A., Nagy, L., Muxworthy, A.R., Williams, W., Fabian, K., 2018. The magnetic structure and palaeomagnetic recording fidelity of sub-micron greigite (Fe_3S_4). Earth and Planetary Science Letters 483, 76–89.

Valet, J.-P., 2003. Time variations in geomagnetic intensity. Reviews of Geophysics 41 (1).

Vreumingen, M.J., 1993. The magnetization intensity of some artificial suspensions while flocculating in a magnetic field. Geophysical Journal International 114 (3), 601–606.

Weninger, B., Jöris, O., 2008. A 14C age calibration curve for the last 60 ka: the Greenland-Hulu U/Th timescale and its impact on understanding the Middle to Upper Paleolithic transition in Western Eurasia. Journal of human evolution 55 (5), 772–781.

White, L.M., Bhartia, R., Stucky, G.D., Kanik, I., Russell, M.J., 2015. Mackinawite and greigite in ancient alkaline hydrothermal chimneys: Identifying potential key catalysts for emergent life. Earth and Planetary Science Letters 430, 105–114.

Wilkin, R.T., Barnes, H.L., 1996. Pyrite formation by reactions of iron monosulfides with dissolved inorganic and organic sulfur species. Geochimica et Cosmochimica Acta 60 (21), 4167–4179.

Winklhofer, M., Chang, L., Eder, S.H.K., 2014. On the magnetocrystalline anisotropy of greigite (Fe_3S_4). Geochemistry, Geophysics, Geosystems 15 (4), 1558–1579.

Worm, H.-U., 1998. On the superparamagnetic-stable single domain transition for magnetite, and frequency dependence of susceptibility. Geophysical Journal International 133 (1), 201–206.

Zhao, X., Egli, R., Gilder, S.A., Müller, S., 2016. Microbially assisted recording of the Earth's magnetic field in sediment. Nature Communications 7, 10673.